



Isotopes and the characterization of extrasolar planets

Yapeng Zhang

张雅鹏

Isotopes and the characterization of extrasolar planets

Proefschrift

ter verkrijging van
de graad van doctor aan de Universiteit Leiden,
op gezag van rector magnificus prof.dr.ir. H. Bijl,
volgens besluit van het college voor promoties
te verdedigen op dinsdag 6 juni 2023
klokke 10:00 uur

door

Yapeng Zhang

geboren te Datong, China
in 1995

Promotor: Prof.dr. I.A.G. Snellen

Co-promotor: Prof.dr. L. Kreidberg (Max Planck Institute for Astronomy)

Promotiecommissie: Prof.dr. S. Viti
Dr. A. De Almeida Vidotto
Prof. dr. M. Hogerheijde
Dr. A. Oklopčić (University of Amsterdam)
Prof.dr. H.A. Knutson (California Institute of Technology)

ISBN: 978-94-6469-382-9

Printed by: ProefschriftMaken

Cover: Gas giant exoplanets with a protoplanetary disk, generated with the AI program Midjourney using a painting by Yapeng Zhang as an image prompt.

An electronic version of this dissertation is available at
<https://openaccess.leidenuniv.nl>.

Two things fill the mind with ever new and increasing admiration and awe, the more often and steadily we reflect upon them: the starry heavens above me and the moral law within me. I do not seek or conjecture either of them as if they were veiled obscurities or extravagances beyond the horizon of my vision; I see them before me and connect them immediately with the consciousness of my existence.

- Immanuel Kant

Contents

1	Introduction	1
1.1	Search for exoplanets.	1
1.2	Probing exoplanet atmospheres	5
1.2.1	Transit spectroscopy	5
1.2.2	Direct-imaging spectroscopy	5
1.2.3	High-resolution spectroscopy	6
1.2.4	Retrieval of exoplanet atmospheres.	8
1.3	Planet formation	8
1.3.1	Formation of gas giant planets	8
1.3.2	Observational probes of formation history	9
1.4	This thesis	10
1.5	Outlook: unravel the origin of planets	12
2	The ^{13}CO-rich atmosphere of a young accreting super-Jupiter	15
2.1	Result	16
2.2	Method.	20
2.2.1	Observations and data analysis.	20
2.2.2	Atmospheric retrieval model	23
2.2.3	Retrievals on the TYC 8998 b spectrum.	24
2.2.4	Effects of clouds	26
2.2.5	Constraining mass accretion rate.	26
2.3	Additional assessments of the reliability of ^{13}CO detection in TYC 8998 b	26
2.3.1	Analysis on data of individual nights and bandheads	27
2.3.2	The impact of telluric absorption	28
2.3.3	Other potential opacity sources	29
2.3.4	Archival reference data of the young brown dwarf 2M0355.	29
3	The $^{12}\text{CO}/^{13}\text{CO}$ isotopologue ratio of a young, isolated brown dwarf	31
3.1	Introduction	32
3.2	Observations and spectrum extraction	34
3.2.1	Keck/NIRSPEC archival data	34
3.2.2	VLT/CRIRES+ science verification observations	36
3.3	Retrieval analysis	36
3.3.1	Atmospheric retrieval model	36
3.3.2	Retrieving 2M0355	37
3.4	Results	39
3.4.1	Retrieval results	39
3.4.2	^{13}CO detection	40
3.4.3	Hint of C^{18}O	41

3.5	Discussion	45
3.5.1	CO isotopologue ratio in 2M0355.	45
3.5.2	Implications for planet formation	45
3.6	Conclusion.	46
4	Search for Helium airglow emission from the hot Jupiter τ Boo b	47
4.1	Introduction	48
4.2	Helium emission from extended atmospheres	49
4.3	The τ Boo system	50
4.4	Observations and Data analysis	51
4.4.1	Data analysis.	52
4.4.2	Extra noise in residual spectra	54
4.5	Result	56
4.5.1	Detection limits	56
4.5.2	Validation of signal recovery	58
4.6	Discussion	59
4.6.1	Detectability of He emission	59
4.6.2	Future prospects	60
4.7	Conclusions	62
4.A	Derivation of helium emission strength with radiative transfer.	63
4.A.1	Optically thick	63
4.A.2	Optically thin	63
5	Transmission spectroscopy of the ultra-hot Jupiter MASCARA-4 b	65
5.1	Introduction	66
5.2	Observations and data reduction	68
5.2.1	Radial velocity measurements with CORALIE and updated planet mass	68
5.2.2	Photometry with EulerCam	69
5.2.3	High-resolution transmission spectroscopy with ESPRESSO	70
5.3	Data analysis.	72
5.3.1	Stellar pulsations.	72
5.3.2	Rossiter-McLaughlin reloaded	73
5.3.3	Modeling RM and CLV effects	74
5.3.4	Transmission spectrum.	74
5.3.5	Cross-correlation analysis	74
5.4	Results	77
5.4.1	Detection of individual lines of H I, Na I, Ca II, Mg I, Fe I, Fe II	77
5.4.2	Detection of species in cross-correlation	77
5.4.3	Neutral and Ionized iron in MASCARA-4b and other UHJs.	78
5.5	Discussion	82
5.5.1	Disentangling the hydrostatic atmosphere and extended exosphere of UHJs.	82
5.5.2	Hydrodynamic exospheres as probed via $H\alpha$ and ions	84

5.6	Conclusion	85
5.A	Analytical estimation of atomic absorption in exospheres	86
5.B	Summary of UHJs with detailed characterisation with high-resolution transmission spectroscopy.	89
6	DESTINYs: Diverse outcomes of binary-disk interactions	91
6.1	Introduction	92
6.2	Individual system properties	94
6.3	Observations and data reduction	95
6.3.1	SPHERE/IRDIS observations	95
6.3.2	Archival HST, VLT/NACO, and SPHERE data	96
6.3.3	Archival ALMA data	97
6.4	Results	97
6.4.1	Polarimetric analysis	97
6.4.2	Astrometry and orbit analysis	101
6.5	Discussion	106
6.5.1	Individual systems	106
6.5.2	Binary-disk interactions and planet formation	109
6.6	Conclusion.	111
6.A	Morphology of disks in S CrA	112
6.B	SPHERE ADI imaging of the system S CrA	113
6.C	Orbit fitting for CHX 22 with the possibility of unbound orbits.	115
6.D	SPHERE and ALMA data overlay.	116
6.E	Coronagraphic images of CHX 22, S CrA, and HP Cha	117
	Bibliography	121
	Summary	139
	Nederlandse Samenvatting	143
	List of Publications	147
	Curriculum Vitæ	149
	Acknowledgments	151

1

Introduction

1.1 Search for exoplanets

How did we come into existence? Are we alone? The origin of life and the uniqueness of our position in the universe have been enduring quests of human beings. Despite speculations of the extrasolar planets and extra-terrestrial life for centuries, only three decades ago did astronomers start to peer into the diverse alien worlds beyond our own solar system. In 1992 Wolszczan & Frail (1992) first discovered planetary-mass objects orbiting the pulsar PSR B1257+12, which is a rapidly rotating neutron star. In contrast to the solar-system objects around our main sequence star, these planets were believed to be second generation products that formed in the debris disk after the catastrophic stellar evolution (Podsiadlowski et al., 1991). The first exoplanet around a main sequence star was discovered by Mayor & Queloz (1995), hallmarking the inception of exoplanetary science and awarded the Nobel Prize in Physics in 2019. This study detected a Jupiter-like gaseous planet orbiting the solar-type star 51 Pegasi. Strikingly, the planet 51 Pegasi b orbits its star at a separation of only 0.05 au (much smaller than Mercury's distance to the Sun), equating to an orbital period of 4.2 days. Ensuing the first breakthrough, a population of such close-in exoplanets has emerged, known as Hot Jupiters. Where did such planets form? How did they get there? Why are they so distinct from solar-system planets? These peculiar new worlds, with no analogs in our solar system, posed great challenges but also opened new windows to our understanding of planet formation and evolution.

Hitherto, over five thousand exoplanets have been discovered with various methods, including radial velocity, transit observations, and direct imaging. The planet mass versus semi-major axis diagram of the known exoplanet population is shown in Figure 1.1, illustrating the great diversity of exoplanets and large range in parameter space. The diagram reveals several classes that have no counterparts in the solar system, such as Hot Jupiters, super Jupiters (wide-orbit massive Jovian planets), and super-Earths and mini-Neptunes (planets with intermediate sizes between the Earth and the Neptune). Each detection technique has its own biases towards certain planet types as discussed below.

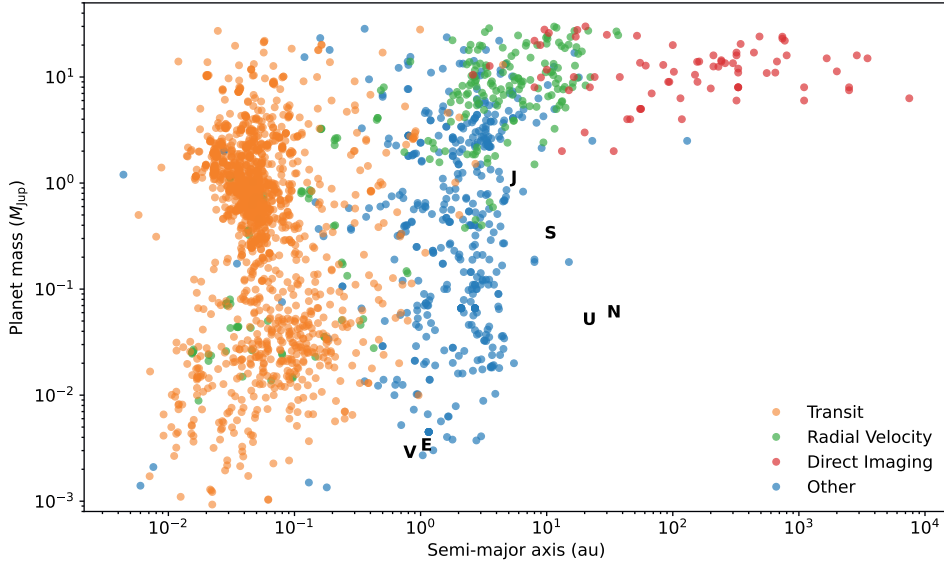


Figure 1.1: Planet mass versus semi-major axis of confirmed exoplanets, color-coded by detection method. The data were collected from the NASA Exoplanet Archive. The black letters denote the planets in the solar system.

Radial velocity

The radial velocity (RV) method makes use of the reflex motion of the host stars induced by the gravitational pull from the planets. These stellar wobbles result in periodic changes of the stellar velocity along the line of sight, which can be detected by measuring the Doppler shift of stellar spectral lines. The amplitude of the RV variation mainly depends on the planet mass and orbital distance as follows.

$$K \propto a^{-1/2} M_p \sin i \quad (1.1)$$

where K is the semi-amplitude of the RV variation, M_p is the planet mass, a is the semi-major axis of the planet orbit, and i is the orbital inclination. Therefore, the radial velocity method provides constraints on planet mass and it is most sensitive to massive planets at close-in orbits. For example, the first exoplanet 51 pegasasi b was discovered by monitoring the RV change of $K \sim 60 \text{ m s}^{-1}$. As the precision of RV measurements improves significantly over the past decades, the current-generation instrument such as ESO's VLT/ESPRESSO (Pepe et al., 2021) pushes to the limit of a few tens of cm s^{-1} , allowing for detection of rocky planets around low-mass stars, such as Proxima Centauri b and d (Anglada-Escudé et al., 2016, Faria et al., 2022) in the solar neighbourhood (4.2 light-years away from the Sun).

Transit observations

The transit method relies on a special geometry where the planetary orbit has an inclination close to 90° such that the planet passes in front of the host star and periodically blocks part of the stellar disc. This leads to periodic decrease in stellar flux during transit,

which can be detected through photometric monitoring. The depth of the transit signal is proportional to the ratio of the planet-to-star disc area R_p^2/R_*^2 . Therefore this method favors large planets at close-in orbits, as the probability of a planetary orbit aligned to the line of sight scales with the inverse of the orbital distance and thus the transit frequency is higher for close-in planets. Following the first observation of the hot Jupiter HD 209458 b (Charbonneau et al., 2000), the transit method has yielded by far the majority of exoplanet detection thanks to dedicated surveys from both ground and space, such as the Wide Angle Search for Planets (WASP; Pollacco et al., 2006), the Kepler space mission (Borucki et al., 2010), and the Transiting Exoplanet Survey Satellite (TESS; Ricker et al., 2015). Moreover, M dwarfs provide golden opportunities to search for terrestrial planets with the transit method due to their small stellar radii. One of the most intriguing examples is the TRAPPIST-1 system with seven Earth-sized planets around the M dwarf host star (Gillon et al., 2017), a few among which are expected to be located in the habitable zone and able to potentially sustain liquid water on their surface.

Transit detection is often complemented with radial velocity measurements. The combination of both techniques breaks the degeneracy of the planet mass and orbital inclination, allowing for constraints on the bulk density given their masses and radii. The mean density can be compared to theoretical models to constrain the bulk composition of exoplanets (Zeng et al., 2019). Furthermore, measuring radial velocity during transit can provide additional constraints on the projected angle between the planetary orbit and stellar spin axis using the Rossiter-McLaughlin (RM) effect (McLaughlin, 1924, Rossiter, 1924). This effect is the perturbation of stellar lines (hence the radial velocity) as a result of the planet blocking rotationally red-shifted or blue-shifted portions of the stellar disc during transit. It in particular depends on the projected spin-orbit angle, which can provide implications on the dynamical history of planetary systems. Therefore the synergy between the two methods plays an important role in understanding structure, formation, and evolution of exoplanets at population level.

Direct imaging

Direct detection of exoplanets is a highly challenging but rewarding way to probe exoplanets. It requires to overcome the small angular separation between the planet and the host star and the extreme planet-to-star brightness contrast. Therefore this method tends to detect wide-orbit massive giant planets that are still young and self-luminous due to the release of remaining internal energy from their formation processes. To approach deep contrast at small spatial separation, the high-contrast imaging method utilizes adaptive optics (correcting for wave-front aberrations caused by the turbulent Earth's atmosphere and pushing to the diffraction limit), coronagraphy (blocking on-axis starlight and boosting the contrast of off-axis objects, see e.g. Mawet et al.; 2012), and imaging/post-processing techniques for optimal subtraction of the stellar point spread function (e.g. Lagrange et al., 2009, Marois et al., 2006, Sparks & Ford, 2002).

The first direct detection of a planetary-mass companion was on 2M1207 b orbiting around a brown dwarf primary at an separation of >55 au (Chauvin et al., 2004). With the development of new instruments and data-processing techniques, more than 50 super Jupiters have been directly imaged so far, some of which are shown in Figure 1.2, such as the HR 8799 with four giant planets (Marois et al., 2010), PDS 70 with two newborn and accreting protoplanets (Haffert et al., 2019, Keppler et al., 2018). In the past decade, direct

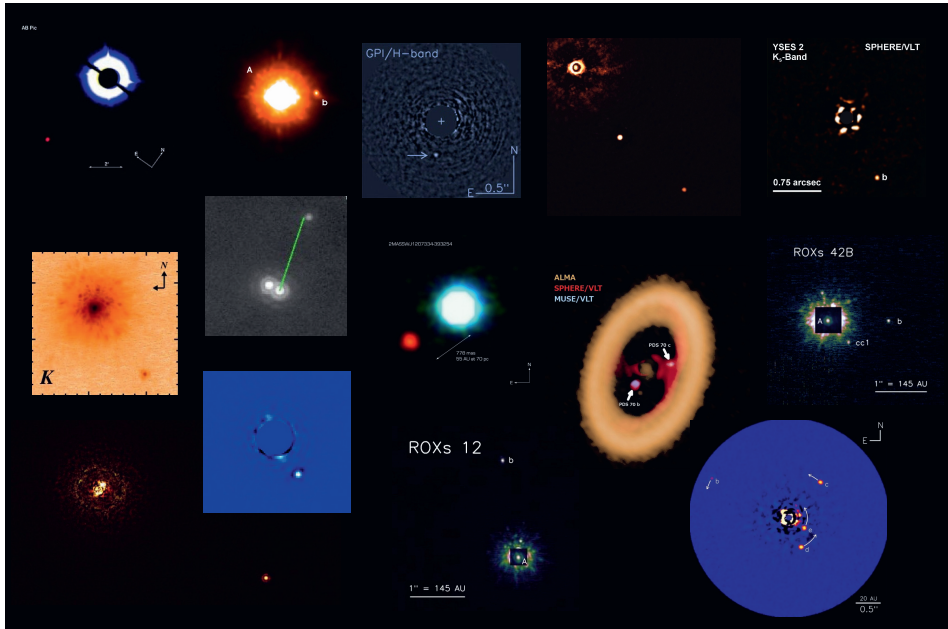


Figure 1.2: Gallery of wide-orbit directly imaged exoplanets collected from the literature (Bohn et al., 2021, 2020, Bowler et al., 2013, Chauvin et al., 2004, 2005, Janson et al., 2021, Keppler et al., 2018, Kraus et al., 2014, Lagrange et al., 2009, Macintosh et al., 2015, Marois et al., 2010, Neuhäuser et al., 2005).

imaging surveys have been delivering new discoveries of exoplanets as well as statistical results on the occurrence rates of super Jupiters, for instance, the Gemini Planet Imager Exoplanet Survey (GPIES, Macintosh et al., 2014), the SpHere INfrared survey for Exoplanets (SHINE, Vigan et al., 2021), the Young Suns Exoplanet Survey (YSES, Bohn et al., 2020), and the Exoplanet Abundance Study (BEAST, Janson et al., 2021). These directly-imaged infant gas giants are excellent laboratories for understanding planet formation.

Direct imaging is powerful to unveil not only exoplanets, but also circumstellar disks, which were composed of gas and dust, and were believed to be the birthplaces of planets. Polarimetric differential imaging (PDI) is one of the most effective methods to capture scattered light from circumstellar disks. The reflected stellar light on dust grains gets polarized through scattering, while the emission from the unresolved central star is predominantly unpolarized. Therefore observing the polarized light assists to filter out the stellar speckle halo and reveal the circumstellar dust. PDI utilizes a polarizing beam splitter to record two orthogonal linear polarization states simultaneously on the detector (de Boer et al., 2020, Dohlen et al., 2008, van Holstein et al., 2020). Since the star exhibits only a low level of polarization, the starlight will be nearly identical in both beams and can be largely removed through the differential between two images, while the polarized scattered light from the disk will show up. A few dozens of circumstellar disks have been imaged in the near-infrared, showing a diverse range of morphological features such as rings, spirals, and shadows (Benisty et al., 2022). Scattered-light observations are suitable for tracing

the surface shape, scale height, and flaring of disks (de Boer et al., 2016), the properties of dust grains as encoded in the intensity and degree of polarization as function of phase angles (Ginski et al. in prep.), providing valuable insights into the birth environment of planets.

1.2 Probing exoplanet atmospheres

As discussed in Section 1.1, it is possible to obtain an initial impression of exoplanet properties especially the bulk density by combining the transit and radial velocity methods. However, large degeneracies hinder detailed analysis of exoplanet compositions using solely planet mass and radius. Spectroscopic observations of exoplanet atmospheres open a critical avenue for a further level of characterization on atmospheric compositions, but also thermal structures and dynamics.

1.2.1 Transit spectroscopy

Transiting planets are ideal targets for atmospheric characterization using transit, secondary eclipse, and phase curve observations. As the planet passes in front of the host star, starlight filters through the terminator region of the planetary atmosphere and gets absorbed due to the opacity of different atoms or molecules. The presence of a certain species results in extra absorption at specific wavelengths, making the planet appear larger. With transmission spectroscopy, we effectively measure the apparent size of the planet as a function of wavelength. The shape of this spectrum depends on the atmospheric composition and other opacity sources such as clouds and hazes.

For example, sodium and water have been detected in exoplanet atmospheres (Charbonneau et al., 2002, Deming et al., 2013, Evans et al., 2016, Kreidberg et al., 2014b). Recently the successful operation of the James Webb Space Telescope (JWST) at infrared wavelengths opens up a new window to other molecules such as CO_2 and SO_2 for the first time (Rustamkulov et al., 2022). The ubiquitous presence of clouds and hazes in exoplanet atmospheres has been inferred by the muted spectral features and even completely featureless transmission spectra (Kreidberg et al., 2014a, Sing et al., 2016). The detection of hydrogen, helium, and ionic species in atmospheres that extend beyond several planetary radii provides direct probes of atmospheric escape by strong high energy stellar irradiation (Ehrenreich et al., 2015, Sing et al., 2019, Spake et al., 2018, Vidal-Madjar et al., 2003).

In addition to probing atmospheric constituents, secondary eclipses (when the planet is eclipsed by the star) and phase curves (the total flux from the system as function of planet orbital phase), probing direct thermal emission from exoplanets, provide constraints on vertical and longitudinal temperature structure, and atmospheric energy transport (Knutson et al., 2008, 2007).

1.2.2 Direct-imaging spectroscopy

Directly imaged planets in wide orbits provide unique opportunities for atmospheric characterization. In contrast to transiting planets, the emission spectra of super Jupiters are directly accessible at higher signal-to-noise (S/N) without significant contamination from their host stars. Spectral observations of direct-imaging planets was first achieved in HR 8799 planets using the medium-resolution ($\lambda/\Delta\lambda = \mathcal{R} \sim 4000$) integral field spectrograph

(IFS) Keck/OSIRIS, providing detection of CO and H₂O, and constraints on temperature and surface gravity (Barman et al., 2011, Konopacky et al., 2013). Another way of probing directly imaged planets with IFS is the molecular mapping method (Hoeijmakers et al., 2018) on β Pictoris b. It takes advantage of the distinct spectral features of the planet and the star to mitigate the starlight contamination and reveal CO and H₂O molecules in the planetary atmosphere. Furthermore, the application of interferometric observations with VLT/GRAVITY on exoplanets shows to be a powerful tool to perform spectroscopy of Jovian planets with small angular separation, such as β Pictoris b and PDS 70 planets (GRAVITY Collaboration et al., 2020, Kammerer et al., 2021, Wang et al., 2021b).

The ground-based spectral observations of directly-imaged planets have been mostly limited to the near-infrared wavelength as a result of exceedingly strong thermal background noise and telluric absorption towards longer wavelengths. Observations from space with JWST will play an important role in unlocking the full infrared spectra of wide-orbit super Jupiters. Recently the 1-20 μm spectrum of VHS 1256-1257b was observed with JWST, unveiling a plethora of spectral details to be exploited (Miles et al., 2022).

1.2.3 High-resolution spectroscopy

High-resolution spectroscopy ($\mathcal{R} > 10000$) has proved to be an important way of studying exoplanet atmospheres. At high spectral resolution, spectral features of different species can be resolved into unique ensembles of individual lines, which allow for unambiguous identification of atoms or molecules and bypass the degeneracy among different absorbing species and clouds at low spectral resolution. However, as light is dispersed into a larger number of spectral channels, the S/N per channel decreases. To enhance the detection of the planetary atmosphere, the cross-correlation method is typically applied in the data analysis of high-resolution spectroscopy. The cross-correlation function (CCF) is calculated as

$$c(\nu, t) = \frac{\sum_i x_i(t) T_i(\nu)}{\sum_i T_i(\nu)}, \quad (1.2)$$

where $x_i(t)$ is the observation at time t and wavelength channel i . $T_i(\nu)$ is the spectral template of a certain species or atmospheric model shifted to a radial velocity ν , such that the CCF effectively co-adds multiple spectral lines weighted by their strengths.

High-resolution spectroscopy can be utilized in parallel with both the aforementioned temporally (close-in exoplanets) and spatially (wide-orbit exoplanets) resolved techniques to provide unprecedented characterization of exoplanet atmospheres. Its first successful application was on the transiting hot Jupiter HD 209458b with VLT/CRIRES by Snellen et al. (2010), leading to the detection of carbon monoxide in the atmosphere and the orbital motion of the planet. This study also suggested the presence of day-to-night winds in the atmosphere of the hot Jupiter, which provides an important probe for the dynamics and energy transport in the highly-irradiated atmospheres. The orbital motion of close-in planets results in a planetary radial velocity variation by a few tens of km s^{-1} during transit. This doppler shift of planetary signal can be resolved with the high-resolution ($\sim 2 \text{ km s}^{-1}$) time-series spectroscopy (see Figure 1.3 for an illustration). The time-varying planetary signal can be disentangled from the relatively static stellar and telluric features using detrending methods such as airmass detrending, principle component analysis, and SYSREM (Birkby et al., 2013, Brogi et al., 2012, de Kok et al., 2013), leading to constraints on

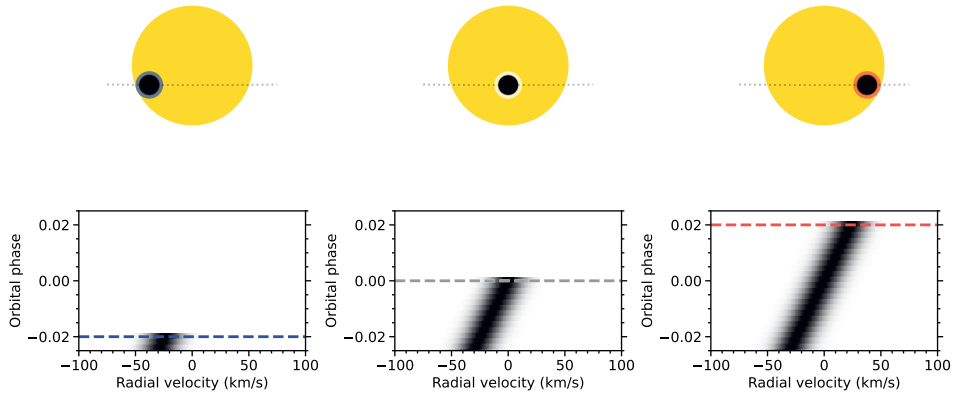


Figure 1.3: Schematic illustration of high-resolution transmission spectroscopy. The top panel comprises the yellow disc denoting the primary star, the black disc representing the transiting planet, and the colored ring showing the terminator region of the planetary atmosphere. Blue color denotes blue-shifted radial velocity of the planet, and red color means red-shifted motion. The bottom panel shows the time-series trace of the noise-free planetary absorption signal (in black shadow) during transit. The slanted planetary signature results from the orbital motion of the planet.

the semi-amplitude of planetary orbital velocity (K_p) and systemic velocity (V_{sys}). Another advantage of the technique is the capability of probing non-transiting close-in exoplanets, such as τ Bootis b and 51 Pegasi b (Birkby et al., 2017, Brogi et al., 2014, 2012). Since then, it has been applied for various species at different wavelength ranges, from atomic to molecular species, from optical to infrared wavelengths (Giacobbe et al., 2021, Hoeijmakers et al., 2018, Prinoth et al., 2022), revealing intriguing physics in hot atmospheres such as the spatial asymmetry of iron absorption in WASP-76b possibly due to condensation of iron or clouds on the nightside (Ehrenreich et al., 2020, Kesseli & Snellen, 2021).

When it comes to the spatially resolved realm, high-resolution spectroscopy can be combined with the high contrast imaging to enhance the S/N (Snellen et al., 2015). The potential of the technique was demonstrated in Snellen et al. (2014), which measured the spin (via the rotational broadening of spectral lines) of the young super-Jupiter β Pictoris b taking advantage of both spatial and spectral distinctions between the planet and its host star (see also Bryan et al., 2018, Schwarz et al., 2016). With the current generation of instruments, efforts to combine high-contrast imaging and high-resolution spectroscopy have been made, such as the Keck Planet Imager and Characterizer (KPIC, Mawet et al., 2016) and High-Resolution Imaging and Spectroscopy of Exoplanets at the VLT (HiRISE, Vigan et al., 2018). This combination facilitates the spectral characterization of super-Jovian companions at small angular separations ($<1''$) such as the HR 8799 planets (Wang et al., 2021a, Xuan et al., 2022). Next-generation facilities (such as ELT/METIS) will allow for probing terrestrial planets around nearby stars (Snellen et al., 2015).

1.2.4 Retrieval of exoplanet atmospheres

Atmospheric retrieval refers to constraining atmospheric properties of exoplanets given spectroscopic observations using inference methods (Madhusudhan, 2018). A retrieval framework is composed of a forward modeling of exoplanet atmospheres coupled with a Bayesian inference algorithm such as Markov chain Monte Carlo (MCMC) or Nested sampling to estimate the posterior distribution of model parameters given the spectral data. As the inference analysis involves over million times of model evaluations, the forward model is typically parametric, one-dimensional, and not self-consistent. The forward model comprises three major parts, the temperature-pressure (T-P) profile, the chemical abundances profile, and the cloud model, prescribing how the temperature, volume mixing ratios of various absorbing species and cloud species change as function of the altitude or pressure in the planetary atmosphere. Subsequently, a radiative transfer code is used to generate synthetic spectra to be compared to observations. In contrast to self-consistent models, the forward model in retrieval analysis provides a higher level of flexibility, therefore leading to better fit to observations, constraining a larger set of atmospheric parameters simultaneously, and further informing missing physical/chemical processes in modeling. Retrievals have been performed with both transmission and emission spectral observations to constrain atmospheric constituents and temperature structure of exoplanets (see e.g. Line et al., 2013, Madhusudhan et al., 2011, Mollière et al., 2020, Waldmann et al., 2015). Recently, retrieval analysis has also been developed for high-resolution spectroscopic observations, which are more sensitive and robust to the relative chemical abundances in atmospheres (Brogi & Line, 2019, Gandhi et al., 2019). The retrieval on the high-resolution spectra of the hot Jupiter WASP-77b provides tight constraints on its metallicity and carbon-to-oxygen ratio (Line et al., 2021) which provides implications on the formation history of this hot Jupiter.

1.3 Planet formation

1.3.1 Formation of gas giant planets

The rapidly growing number and diversity of exoplanets challenge our conventional understanding of planet formation, which had been predominantly established upon studies on the solar system. The routinely discovered super-Earths, mini-Neptunes, and hot Jupiters located in extremely close orbits indicate missing processes in the formation and evolution recipes. The wide-orbit, massive super Jupiters are on the other extreme, which usually straddle the mass boundary of planets and brown dwarfs, and cannot be easily reconciled with in-situ bottom-up formation pathways (Rafikov, 2011). The fundamental questions about gaseous planet formation remain unclear, while three major scenarios have been proposed (see the cartoon illustration in Figure 1.4).

1. Cloud fragmentation. The pre-stellar nebula may fragment and collapse into multiple objects, akin to the formation of multiple stellar systems (Chabrier, 2003, Kroupa, 2001).
2. Gravitational instability. The dense and self-gravitating regions in circumstellar disks may undergo top-down gravitational collapse due to instability (Boss, 1997, Kratter & Lodato, 2016).


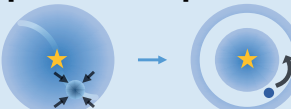
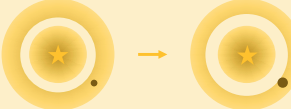
Formation Scenario	Metallicity	C/O	$^{12}\text{C}/^{13}\text{C}$
Cloud fragmentation 	Proto-stellar Same distribution as the brown dwarf population		
Gravitational instability + planetesimal pollution 	Metal enrichment ↑	Proto/sub-stellar — ↓	Proto/sub-stellar — ↓
Core accretion 	Super/sub/proto-stellar higher dispersion in distribution ↑ ↓ —		Bimodal distribution — ↓

Figure 1.4: Schematic overview of possible formation scenarios of super Jupiters and expectation of the distribution of observational properties (metallicity, C/O, and carbon isotopic ratios) in comparison with the brown dwarf population.

3. Core accretion. The dust in protoplanetary disks coagulates and grows into planetesimals which further grow to form proto-planetary cores (via mutual collision or pebble accretion) that are massive enough to initiate runaway gas accretion (Lambrechts & Johansen, 2012, Pollack et al., 1996).

In addition to the unclear formation mechanisms, another complication lies in that planets do not form in isolation. The interactions of proto-planets with gas and dust in circumstellar disks, sibling planets, stellar companions and flybys play important roles in the outcome of planet formation. High angular resolution observations of circumstellar disks across a wide wavelength range reveal ubiquitous substructures (rings, spirals, and cavities) which may be carved by newborn planets (Andrews et al., 2018, Bae et al., 2018, Benisty et al., 2022, Lodato et al., 2019). The (areo)dynamical interactions with the disk can result in the transfer of angular momentum and hence planet migration (Lin & Papaloizou, 1986). This has been considered as one of the main mechanisms to explain the presence of hot Jupiters in close-in orbits (Lin et al., 1996). Planet-planet scattering may also cause migration of gas giant planets to large orbital distances beyond 100 au (Veras et al., 2009). It may account for some wide-orbit planets that are too massive to form in-situ via core accretion given the fast timescale of dust drift in the outer disks.

1.3.2 Observational probes of formation history

One important observational avenue of unraveling planet formation is to probe the chemical composition of planets. The atmospheric elemental abundance ratios such as carbon-to-oxygen (C/O) and nitrogen-to-carbon (N/C) have been proposed as important tracers. As the temperature decreases in protoplanetary disks with the distance to the central star,

molecules will freeze out onto dust grains and get removed from the gas phase to the solid phase, which changes the elemental abundance ratios in the gas and solid reservoirs. Planets formed at different locations with respect to molecular icelines and/or incorporated different amounts of solids, are expected to show distinct chemical abundance ratios in atmospheres (Öberg et al., 2011, Turrini et al., 2021), therefore providing compelling implications on formation pathways, birth locations, and relative contributions of gas versus solid accretion. Observational constraints on C/O ratios in exoplanets, such as β Pic b, HR 8799e, and WASP-77b, allow for interpretation of the formation history. For instance, the substellar C/O ratio in β Pic b supports a core-accretion scenario with substantial planetesimal enrichment (GRAVITY Collaboration et al., 2020), while the HR 8799 planets with C/O ratios consistent with the stellar value may have formed outside the CO₂ or CO iceline (Mollière et al., 2020).

However, none of the single tracers is an unique indicator for planet formation. The process is complicated by intricate substructures, chemical and dust evolution in protoplanetary disks, let alone nuances in orbital migration of planets, evolution of planetary interior and envelope (Guillot & Hueso, 2006, Madhusudhan et al., 2014, Mordasini et al., 2016, van der Marel et al., 2021), making it challenging to draw the exact link between formation histories and observed atmospheric properties. Current studies have been focused on the most accessible probe, C/O ratios, in individual objects, including a few hot Jupiters and young massive super Jupiters. Whereas, the important lessons from the perspective of planet formation suggest that: i) combining multiple observational probes is essential for disentangling the degeneracy and subtlety of planet formation processes; ii) it is crucial to investigate the population-level trends of the observables with planetary properties.

1.4 This thesis

The work presented in this dissertation focuses on spectroscopic characterization of atmospheres in close-in hot Jupiters and wide-orbit super Jupiters. With medium and high-resolution spectroscopic observations, this research investigates a variety of topics on atmospheric compositions, structures, and dynamics of gas giant planets, forming an important step to link the spectral observations of exoplanet atmospheres to planet formation and evolution processes.

Chapter 2: First detection of minor isotopologue ¹³CO in an exoplanet

Isotopes in exoplanet atmospheres have been proposed as interesting tracers of planet formation (Mollière & Snellen, 2019, Morley et al., 2019), as inspired by solar system measurements of deuterium-to-hydrogen (D/H) ratios, which show significant variations across different planets. This is believed to be linked to the varying isotope ratios in protoplanetary disks due to isotope selective processes (called fractionation) that are temperature dependent. Therefore, the location of planet formation, the relative contribution of gas or solid accretion, and the atmospheric loss (as heavy isotopes are less prone to escape from atmospheres) are expected to leave imprints in the planetary isotope ratios. This chapter presents the first detection of the minor isotopologue of carbon monoxide ¹³CO in the atmosphere of the super Jupiter YSES-1 b using the near-infrared integral-field spectrograph SINFONI at the VLT, extending isotopic measurements to exoplanets for the first time. Through modeling of planetary atmospheres and Bayesian retrieval analyses, we deter-

mined the carbon isotope ratio in the planetary atmosphere to be $^{12}\text{CO}/^{13}\text{CO}\sim 31$, which means a factor of two enhancement of ^{13}C compared to the local interstellar medium ($^{12}\text{C}/^{13}\text{C}\sim 68$). To explain this enhancement, we suggested that the planet was formed outside the CO iceline, so as to attain carbon contents mainly from accretion of ^{13}C -enriched ices.

Chapter 3: First detection of minor isotopologue ^{13}CO in a brown dwarf

Following the successful detection of ^{13}CO in the exoplanet YSES 1b, we applied the same method to an exoplanet analog 2M0355, which is a young, isolated brown dwarf with a similar mass and effective temperature as the super Jupiter companion. This study found no enrichment of ^{13}CO in the brown dwarf using archival observations taken with the high-resolution spectrograph NIRSPEC at the Keck observatory. The carbon isotope ratio in this brown dwarf ($^{12}\text{CO}/^{13}\text{CO}\sim 100$) forms stark contrast to that in the exoplanet, hinting at distinct formation pathways. Recently, with follow-up observations of this benchmark brown dwarf taken with the upgraded state-of-the-art spectrograph CRIRES at the VLT, we confirmed the constraint on the carbon isotope ratio and further suggest that even the more challenging oxygen isotope ($^{16}\text{O}/^{18}\text{O}$) ratio is now accessible for brown dwarfs and bright super Jupiters with high-resolution spectroscopy.

Chapter 4: Search for He I airglow emission from hot Jupiter

The closeness of gaseous planets to their host stars can lead to drastic escape of their upper atmospheres due to high-energy stellar radiation, potentially driving the evolution of atmospheres (especially for planets smaller than Neptune). The near-infrared absorption by helium atoms in exoplanet atmospheres has been suggested to be a powerful probe of atmospheric escape in transiting gas giants (Oklopčić & Hirata, 2018, Seager & Saselov, 2000). However, constraining the mass loss rate using helium in absorption alone remains inconclusive because of the degeneracy with the exospheric temperature. To break this degeneracy through combining the same transition in re-emission, we carried out the first search for helium airglow emission in the non-transiting hot Jupiter τ Bootis b with the near-infrared spectrograph CARMENES at the Calar Alto Observatory. This search resulted in a non-detection. We concluded that the current detection limit has not reached the contrast level of the helium emission, but next-generation telescopes will be able to measure this emission. Detecting the helium emission will be important for probing exospheric structure and mass loss rates, hence understanding the bulk-atmospheric evolution of close-in gaseous planets.

Chapter 5: Disentangle hydrostatic and exospheric regimes of ultra-hot Jupiters

The strong high-energy stellar irradiation on close-in hot Jupiters results in two distinct regimes in their atmospheres, the hydrostatic lower atmosphere and the hydrodynamic exosphere, that can be probed with different atoms or molecules. Measuring these species in action will provide essential insights into these unknown processes. The study in this chapter entails the characterization of the ultra-hot Jupiter MASCARA-4b (UHJ, with equilibrium temperatures above 2000 K) using transmission spectroscopic observations taken with the optical high-resolution spectrograph ESPRESSO at the VLT. In addition to detecting a profusion of absorbing species such as H I, Na I, Fe I, and Fe II in the planetary atmosphere, we put the measurements in the context of a sample of seven ultra-hot Jupiters

and investigated the trend of these atomic absorption strengths. The comparison suggested that the neutral metal species trace the hydrostatic regime, while hydrogen and ionized metals probe the hydrodynamic exosphere and the atmospheric escape. This represents the first step towards the population-level analysis of high-resolution spectroscopic results, which enables disentangling different dynamic regimes of highly-irradiated atmospheres.

Chapter 6: Diverse outcomes of binary-disk interactions

To get insights into planet formation, we need to understand circumstellar disks, the cradle of planets. As about half of solar-type stars were born in multiple stellar systems, the presence of stellar companions can modify the morphology and evolution of disks, potentially affecting the outcomes of planet formation. In this chapter, we resolved circumstellar disks using polarimetric differential imaging with SPHERE/IRDIS at the VLT for three multiple systems, namely, CHX 22, S CrA, and HP Cha, as part of the Disk Evolution Study Through Imaging of Nearby Young Stars (DESTINYs) large program. The observed disk morphology in combination with astrometric and orbit analyses for the stellar companions allow for a better understanding of the interplay between disks and companions. The comparison of the three systems spans a wide range of binary separation (50 – 500 au) and illustrates the decreasing influence on disk structures with the distance of companions. This agrees with the statistical analysis of exoplanet population in binaries, that planet formation is likely obstructed around close binary systems, while it is not suppressed in wide binaries.

1.5 Outlook: unravel the origin of planets

Fundamental questions about when, where, and how gas giants form remain open. Do they form via bottom-up or top-down pathways? Do they form in-situ or undergo migration and scattering from a different birth-location? With the ability of reliably retrieving the formation tracers such as elemental and isotopic compositions from near-infrared high-resolution spectra, we will be able to address the questions through population-level analyses of young giant planets and brown dwarfs. Our team at Leiden is carrying out a large observational program with the newly upgraded high-resolution ($\mathcal{R} \sim 100\,000$) spectrograph VLT/CRIRES to survey over twenty super Jupiters, free-floating planets, and brown dwarfs (the **SupJup** Survey). This will provide the first homogeneous comparison of elemental and isotopic constituents in different classes of sub-stellar objects.

We will focus on disentangling formation pathways of planets and brown dwarfs by investigating the extent to which they are chemically and isotopically distinguishable. For instance, if the distribution of chemical properties (such as the median and dispersion of the C/O and carbon isotope ratios) are similar for super Jupiters and brown dwarfs, they may share the same star-like formation pathways (see Figure 1.4). Otherwise, it means that distinct formation scenarios apply to different classes of objects, and we can further explore the trends in elemental and isotopic ratios with stellar and planetary properties such as mass and orbital separation. Either the presence or lack of trends is crucial for assessing the plausibility of various formation scenarios. An interesting example is shown in Figure 1.5 where I compile the current knowledge of C/O and $^{12}\text{C}/^{13}\text{C}$ ratios in super Jupiters and brown dwarfs from our preliminary analysis of archival data and the

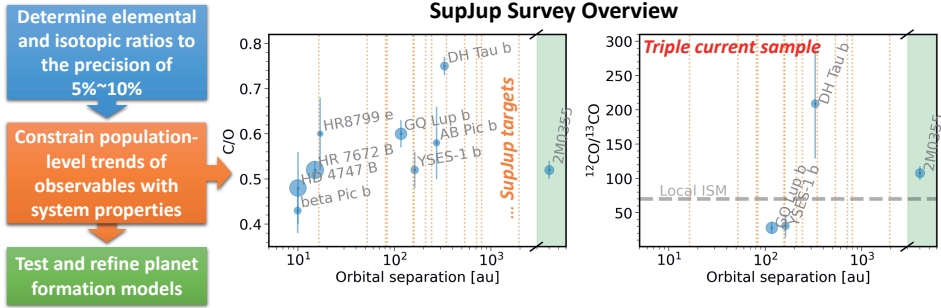


Figure 1.5: Atmospheric C/O and $^{12}\text{CO}/^{13}\text{CO}$ ratios against orbital distances of super Jupiters and brown dwarfs, suggesting a marginal trend of higher ratios at larger orbital distances. The size of the symbols indicates the estimated mass of the object. The vertical dotted lines suggest additional targets to be observed in the SupJup survey, which will triple the sample size, expand the coverage of the parameter space, and reveal a clearer picture of the presence or lack of trends.

literature (GRAVITY Collaboration et al., 2020, Mollière et al., 2020, Wang et al., 2022, Xuan et al., 2022, Zhang et al., 2021a,b). The marginal yet emerging trend of the ratios with orbital separations, which, as a key prediction of planet formation models, can be utilized for testing their validity. With the upcoming SupJup survey we will gain insights into such trends as we expand the sample size and improve the precision of measurements (see Figure 1.5). The census of chemical composition will contribute to bridging the gap between atmospheric observations and planet formation and evolution, and addressing the fundamental question of what distinguishes planets from brown dwarfs.

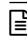
Furthermore, observations from space (JWST) with high sensitivity and unique wavelength coverage allow for filling the gap in the parameter space that is not accessible from the ground, such as studying colder gas giants on wide orbits and probing emission in the mid-infrared. The cross-validation and synergy between the space-based medium-resolution observations and the ground-based high-resolution data will provide complementary information on atmospheric properties (Brogi & Line, 2019) and mark an important step towards more accurate measurements of atmospheric constituents.

Looking further towards the future, the upcoming thirty-meter class telescopes such as the Extremely Large Telescope (ELT, first light expected in five years) and the next-generation flagship space telescope will routinely deliver characterization for smaller exoplanets with the potential of investigating atmospheric biosignatures and habitability (Kaltenegger, 2017, Meadows et al., 2018, Serindag & Snellen, 2019). The ELT will be promising for probing rare isotopes such as deuterium in exoplanets (Mollière & Snellen, 2019), which is one of the most informative tracers of planet formation and atmospheric evolution. Hopefully, we will be able to start answering the ultimate questions of how unique our solar system is and how we get here.

2

The ^{13}C O-rich atmosphere of a young accreting super-Jupiter

Isotope abundance ratios play an important role in astronomy and planetary sciences, providing insights in the origin and evolution of the Solar System, interstellar chemistry, and stellar nucleosynthesis. In contrast to deuterium/hydrogen ratios, carbon isotope ratios are found to be roughly constant (~ 89) in the Solar System, but do vary on galactic scales with $^{12}\text{C}/^{13}\text{C} \sim 68$ in the current local interstellar medium. In molecular clouds and protoplanetary disks, $^{12}\text{CO}/^{13}\text{CO}$ isotopologue ratios can be altered by ice and gas partitioning, low-temperature isotopic ion exchange reactions, and isotope-selective photodissociation. Here we report on the detection of ^{13}CO in the atmosphere of the young, accreting giant planet TYC 8998-760-1 b at a statistical significance of $> 6\sigma$. Marginalizing over the planet's atmospheric temperature structure, chemical composition, and spectral calibration uncertainties, suggests a $^{12}\text{CO}/^{13}\text{CO}$ ratio of 31_{-10}^{+17} (90% confidence), a significant enrichment in ^{13}C with respect to the terrestrial standard and the local interstellar value. Since the current location of TYC 8998 b at ≥ 160 au is far beyond the CO snowline, we postulate that it accreted a significant fraction of its carbon from ices enriched in ^{13}C through fractionation. Future isotopologue measurements in exoplanet atmospheres can provide unique constraints on where, when and how planets are formed.

 **Zhang, Y.**, Snellen, I. A. G., Bohn, A. J., Mollière, P., Ginski, C., Hoeijmakers, H. J., Kenworthy, M. A., Mamajek, E. E., Meshkat, T., Reggiani, M., & Snik, F. (2021) The ^{13}C O-rich atmosphere of a young accreting super-Jupiter. *Nature*, 595, 370.

2.1 Result

TYC 8998-760-1 b (Bohn et al., 2020) is a widely-separated planetary mass companion around a young solar analog TYC 8998-760-1 (also known as 2MASS J13251211-6456207) with an age of ~ 17 Myr (Pecaut & Mamajek, 2016). With the recent detection of a second planet (Bohn et al., 2020), it is part of the first directly imaged multi-planet system around a solar-type star. TYC 8998 b is located at a projected separation of 160 au, with an estimated mass of $14 \pm 3 M_{\text{Jup}}$. We observed the planet on two nights, 2019 June 5 and June 19, using Spectrograph for INtegral Field Observations in the Near Infrared (SINFONI) (Bonnet et al., 2004, Eisenhauer et al., 2003) installed at the Cassegrain focus of UT3 of the Very Large Telescope of the European Southern Observatory at Cerro Paranal, Chile. The observations were performed in K-band ($1.95 - 2.45 \mu\text{m}$), providing a spectral resolving power ($\lambda/\Delta\lambda$) of ~ 4500 . We extracted the spectrum of TYC 8998 b from 2.10 to $2.45 \mu\text{m}$ as detailed in Methods. As shown in Figure 2.1, the planet spectrum is dominated by molecular features from H_2O and CO . The ^{12}CO $v=2-0$, $3-1$, $4-2$ bandheads are visible at 2.2935, 2.3227, and $2.3535 \mu\text{m}$ respectively. When we compare the observed spectrum with the best-fit model obtained by atmospheric retrieval, an extra emission signature at $2.166 \mu\text{m}$ is seen in Figure 2.1c, which is identified as the hydrogen Brackett γ recombination line. This is likely an indication of on-going accretion of circumplanetary material onto the planet. We estimated a mass accretion rate of $10^{-9.4 \pm 1.3} M_{\odot} \text{ yr}^{-1}$ using the Br γ line luminosity (see Methods). Future observations at longer wavelengths and polarimetric data can provide further insights into the circumplanetary disk and accretion process (van Holstein et al., 2021).

In order to characterize the atmosphere of the planet, we performed a Bayesian retrieval analysis on the spectrum using the radiative transfer tool petitRADTRANS (pRT) (Mollière et al., 2019), connected to the nested sampling tool PyMultiNest (Buchner et al., 2014). We focus on revealing the presence of ^{13}CO , which is expected to be the most detectable isotopologue in atmospheres of gas giants (Mollière & Snellen, 2019), and measuring the isotopologue abundance ratio $^{12}\text{CO}/^{13}\text{CO}$. In addition, we aim to constrain atmospheric properties of the planet such as the carbon-to-oxygen ratio C/O , which may shed light on the conditions during the formation of the planet (Öberg et al., 2011).

We set up the retrieval model in a similar way as used in previous work on HR 8799 e (Mollière et al., 2020) (see Methods). The model consists of nine free parameters: the planet radius R_p , surface gravity $\log(g)$, metallicity $[\text{Fe}/\text{H}]$, carbon-to-oxygen ratio C/O , the isotopologue abundance ratio $^{12}\text{CO}/^{13}\text{CO}$, three parameters for the Temperature-Pressure (T-P) profile, and a spectral slope correction factor f_{slope} , arising from uncertainties in the calibration of the observed spectrum. We ran retrievals on the spectrum of TYC 8998 b using two sets of models: the full model including ^{13}CO and the reduced model excluding ^{13}CO . The setups of the two models are identical except that we removed ^{13}CO from the opacity sources (and therefore the $^{12}\text{CO}/^{13}\text{CO}$ parameter) in the latter. The best-fit model spectra are compared to the observed spectrum shown in Figure 2.1. The difference between the two models is visible at the ^{13}CO bandheads around $2.345 \mu\text{m}$ (see Figure 2.1b). The full model provides a significantly better fit in terms of χ^2 (see Figure 2.5c) as a result of the additional ^{13}CO opacity.

To qualitatively reveal the signature, we compare the observational residuals (that is, the observed spectrum with the best-fit reduced model subtracted off) to the noise-

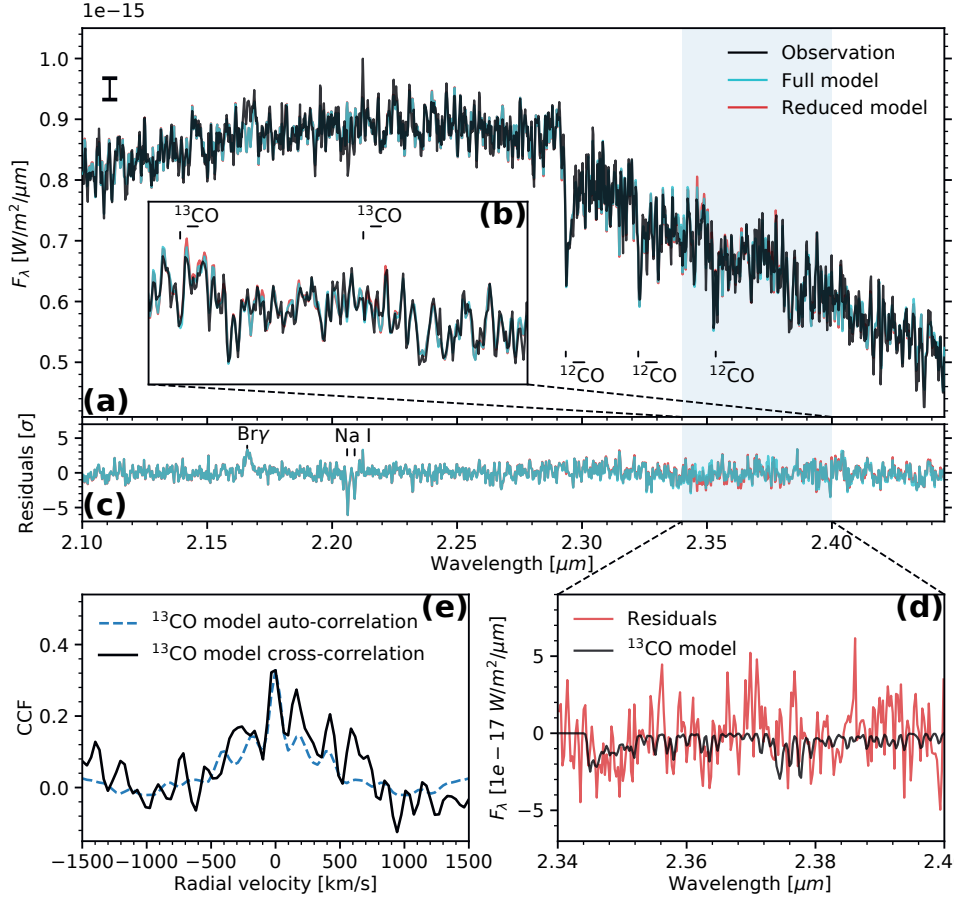


Figure 2.1: Observed SINFONI spectrum of exoplanet TYC 8998 b and cross-correlation signal of ^{13}CO . Panel (a): The observed spectrum is shown in black, the best-fit model including all carbon isotopes in cyan, and the best-fit reduced model, without ^{13}CO , is shown in red. The typical uncertainty per pixel in the observed spectrum is denoted by the error bar (1σ) on the upper left. Sub-panel (b) shows a zoom-in over the 2.34 - 2.40 μm spectral region, centered on the ^{13}CO bandhead. Specific opacity from ^{13}CO is located where the reduced model without ^{13}CO (in red) is higher than the observed spectrum. Panel (c) shows the residuals (spectrum minus best-fit models, with the residuals of the reduced model in red) revealing the Brackett γ emission feature at 2.166 μm , and Na I absorption lines. Panel (d): Observational residuals in red are compared with the ^{13}CO absorption model in black (the difference between the best-fit full model minus the same model with the ^{13}CO opacity removed), revealing the similarity between the observations and models. Panel (e): Cross-correlation functions (CCF) between observational residuals and the ^{13}CO model, as shown in black. The dashed line shows the auto-correlation of the ^{13}CO model, scaled to the peak of the CCF.

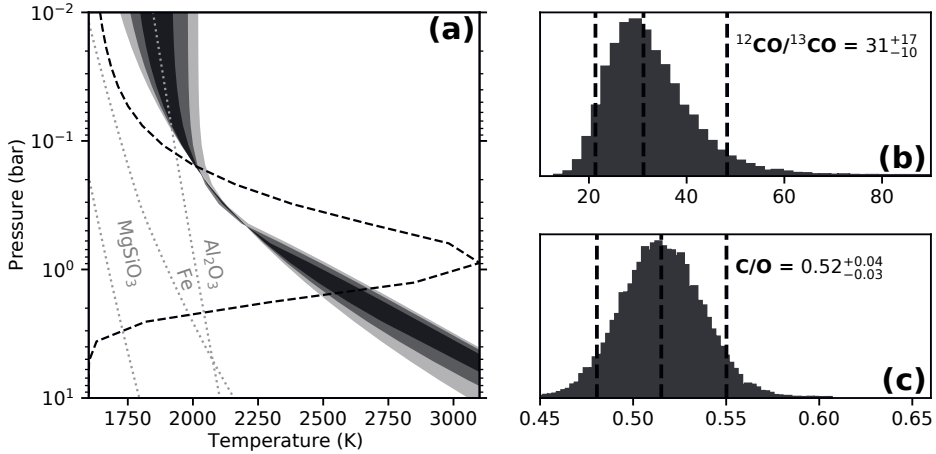


Figure 2.2: Spectral retrieval results. (a) The retrieved temperature-pressure profile. The shaded regions with decreasing grey scale show 1σ , 2σ , and 3σ temperature uncertainty envelopes respectively. The gray dotted lines represent the condensation curves of three potential cloud species. The black dashed line shows the flux average of the emission contribution function. (b) Posterior distribution of CO isotopologue abundance ratio $^{12}\text{CO}/^{13}\text{CO}$. The vertical dashed lines denote the 5%, 50%, 95% quantiles (90% uncertainties) of the distribution. (c) Posterior distribution of carbon to oxygen ratio C/O .

free template of the ^{13}CO signal (that is, the best-fit full model subtracted by the same full model with the ^{13}CO abundance set to zero). The observational residuals follow the expected ^{13}CO signal, especially the dip caused by the ^{13}CO bandheads and well-aligned individual lines (Figure 2.1d), which indicates the presence of ^{13}CO in the data. We also cross-correlated the residuals with the ^{13}CO model (Figure 2.1e). The cross-correlation function (CCF) between the observation and model follows the auto-correlation (ACF) of the model well. The broad feature in the CCF (and ACF) reflects the effect of ^{13}CO bandheads, and the peak at zero radial velocity co-adds the individual lines of the ^{13}CO signal.

In terms of the significance of the ^{13}CO detection, comparing the Bayesian evidence (Z) of the reduced model with the full model, allows us to assess the extent to which the model including ^{13}CO is favored by the observations. In Bayesian model comparison, the Bayes factor B_m (calculated by the ratio of Z) is used as a proxy for the posterior odds ratio between two alternative models²¹. As a result, the Bayes factor between two models is $\ln(B_m) = \Delta\ln(Z) = 18$, meaning that the observation favors the full model (including ^{13}CO) at a significance level of $> 6\sigma$.

The central values of the inferred parameters and their 90% uncertainties from the atmospheric retrieval are $R_p = 1.82 \pm 0.08 R_J$, $\log(g) = 4.51_{-0.29}^{+0.34}$, $[\text{Fe}/\text{H}] = 0.07_{-0.18}^{+0.31}$, $\text{C}/\text{O} = 0.52_{-0.03}^{+0.04}$, and $^{12}\text{CO}/^{13}\text{CO} = 31_{-10}^{+17}$ (Figure 2.2b and 2.2c). Hence, while the C/O ratio is measured to be near the solar value, the planet atmosphere is observed to be rich in ^{13}CO . The inferred T-P profile and posterior distribution of parameters for both models are shown in Figure 2.5.

The $^{12}\text{CO}/^{13}\text{CO}$ ratio of 31_{-10}^{+17} we infer for TYC 8998 b is lower (2.5σ) than measured in

the local interstellar medium (ISM) ~ 68 (Langer & Penzias, 1993, Milam et al., 2005), with the latter also lower than the ratio of ~ 89 observed in the Solar System¹, which is partly thought to be the consequence of galactic chemical evolution, and reflects the relative degree of primary to secondary processing in stars (Langer & Penzias, 1993, Milam et al., 2005, Prantzos et al., 1996). Young systems formed in the local environment are expected to inherit the $^{12}\text{C}/^{13}\text{C}$ ratio of ~ 68 . However, the measurements of complex carbon-bearing molecules (which formed at low temperature from CO on grains) towards protostars result in a low $^{12}\text{C}/^{13}\text{C}$ ratio of ~ 30 , indicating an enhancement of ^{13}CO or ^{13}C in the ice (Jørgensen et al., 2018, 2016). This may be attributed to carbon fractionation processes, including isotopic ion exchange reactions⁸, isotope-selective photodissociation⁹ and ice-/gas isotopologue partitioning (Smith et al., 2015). The isotopic ion exchange reactions enhance the ^{13}CO abundance in the gas at low temperatures, followed by the freeze-out of CO gas onto the grains to increase the ^{13}CO abundance in the ice (Jørgensen et al., 2016). The ice/gas isotopologue partitioning, due to slightly different binding energies of the two isotopologues, may contribute to the enrichment of ^{13}CO in the ice, but only in very narrow temperature ranges as shown by laboratory experiments (Acharyya et al., 2007). The isotope-selective photodissociation alters the $^{12}\text{CO}/^{13}\text{CO}$ ratios at different layers in circumstellar disks because the self-shielding of the rarer isotopologues kicks in at a deeper layer into the disk (Miotello et al., 2014). The preferential photodissociation of ^{13}CO generates more atomic ^{13}C which freezes out onto the ices in the midplane to enrich the ^{13}C in other complex carbon-bearing molecules. Detailed modeling incorporating these fractionation processes in protoplanetary disks suggests that the ^{13}CO in the gas could also be enhanced at intermediate layers (Miotello et al., 2014). Planets may be able to accrete the ^{13}CO -rich gas from these intermediate layers through vertical accretion (Cridland et al., 2020). Alternatively, with the warm gas cycling to cold regions through vertical mixing and then freezing out onto grains, the enrichment may be inherited by pebbles and planetesimals forming there.

In this light, we postulate a framework to explain the ^{13}CO -rich atmosphere of TYC 8998 b, and the near-constant ^{13}C abundance in solar-system objects. It is generally accepted that in the inner parts of a protoplanetary disk, carbon is mostly present in the gas phase as CO, but locked into ices at larger distances, in particular in the disk midplane (Figure 2.3). The CO-snowline, the transition region between the gaseous and solid phase, is governed by the level of stellar irradiation and is expected to be at ~ 20 au for young solar-mass stars (Qi et al., 2013) such as TYC 8998. The current location of TYC 8998 b at >160 au is so far out that it has likely formed outside the CO-snowline. This implies that it has accreted the bulk of its carbon from ices, which is generally enhanced in ^{13}CO and ^{13}C as is discussed above, resulting in the observed ^{13}CO -rich atmosphere. Our spectral analysis also points to an atmospheric C/O ratio of $0.52_{-0.03}^{+0.04}$, further suggesting that the planet was indeed formed beyond the CO-snowline (Öberg et al., 2011). Similarly, for other widely separated exoplanets formed outside the CO-snowline with significant ice accretion, we would also expect ^{13}CO -rich atmospheres.

Since, in contrast, the solar-system planets are thought to be formed within the CO-snowline, we argue that the lack of any substantial enrichment in ^{13}C in their atmospheres is because the bulk of their carbon reservoirs originate from CO gas, not ices. Although Oort-cloud comets now reside in the outer Solar System far beyond the snowline, they

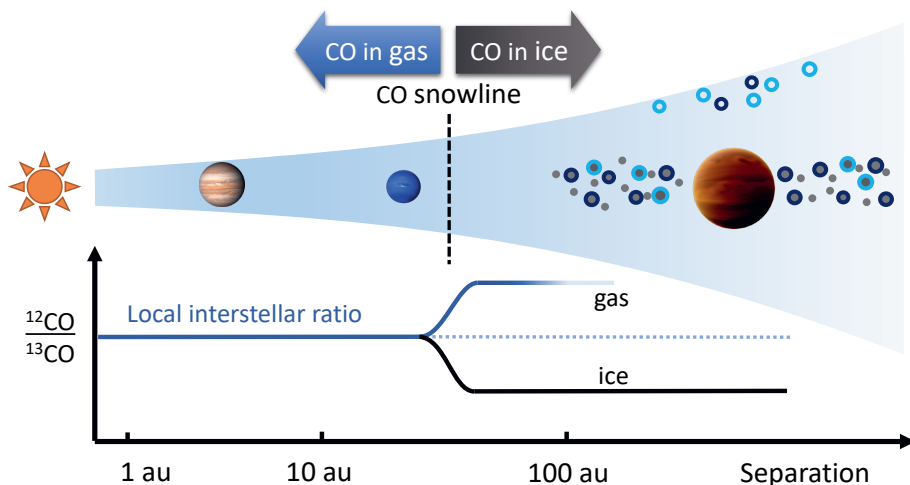


Figure 2.3: Cartoon of the birth environments of planets in a proto-planetary disk. The two planets inside the CO snowline denote Jupiter and Neptune at their current locations, while TYC 8998 b is formed far outside this regime, where most carbon is expected to have been locked up in CO-ice and formed the main reservoir of carbon in the planet. We postulate that, this far outside the CO snowline, the ice was ^{13}CO - or ^{13}C - rich through carbon fractionation, resulting in the observed ^{13}CO -rich atmosphere of the planet. A similar mechanism has been invoked to explain the trend in D/H within the Solar System. Future isotopologue measurements in exoplanet atmospheres can provide unique constraints on where, when and how planets are formed.

may have also formed in the inner disk and later been scattered out through the interaction with giant planets (Morbidelli et al., 2005), therefore exhibiting the same ^{13}C ratios as other objects in the Solar System.

As an analogy of ^{13}CO enrichment through ice accretion, the deuterium to hydrogen ratios (D/H) of Uranus and Neptune are found to be enhanced in comparison with Jupiter, attributed to an increasing contribution from accretion of HDO-rich ices beyond the water snowline (Feuchtgruber et al., 2013). With the caveat that carbon-fractionation is orders of magnitude smaller than D-fractionation, it could still result in a ^{13}C enrichment of a factor of two. For a further understanding of the role of carbon-fractionation in planet formation it will be important to obtain a quantitative assessment of the effects through detailed disk modelling. Future measurements of exoplanet $^{12}\text{C}/^{13}\text{C}$ (and D/H) ratios (Mollière & Snellen, 2019, Morley et al., 2019) can provide an exciting new way to constrain when, where, and how planets are formed.

2.2 Method

2.2.1 Observations and data analysis

We observed TYC 8998 b on two nights, 2019 June 5 and June 19, using Spectrograph for INtegral Field Observations in the Near Infrared (SINFONI) installed at the Cassegrain focus of UT3 of the Very Large Telescope of the European Southern Observatory at Cerro Paranal in Chile, under the ESO programme 2103.C-5012(C) (PI: Bohn). The observations

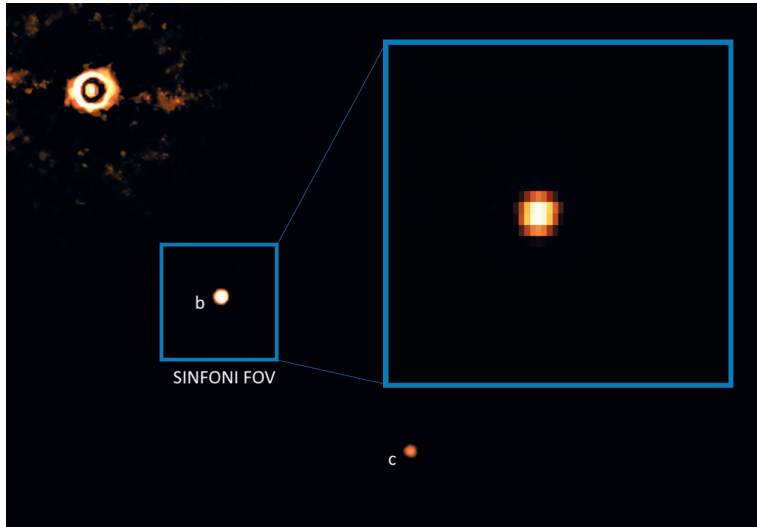


Figure 2.4: Schematics of the observations of TYC 8998-760-1 b using SINFONI at the Very Large Telescope. The background image is captured by the SPHERE instrument on the VLT (Credit: ESO/Bohn et al.). The small blue box marks the field of view (FOV) of SINFONI observations targeting the planet b. Both the host star and planet c are outside the FOV. An example of the wavelength-collapsed image is shown in the enlarged blue box, showing negligible contribution from starlight.

were performed in K-band ($1.95 - 2.45 \mu\text{m}$), providing a spectral resolving power of ~ 4500 . The spatial pixel scale is $0.025''$ per image slice, therefore 32 slices in total amount to a field of view (FOV) of $0.8''$. Both the primary star and the planet c are outside the FOV (see Figure 2.4). As a result of the large planet-star separation ($\sim 1.7''$) and the planet-to-star contrast ($\Delta\text{mag} \sim 6.4$) (Bohn et al., 2020), the starlight contamination is small. We obtained 2×24 science frames with an NDI of 2 and an exposure time of 150 seconds each. The observations were performed in pupil stabilized mode. During the first night, the airmass ranged from 1.31 to 1.34, the seeing varied from $0.81''$ to $2.63''$, and the atmospheric coherence time reached 12 milliseconds with the intervention by clouds. Given the unstable atmospheric conditions of night 1, a second night of observation was performed, delivering a seeing ranging from $0.51''$ to $1.07''$ at an airmass between 1.31 and 1.41 and a coherence time between 2.4 and 9.1 milliseconds. During each night, we took three frames of the sky before, amidst, and after the science frames with the same exposure setup. In addition to the science target, one featureless B-type standard star was observed each night, HIP 57861 and HIP 72332 respectively, serving for telluric and spectrophotometric calibration.

The raw data was first reduced using the SINFONI pipeline to correct for bias, flat fielding, sky background, and bad pixels. Then we obtained the intermediate 2D data products, which are composed of 32 vertical strips, each representing the spectra taken over an individual slitlet with its own wavelength solution. The target spectrum shows as vertical trails on slitlet images. For each science exposure, we extract the target spectrum from the intermediate 2D frame. We focus our analysis on the brightest four slitlet images, where the spectrum was extracted using the optimal extraction algorithm (Horne, 1986).

This algorithm accounts for background (including the starlight contamination) and automatically rejects outliers caused by bad pixels and cosmic rays, and delivers an optimal signal-to-noise ratio (SNR). We subsequently obtained four target spectra for every science exposure. All the spectra were then linearly interpolated to a common wavelength grid and optimally combined to form a combined spectrum for each night. During the process, we discarded two frames taken in night 1, of which the data quality was too low to clearly identify the target in the data (using a threshold of $3\times$ background noise level) as a result of the poor atmospheric conditions.

The broad-band shapes of the final spectra per night obtained above require cautious calibration. First, the efficiency of the instrument+telescope varies over wavelength. This effect can be corrected by comparing the observed spectral shape of the standard star to its theoretical spectrum. For the standard stars in night 1 and 2, we used PHOENIX stellar models (Husser et al., 2013) with an effective temperature of 13500 K and 10800 K respectively (McDonald et al., 2012, Shokry et al., 2018). Since the observed standard star spectra are firmly in the Rayleigh-Jeans regime, potential uncertainties in effective temperature have only marginal effects on the spectral slope. Second, atmospheric dispersion affects the overall spectral shape differently for different slitlets. The optimal extraction method we adopted can further aggravate this bias as different weights were assigned to slitlets when combining the spectra. To determine the most accurate spectral shape, we extracted spectra again while avoiding weighting. We started from the data cubes reconstructed by the SINFONI pipeline, and took a circular aperture of $\sim 5\times$ FWHM to sum up the flux at each wavelength, ensuring that all the flux from the object was included. This plain extraction method was performed to the target as well as standard stars on both nights. In this way, we derived spectra for the target, which have lower SNR but a more accurate spectral shape. The broad-band shape of this spectrum for each night was then applied to the optimally extracted spectrum by fitting a second order polynomial to the division between both spectra. After the spectrophotometric correction, the shape of the combined spectra for the two nights differ by $\sim 2\%$ between 2.1 and 2.4 μm .

We used the ESO sky software tool Molecfit (Smette et al., 2015) v3.0.1 to perform telluric corrections on the final spectra of each night. The tool uses a Line-By-Line Radiative Transfer Model (LBLRTM) to derive telluric atmospheric transmission spectra that can be fitted to observations. For telluric model fitting, we removed a preliminary planetary model from the observed spectrum to minimize effects from the planetary spectrum on the telluric features. The fitting wavelength region is 2.19 - 2.43 μm , which contains the majority of strong telluric lines caused by CH_4 , and H_2O in Earth's atmosphere. Molecfit accounted for molecular abundances, instrument resolution, continuum level and wavelength solution that can fit observations best. The atmospheric transmission model for the entire wavelength range was then derived based on the best-fit parameters. Subsequently, the telluric model was removed from the combined spectrum to obtain the telluric-corrected spectrum. However, the correction is not perfect, resulting in artifacts at the red end of the spectra. The wavelength region beyond 2.4 μm , not important for our goals, is therefore masked in further analysis.

After telluric removal, we combined spectra of both nights into one master spectrum. We noted that the spectrum of the first night turned out to be of lower signal to noise than that of the second night, as expected from the observational conditions. We shifted the

two spectra to the planetary rest frame and weighted-combined them by signal-to-noise ratio (SNR) squared. The SNR of each spectrum was measured by the standard deviation of the residuals (i.e. the observation minus the model spectrum generated by retrieval fitting) in the wavelength range from 2.35 to 2.4 μm . The master spectrum was finally scaled to the photometric flux of $8.8 \times 10^{-16} \text{ W/m}^2/\mu\text{m}$ at 2.25 μm (Bohn et al., 2020). In this way, we obtained a final master spectrum of the companion shown in Figure 2.1, with a SNR of ~ 50 near 2.2 μm and ~ 40 at the red end. We note that the uncertainty per wavelength-step is almost constant along the wavelengths and independent of the flux of the object because the observations are read-noise limited. The red end of the spectrum therefore has lower SNR because of the lower object flux level and strong telluric absorption.

2.2.2 Atmospheric retrieval model

For our atmospheric retrieval we performed a Bayesian analysis using the radiative transfer tool `petitRADTRANS` (pRT) (Mollière et al., 2019), connected to the nested sampling tool `PyMultiNest` (Buchner et al., 2014), which is a Python wrapper of the `MultiNest` method (Feroz et al., 2009). To model the temperature structure of the planet atmosphere, we consider two classes of parameterization of the Temperature-Pressure (T-P) profile: the analytical and flexible model. The first temperature model involves analytical solutions for self-luminous atmospheres assuming a gray opacity. We set the temperature according to Eddington approximation: $T(\tau)^4 = 0.75 T_{\text{int}}^4 (2/3 + \tau)$, where the optical depth τ is linked to the pressure by $\tau = \delta P^\alpha$. We defined P_{phot} as the pressure where $\tau = 1$. Hence, $\delta = P_{\text{phot}}^{-\alpha}$. This temperature model therefore has three free parameters, T_{int} , α and P_{phot} . The Eddington solution leads to an isothermal upper atmosphere. Although this seems unrealistic, the model still works well because the medium-resolution observations barely probe that high up in the atmosphere. At low altitudes, the atmosphere transitions to convective, where we force the temperature gradient onto a moist adiabat.

In the flexible temperature model, we focus on the temperature from 0.01 bar to 10 bar, where the contribution function of the observed spectrum peaks. The temperature outside this range is considered to be isothermal. We set four temperature knots spaced evenly on a log scale pressure within 0.02 to 5 bar. The T-P profile is obtained by spline interpolation of the temperature knots in the log space of pressure. There is no physical reasoning behind this T-P profile, therefore imposing less prior constraints on the solution.

The chemistry model used in our retrievals is detailed in Benneke & Seager (2013). In short, the chemical abundances are determined via interpolation in a chemical equilibrium table using pressure P , temperature T , carbon-to-oxygen ratio C/O , and metallicity $[\text{Fe}/\text{H}]$ as inputs. Then pRT computes synthetic emission spectra using temperature, chemical abundances, and surface gravity as inputs.

We tested the retrieval framework to ensure parameters can be correctly recovered by using synthetic spectra. Using the forward model presented above, we generated a mock spectrum at 2.1 - 2.45 μm , with a spectral resolution of 4500. The flux error was set to be constant, leading to a SNR of around 50 at 2.2 μm , which is similar as in the master spectrum. The mock spectrum was then perturbed by random noise generated according to this uncertainty in flux. We were able to recover all parameters within 1σ interval, validating the capability of the retrieval model.

Table 2.1: Priors and posteriors (90% uncertainties) of the TYC 8998 b retrieval.

Parameter	Prior	Posterior
R_p [R_{Jup}]	$\mathcal{U}(1, 3)$	1.82 ± 0.08
$\log(g)$ [cgs]	$\mathcal{U}(2.5, 6.0)$	$4.51^{+0.34}_{-0.29}$
[Fe/H]	$\mathcal{U}(-1.5, 1.5)$	$0.07^{+0.31}_{-0.18}$
C/O	$\mathcal{U}(0.1, 1.5)$	$0.52^{+0.04}_{-0.03}$
T_{int} [K]	$\mathcal{U}(1000, 3000)$	2174^{+162}_{-150}
α	$\mathcal{U}(0.1, 2)$	$0.8^{+0.8}_{-0.2}$
P_{phot} [bar]	$\mathcal{U}(-3, 2)$	$-0.19^{+0.10}_{-0.29}$
$\log(^{12}\text{CO}/^{13}\text{CO})$	$\mathcal{U}(-12, 0)$	$-1.49^{+0.16}_{-0.19}$
f_{slope}	$\mathcal{U}(-0.05, 0.05)$	-0.007 ± 0.007

$\mathcal{U}(a, b)$ represents a uniform distribution ranging from a to b .

2.2.3 Retrievals on the TYC 8998 b spectrum

We set up the retrieval model using the analytical T-P profile, with eight free parameters, R_p , $\log(g)$, [Fe/H], C/O, T_{int} , α , P_{phot} and $^{12}\text{CO}/^{13}\text{CO}$. The priors of these free parameters are listed in Table 2.1. In the full model, we included ^{12}CO , H_2O , CH_4 , NH_3 and the isotopologue ^{13}CO as line opacity species, and the collision induced absorption of $\text{H}_2\text{-H}_2$, $\text{H}_2\text{-He}$. As for the reduced model, we removed ^{13}CO from the opacity sources. We used the line-by-line mode of pRT to calculate the emission spectra at high spectral resolution. To speed up the calculation, we took every fifth point of opacity tables with $\lambda/\Delta\lambda \sim 10^6$. This sampling procedure, which has been benchmarked against the full tables, shows negligible effects on the synthetic spectra and retrieval results. The synthetic high-resolution spectra were convolved with a Gaussian kernel to match the resolving power of the instrument ($\lambda/\Delta\lambda \sim 4500$), then binned to the wavelength grid of the master spectrum, and scaled to the observed flux according to RP and distance of the target.

In addition, as we noted above, there exists up to 2% discrepancy in terms of the broad-band spectral shape between two nights of observations. Therefore, before comparing the synthetic model spectra to the observation, we multiplied the models by a linear slope spanning from $1 - f_{\text{slope}}$ to $1 + f_{\text{slope}}$ in the wavelength range from 2.1 to 2.4 μm , where we introduced the slope correction factor f_{slope} as a nuisance parameter to marginalize the uncertainty in the spectral shape. The retrieval process was performed by PyMultiNest, which uses 4000 live points to sample the parameter space and derives the posterior abundances of the fit. We ran MultiNest in Importance Nested Sampling mode with a constant efficiency of 5%. The outcome is shown in Figure 2.5. We also utilized the flexible T-P profile to consolidate the retrieval results. The inferred parameters are found to be robust for different T-P model setups.

The retrieved value of $\log(g)$ should be treated with caution, because we note that any small changes in the wavelength coverage of the fitting or the broad-band shape of the spectrum can result in significantly different values. As also indicated in other retrieval studies (GRAVITY Collaboration et al., 2020), CO and H_2O features at K-band are not very sensitive to $\log(g)$. Free retrievals at K-band alone are therefore unable to place robust

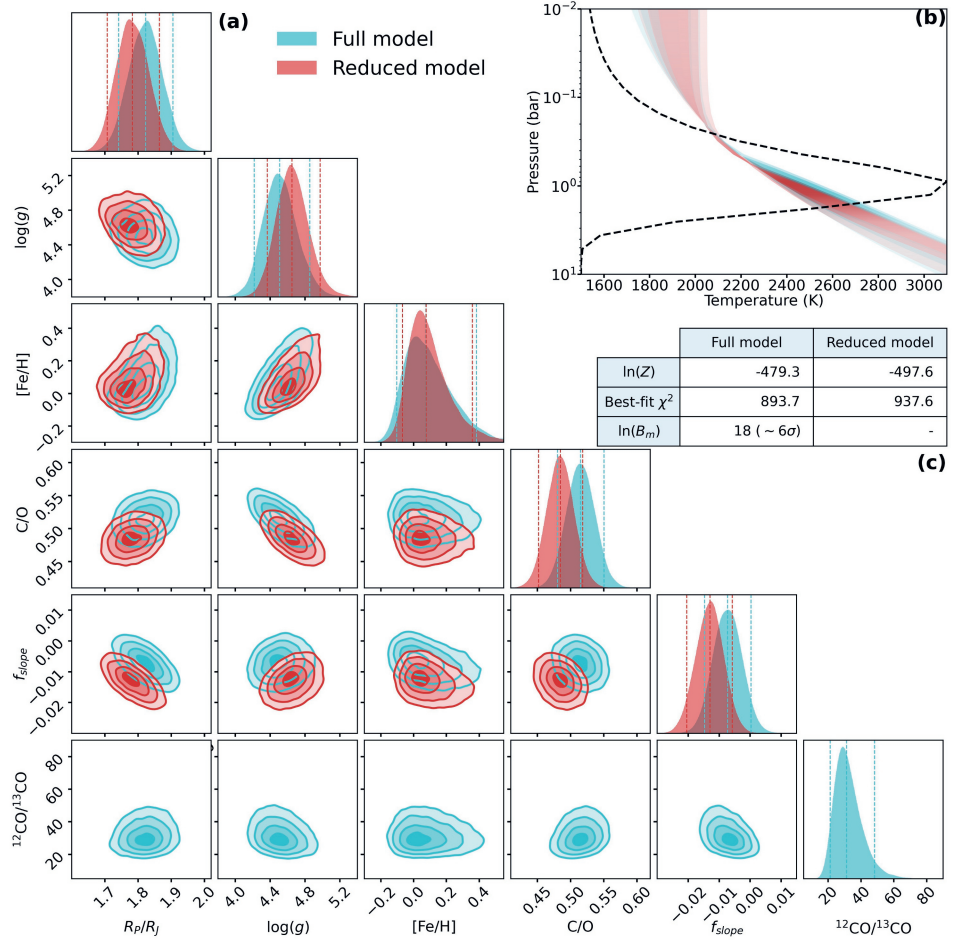


Figure 2.5: Posteriors of the retrieved parameters and temperature structure for the full (cyan) and reduced (red) models. The vertical dashed lines denote the 5%, 50%, 95% quantiles (90% uncertainties) of the distribution. Panel (b): T-P profile. The shaded regions with decreasing color saturation show 1 σ , 2 σ , and 3 σ temperature uncertainty envelopes respectively. The black dashed line shows the flux average of the emission contribution function. The opaqueness of the temperature uncertainty envelopes has been scaled by this contribution function. Panel (c): fitting statistics of the full and reduced retrieval model, where $\ln(Z)$ and $\ln(B_m)$ represent the logarithm of Bayesian evidence and Bayes factor.

constraints on the surface gravity and hence the planet mass. We also run retrievals with prior constraint on the planet mass. The solution converges to a lower surface gravity and the same isotopologue ratio, suggesting that the inaccurate $\log(g)$ does not affect the inference of the $^{12}\text{CO}/^{13}\text{CO}$ ratio.

We compared the Bayesian evidence (Z) of the reduced model with the full model (Figure 2.5c), the difference of which is related to the Bayes factor B_m that translates to a frequentist measure (Benneke & Seager, 2013) of $> 6\sigma$ significance of the ^{13}CO detection. Although the evidence is dependent on the prior of the ^{13}CO abundance (Table 2.1), we noted that increasing the prior range of $\log(^{13}\text{CO}/^{12}\text{CO})$ from $(-12,0)$ to $(-20,0)$ did not lead to significant change in the final evidence, and both of the priors are much broader than the ratio that one would expect in reality.

2.2.4 Effects of clouds

Clouds are ubiquitous in planetary atmospheres and can play an important role in the interpretation of spectra. We investigated their potential effects on the ^{13}CO measurement by including clouds in the retrieval models. We used the cloud model detailed in Mollière et al. (2020), which introduced four additional free parameters: the vertical eddy diffusion coefficient K_{zz} , the settling parameter f_{sed} , the width of the log-normal particle size distribution σ_g and the mass fraction of the cloud species at the cloud base $\log(X)$. The temperature of TYC 8998 b is too high to form Mg and Fe bearing condensates in the atmosphere. We therefore considered a more refractory species Al_2O_3 as the source of cloud opacity (Wakeford et al., 2017). After testing cloudy models, we found the solution converged to cloud-free atmospheres, and the inferred parameter values remain unaffected, because the atmospheric temperature (Figure 2.2a) is too warm to form optically thick clouds that could make a significant impact on the spectrum. Therefore, we did not include clouds in our nominal models.

2.2.5 Constraining mass accretion rate

The Brackett γ emission line (see Figure 2.1) provides constraints on the mass accretion rate of the planet. We measured a Br γ line flux of $7.6(\pm 0.9) \times 10^{-18} \text{ W/m}^2$, and a line luminosity $\log(L_{\text{Br}\gamma}/L_{\odot})$ of -5.7 ± 0.5 , from which we estimated the accretion luminosity $\log(L_{\text{acc}}/L_{\odot})$ to be -2.7 ± 1.3 using the linear correlation given by Muzerolle et al. (1998). Combining this with the retrieved values of radius and surface gravity, we derived a mass accretion rate of $10^{-9.4 \pm 1.3} M_{\odot} \text{ yr}^{-1}$.

2.3 Additional assessments of the reliability of ^{13}CO detection in TYC 8998 b

We further assess the reliability of the ^{13}CO detection in several ways. We study the ^{13}CO signal for the individual nights and that from the first and second bandheads separately, investigate the impact of inaccurate telluric line removal, and the effects of possible other opacity sources. In addition, we show that for an easier accessible, nearby, isolated brown dwarf, archival spectroscopy data of the same ^{13}CO features at higher spectral resolving power, show a strong signal - as expected from our TYC 8988 b observations (albeit with a more typical $^{12}\text{CO}/^{13}\text{CO}$ ratio).

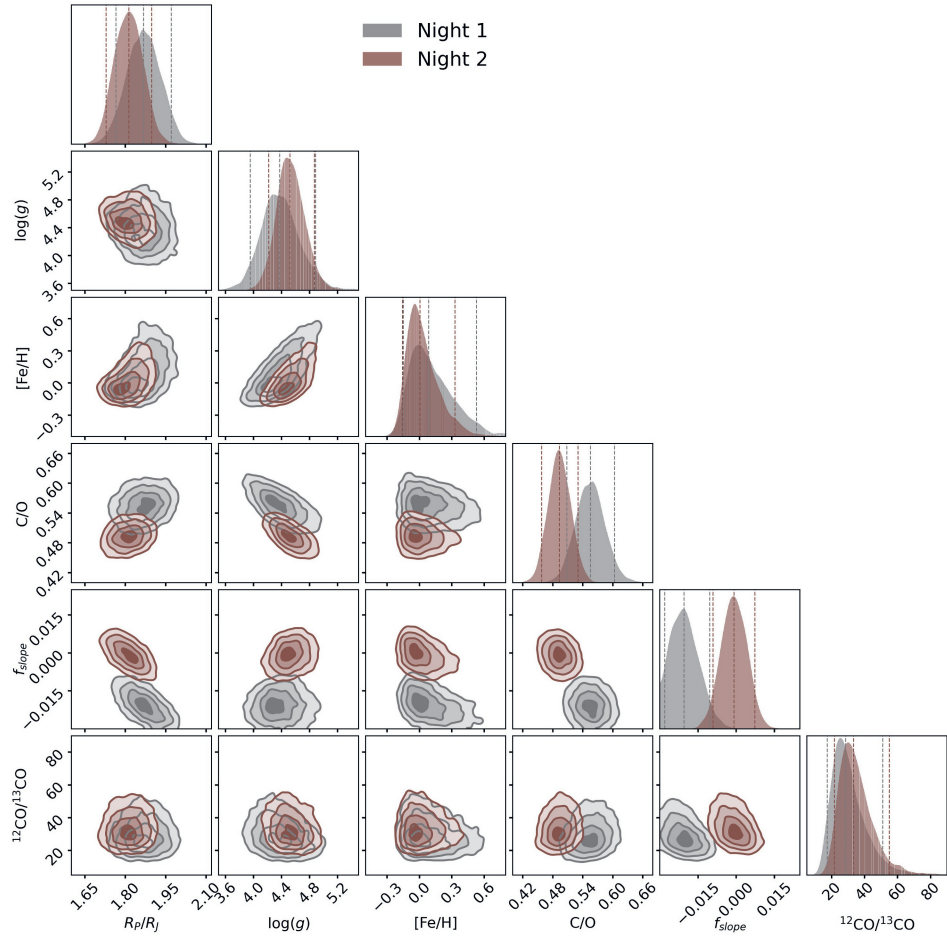


Figure 2.6: Posteriors of the retrieved parameters for the data of individual nights. Similar as Figure 2.5a.

2.3.1 Analysis on data of individual nights and bandheads

To assess whether the ^{13}CO signal is present in both nights, we performed the retrieval and cross-correlations analyses as detailed above for each night separately. The retrieval results are shown in the Figure 2.6. ^{13}CO is detected in both nights but at a lower significance, as expected. The derived constraints on $^{12}\text{CO}/^{13}\text{CO}$ are consistent with each other. There is a $\sim 2\%$ difference in the slope correction factor f_{slope} in the two nights, as was already noted in the spectral calibration above. This likely contributes to the slight discrepancies in the derived values for $\log(g)$ and C/O. The cross correlation functions are shown in Figure 2.7, also indicating that ^{13}CO is detected in both nights individually, albeit at lower significance.

We also investigated whether the two bands of ^{13}CO , starting at 2.345 and 2.374 μm , can both be detected individually. We examined this by separating the wavelength region

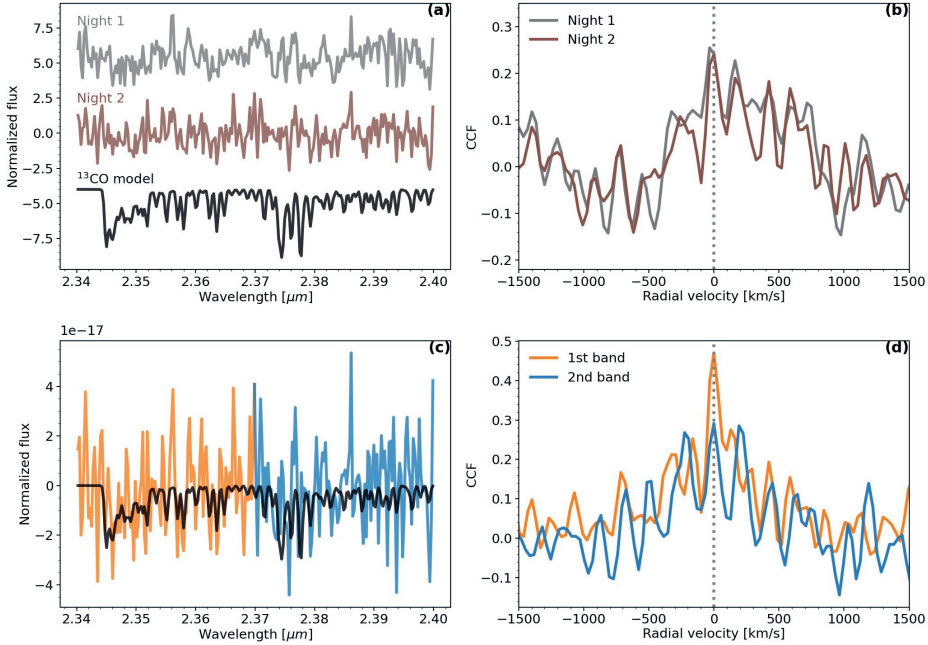


Figure 2.7: Cross-correlation signal of ^{13}CO from individual nights and bandheads. Panel a: observational residuals of two nights separately. Panel b: cross-correlation signal from individual nights. Panel c: filtered observational residuals of two ^{13}CO bandheads separately. Panel d: cross-correlation signal from individual bandheads.

into two parts, 2.34-2.37 and 2.37-2.40 μm , then calculating the cross-correlation in each part. Prior to the cross-correlation, the residuals were high-pass filtered using a Gaussian kernel with a width of 3 nm to remove the low-frequency variation in residuals and enhance the signal. The low-frequency variation, especially apparent in the second part of the data, introduces broad-band shape in the CCF which suppresses the signal. The filtered residuals are shown in panel c of the Figure 2.7, and the cross-correlation results in panel d. The CCF for both bands show peaks at zero velocity, while the signal from the second band is less significant. We argue that although the expected absorption from the two bands is similar, the signal-to-noise of the spectral data at the 2.374 μm bandhead is lower due to the stronger telluric absorption in this region. This is highlighted in panel a of Figure 2.8, showing the telluric transmission spectrum, observational residuals from the reduced model (without ^{13}CO), and the ^{13}CO -model. We believe that it is for this reason that the ^{13}CO signal from the second bandhead is not as significant as from the first bandhead.

2.3.2 The impact of telluric absorption

Panel b of Figure 2.8 shows the cross-correlation function between the ^{13}CO model and the telluric line spectrum, demonstrating no evident signal. It indicates that the observed

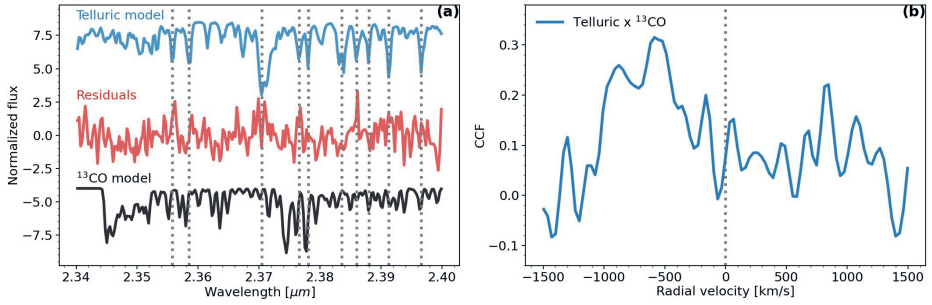


Figure 2.8: Impact of telluric absorption lines and cross-correlation signal of ^{13}CO at the extended wavelength region. Panel (a): Comparison of the telluric transmission model with residuals. Some noise is attributed to imperfect telluric correction as noted by dotted gray lines. Panel (b): Cross-correlation function between the telluric model and the ^{13}CO model, showing no correlation between them.

^{13}CO signal is not caused by any under or overcorrection of telluric lines.

2.3.3 Other potential opacity sources

In the retrieval models, we include the major molecular opacity sources (CO , H_2O , CH_4 , NH_3) that play a role at the K-band. We inspected other potential absorbers given the expected temperature, including CO_2 , HCN , and C_2H_2 . None of them show significant features at the same wavelength region as ^{13}CO . Moreover, we performed retrieval analysis to marginalize over these absorbers. Adding these molecules to the retrieval model does not change the inferred value of any parameter. Therefore, it is not plausible that the detected ^{13}CO feature is caused by these molecules.

2.3.4 Archival reference data of the young brown dwarf 2M0355

To boost confidence in the detection of ^{13}CO in TYC 8998 b, we analysed archival data of the young brown dwarf 2M0355 (Faherty et al., 2013). This object resembles in several ways a young super Jupiter like TYC 8998 b, but since it is isolated and, located nearby at 8 parsec, it is spectroscopically significantly more accessible. From our ^{13}CO detection in TYC 8988 b, it is expected that ^{13}CO should be straightforward to see in 2 hrs of NIRSPEC data (Bryan et al., 2018) from the KECK telescope, in particular at a spectral resolving power of ~ 27500 . Our detailed analysis will be presented in a forthcoming publication. Figure 2.9 shows the spectrum, best-fit model, and the ^{13}CO cross-correlation signal, after performing an identical analysis - targeting the same features as our SINFONI data of TYC 8998 b. We retrieve a $^{12}\text{CO}/^{13}\text{CO}$ isotopologue abundance of ~ 100 , similar to the solar value. It will be intriguing to compare measurements between isolated brown dwarfs and exoplanets, revealing the role of carbon isotopologue ratio as a tracer of planet formation.

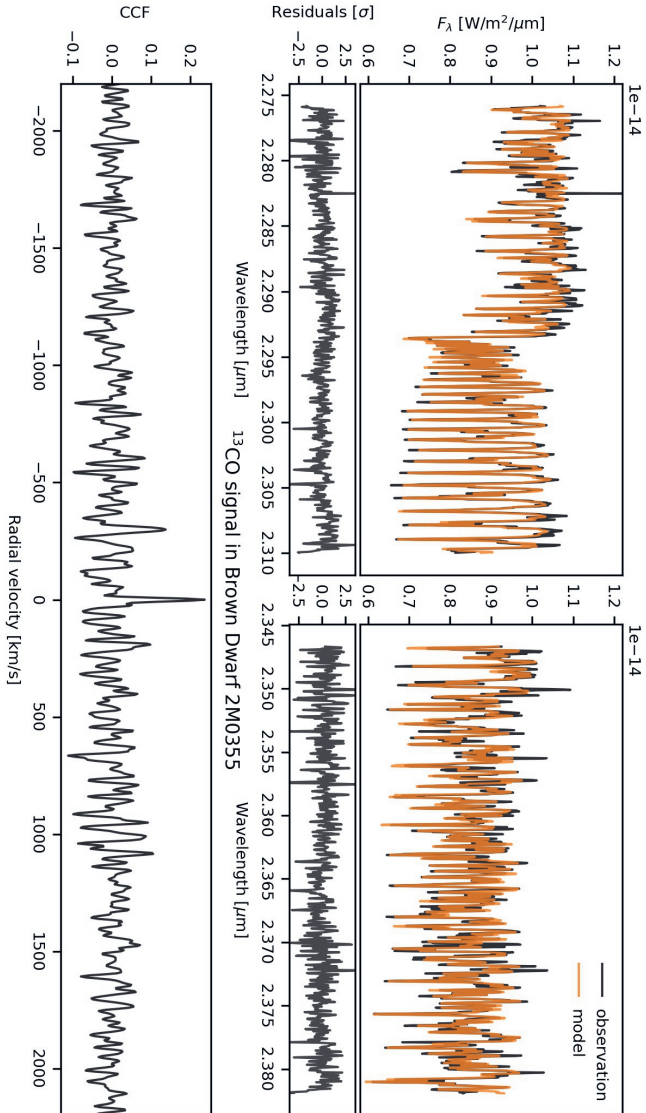
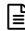


Figure 2.9: K-band spectrum of the brown dwarf 2M0355 taken by Keck/NIRSPEC and the cross-correlation signal of ^{13}CO . The black line shows the observed spectrum and the orange line is the best-fit model obtained by retrieval analysis. Bottom panel: Cross-correlation function (CCF) between the ^{13}CO model and observational residuals. The peak at zero velocity clearly shows the detection of ^{13}CO .

3

The $^{12}\text{CO}/^{13}\text{CO}$ isotopologue ratio of a young, isolated brown dwarf

Linking atmospheric characteristics of planets to their formation pathways is a central theme in the study of extrasolar planets. Although the $^{12}\text{C}/^{13}\text{C}$ isotope ratio shows little variation in the Solar System, the atmosphere of a super-Jupiter was recently shown to be rich in ^{13}CO , possibly as a result of dominant ice accretion beyond the CO snow line during its formation. Carbon isotope ratios are therefore suggested to be a potential tracer of formation pathways of planets. In this work, we aim to measure the $^{12}\text{CO}/^{13}\text{CO}$ isotopologue ratio of a young, isolated brown dwarf. While the general atmospheric characteristics of young, low-mass brown dwarfs are expected to be very similar to those of super-Jupiters, their formation pathways may be different, leading to distinct isotopologue ratios. We analysed archival K-band spectra of the L dwarf 2MASS J03552337+1133437 taken with NIRSPEC at the Keck telescope. A free retrieval analysis was applied to the data using the radiative transfer code petitRADTRANS coupled with the nested sampling tool PyMultiNest to determine the isotopologue ratio $^{12}\text{CO}/^{13}\text{CO}$ in its atmosphere. The isotopologue ^{13}CO is detected in the atmosphere through the cross-correlation method at a signal-to-noise of ~ 8.4 . The detection significance is determined to be $\sim 9.5\sigma$ using a Bayesian model comparison between two retrieval models (including or excluding ^{13}CO). We retrieve an isotopologue $^{12}\text{CO}/^{13}\text{CO}$ ratio of 97_{-18}^{+25} (90% uncertainty), marginally higher than the local interstellar standard. Its C/O ratio of ~ 0.56 is consistent with the solar value. Although only one super-Jupiter and one brown dwarf now have a measured $^{12}\text{CO}/^{13}\text{CO}$ ratio, it is intriguing that they are different, possibly hinting to distinct formation pathways. Regardless of spectroscopic similarities, isolated brown dwarfs may experience a top-down formation via gravitational collapse, which resembles star formation, while giant exoplanets favourably form through core accretion, which potentially alters isotopologue ratios in their atmospheres depending on the material they accrete from protoplanetary disks. This further emphasises atmospheric carbon isotopologue ratio as a tracer of the formation history of exoplanets.

 **Zhang, Y., Snellen, I. A. G., & Mollière, P. (2021) The $^{12}\text{CO}/^{13}\text{CO}$ isotopologue ratio of a young, isolated brown dwarf. A&A, 656, A76.**

3.1 Introduction

Planet formation and evolution are expected to leave imprints on the observed spectra of exoplanets. In bridging the gap between the spectral characterisation and formation mechanisms, isotopologue ratios have been suggested as informative tracers of planet formation conditions and evolutionary history (Clayton & Nittler, 2004, Zhang et al., 2021a). In the Solar System, deuterium/hydrogen (D/H) ratios demonstrate significant variations across planets, comets, and meteorites (Altwegg et al., 2015). While the D/H ratios in Jupiter and Saturn are consistent with the protosolar value, Uranus and Neptune are found to be enhanced in deuterium (Feuchtgruber et al., 2013), which is attributed to a likely increased contribution from accretion of D-rich ices beyond the water snow line. The terrestrial planets Earth, Mars, and Venus have higher D/H ratios (Drake, 2005), indicating not only solid accretion, but also atmospheric loss. Therefore, isotope ratios in planetary atmospheres can reflect the material reservoir of the birth environment, the formation mechanism (via core accretion or gravitational collapse), the relative importance of gas or ice accretion, and the atmospheric evolution.

In contrast with D/H ratios, carbon isotope ratios are found to be roughly constant in the Solar System (Woods, 2009), and therefore they are less effective diagnostic tools. However, the recent measurement of the $^{12}\text{CO}/^{13}\text{CO}$ isotopologue abundance ratio in an exoplanet may require a reassessment of its diagnostic value. The ^{13}CO isotopologue was detected at a significance of 6σ in the atmosphere of the super-Jupiter TYC 8998 b. Intriguingly, the atmosphere is reported to be ^{13}CO -rich with a $^{12}\text{CO}/^{13}\text{CO}$ abundance ratio of 31, which is significantly lower than the local interstellar standard at ~ 68 (Zhang et al., 2021a). A formation outside the CO snow line with a large contribution from ice-accretion (as an analogy to the D-enrichment in Solar System planets) has been invoked to explain the enrichment. Since the Solar System planets are thought to be formed within the CO snow line, no substantial enrichment in ^{13}C is expected, because the bulk of their carbon reservoirs originate from CO gas in the inner disk, where ^{13}C is not enhanced. It therefore suggests that the atmospheric carbon isotopologue ratios could also shed light on the formation history of exoplanets, especially for the directly imaged populations, which are observed at wide orbits beyond the CO snow line.

Several carbon fractionation processes in molecular clouds, young stellar objects (YSOs), and protoplanetary disks are suggested to alter the CO isotopologue ratios in the birth environment of planets, including isotopic ion exchange reactions (Langer et al., 1984, Milam et al., 2005), isotope-selective photodissociation (Bally & Langer, 1982, Miotello et al., 2014, van Dishoeck & Black, 1988, Visser et al., 2009), and gas-to-ice isotopologue partitioning (Acharyya et al., 2007, Smith et al., 2015). Depending on the location of the proto-planets and the material (gas or ice) they accrete from the environment, the isotopologue ratios in the atmospheres may deviate from the ISM standard. Therefore, detailed modelling of carbon fractionation in protoplanetary disks coupled with planet formation models have the potential to locate the birthplace and identify the formation mechanism of planets, like suggested for carbon-to-oxygen (C/O) ratios (Cridland et al., 2020, Madhusudhan et al., 2014, Mordasini et al., 2016, Öberg et al., 2011). Moreover, combining evidence from different observables, such as $^{12}\text{C}/^{13}\text{C}$, D/H, and C/O ratios, allows for a more comprehensive understanding of the formation process.

Compared to the D/H ratios ($\sim 10^{-5}$) which can potentially be probed via HDO/H₂O

and $\text{CH}_3\text{D}/\text{CH}_4$ (Mollière & Snellen, 2019, Morley et al., 2019), the $^{12}\text{C}/^{13}\text{C}$ ratios ($\lesssim 100$) are more readily detectable and attained from the ground with high-resolution spectroscopy targeting $^{12}\text{CO}/^{13}\text{CO}$ (Mollière & Snellen, 2019). In addition to the recent result for a super-Jupiter, carbon isotopologue ratios have been measured toward various sources beyond the Solar System, including the interstellar medium (ISM) (Langer & Penzias, 1993, Milam et al., 2005, Yan et al., 2019), YSOs and protostars in gas and ices (Boogert et al., 2002, 2000, Jørgensen et al., 2018, 2016, Pontoppidan et al., 2005, Smith et al., 2015), giant stars, solar-type stars, and M dwarfs (Botelho et al., 2020, Crossfield et al., 2019b, Sneden et al., 1986, Tsuji, 2016), but not yet towards brown dwarfs. In this paper, we carry out a similar analysis to Zhang et al. (2021a) on archival high-resolution Keck/NIRSPEC data of a young, isolated brown dwarf. While its general atmospheric characteristics are expected to be very similar to those of super-Jupiters, its formation pathways may be different, leading to distinct isotopologue ratios. In addition, its spectrum can be studied at high signal-to-noise, and hence is more accessible.

We present the observations and spectrum extraction in Section 3.2, followed by a description of the retrieval model in Section 3.3. The retrieval results and the measurement of CO isotopologue ratio can be found in Section 3.4 and are discussed in Section 3.5.

Table 3.1: Properties of 2M0355, including those derived in this work.

Parameter	Symbol	Value
R.A. (J2000) ^a	α	03:55:23.377
Dec. (J2000) ^a	δ	+11:33:43.7
Distance (pc) ^a	d	9.1 ± 0.1
Systemic velocity (km s^{-1}) ^b	v_{sys}	11.8 ± 0.5
Rotational velocity (km s^{-1}) ^b	$v \sin(i)^*$	14.7 ± 2.3
Spectral type ^c		L5y/L3
2MASS K-magnitude (mag) ^d	K_{mag}	11.526 ± 0.021
Age (Myr) ^e		~ 125
Effective temperature (K) ^e	T_{eff}	1430 ± 40
Mass (M_{Jup}) ^f	M_p	19_{-5}^{+7}
Surface gravity (cgs) ^f	$\log g$	4.69 ± 0.15
Carbon-to-Oxygen ratio ^f	C/O	0.56 ± 0.02
CO isotopologue ratio ^f	$^{12}\text{CO}/^{13}\text{CO}$	97_{-18}^{+25}

* our work indicates a smaller rotation velocity than found in the literature.

^a Gaia Collaboration et al. (2018);

^b Blake et al. (2010), Bryan et al. (2018);

^c Cruz et al. (2009);

^d Cutri et al. (2003);

^e Aller et al. (2016), Faherty et al. (2013), Liu et al. (2013);

^f this work.

3.2 Observations and spectrum extraction

2MASS J03552337+1133437 (hereafter 2M0355) is a free-floating, young brown dwarf discovered from 2MASS (Reid et al., 2008) and is likely a member of AB Doradus moving group (Liu et al., 2013). With a distance of 9.1 parsec and a spectral type of L5 γ (with γ denoting a very low surface gravity), it is among the nearest and reddest L dwarfs (Cruz et al., 2009, Faherty et al., 2013). The properties of 2M0355 are summarised in Table 3.1. Its spectrum demonstrates signatures of low surface gravity and resembles those of directly imaged planetary mass objects, while being orders of magnitudes brighter and not contaminated by starlight. It is therefore an excellent target for high-resolution spectroscopic studies, providing insights into atmospheric properties under similar conditions to those of exoplanets.

3.2.1 Keck/NIRSPEC archival data

We used the archival K-band (2.03–2.38 μm) spectra of 2M0355 taken with the near-infrared spectrograph NIRSPEC ($\lambda/\Delta\lambda \sim 25000$) at the Keck II 10 m telescope (McLean et al., 1998) on January 13, 2017. The data were obtained in natural seeing mode with a $0.432 \times 24''$ slit. The observations were performed with a standard ABBA nod pattern, resulting in 14 science exposures between 400 and 600 seconds, which amount to a total exposure time of two hours. The data have previously been used to measure the spin of the brown dwarf by Bryan et al. (2018).

As for the pre-processing, we first corrected the data using dark and flat field calibration frames, and then differenced each nodded AB pair to subtract the sky background. This led to 2D differenced images with two spectral traces (positive and negative) for each order. In the subsequent analysis, we focussed on the last two orders with the wavelength coverage of 2.27 – 2.31 μm (blue order) and 2.34 – 2.38 μm (red order), respectively. Subsequently, we straightened the 2D images on an order-by-order basis to align the curved spectral traces along the dispersion (x-)axis by fitting the traces with a third-order polynomial. Similarly, we also adjusted the spectral traces to correct for the tilted spectral lines on the y-axis due to instrument geometry. The tilt was measured by fitting the brightest sky line in the flat-fielded raw image with a linear function, which was then applied to the differenced frames. We then combined all the rectified 2D images to a single frame for each order.

From the combined 2D frames, we extracted 1D spectra for both the positive and negative traces, using the optimal extraction algorithm by Horne (1986). This method takes the weighted sum of the flux along the spatial dimension (the cross-dispersion axis), based on the empirical point spread function (PSF) constructed from the 2D frame, while rejecting outliers caused by cosmic rays or bad pixels. After obtaining 1D spectra for both traces, we add them up to form the master spectrum, resulting in an average signal-to-noise ratio (S/N) of ~ 35 per unit of dispersion (pixel). This S/N value was estimated by comparing the master spectrum to a model spectrum obtained by the retrieval analysis (detailed in Section 3.3). Using the statistical flux uncertainties as calculated in the spectrum extraction process (accounting for shot noise and readout noise), we expect the S/N to be ~ 115 , which differs from the former estimation by a factor of 3.3. This indicates the presence of correlated noise in the data and/or the imperfect modelling of telluric transmission and planetary spectra. Nevertheless, the S/N estimated via the comparison to models repre-

sents a lower limit to the data quality. We therefore base our further analysis on the assumption of this lower S/N.

To determine the wavelength solution for each order, we took advantage of the standard star spectra obtained under the same instrument configuration immediately before the observation, assuming that the wavelength solution remains the same. We compared the standard star spectrum with a telluric transmission model generated with ESO sky model calculator `SkyCalc`¹ (Jones et al., 2013, Noll et al., 2012) and fitted the wavelengths as functions of pixel positions using ~ 25 telluric lines spread across each order with a third-order polynomial. This solution was then applied to the target spectrum.

We then used the ESO sky software tool `MoleculeFit v3.0.1` (Smette et al., 2015) to perform telluric corrections on the master spectrum. The tool uses a line-by-line radiative transfer model (LBLRTM) to derive telluric atmospheric transmission spectra that can be fitted to observations. For model fitting, we selected two wavelength regions, 2.276 - 2.293 μm and 2.347 - 2.382 μm , which include strong telluric lines caused by CH_4 and H_2O . The software accounted for the molecular abundances, instrument resolution, continuum level, and wavelength solution that can best fit observations. Using the best-fit Gaussian kernel width, we estimated the spectral resolution to be $\lambda/\Delta\lambda \sim 27500$. The atmospheric transmission model for the entire wavelength range was then derived based on the best-fit parameters. The model was removed from the master spectrum to obtain the telluric-corrected spectrum. Subsequently, we shifted the spectrum to the target's rest frame by accounting for the systemic and barycentric radial velocity. The flux was finally scaled to the K-band photometry of $1.05 \times 10^{-14} \text{ W/m}^2/\mu\text{m}$ (Cutri et al., 2003). The scaling factor was determined by generating the planetary model spectrum at a larger wavelength coverage and then integrating the flux over the band pass of the K-band filter, and comparing it to the photometric value.

We note that measuring the CO isotopologue ratio requires careful calibration of the broad-band spectral shape. Because the CO absorption features span across the two spectral orders in the observations, the CO abundance inferred from the spectrum is sensitive to slight changes in the relative flux between the two orders. To calibrate this, we inspected spectra of two standard stars taken immediately before and after the target observations. We reduced the standard star spectra following the same procedure as described above and compared the telluric-corrected spectrum of the standard stars to a PHOENIX stellar model (Husser et al., 2013) with an effective temperature of 8200 K, as estimated for the stars (Gaia Collaboration et al., 2018). Since the standard star spectra are firmly in the Rayleigh-Jeans regime, potential uncertainties in effective temperature have negligible effects on the spectral shape. The comparison suggested that the observed flux ratio between the red and blue order was on average 3% higher than that of the model. We therefore decreased the flux in the red order by 3% to compensate for this.

The final spectrum of 2M0355 is shown in Fig. 3.1. The ^{12}CO $\nu=2-0$ bandhead is clearly visible at 2.2935 μm , while the first bandhead of ^{13}CO at 2.3448 μm falls outside of the detector. On the order of thirty ^{13}CO lines are covered by the red order (see Fig. 3.2, left panel).

¹<https://www.eso.org/observing/etc/skycalc>

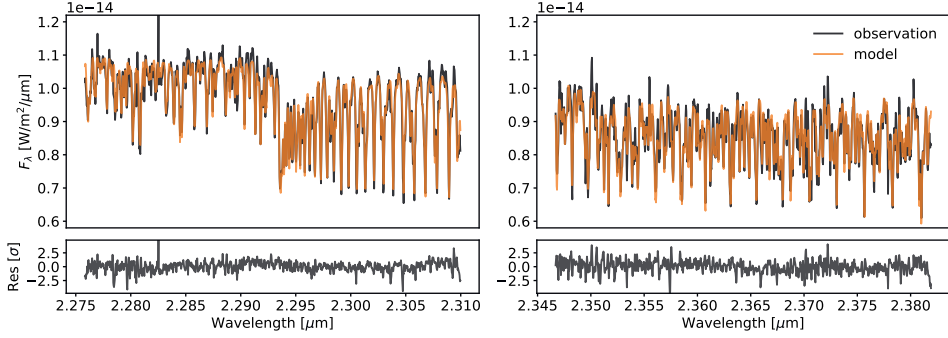


Figure 3.1: Last two orders (containing CO opacity) of the K-band spectrum of the brown dwarf 2M0355 taken with Keck/NIRSPEC. The orange line is the best-fit model with $\log(g)=4.69$, $[\text{Fe}/\text{H}]=0.2$, $\text{C}/\text{O}=0.55$, and $^{12}\text{CO}/^{13}\text{CO}=97$, obtained from the maximum likelihood model in the retrieval analysis. The bottom panel shows the residuals of the observed spectrum with respect to the model.

3.2.2 VLT/CRIRES+ science verification observations

We obtained high-resolution ($\mathcal{R} = \lambda/\Delta\lambda \sim 80\,000$) emission spectra of 2M0355 at the K-band as part of science verification observations with the upgraded CRIRES at the VLT on September 19, 2021 under ESO programme 107.22TG. The observations were performed in seeing-limited mode with a standard ABBA nodding pattern, resulting in 4 science exposures of 300 seconds each. The data were taken at an airmass of 1.25 and a seeing of $0.5''$. The sky transparency is sub-optimal with variable, thick clouds.

The raw data were first reduced using the CRIRES pipeline to correct for bias, flat fielding, sky background, and bad pixels. We then used the intermediate data products to optimally extract the spectrum, taking into account the curvature of the spectral trace on the detectors. The wavelength solution was calibrated against a telluric transmission model generated with ESO sky model calculator SkyCalc² (Noll et al., 2012). We corrected for telluric absorption lines using Molecfit (Smette et al., 2015), and shifted the spectrum to the target’s rest frame.

3.3 Retrieval analysis

3.3.1 Atmospheric retrieval model

For our atmospheric free retrieval, in which all fitted parameters varied freely under the condition of chemical equilibrium but the temperature structure is unconstrained, we used a Bayesian framework composed of the radiative transfer tool petitRADTRANS (pRT) (Mollière et al., 2019) and the nested sampling tool PyMultiNest (Buchner et al., 2014), which is a Python wrapper of the MultiNest method (Feroz et al., 2009). Synthetic emission spectra are generated by pRT using a set of inputs, including the temperature structure, chemical abundances, and surface gravity. The PyMultiNest samples the parameter space and derives the posterior distribution of the fit.

The forward modelling consists of three major components: the temperature model, the chemistry model, and the cloud model. We parameterised the temperature-pressure

²<https://www.eso.org/observing/etc/skycalc>

(T-P) profile using four temperature knots spaced evenly on a log scale pressure within 0.02 to 5 bar, where the contribution function of the observed spectrum peaks (see upper right panel in Fig. 3.3). The entire T-P profile was obtained by spline interpolation of the four temperature knots in the log space of pressure. The temperature profile outside this range is barely probed by the observations, and is simply considered to be isothermal in our model. There is no physical reasoning behind this T-P profile, and therefore few prior constraints are imposed on the solution.

The chemistry model used in our retrievals assumes chemical equilibrium as detailed in Mollière et al. (2020, 2017). In short, the chemical abundances are determined via interpolation in a chemical equilibrium table using pressure P , temperature T , carbon-to-oxygen ratio C/O , and metallicity $[Fe/H]$ as inputs.

As for the cloud model, the same setup as in Mollière et al. (2020) is implemented using the Ackerman & Marley (2001) model. It introduces four additional free parameters: the mass fraction of the cloud species at the cloud base X_0^c , the settling parameter f_{sed} (controlling the thickness of the cloud above the cloud base), the vertical eddy diffusion coefficient K_{zz} (effectively determining the particle size), and the width of the log-normal particle size distribution σ_g . The location of the cloud base P_{base} is determined by intersecting the condensation curve of the cloud species with the T-P profile of the atmosphere. $MgSiO_3$ and Fe clouds are expected to be the dominant cloud species in L dwarfs (Morley et al., 2012). Here, we only consider the $MgSiO_3$ clouds, because Fe is not expected to be the dominant aerosol composition according to the microphysics model by Gao et al. (2020), and (even if the cloud forms) it condensates at a higher temperature which occurs at lower altitudes than the photosphere of the target.

3.3.2 Retrieving 2M0355

The cloudy retrieval model has 14 free parameters: R_p , $\log(g)$, $[Fe/H]$, C/O , $^{12}CO/^{13}CO$, $X_0^{MgSiO_3}$, f_{sed} , K_{zz} , σ_g , $vsin(i)$ and four temperature knots for the T-P profile. The priors of these free parameters are listed in Table 3.2. We included H_2O , CH_4 , NH_3 , ^{12}CO , and the isotopologue ^{13}CO as line opacity species. The model also accounts for the Rayleigh scattering of H_2 , He, the collision induced absorption of H_2-H_2 , H_2-He , the scattering and absorption cross sections of crystalline, irregularly shaped $MgSiO_3$ cloud particles.

We used the line-by-line mode of pRT to calculate the emission spectra at high spectral resolution. To speed up the calculation, we took every fifth point of opacity tables with $\lambda/\Delta\lambda \sim 10^6$. This sampling factor of 5 has been benchmarked against the original sampling to ensure unbiased inference of parameters. The synthetic high-resolution spectra were rotationally broadened by $vsin(i)$ and convolved with a Gaussian kernel to match the resolving power of the instrument ($\lambda/\Delta\lambda \sim 27500$ for NIRSPEC and $\lambda/\Delta\lambda \sim 80000$ for CRIRES+), then binned to the wavelength grid of the observed spectrum (2020 data points in total), and scaled to the observed flux according to R_p and distance of the target. The retrievals were performed by PyMultiNest in importance nested sampling mode with a constant efficiency of 5%. It uses 2000 live points to sample the parameter space and derives the posterior abundances.

In addition to the retrievals with individual dataset, we also performed joint retrieval using spectra taken with both spectrographs VLT/CRIRES+ and Keck/NIRSPEC. As the

Table 3.2: Priors and posteriors (90% uncertainties) of the 2M0355 retrievals.

Parameter	Prior	Posterior	Posterior2
$\log(^{12}\text{CO}/^{13}\text{CO})$	$\mathcal{U}(-12, 0)$	-1.99 ± 0.10	-2.03 ± 0.09
R_p [R_{Jup}]	$\mathcal{U}(0.3, 2.5)$	0.97 ± 0.02	1.13 ± 0.03
$\log(g)$ [cgs]	$\mathcal{U}(3.0, 6.0)$	4.69 ± 0.15	4.32 ± 0.15
[Fe/H]	$\mathcal{U}(-1.5, 1.5)$	0.21 ± 0.10	0.05 ± 0.11
C/O	$\mathcal{U}(0.1, 1.5)$	0.56 ± 0.02	0.55 ± 0.02
T_0 [K]	$\mathcal{U}(1500, 4000)$	2322 ± 138	2906 ± 224
T_1 [K]	$\mathcal{U}(0.5, 1) * T_0$	1731 ± 17	1671 ± 35
T_2 [K]	$\mathcal{U}(0.5, 1) * T_1$	1640 ± 18	1478 ± 20
T_3 [K]	$\mathcal{U}(0.5, 1) * T_2$	1452 ± 21	1446 ± 16
$\log(\tilde{X}_0^{\text{MgSiO}_3})$	$\mathcal{U}(-2.3, 1)$	-1.3 ± 1.2	-
f_{sed}	$\mathcal{U}(0, 10)$	5.8 ± 4.1	8.0 ± 2.2
$\log(K_{zz})$	$\mathcal{U}(5, 13)$	10.5 ± 3.2	10.0 ± 1.8
σ_g	$\mathcal{U}(1.05, 3)$	2.0 ± 0.8	1.89 ± 0.82
$\text{vsin}(i)$	$\mathcal{U}(0, 20)$	2.0 ± 1.3	1.2 ± 1.3
$\log(\tau_{\text{cloud}})$	$\mathcal{U}(0, 1)$	-	0.02 ± 0.03

Posterior column shows values for the nominal model, while Posterior2 refers to the alternative model with enforced clouds. $\mathcal{U}(a, b)$ represents a uniform distribution ranging from a to b . The $\tilde{X}_0^{\text{MgSiO}_3}$ denotes $X_0^{\text{MgSiO}_3}/X_{\text{eq}}^{\text{MgSiO}_3}$, where $X_{\text{eq}}^{\text{MgSiO}_3}$ is the mass fraction predicted for the cloud species when assuming equilibrium condensation at the cloud base location.

accurate calibration of the broad-band spectral feature is challenging in high-resolution observations, we discarded the absolute flux information by removing the low-frequency variation in both observations and models using a Gaussian smoothing filter with a width of 2 nm, only preserving the line-by-line variations. We included in our fit the near-infrared (2MASS and WISE) photometric measurements (Faherty et al., 2016) to assist constraints on the radius, temperature and surface gravity. The photometry was converted from magnitudes to fluxes using the `species` package³ (Stolker et al., 2020). We observed in this analysis that the high-resolution spectra were more constraining than the photometric points, to the point where our retrieval would not correctly fit the SED if equal weighting is assigned to the photometry and the high-resolution data. On the other hand, we found that scaling the log-likelihood of the photometric data points by a factor of 100 ($\sim \sqrt{\mathcal{R}_{\text{high}}/\mathcal{R}_{\text{photom}}}$) produced a good fit of both datasets. Although the validity of the procedure remains to be further studied, we note that the different weighting does not significantly affect the resulted isotopic ratios.

³<https://species.readthedocs.io/>

3.4 Results

3.4.1 Retrieval results

The retrieval results are shown in Fig.3.3, including the retrieved temperature-pressure profile and the posterior distribution of the free parameters. The central values of the inferred parameters and their 90% uncertainties are summarised in Table 3.2, including $^{12}\text{CO}/^{13}\text{CO} = 97_{-18}^{+25}$, $\text{C/O} = 0.56_{-0.02}^{+0.02}$, $[\text{Fe}/\text{H}] = 0.21_{-0.10}^{+0.11}$, $\log(g) = 4.69_{-0.15}^{+0.15}$, and $R_p = 0.97_{-0.02}^{+0.03}$. It suggests that 2M0355 has a solar C/O ratio and a super-solar metallicity. The inferred mass of $19_{-5}^{+7} M_{\text{Jup}}$ is in line with previous estimations using evolutionary models based on its photometry and membership (age) of AB Dor moving group (Faherty et al., 2013). Using the evolutionary models for low-mass objects by Baraffe et al. (2015), we estimate the radius of a $\sim 20M_{\text{Jup}}$ dwarf to be $\sim 1.15R_{\text{Jup}}$ for an age of 120 Myr. The radius constrained from our retrieval model ($\sim 0.97R_{\text{Jup}}$) is smaller than that expected from evolutionary tracks. This is likely associated with the temperature structure in the retrieval models. We note that the alternative retrieval model (described below) converges to different T-P profiles, leading to radii in agreement with the estimation from evolutionary models (see Table 3.2).

Moreover, we retrieved a much smaller rotational velocity ($< 4 \text{ km s}^{-1}$) than the value (14.7 km s^{-1}) found by Bryan et al. (2018) using the same data, as listed in Table 3.1. Broadening synthetic spectra with a $v\sin(i)$ of 14.7 km s^{-1} result in spectral lines too broad to fit the observation with a $\lambda/\Delta\lambda \sim 27500$. In our case, the widths of spectral lines are therefore dominated by the instrument resolution instead of the spin of the target. Regardless, the rotational broadening shows no impact on the inference of the isotopologue ratio.

Fig.3.3 shows that the properties of clouds are barely constrained. The inferred values of the parameters are similar to the cloud-free case that we tested, indicating that the retrieval converges to solutions with optically thin clouds. We suggest that this behaviour is a cooperative consequence of the freely adjustable temperature structure and properties of clouds. Since the presence of thick clouds can block the emission from high-temperature regions of the atmosphere below, the cloudy atmosphere is spectrally equivalent to the case of a cloudless atmosphere combined with a shallow (isothermal) temperature gradient. This effect has been put forward as an alternative (cloud-free) explanation for the red spectra of brown dwarfs and self-luminous exoplanets (Tremblin et al., 2016, 2015, 2017, 2019). Both cases provide good fits to the observed spectrum, but here the free retrieval model tends to converge to cloudless solutions, potentially because they occupy a larger volume in the parameter space than the cloudy solutions. The problem of too isothermal temperature structures in free retrievals of cloudy objects has also been discussed in Burningham et al. (2017), Mollière et al. (2020), and Burningham et al. (2021). Classical 1-d self-consistent calculations will predict a steeper temperature profile, requiring clouds to fit the data. It is therefore important to examine how the inference of other parameters is affected in both cases.

To obtain a more reasonable temperature structure incorporating the effect of clouds, we have to enforce a cloudy atmosphere with a free parameter τ_{cloud} , which artificially sets the optical depth of the cloud at the photosphere of the clear component of the atmosphere (where the major emission contribution lies assuming no clouds). In this case, we no longer fit for the cloud mass fraction X_0^{C} . Instead, the optical depth of clouds at all pressure levels is scaled to fulfill the prescribed τ_{cloud} . A strict prior is set to enforce optically thick clouds

($\tau_{\text{cloud}} > 1$). Moreover, we also ensure that the prescribed τ_{cloud} is physically plausible by constraining the scaling factor of the cloud optical depth to be less than $2(f_{\text{sed}} + 1)$. This factor $f_{\text{sed}} + 1$ results from the requirement that the cloud surface density (i.e. integrating the product of density with cloud mass fraction vertically) be constrained by the available mass above the cloud base before condensation takes place (i.e. with the equilibrium mass fraction X_{eq}^{c}). With the cloud mass fraction depending on the altitude via $X^{\text{c}}(P) \propto P^{f_{\text{sed}}}$, this leads to the constraint for the mass fraction at the cloud base: $X_0^{\text{c}} \leq X_{\text{eq}}^{\text{c}}(f_{\text{sed}} + 1)$. We added a factor of two to offer some flexibility.

This alternative model results in more pronounced clouds and less isothermal T-P profiles, as is shown in Fig. 3.4. Comparing the retrieved values of other atmospheric properties (see Table 3.2), we note that the atmospheric gravity and radius are significantly modified as a result of the heavy cloud and the altered temperature structure. The alternative model no longer probes as deep as the cloudless model because the clouds hide the region below. In addition, the metallicity becomes smaller when clouds are enforced in the retrieval, because the steeper temperature gradient requires less absorbing gas to achieve a similar absorption in emergent flux, as also explained in Burningham et al. (2021). Retrievals over a larger wavelength coverage (in particular, probing silicate absorption features at $10 \mu\text{m}$) will reveal the nature of clouds and help better constrain other properties of the atmospheres (Burningham et al., 2021). Nevertheless, it is reassuring that the retrieval of the C/O and $^{12}\text{CO}/^{13}\text{CO}$ ratios does not strongly rely on the accurate inference of temperature structure and clouds, which was also found in Mollière et al. (2020) and Burningham et al. (2021).

3.4.2 ^{13}CO detection

To reveal the presence of ^{13}CO signal, we compare the observed spectrum to the retrieved best-fit model ($\log(g)=4.69$, $[\text{Fe}/\text{H}]=0.2$, $\text{C}/\text{O}=0.55$, and $^{12}\text{CO}/^{13}\text{CO}=97$) in Fig. 3.1, and calculate the cross-correlation function (CCF) between the residuals (the observed spectrum minus the best-fit model without ^{13}CO) and a ^{13}CO model (Fig. 3.2). The ^{13}CO model spectrum is constructed by taking the difference between the best-fit model and the same model with the ^{13}CO abundance set to zero. As is shown in the right panel of Fig. 3.2, the CCF peaks at zero radial velocity, signifying the detection of ^{13}CO at a S/N of 8.4. This value varies slightly depending on the choice of velocity ranges where the standard deviation of the noise is measured.

We also determined the significance of the ^{13}CO detection using Bayesian model selection. We performed the retrieval again while excluding ^{13}CO opacity and the parameter $^{12}\text{CO}/^{13}\text{CO}$. Comparing its Bayesian evidence (Z) to that of the full model (as listed in Table 3.3) allows us to assess the extent to which the model including ^{13}CO is favoured by the observations. In Bayesian model comparison, the Bayes factor B_m (calculated by the ratio of Z) is used as a proxy for the posterior odds ratio between two models. We then translated B_m to the frequentist measures of significance following Benneke & Seager (2013). As a result, the difference of $\ln(Z)$ between two models is $\Delta \ln(Z) = \ln(B_m) = 44$, meaning that the observation favours the full model (including ^{13}CO) at a significance level of 9.5σ . The detection remains the same significance (9.5σ) when we use the alternative model with enhanced clouds.

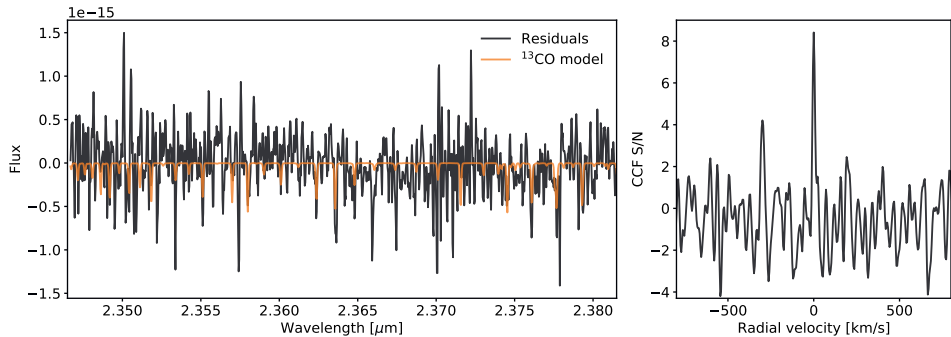


Figure 3.2: Left panel: observational residuals (observed spectrum minus best-fit model with the ^{13}CO abundance set to zero) in black and ^{13}CO model spectrum given the best-fit $^{12}\text{CO}/^{13}\text{CO}$ ratio (~ 97) in orange. Right panel: cross-correlation function (CCF) between the ^{13}CO model and residuals. The CCF is normalised by its standard deviation within the velocity ranges $[-2200, -800]$ and $[800, 2200]$ km s^{-1} , so that the y-axis represents the signal-to-noise of the CCF peak.

Table 3.3: Results of Bayesian model comparison for the two retrieval models with and without ^{13}CO .

Model	$\ln(Z)$	$\chi^2_{\text{best-fit}}$	$\ln(B_m)$
Full model	-1181	2372	44 ($\sim 9.5\sigma$)
^{13}CO excluded	-1225	2470	-

Z denotes the Bayesian evidence, $\chi^2_{\text{best-fit}}$ the best-fit χ^2 , and B_m the Bayes factor.

3.4.3 Hint of C^{18}O

The observed spectra at $2.32\text{--}2.37 \mu\text{m}$ and the best-fit model are shown in panel a in Fig. 3.5. The retrieved posterior distribution of the isotope ratios are shown in panel c and d. The cross-correlation functions (CCF) with the ^{13}CO and C^{18}O templates are shown in panel b. We confirmed the previous detection of ^{13}CO as suggested by the CCF peak at zero velocity, and obtained a consistent and tighter constraint on the carbon isotope ratio $^{12}\text{CO}/^{13}\text{CO} = 108 \pm 10$. As for the oxygen isotope ratio, the retrieval provided a tentative constraint of $^{16}\text{O}/^{18}\text{O} = 1489^{+1027}_{-426}$. The value is higher than the typical ratio (~ 500) found in the solar system or local interstellar medium (Wilson, 1999), while comparable to the measurements towards several young stellar objects (YSOs) (Smith et al., 2015) and an M dwarf binary (Crossfield et al., 2019b). We refrain from further interpretation of the provisional measurement of the oxygen isotope ratio, as we did not detect the C^{18}O in the cross-correlation analysis, indicating that $\text{S/N} \lesssim 2$. This is likely attributed to the lower than expected signal-to-noise ratio of the CRIFES spectrum due to the far from optimal observing condition. Nevertheless, the tentative constraint of the oxygen isotope ratio in the brown dwarf suggests the prospect of exploiting the isotope inventory in sub-stellar objects with future data of higher quality.

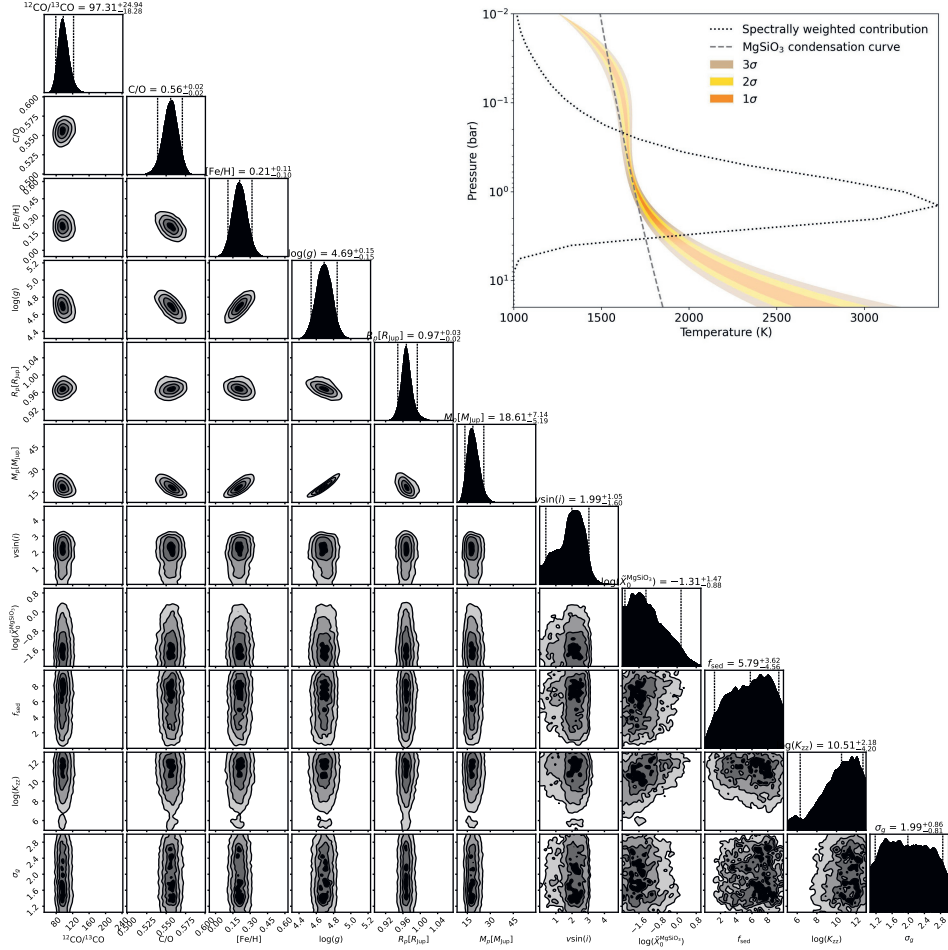


Figure 3.3: Retrieved parameters and temperature structure of 2M0355 using the nominal model. Upper right panel: retrieved temperature-pressure confidence envelopes. The coloured regions represent 1 σ , 2 σ , 3 σ confidence envelopes. The black dotted line shows the flux average of the emission contribution function. The gray dashed line represents the condensation curve of MgSiO₃ clouds. Lower left panel: posterior distributions of parameters. The vertical dashed lines denote the 5%, 50%, 95% quantiles (90% uncertainties) of the distribution.

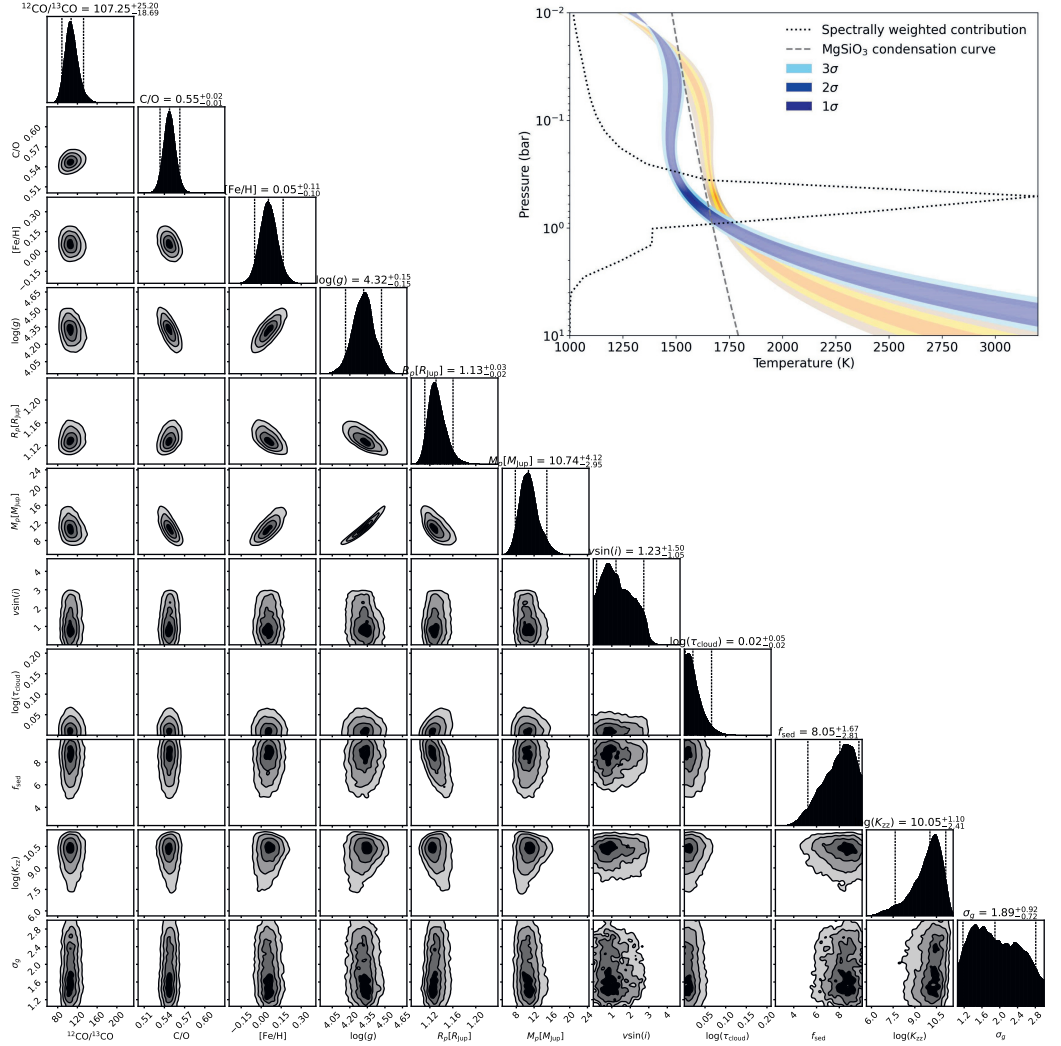


Figure 3.4: Similar to Fig. 3.3, but for the alternative model with enforced clouds. Upper right panel compares the temperature-pressure profiles of the nominal model in Fig. 3.3 (in orange) to this alternative model (in blue).

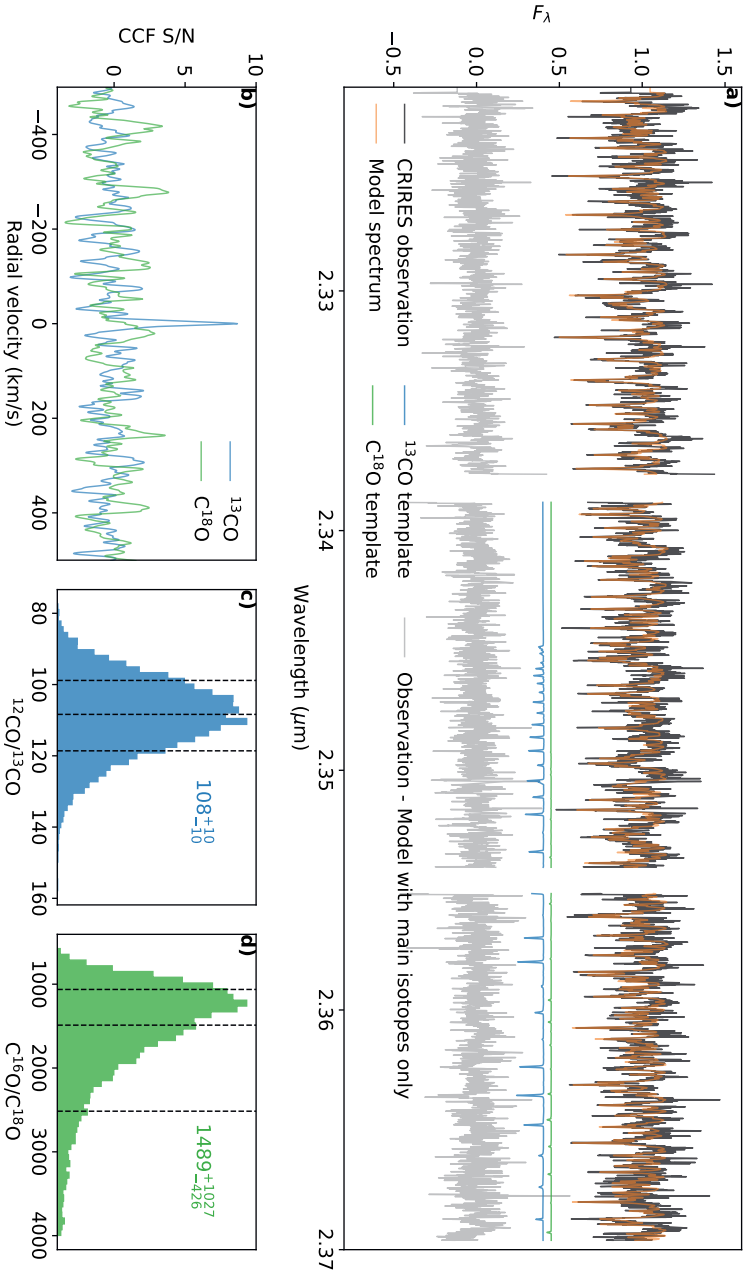


Figure 3.5: *Panel (a)*: K-band (2.32-2.37 μm) spectrum of the brown dwarf 2M0355 taken with VLT/CRIRES. The orange line shows the best-fit model obtained through the retrieval analysis. The blue and green lines are the template spectra of ^{13}CO and C^{18}O . The observational residuals (namely, observations minus the model with main isotopes only) are shown in gray. *Panel (b)*: Cross-correlation functions of the observational residuals of the ^{13}CO or C^{18}O template. *Panel (c)*: Posterior distribution of the carbon isotope abundance ratio constrained by the retrieval. The vertical dashed lines denote the 1σ interval. *Panel (d)*: Same as *panel (c)*, but for the oxygen isotope ratio.

3.5 Discussion

3.5.1 CO isotopologue ratio in 2M0355

We found the CO isotopologue ratio in 2M0355 ($^{12}\text{CO}/^{13}\text{CO} = 97_{-18}^{+25}$) to be similar to the carbon isotope ratio measured in for the Sun (93.5 ± 3 by Lyons et al., 2018), while it is marginally higher than the ratio in today's local ISM (68 ± 15 by Milam et al., 2005), which is expected to be inherited by young objects. However, recent measurements of carbon isotope ratios towards a sample of solar twins suggest a current local value of ~ 81.3 (Botelho et al., 2020), which is within the uncertainty of our measurement. Therefore, it remains unclear whether the CO isotopologue ratio in 2M0355 is indeed higher than its local environment.

We note that high $^{12}\text{CO}/^{13}\text{CO}$ ratios were also observed towards some diffuse clouds, molecular clouds and YSOs in the solar neighbourhood (Federman et al., 2003, Goto et al., 2003, Lambert et al., 1994, Smith et al., 2015). If the high $^{12}\text{CO}/^{13}\text{CO}$ ratios in molecular clouds and YSOs do not result from observational biases, it may not be surprising that the brown dwarf 2M0355 might inherit the high ratio from a ^{13}CO -diminished parent cloud. One possible explanation for the high ratios towards diffuse clouds is the isotope-selective photodissociation (Bally & Langer, 1982, van Dishoeck & Black, 1988, Visser et al., 2009). Because of the lower column density of the rarer isotopologue, the self-shielding of ^{13}CO takes effect at a deeper layer in the cloud. Consequently, ^{13}CO is preferably destructed by far-ultraviolet (FUV) radiation, increasing the $^{12}\text{CO}/^{13}\text{CO}$ ratios in the ISM. However, this explanation is not as plausible for molecular clouds and YSOs, because these objects with high extinction are supposed to be well shielded from FUV radiation. The isotope-selective photodissociation is unlikely to significantly alter the globally isotopologue ratios (van Dishoeck & Black, 1988). Other hypotheses were also suggested, such as higher excitation temperature in ^{12}CO than in ^{13}CO resulted from photon trapping in ^{12}CO rotational transitions (Goto et al., 2003), CO gas-to-ice reservoir partitioning (Smith et al., 2015), and ISM enrichment caused by ejecta from carbon-rich giant stars or supernovae (Crossfield et al., 2019b), but no general and conclusive interpretation.

3.5.2 Implications for planet formation

It is intriguing to compare the $^{12}\text{CO}/^{13}\text{CO}$ measurements between the L dwarf 2M0355 (~ 97) and the wide-orbit exoplanet TYC 8998 b (~ 31 by Zhang et al., 2021a). Despite similarities in several aspects, the young super-Jupiter has possibly undergone a different formation pathway to the isolated brown dwarf, leading to the difference in isotopologue ratio in their atmospheres. While isolated brown dwarfs may experience a top-down formation via gravitational collapse (which resembles star formation) or disk instability (Boss, 1997, Kratter & Lodato, 2016), super-Jupiters possibly form through the bottom-up core-accretion (of planetesimals and pebbles) (Lambrechts & Johansen, 2012, Pollack et al., 1996). Previous demographics on giant planets and brown dwarfs (Bowler et al., 2020, Nielsen et al., 2019) also support the two distinct formation pathways. As argued in Zhang et al. (2021a), the core-accretion scenario could possibly lead to ^{13}CO enrichment through ice accretion, lowering the $^{12}\text{CO}/^{13}\text{CO}$ ratio in observed super-Jupiter atmospheres.

Admittedly, it is preliminary to draw any conclusive interpretation based on a sample of two objects. Another caveat is that the two measurements towards the super-Jupiter

and the L dwarf are carried out under different spectral resolutions. It is so far unclear whether a smaller spectral resolving power can lead to any observational biases because it probes unresolved molecular lines. This calls for more future observations that enable homogeneous comparisons between different objects, in order to better understand the potential and limitations of carbon isotopologue ratio as a tracer for planet formation. It is also essential to interpret the isotopologue measurements in light of carbon fractionation in protoplanetary disks (Miotello et al., 2014), disk evolution (Trapman et al., 2021), CO ice chemistry (Krijt et al., 2020), and planet formation (Cridland et al., 2020), in order to provide constraints on the birth location, the relative importance of ice accretion, and possible vertical gas accretion processes during formation.

3.6 Conclusion

We analysed archival high-resolution spectra (from 2.275 to 2.385 μm) from Keck/NIR-SPEC of the isolated brown dwarf 2M0335 and carried out a free retrieval analysis. After removing the retrieved best-fit model that includes only the main isotopologues, we detected a ^{13}CO signal using the cross-correlation method with a S/N of ~ 8.4 . The detection significance was determined to be $\sim 9.5\sigma$ with a Bayesian model comparison between the two retrieval models including or excluding ^{13}CO . The isotopologue ratio $^{12}\text{CO}/^{13}\text{CO}$ is inferred to be 97^{+25}_{-18} , similar to the value found in the Sun, while marginally higher than the local ISM standard. If this deviation is real, it is possibly inherited from its parent cloud that has a high $^{12}\text{CO}/^{13}\text{CO}$ ratio.

Although based on only two objects, it is also intriguing to note the difference between carbon isotopologue ratios in giant exoplanets and brown dwarfs, potentially implying distinct formation pathways. Despite spectroscopic similarities, brown dwarfs may experience a top-down formation via gravitational collapse, which resembles star formation, while giant exoplanets likely form through a bottom-up accretion process, which may alter isotopologue ratios in their atmospheres with dependencies on the accretion location and pathway in protoplanetary disks. This further emphasises the atmospheric carbon isotopologue ratio as a tracer for planet formation history. In the future, such an analysis can be implemented on spectra of more exoplanets to measure the carbon isotopologue ratios in their atmospheres and shed light on the location and mechanisms of planet formation.

4

Search for Helium airglow emission from the hot Jupiter τ Boo b

The helium absorption line at 10830 Å originating from the metastable triplet state 2^3S , has been suggested as an excellent probe for the extended atmospheres of hot Jupiters and their hydrodynamic escape processes, and has recently been detected in the transmission spectra of a handful of planets. The isotropic re-emission will lead to helium airglow that may be observable at other orbital phases. The goal of this paper is to investigate the detectability of He I emission at 10830 Å in the atmospheres of exoplanets using high-resolution spectroscopy, providing insights into the properties of the upper atmospheres of close-in gas giants. We estimate the expected strength of He I emission in hot Jupiters based on their transmission signal. We search for the He I 10830 Å emission feature in τ Boo b in three nights of high-resolution spectra taken by CARMENES at the 3.5m Calar Alto telescope. The spectra in each night were corrected for telluric absorption, sky emission lines and stellar features, and shifted to the planetary rest frame to search for the emission. The He I emission is not detected in τ Boo b, reaching a 5σ contrast limit of 4×10^{-4} for emission line widths of $>20 \text{ km s}^{-1}$. This is roughly a factor ~ 8 above the expected level of emission (assuming a typical He I transit absorption of 1% for hot Jupiters). This suggests that targeting the He I emission with well-designed observations using upcoming instruments such as VLT/CRIRES+ and E-ELT/HIRES is possible.

4.1 Introduction

The atmospheres of close-in exoplanets are strongly affected by the high-energy irradiation from their host stars, making their upper atmospheres weakly bound and susceptible to hydrodynamic escape (Owen, 2019). For gas-giant planets, Lyman- α absorption in transit measurements has been the primary probe for their extended atmospheres, e.g., HD 209458b (Vidal-Madjar et al., 2003), GJ 436b (Ehrenreich et al., 2015, Kulow et al., 2014) and GJ 3470b (Bourrier et al., 2018). Such observations trace the exospheres with neutral hydrogen extending far beyond the Roche lobe radius, and cast light on the hydrodynamic escape and mass loss, which drives the evolution of the atmospheric and bulk composition of close-in exoplanets (Ehrenreich et al., 2015).

In addition to Ly α , helium at 10830 Å was also identified to be a powerful tracer of the extended atmospheres (Seager & Sasselov, 2000), which was recently reassessed by Oklopčić & Hirata (2018). This helium line has several advantages over Ly α because it suffers less from the interstellar absorption and can be observed from the ground with high-resolution spectrographs, opening a new window into the characterization of exospheres.

The theoretical work by Oklopčić & Hirata (2018) has resulted in a breakthrough in helium measurements. Excess absorption was first detected by the Hubble Space Telescope/Wide Field Camera 3 in WASP-107b (Spake et al., 2018) and independently confirmed by ground-based observations (Allart et al., 2019, Kirk et al., 2020) showing an absorption level of $5.54 \pm 0.27\%$. In addition, another five planets have been reported with helium signals, namely, HAT-P-11b at a level of $1.08 \pm 0.05\%$ (Allart et al., 2018, Mansfield et al., 2018), HD 189733b at $0.88 \pm 0.04\%$ (Guilluy et al., 2020, Salz et al., 2018), WASP-69b at $3.59 \pm 0.19\%$ (Nortmann et al., 2018), HD 209458b at $0.91 \pm 0.10\%$ (Alonso-Floriano et al., 2019), and GJ 3470b at $1.5 \pm 0.3\%$ (Ninan et al., 2020, Palles et al., 2020). Upper limits in He I absorption were derived for Kelt-9b and GJ 436b at 0.33% and 0.41% (Nortmann et al., 2018), for WASP-12b at 59 ± 143 ppm over a 70 Å band (Kreidberg & Oklopčić, 2018), for GJ 1214b at $3.8 \pm 4.3\%$ (Crossfield et al., 2019a), for K2-100b with an equivalent width less than 5.7 mÅ (Gaidos et al., 2020), and AU Mic b with EW of 3.7 mÅ (Hirano et al., 2020).

The wide range of helium absorption levels seen in the transmission spectra of hot gas giants is likely due to the variety in the stellar radiation fields. The helium absorption line at 10830 Å originates from atoms in a metastable triplet state 2^3S , which is mainly populated via recombination of ionized helium. The ionization of He I requires photons with wavelengths smaller than 504 Å, i.e. X-ray and extreme-ultraviolet (EUV). Therefore, the helium absorption is expected to be enhanced for planets irradiated with higher X-ray and EUV flux (Nortmann et al., 2018). However, the level of EUV irradiation may not be the only determining factor. The mid-ultraviolet radiation near 2600 Å can de-populate the triplet state 2^3S via ionization. Therefore, the strength of the helium absorption has been proposed to depend on the ratio between EUV and mid-UV stellar fluxes, and K-type stars may provide the most favorable stellar environment (Oklopčić, 2019). Hitherto, the exoplanets with detected helium absorption generally support this trend with four out of six orbiting K-type stars. More detections will help to better understand the factors that affect the He I absorption level.

As helium atoms at the triplet state 2^3S absorb photons to reach 2^3P state, the opposite transition will happen concurrently, with 10830 Å photons re-emitted in random

directions. Based on the absorption level, we estimate the amount of emission expected from the planetary atmospheres. The study of He I airglow emission allows for better understanding of the radiation fields and level populations under non-local thermodynamic equilibrium in the upper atmospheres. In addition, it provides a way of probing the extended atmospheres of non-transiting close-in gas giants, which have not been investigated before.

In this paper, we address the detectability of He I emission in the atmospheres of close-in exoplanets. We first calculate the expected emission level (Section 4.2), then perform a case study on τ Boo b (Section 4.3) searching for helium airglow emission in high-resolution spectroscopic data from CARMENES (Calar Alto high-Resolution search for M dwarfs with Exoearths with Near-infrared and optical Echelle Spectrographs) in Section 4.4 and 4.5. We discuss our results and future prospects in Section 4.6.

4.2 Helium emission from extended atmospheres

The concept of probing He I airglow emission is illustrated in Fig. 4.1. We consider the extended atmosphere as an optically thin cloud surrounding the exoplanet. The cloud absorbs a fraction of irradiation from the host star due to the transition at 10830 Å, resulting in the helium atoms at state 2^3S to be excited to the higher state 2^3P . The absorbed radiation is reemitted isotropically when the excited electrons jump back down to the metastable triplet state. Assuming the extended atmosphere has a low density and is optically thin, the reemitted photons can freely escape and be observed as an emission feature. We would like to point out that during transit the feature is seen in absorption because only a small fraction of the radiation is reemitted along the line-of-sight. Consequently, we can detect He I absorption lines during transit, while emission lines from other viewing angles.

To estimate the strength of the He I emission, the cloud is assumed to absorb a fraction of the incident stellar energy at 10830 Å, emitting it back isotropically. Assuming the upper energy level not being (de-)populated in another way, we can estimate (see Seager, 2010, Chap. 3)

$$4\pi R_c^2 F_c^S = F_*^S f_{\text{abs}} \left(\frac{R_*}{a}\right)^2 \pi R_c^2 \quad (4.1)$$

where R_c is the radius of the cloud that absorbs radiation at that wavelength, R_* is the stellar radius, a is the orbital distance of the planet, f_{abs} is the fraction of energy absorbed at 10830 Å, which is linked to the column density of helium atoms at state 2^3S in the cloud, F_c^S and F_*^S denote the 10830 Å flux at the surface of the planet and the star respectively. The corresponding fluxes that we observe at Earth are

$$\mathcal{F}_c = F_c^S \left(\frac{R_c}{D}\right)^2, \quad \mathcal{F}_* = F_*^S \left(\frac{R_*}{D}\right)^2 \quad (4.2)$$

where D is the distance of the system to Earth. Thus, the planet to star contrast at 10830 Å is

$$\frac{\mathcal{F}_c}{\mathcal{F}_*} = \frac{f_{\text{abs}} R_c^2}{4a^2} = \frac{R_*^2}{4a^2} T_\lambda = 10^{-4} \left(\frac{T_\lambda}{1\%}\right) \left(\frac{5}{a/R_*}\right)^2 \quad (4.3)$$

T_λ is the excess absorption at 10830 Å that can be measured by transmission spectroscopy, with $T_\lambda = f_{\text{abs}} R_c^2 / R_*^2$.

Uncertainties regarding this estimate are further discussed in Section 4.6.1. A more detailed derivation involving radiative transfer is presented in Appendix 4.A. Given Equation 4.3, we expect contrast levels of $\sim 10^{-4}$, which may be reached by combining multiple nights of observations.

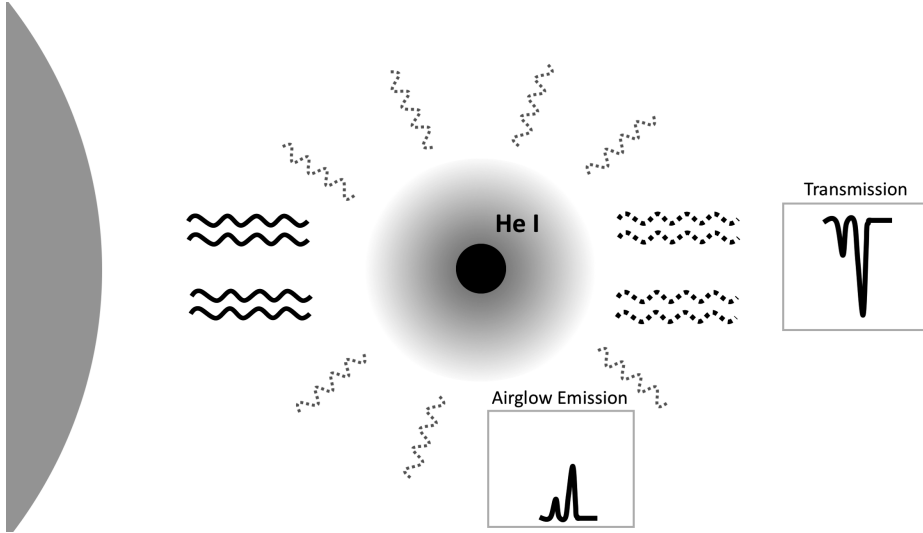


Figure 4.1: Illustration of He I emission from an exosphere of a close-in planet. The gray disk represents the extended atmosphere around such planet. He I absorption is observed during transit, while airglow emission can be probed at other orbital phases.

4.3 The τ Boo system

The hot Jupiter τ Bootis b is among the first exoplanets discovered (Butler et al., 1997), orbiting a bright F7V type main-sequence star ($V=4.5$ mag) at a distance of 15.6 pc from Earth. Although the planet is not transiting, its orbital inclination was determined to be 45° by tracking CO absorption in its thermal dayside spectrum (Brogi et al., 2012), confirmed by measurements of H_2O (Lockwood et al., 2014). The properties of the τ Boo system are summarized in Table 4.1. Unfortunately, because the planet is not transiting, there is no direct measure of its radius (meaning that its surface gravity is unknown), and the He I 10830 Å line cannot be probed in transmission.

The system has been an interesting target for investigating star-planet interactions because of its strong stellar activity. The star has a high S-index of 0.202 (Wright et al., 2004), indicating strong emission cores in the Ca II H&K lines. It exhibits an X-ray luminosity of 9×10^{28} erg s^{-1} (Huensch et al., 1998), and a reconstructed EUV luminosity of 2.5×10^{29} erg s^{-1} (Sanz-Forcada et al., 2011), which are among the highest values found in the planet-hosting stars. The intense X-ray and EUV radiation can deposit substantial energy in the planetary atmosphere, facilitating the expansion and evaporation of gas. Although τ Boo is not a K-type star (which is possibly the most favorable spectral type for probing the helium line), however, due to the high level of stellar X-ray and EUV emission, τ Boo b

could well have an extended atmosphere with a large population of helium at the triplet state, and forms a promising target to search for the He I emission at 10830 Å.

Table 4.1: Properties of the star τ Boo (upper part) and τ Boo b (lower part).

Parameter	Symbol	Value
Distance (pc) ^a	d	15.66 ± 0.08
Effective temperature (K) ^b	T_{eff}	6399 ± 45
Luminosity (L_{\odot}) ^b	L_{*}	3.06 ± 0.16
Mass (M_{\odot}) ^b	M_{*}	1.38 ± 0.05
Radius (R_{\odot}) ^b	R_{*}	1.42 ± 0.08
Surface gravity (cgs) ^c	$\log g$	$4.27^{+0.04}_{-0.02}$
Systemic velocity (km s ⁻¹) ^d	γ	-16.4 ± 0.1
Rotation velocity (km s ⁻¹) ^b	$v \sin(i)$	14.27 ± 0.06
Semi-amplitude (m s ⁻¹) ^e	K_{*}	468.42 ± 2.9
Metallicity (dex) ^b	[M/H]	0.26 ± 0.03
Age (Gyr) ^b		0.9 ± 0.5
Orbital period (days) ^e	P	$3.312454 \pm 3.3 \cdot 10^{-6}$
Semi-major axis (AU) ^b	a	0.049 ± 0.003
Orbital inclination (deg) ^d	i	44.5 ± 1.5
Eccentricity ^b	e	0.011 ± 0.006
Mass (M_J) ^b	M_p	6.13 ± 0.17
Phase zero-point (HJD) ^e	T_0	56401.8797 ± 0.0036
Semi-amplitude (km s ⁻¹) ^d	K_p	110.0 ± 3.2

^a Gaia Collaboration et al. (2018);

^b Borsa et al. (2015);

^c Takeda et al. (2007);

^d Brogi et al. (2012);

^e Justesen & Albrecht (2019)

4.4 Observations and Data analysis

We observed and analyzed the τ Boo system for five nights with the CARMENES spectrograph mounted on the 3.5m Calar-Alto Telescope (Quirrenbach et al., 2016), on 26 March 2018, 11 May 2018, 12 March 2019, 15 March 2019 and 11 April 2019. CARMENES has two channels, VIS and NIR, covering the optical wavelength range (520-960 nm) and the near-infrared wavelength range (960-1710 nm) respectively. The resolving power is 94,600 in the VIS channel and 80,400 in the NIR channel. Each channel is fed with two fibers: fiber A targeting the star and fiber B obtaining a sky spectrum simultaneously. The He I line at 10830 Å falls on echelle order 56 (10801-11001 Å) in the NIR channel, on which we focused our analysis.

The details of the observations are shown in Table 4.2 and Fig. 4.2. The observations probed thermal emission from τ Boo b, covering a wide range in planet orbital phases each night (see Fig. 4.2). The exposure times were adjusted according to the weather conditions, maintaining a S/N \geq 100. The observations in the first two nights were taken with exposure

times of 40 s with a seeing of $2''$ and $1.4''$ respectively, delivering lower S/N per spectrum than during the other nights with longer exposures and better weather conditions. The drop-off in S/N during the end of night 2 was due to the increasingly high airmass. The relative humidity during night 1, 2 and 5 continuously exceeded 85%, in contrast to the lower value ($\sim 45\%$) during night 4. This agrees well with the behavior of S/N in these nights. For night 3, although the relative humidity was not as high as the first two nights, it underwent strong variation overnight, possibly accounting for the drastic change in S/N.

The standard data reduction, such as bias removal, flat fielding, cosmic ray corrections, and wavelength calibration, was performed with the CARMENES pipeline CARACAL v2.10 (Caballero et al., 2016). The output of the pipeline was provided in the observer’s frame with a vacuum wavelength solution. We converted the vacuum wavelength solution into air wavelengths and used it throughout our analysis.

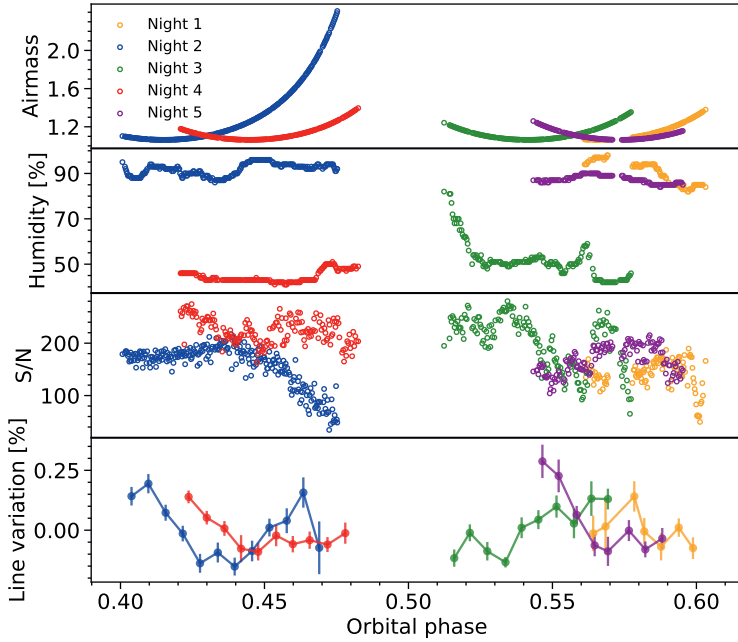


Figure 4.2: Variation in airmass (upper panel), relative humidity (mid panel), S/N (lower panel) and variation around the mean of the stellar He I line (bottom panel) during observations in the different nights. The S/N of each spectrum is defined as the average signal-to-noise ratio of the continuum near the He I 10830 Å line.

4.4.1 Data analysis

First, we manually corrected for additional hot pixels and cosmic rays present in the pipeline-reduced spectra by substituting those values with the linear interpolation of adjacent pixels or adjacent time series. Subsequently, each spectrum was normalized to unity using the continuum both at the blue and red side of the helium line over the

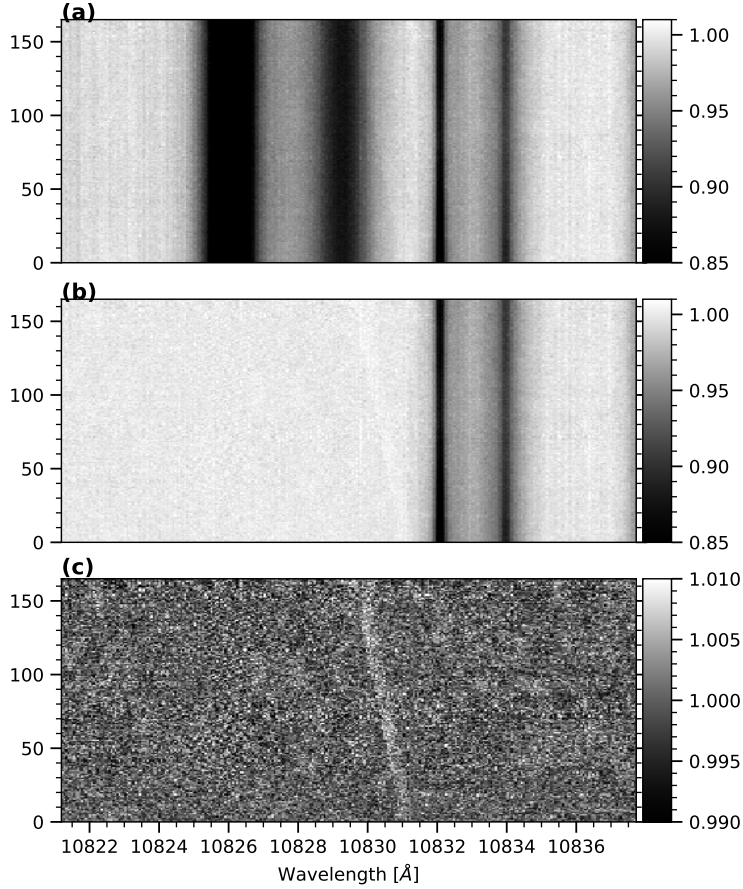


Figure 4.3: Illustration of our data reduction steps applied to the spectral series taken on Night 4. Each row in the matrix represents one spectrum, with the y-axis corresponding to time. As detailed in Section 4.4.1, the steps include: (a) normalization of the continuum; (b) correction for stellar lines in each spectrum using an empirical model; (c) removal of telluric contamination by correcting the temporal variation of the flux in telluric lines using a column-by-column linear regression. The trail of an artificially injected planetary helium line (with a magnitude of 0.3% and a width of 11 km s^{-1}) can be seen as a slanted white band near 10830 \AA , shifting in time due to the change in the radial component of the orbital velocity of the planet.

Table 4.2: Observations Summary

Night	Date	Proposal No.	Program PI	No. of spectra	Exposure time (s)	On-target time (h)	S/N
1	2018-03-26	F18-3.5-012	J.A.Caballero &	110	40	1.2	140
2	2018-05-11	F18-3.5-012	F.J.Alonso-Floriano	261	40	2.9	160
3	2019-03-12	F19-3.5-051	M.Brogi	161	66	3.1	200
4	2019-03-15	F19-3.5-051	M.Brogi	165	65	3.0	220
5	2019-04-11	F19-3.5-051	M.Brogi	133	66	2.4	170

ranges 10804.0-10805.2 Å, 10818.5-10819.0 Å and 10839.0-10840.3 Å. After normalization, the spectral series of each night were handled as a two-dimensional matrix as shown in Fig. 4.3(a). Each row in the matrix represents one spectrum, with the frame number on the y-axis, corresponding to orbital phase or time.

Before correcting for the telluric lines, we first removed the stellar Si line and He I triplet at 10827.1 Å and 10829.09, 10830.25 and 10830.34 Å. In order to achieve this, we built an empirical stellar model for each night by combining all spectra with S/N>100 in the stellar rest frame, where we set all values outside of the two stellar features to unity. This model was then shifted to the observer's rest frame, scaled and removed from each spectrum. Subsequently, the spectra were free of stellar lines in the wavelength region near the planetary helium line (see Fig. 4.3(b)).

The residual matrix in Fig. 4.3(b) shows the telluric lines near the planetary helium signal that required removal, including the H₂O absorption features at 10832.1 Å and 10834.0 Å, and the OH emission lines at 10824.7 Å, 10829.8 Å and 10831.3 Å. The strengths of telluric lines vary overnight, which mainly results from the change in airmass and/or water column. To correct for telluric absorption lines, we measured the temporal variation of the flux at the centers of several deep H₂O absorption features and combined them to serve as a representation for the atmospheric change overnight. Such temporal variation was then removed using a column-by-column linear regression while avoiding the columns that contain the assumed planetary He I emission. We removed the sky emission lines in a similar way, using their mean-variation overnight. After telluric correction, each column of the matrix was subsequently normalized as follows. The spectra were combined via weighted average, with the weights defined as the squared S/N of each exposure, to build a master spectrum. Each individual spectrum was subsequently divided by this master spectrum to obtain the residual spectral series as shown in Fig. 4.3(c).

We note that during the telluric removal and final normalisation, we masked the region in each spectrum where the planetary He line is expected to appear, so that we could avoid self-subtraction of the signal, if present. This is particularly important if the planetary He I line is broad. In the case that the line width is larger than the change of the planetary radial velocity overnight, the planetary signal would be (partially) subtracted out, making it less likely to be detected.

4.4.2 Extra noise in residual spectra

After correcting for the stellar and telluric effects, we shifted the residual spectral series of all five nights into the stellar rest frame by correcting for the systemic velocity, barycentric velocity, and stellar reflex motion of τ Boo, as shown in Fig. 4.4. The spectra were binned to 0.006 in phase (y-axis) for a better identification of the noise structure. We noticed that the observations in nights 2 and 3 suffer from broad noise structures, which may originate from the variability of stellar lines or the residuals of telluric corrections.

As we noted in section 4.3, the star τ Boo shows a high level of chromospheric activity. The stellar He I line as a chromospheric diagnostic may undergo temporal variation due to flaring. The strength of the stellar He I line can also show periodic modulation by rotation if the line is not homogeneous on the stellar disk (Andretta et al., 2017). Moreover, the fast spin of τ Boo may result in residual noise features shifting in wavelength up to its rotation velocity ($\sim 15 \text{ km s}^{-1}$). To quantify the effect of stellar variability, we measured the strength

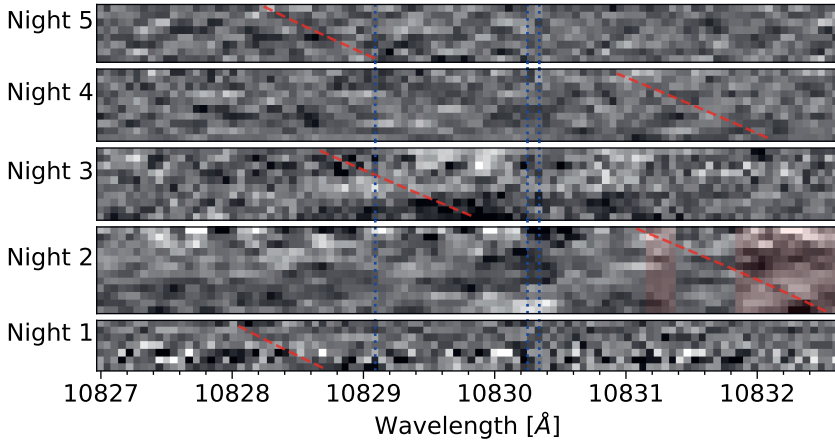


Figure 4.4: Residual spectral series from night 1 to 5. The y-axis represents the time or orbital phase. The residuals are binned to 0.006 in phase for clarity. The slanted dashed lines in red trace the expected planetary helium line. The dotted lines in blue denote the positions of the stellar He I triplet. The shaded region in night 2 contains the telluric H_2O absorption and OH emission line, overlapping with the expected planetary helium line.

of the stellar He I line at 10830 \AA during each night by fitting a Gaussian profile to the data and measuring the amplitude of the best-fit Gaussian profile. We define the line variation as the relative depth with respect to the average stellar spectrum of each night, and then bin the results to 0.006 in phase (see Fig. 4.2 bottom panel). During a single night, the variation is generally $\leq 0.25\%$, which is within the noise level of the data, therefore should not significantly affect our analysis. However, it is possible that the variation can build up as we combine different frames during the night, leading to systematic noise in the combined residual spectrum. For example, the variability of He I line may be responsible for the variation in the residual flux at 10830.3 \AA in night 2 (see Fig. 4.4). We also compared the average line profile of different nights (Fig. 4.5). On a night-to-night basis, we note that the helium line profile in night 2 is distinct from other nights, perhaps due to the influence of the nearby strong telluric line or the higher level of stellar activity.

In addition, we note that the spectral S/N in the middle of night 3 abruptly dropped by a factor of two as shown in Fig. 4.2, probably due to the changing weather condition. This may lead to the inconsistency of the data in the region from 10829.4 to 10830.2 \AA . Unfortunately, the trail of the planetary signal in night 3 resides exactly in this problematic wavelength range, overwhelmed by artifacts (see Fig. 4.4). As for the night 2 observations, telluric lines show a high level of strength and variability due to the high relative humidity and the variation of the precipitable water vapor, which could not completely be removed. The residuals of the deep telluric H_2O line at 10832.1 \AA and OH sky emission at 10831.3 \AA coincide with the trail of the planetary signal (see Fig. 4.4), making it difficult to preserve it while removing the telluric contamination. In such condition, adding the night 2 data does not enhance the S/N because more noise was introduced along with the diminished signal. Consequently, we excluded the observations of night 2 and 3 from further analysis.

Based on the ephemeris listed in Table 4.1, we shifted the residual spectra to the plan-

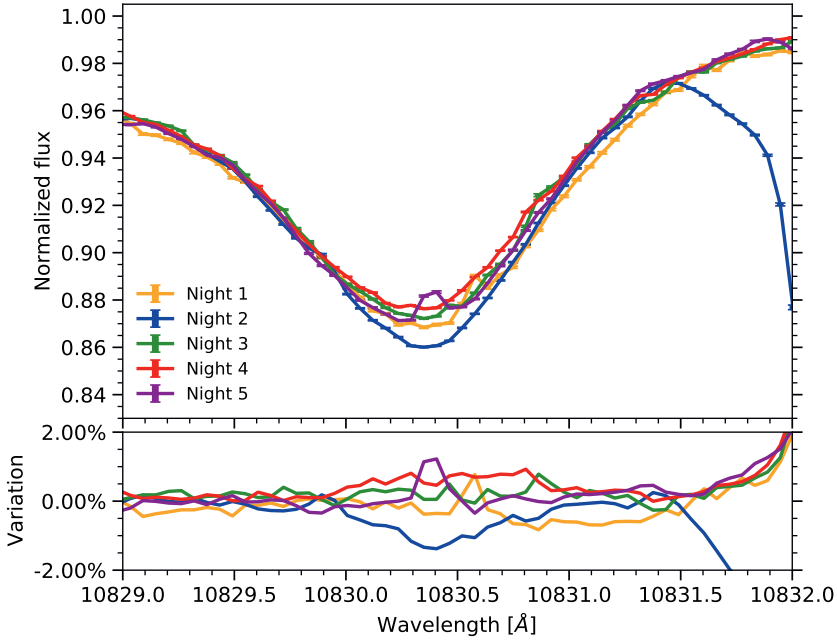


Figure 4.5: Upper panel: the average profile of the stellar helium line in each night. Lower panel: the difference of each profile with respect to the mean. The deep absorption line at 10832.2 Å in night 2 (blue curve) is a telluric H₂O line. The small peaks on top of the helium line in night 1 and 5 are caused by sky OH emission.

etary rest frame. The residual spectral series from different nights were then combined with each residual spectrum weighted by its variance over the radial velocity ranges from -150 to -50 km s⁻¹ and from 50 to 150 km s⁻¹.

4.5 Result

Fig. 4.6 shows the time-averaged spectrum around the helium line in the planet rest-frame, with the amplitude scaled to make the standard deviation equal to unity around the targeted He I 10830 Å line. We find no statistically significant signal from the planetary He I 10830 Å line within the three nights of observations.

4.5.1 Detection limits

As we have no information on the profile of the potential He I line originating from τ Boo b, we assumed a box profile centered at 10830.3 Å, which has a clear definition of the line width compared to a Gaussian profile. We performed signal injections considering various widths (W) of the planetary emission, ranging from 3.7 km s⁻¹ (equal to the instrument resolution) to 37 km s⁻¹ (which is limited by the self-subtraction of broad signals). The combined residuals of both the observations and injections are shown in Fig. 4.6 for three different line widths as examples. We regarded the original residuals (without signal

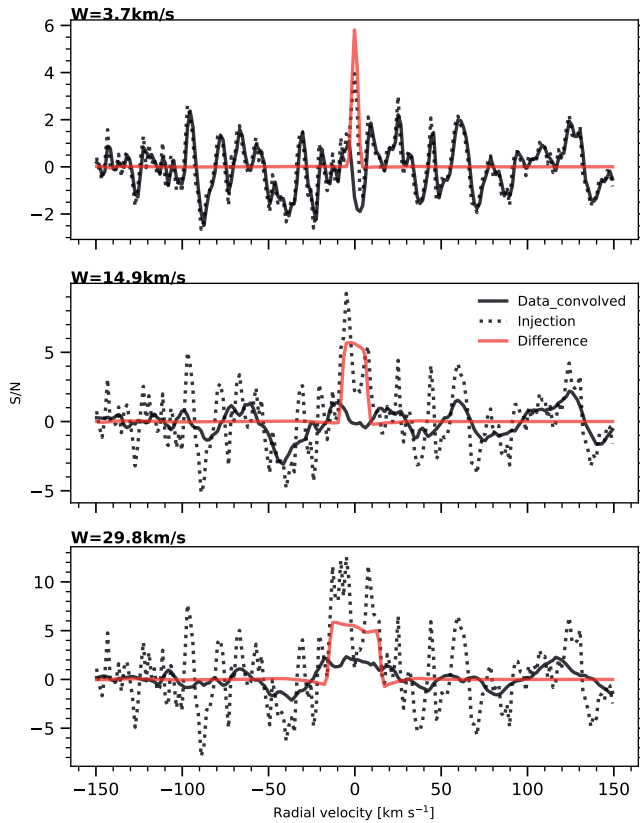


Figure 4.6: Combined (3 nights) residual spectra in the planetary rest frame centered at the 10830 Å He I line. In the three panels, the solid black line indicates the residual spectra, boxcar-smoothed by 3.7 km s⁻¹(top), 14.9 km s⁻¹(middle), and 29.8 km s⁻¹(bottom). The dotted curves show an artificially injected signal at a S/N of 5, with the solid red curve the difference between the injected and original data. The values are scaled by the standard deviation of the observed residuals so that the y-axis represents the S/N.

injection) as the noise, and convolved it with the corresponding signal profile to take the width of the signal into account. The noise level is defined as the standard deviation (from -150 to +150 km s⁻¹) of the convolved residuals. These were then scaled by this noise level, so that the y-axis represents the signal-to-noise ratio (S/N). The strength of the signal in each injection case was determined by measuring the amplitude of the recovered signal, which is the difference between the injected and the original residuals, as shown by the red curves in Fig. 4.6. The 5 σ detection limits were thus determined as the minimum line emission leading to a recovered S/N of 5 in our injection tests. The detection limit as a function of the line width is shown in Fig. 4.7. We note that the S/N is determined at the peak of the emission signal (namely the amplitude of the box profile). Therefore, detecting a broader signal requires a lower level of the peak contrast, as shown in the black line in Fig. 4.7. However, this does not mean that the detectability increases when it comes to

broad signals. As the flux is distributed into wider velocity space due to broadening mechanisms, it actually requires larger amount of integrated flux (namely higher Equivalent Width) to detect broader signals. The corresponding Equivalent Width limit required for 5σ detection is plotted in the red curve in Fig. 4.7.

The width of the signal is affecting the S/N of a potential detection in the following ways. First, the level of white noise decreases with the square root of the line width. Although the residual noise in our case is not fully uncorrelated due to imperfect stellar and telluric corrections, the S/N can still be enhanced, if not as much as by a factor of \sqrt{W} . Secondly, for a larger W a wider part of the planet emission line trail is masked out, changing the residual noise pattern of the data, as shown in Fig. 4.6, where the observed residuals (solid black curves) for different widths are not identical. Furthermore, the detection of broad planetary signals is hindered by the self-subtraction problem as discussed in section 4.4.1. Hence, the detectability drops significantly for widths larger than 25 km s^{-1} , which is comparable to the radial velocity change of the planet during a night. Overall, the detection limit drops significantly towards larger W , but reaches a plateau at $W > 20 \text{ km s}^{-1}$, for which we reach a 5σ limit of 4×10^{-4} .

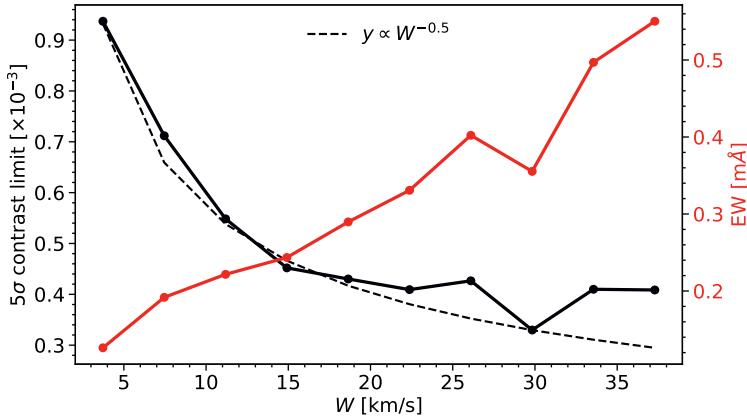


Figure 4.7: The 5σ detection limit of the He I airglow emission as a function of the line width of the potential signal using 3 nights of observations of τ Boo b (solid black line), and corresponding equivalent widths of the detection limit (solid red curve). The dashed line represents a scaled relation of $W^{-1/2}$, expected for pure Gaussian white noise.

4.5.2 Validation of signal recovery

Prior knowledge of the planetary orbit was used to mask the trail in the spectral series to avoid self-subtraction of the potential signal (see section 4.4.1). In order to assess the influence of this procedure on the final result, we repeated the whole analysis adopting a grid of planetary orbits with different semi-amplitude K_P and phase offset $\Delta\phi$ when applying the mask. In Fig. 4.8, we mapped the S/N of the residuals at 10830.3 \AA in the planetary rest frame for each hypothetical orbit in the grid. As a comparison, we produced a similar map when injecting an artificial planetary signal with a strength of 3.3×10^{-4} and

a width of 30 km s^{-1} , which is recovered at $K_p = 110 \text{ km s}^{-1}$ and $\Delta\phi = 0$ in Fig. 4.8, also without prior knowledge of the planetary orbit.

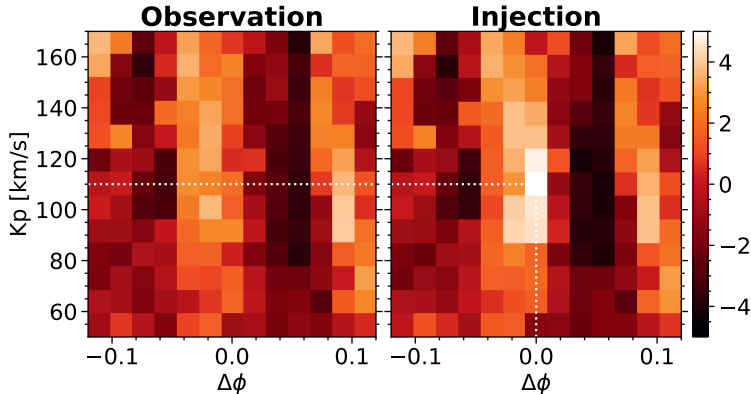


Figure 4.8: The S/N map for a grid of planetary orbits with different semi-amplitude K_p and phase offset $\Delta\phi$. There is no salient signal in the observations (left panel). An injected signal at $K_p = 110 \text{ km s}^{-1}$ and $\Delta\phi = 0$ is clearly recovered (right panel).

4.6 Discussion

4.6.1 Detectability of He emission

Using three nights of observations (~ 6.5 hours of integration) on τ Boo b using CARMENES, we reached a contrast limit of 4×10^{-4} for a planetary He I emission with a boxcar profile with a width $> 20 \text{ km s}^{-1}$. However, following Equation 4.3, the estimated amplitude of the He I emission is typically $\leq 10^{-4}$. At this stage, no detection is expected with these observations.

We note that we made several assumptions for simplicity. First, we assume the atmosphere extends significantly beyond the planet radius and the He I cloud is considered to be optically thin. The stellar radiation is absorbed uniformly in the cloud and reemitted isotropically. In addition, Equation 4.3 assumes that the energy is conserved at the particular wavelength 10830 \AA , meaning that we only take into account the transition between the helium 2^3S and 2^3P states.

In practice, the flux ratio can deviate from this simplified model in the following ways. (a) The flux emission of the cloud can be higher than our estimation if the extent of the exosphere is even larger than the stellar disk, in which case the measured f_{abs} in the transmission spectrum is lower than the actual absorption level of the entire cloud. (b) Analysis on the line ratio of He I triplet detected in transmission observations suggests that the planetary signal could also originate from an optically thick part of the atmosphere, especially for Jupiter-mass planets such as HD 189733b and HD 209458b, where the He I absorption feature traces compact atmospheres with an extent of only a fraction of planetary radii (Lampón et al., 2020, Salz et al., 2018). If the cloud is not optically thin or the He I atmosphere is not significantly larger with respect to the planet, the reradiation is not

isotropically emitted from the cloud in 4π but with preferential directions, as an analogy to scattered light. In this case, the emission flux at the full phase (i.e. when the illuminated hemisphere is totally in view) is enhanced as compared to the value in Equation 4.3, yet it also needs to be scaled with the phase function Φ_α at different orbital phases (where we observe different portions of the illuminated hemisphere). (c) If the He I cloud is not optically thin, the planetary thermal emission passing through the cloud can be absorbed along the line of sight, which cancels out a portion of the airglow emission. To evaluate this effect, we compare the absorbed thermal emission to the airglow emission flux as follows. Assuming the planet emits as a blackbody with an equilibrium temperature of T_p , we can calculate the planetary thermal emission flux in contrast to the stellar flux at 10830 Å. Taking τ Boo system as an example, the flux contrast is $\mathcal{F}_{th}/\mathcal{F}_* \sim 10^{-5} \sim 0.25\mathcal{F}_c/\mathcal{F}_*$. To the optically thick limit, where all thermal emission is absorbed by the He I cloud, it counterbalances $\sim 25\%$ of the airglow emission. Consequently, even in the extreme optically thick case, the helium is expected to be seen in emission. (d) The emission level of He I 10830 Å is determined by the population of helium in the 2^3P state as well as the rates of the stimulated and spontaneous decay of 2^3P state. Studying this requires detailed accounts and comparisons of other de-populating processes including photoionization from 2^3P state, electron/H-atom collisions, and radiative excitation to 2^3D state (D3 line). Previous models of helium atmospheres, such as Lampón et al. (2020), Oklopčić & Hirata (2018), neglect transitions related to 2^3P state because the metastable 2^3S state population is not significantly affected by these processes as an atom in 2^3P state just decays back to 2^3S state (Oklopčić & Hirata, 2018). This indicates that the 2^3P to 2^3S decay is the major way of de-populating the 2^3P state. Therefore, we can argue for the connection between the level of absorption and airglow emission at 10830 Å.

In addition to the amplitude of the He I emission, the velocity profile is rather uncertain. Current detections suggest that the He I excess absorption spans a wide range of line widths. For instance, Saturn or Neptune mass planets such as WASP-69b and HAT-P-11b (Allart et al., 2018, Nortmann et al., 2018) are reported to have broad absorption feature (up to $\sim 30 \text{ km s}^{-1}$), while Jupiter-mass planets such as HD 209485b (Alonso-Floriano et al., 2019) show a more narrow signature of $\sim 10 \text{ km s}^{-1}$, implying a lower rate of atmospheric escape and mass loss. The line profile depends on the physical and hydrodynamic properties such as the kinematic temperature of the exosphere and the atmospheric escape, which are not well understood (Salz et al., 2016). Considering the diverse nature of planetary atmospheres, it is therefore recommended to explore a variety of line widths and line positions in data analysis.

4.6.2 Future prospects

Observation design

Based on our data analysis, we find several aspects that should be taken into account when designing future observations to search for He I airglow emission. Firstly, the observations should avoid blending the planetary helium signal with strong telluric absorption lines (such as during our night 2 observations). In such situation, a large portion of the emission signal is removed along with the telluric correction. Even if the signal is preserved with other methods, strong telluric features cannot be corrected perfectly, introducing artifacts around the helium signal. Furthermore, the S/N of observations at the core of strong

telluric absorption lines is significantly lower than in the continuum. Hence, the potential signal falling in such region is more difficult to detect. Therefore, taking into account the relative position between the planetary and telluric lines, and selecting the proper time for observations according to the barycentric Earth radial velocity (BERV) and the planetary radial velocity are desirable.

The stellar activity is yet another factor to consider in data analysis because the stellar He I line as a chromospheric diagnostic may undergo temporal variation during observations. For an active star like τ Boo, this is likely to happen and introduce extra noise. Cauley et al. (2018), Salz et al. (2018) and Guilluy et al. (2020) evaluated the impact of stellar activity on probing the planetary helium atmosphere in transmission. However, unlike transit observations, additional noise related to stellar activity should not significantly affect measurements of emission signals from a planet, because there is always a radial velocity offset between the star and planet when probing emission. Only when the radial velocity difference is small (that is, during transit and secondary eclipse), can stellar activity contribute to noise at the planetary rest frame and result in pseudo-signals. In terms of detecting airglow emission, the likely consequence of the variability of stellar He I line is to introduce systematic noise structure nearby the planetary signal in the temporal-combined residual spectrum, instead of affecting the level of planetary signal. Consequently, for highly active stars, there needs to be sufficient difference between the planet and stellar radial velocity, which depends on the orbital phase, during observations.

In terms of target selection, we performed the case study on τ Boo because the star is significantly brighter than other known hot-Jupiter systems, enabling high S/N observations. In addition, its high level of stellar activity likely results in an extended planetary atmosphere with the He I 2^3S populated. As shown in Fig 4.9, accounting for both the stellar brightness and the airglow emission signal estimated using Equation 4.3, τ Boo b falls closest to our detection limit (denoted by the dashed line) among other potential targets. In the emission signal calculation, as we have no measurements of the He I absorption by the non-transiting τ Boo b, we assume an absorption level of 1%, which, however, brings about some uncertainty. τ Boo as an F-type star may also have high levels of mid-UV radiation that can de-populate the helium triplet states, leading to a weaker signal. It remains unclear to what extent these various factors contribute to the He I signal as a whole. In addition, the planet mass is significantly higher than that of most hot Jupiters, increasing the surface gravity, possibly making atmospheric escape more difficult (Salz et al., 2016). A more secure choice is to investigate those targets with He I absorption already measured via transmission spectroscopy (denoted with red dots in Fig 4.9), so that we have an expectation of the emission amplitude beforehand. Another benefit of targeting a transit planet is that we could obtain the stellar spectrum without any contribution from the planet during secondary eclipse. Using that as a reference spectrum, we can avoid self-subtracting the planetary signal in analysis, which is particularly important for broad signatures. Furthermore, as discussed in Section 4.6.1, the airglow emission signal is partially counterbalanced by absorption of planet thermal emission through the He I cloud when it is compact. Consequently, planets with puffy and optically thin He I clouds are better targets for this purpose.

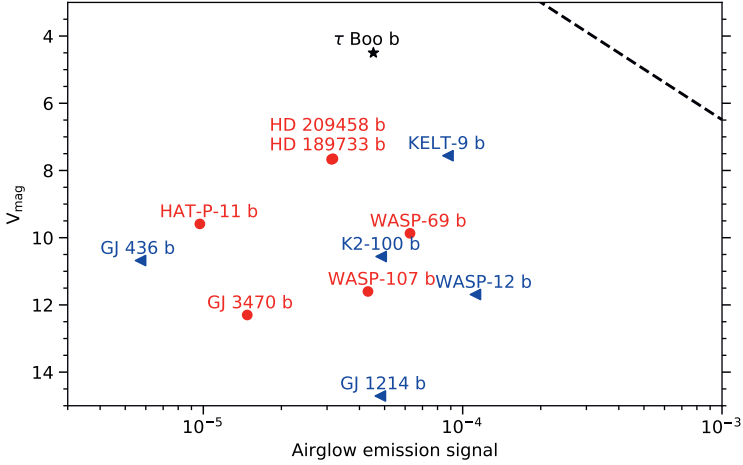


Figure 4.9: The V magnitude of host stars plotted against the airglow emission signal estimated using Equation 4.3 for exoplanets with He I absorption detections (in red dots) or upper limits (in blue triangles). The black star represents the estimated signal of τ Boo b assuming a typical absorption level of 1%. The black dashed line shows the detection limit of our analysis.

Search with VLT/CRIRES+ and E-ELT/HIRES

CRIRES+ is an upgrade of the cryogenic high-resolution infrared echelle spectrograph (CRIRES) located at the focus of UT1 of the Very Large Telescope (VLT), providing a spectral resolving power of 100,000 (Follert et al., 2014). If we simply scale the expected S/N for observations with CRIRES+ by the larger telescope diameter of the 8.2m VLT compared to the 3.5m Calar Alto Telescope, also considering that the throughput of CRIRES+ may be a factor of 1.5 lower than that of CARMENES, while the observing condition at VLT site is generally better, we expect in the same observing time to go a factor ~ 2 deeper. Accordingly, we expect to reach a detection limit of 2×10^{-4} for a broad He I emission given the same amount of integration (~ 6.5 hours). Taking τ Boo b as an example, following Equation 4.3, we estimate the amplitude of the emission to be $\sim 5 \times 10^{-5}$ assuming a typical "transit" absorption level of 1%. This means that a 3σ detection of He I airglow emission could be obtained in ~ 5 nights of observations. Although probing He I emission is demanding using the current generation of telescopes, it is promising with the High Resolution Spectrograph (HIRES) at ESO's forthcoming Extremely Large Telescope (E-ELT) (Marconi et al., 2016). Thanks to the significantly larger diameter of the 39m E-ELT, the 5σ detection of He I airglow emission could be achieved with ~ 3 hours of integration. Of course there is a large uncertainty in the expected level of emission, which can be at least partly mitigated by choosing a transiting planet.

4.7 Conclusions

This paper explores the possibility of probing He I emission at 10830 \AA in the extended atmospheres of hot Jupiters, the amplitude of which is estimated based on the He I ab-

sorption level as observed during transit. We search for this emission from τ Boo b using CARMENES spectra. We correct for the telluric and stellar features nearby the expected He I signal and combine multiple nights of observations. Given our estimation of the contrast of $\leq 10^{-4}$, the 6.5-hour data combined is not sufficient to put meaningful constraints on the He I emission from the planet. The detection limit that we derive from our analysis is 4×10^{-4} for a broad emission signal with a width of $>20 \text{ km s}^{-1}$. While we do not reach the required contrast with the current CARMENES data, the He I airglow emission from hot-Jupiters is still promising to probe with future instruments.

4.A Derivation of helium emission strength with radiative transfer

During transit, the stellar flux \mathcal{F}_* decreases by $\Delta\mathcal{F}_*$ due to the absorption by helium atoms at 2^3S state. The absorption depth T_λ measured by transmission spectroscopy is

$$T_\lambda = \frac{\Delta\mathcal{F}_*}{\mathcal{F}_*} = \frac{R_c^2}{R_*^2} f_{\text{abs}} = \frac{R_c^2}{R_*^2} (1 - e^{-\tau_c}), \quad (4.4)$$

where τ_c is the optical depth of the He I cloud around the planet, and the structure of the cloud is neglected.

4.A.1 Optically thick

For optically thick clouds, namely, $\tau_c \gg 1$, Equation 4.4 becomes

$$R_c = R_* \sqrt{T_\lambda}. \quad (4.5)$$

The emission flux from the cloud can be approximated as isotropic scattering with an albedo of 1, resulting in a factor of 2/3 of the received flux (Seager, 2010, Chap. 3):

$$F_c^S = \frac{2}{3} F_*^S \left(\frac{R_*}{a} \right)^2. \quad (4.6)$$

Substituting Equation 4.2 and 4.5 into Equation 4.6, we get

$$\frac{\mathcal{F}_c}{\mathcal{F}_*} = \frac{2}{3} \frac{\Delta\mathcal{F}_*}{\mathcal{F}_*} \left(\frac{R_*}{a} \right)^2 = \frac{2}{3} T_\lambda \left(\frac{R_*}{a} \right)^2. \quad (4.7)$$

4.A.2 Optically thin

For optically thin cases, we consider the simplified 1D plane-parallel equation of radiative transfer

$$\frac{dI}{d\tau} = I(\tau) - S(\tau), \quad (4.8)$$

where I_ν is the spectral radiance, S is the source function, and τ is the extinction optical depth which increases towards interior of the cloud (i.e. the optical depth at the interior is τ_c and that at the surface is 0).

The source function is approximated as

$$S(\tau) = J_*(\tau) = \frac{1}{4\pi} \int I_*(\tau) d\Omega = \frac{1}{4\pi} \left(\frac{R_*}{a}\right)^2 F_*^S e^{-\tau}. \quad (4.9)$$

Hence, the solution for the equation of radiative transfer can be composed as

$$I(\tau) = ce^\tau + \frac{1}{8\pi} \left(\frac{R_*}{a}\right)^2 F_*^S e^{-\tau}. \quad (4.10)$$

Using the boundary condition $I(\tau_c) = 0$, the integral constant c is determined, making the solution simplified as

$$I(\tau) = \frac{1}{8\pi} \left(\frac{R_*}{a}\right)^2 F_*^S (e^{-\tau} - e^{\tau-2\tau_c}). \quad (4.11)$$

Then the emergent radiance from the cloud I_c is

$$I_c = I(0) = \frac{1}{8\pi} \left(\frac{R_*}{a}\right)^2 F_*^S (1 - e^{-2\tau_c}). \quad (4.12)$$

The observed flux of the cloud is

$$\mathcal{F}_c = \int I_c (n_c \cdot n_{\text{detector}}) d\Omega = \frac{1}{8\pi} \left(\frac{R_*}{a}\right)^2 F_*^S (1 - e^{-2\tau_c}) \frac{\pi R_c^2}{D^2}, \quad (4.13)$$

where n_c and n_{detector} represent the unit vectors along the intensity of the cloud and the normal direction of the detector surface respectively. Since the targets are far away, we can safely assume $n_c \cdot n_{\text{detector}} = 1$ in Equation 4.13.

Substituting $\mathcal{F}_* = F_*^S R_*^2/D^2$ and Equation 4.4 into Equation 4.13, we have

$$\mathcal{F}_c = \frac{1}{8} \Delta F_* \left(\frac{R_*}{a}\right)^2 \frac{1 - e^{-2\tau_c}}{1 - e^{-\tau_c}}. \quad (4.14)$$

At the optically thin limit ($\tau_c \ll 1$), Equation 4.14 reduces to

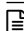
$$\frac{\mathcal{F}_c}{\mathcal{F}_*} = \frac{1}{4} \frac{\Delta \mathcal{F}_*}{\mathcal{F}_*} \left(\frac{R_*}{a}\right)^2 = \frac{1}{4} T_\lambda \left(\frac{R_*}{a}\right)^2, \quad (4.15)$$

which agrees with Equation 4.3.

5

Transmission spectroscopy of the ultra-hot Jupiter MASCARA-4 b

Ultra-hot Jupiters (UHJs), rendering the hottest planetary atmospheres, offer great opportunities of detailed characterisation with high-resolution spectroscopy. MASCARA-4 b is a recently discovered close-in gas giant belonging to this category. We aim to characterise MASCARA-4 b, search for chemical species in its atmosphere, and put these in the context of the growing knowledge on the atmospheric properties of UHJs. In order to refine system and planet parameters, we carried out radial velocity measurements and transit photometry with the CORALIE spectrograph and EulerCam at the Swiss 1.2 m Euler telescope. We observed two transits of MASCARA-4 b with the high-resolution spectrograph ESPRESSO at ESO's Very Large Telescope. We searched for atomic, ionic, and molecular species via individual absorption lines and cross-correlation techniques. These results are compared to literature studies on UHJs characterised to date. With CORALIE and EulerCam observations, we update the mass of MASCARA-4 b ($M_p = 1.675 \pm 0.241 M_{\text{Jup}}$) as well as other system and planet parameters. In the transmission spectrum derived from ESPRESSO observations, we resolve excess absorption by $H\alpha$, $H\beta$, Na I D1&D2, Ca II H&K, and a few strong lines of Mg I, Fe I, and Fe II. We also present the cross-correlation detection of Mg I, Ca I, Cr I, Fe I, and Fe II. The absorption strength of Fe II significantly exceeds the prediction from a hydrostatic atmospheric model, as commonly observed in other UHJs. We attribute this to the presence of Fe II in the exosphere due to hydrodynamic outflows. This is further supported by the positive correlation of absorption strengths of Fe II with the $H\alpha$ line, which is expected to probe the extended upper atmosphere and the mass loss process. Comparing transmission signatures of various species in the UHJ population allows us to disentangle the hydrostatic regime (as traced via the absorption by Mg I and Fe I) from the exospheres (as probed by $H\alpha$ and Fe II) of the strongly irradiated atmospheres.

 **Zhang, Y., Snellen, I. A. G., Wyttenbach, A., Nielsen, L. D., Lendl, M., Casasayas-Barris, N., et al. (2022) Transmission spectroscopy of the ultra-hot Jupiter MASCARA-4b. Disentangling the hydrostatic and exospheric regimes of ultra-hot Jupiters. A&A, 666, A47.**

5.1 Introduction

Transmission spectroscopy of close-in giant planets provides great opportunities to characterise the composition, structure, and dynamics of exoplanet atmospheres (Charbonneau et al., 2002, Huitson et al., 2012, Madhusudhan, 2019, Redfield et al., 2008, Snellen et al., 2010). These strongly irradiated planets undergo significant atmospheric escape as traced by absorption signatures from exospheres extending beyond the Roche limit (Spake et al., 2018, Vidal-Madjar et al., 2004, 2003). The mass loss drives the evolution of close-in planets and shapes the exoplanet population as observed today (Owen, 2019).

Ultra-hot Jupiters (UHJs) represent a subclass of close-in hot Jupiters that are extremely irradiated, with day-side temperatures above 2200 K. As a result of such high temperatures, their day-side atmospheres are predicted to be cloud-free and with effective thermal dissociation of molecules such as H_2O to produce OH (Landman et al., 2021, Nugroho et al., 2021, Parmentier et al., 2018). The transmission spectra are dominated by neutral and ionized atomic species in the optical, similar to the photosphere of dwarf stars (Kitzmann et al., 2018, Lothringer et al., 2018), which are well suited for atmospheric characterisation. The dissociation of hydrogen combined with electrons from metal ionisation to form H^- , adds strong continuum opacity which plays an important role in shaping the spectra (Arcangeli et al., 2018). The extreme irradiation also makes UHJs interesting targets for studying the mass loss via hydrodynamic escapes (Fossati et al., 2018, Sing et al., 2019).

Transmission spectra under high spectral resolution ($\mathcal{R} = \lambda/\Delta\lambda \sim 10^5$) provide unique access to the information contained in resolved absorption lines, such as Na I D lines, H I Balmer series, and He I triplet, allowing better constraints on the atmospheric structure and the escaping process (e.g. Allart et al., 2018, Casasayas-Barris et al., 2019, Nortmann et al., 2018, Wyttenbach et al., 2015, 2017, 2020, Yan & Henning, 2018). In addition, high-resolution spectroscopy has been a powerful tool that leads to the detection of a profusion of metal species in UHJs using the cross-correlation method that co-adds a forest of spectral lines to enhance the signal of a certain species (Brogi et al., 2012, Snellen et al., 2010). For example, Hoeijmakers et al. (2018, 2019) detected neutral and ionized metals (such as Fe I, Fe II, Ti II, Cr II, etc.) in KELT-9b, the hottest known planet ($T_{\text{eq}} \sim 4000$ K, Gaudi et al., 2017). Subsequent studies have quickly extended detections to more UHJs, including WASP-121b (Ben-Yami et al., 2020, Gibson et al., 2020, Hoeijmakers et al., 2020b, Merritt et al., 2021), MASCARA-2b (Hoeijmakers et al., 2020a, Nugroho et al., 2020, Stangret et al., 2020), WASP-76b (Kesseli et al., 2022), TOI-1518b (Cabot et al., 2021), WASP-189b (Prinoh et al., 2022), and HAT-P-70b (Bello-Arufe et al., 2022).

Here we present the transmission spectroscopy of MASCARA-4 b (Dorval et al., 2020), an ultra-hot Jupiter with an equilibrium temperature of ~ 2250 K, orbiting at 0.047 au away from an A7V star ($m_V = 8.2$) with an effective temperature of ~ 7800 K. The properties of the system are summarised in Table 5.1. Two transit observations were taken with Echelle SPectrograph for Rocky Exoplanets and Stable Spectroscopic Observations (ESPRESSO, Pepe et al., 2021) at the VLT. This analysis adds MASCARA-4 b to the ensemble of UHJs that have been characterised with high-resolution transmission spectroscopy and show absorption features from various atomic species.

We describe the observations and data reduction in Section 5.2. The analyses are presented in Section 5.3, including fitting the spin-orbit misalignment angle, modeling the Rossiter-McLaughlin (RM) effect, extracting transmission spectra, and carrying out cross-

correlation. We then present in Section 5.4 the detection of planetary absorption signals in the transmission spectrum from both single-line and cross-correlation analysis. In Section 5.5, we put the results of MASCARA-4 b in context of the UHJ population and discuss trends of absorption strengths among UHJs that may shed light on the atmospheric structures.

Table 5.1: Properties of the MASCARA-4 system.

Parameter	Value
<i>..... Stellar parameters </i>	
Effective temperature, T_{eff} (K) ¹	7800 ± 200
Stellar mass, M_* (M_{\odot}) ¹	1.75 ± 0.05
Stellar radius, R_* (R_{\odot}) ²	1.79 ± 0.04
Surface gravity, $\log(g)$ ¹	4.10 ± 0.05
Projected spin, $v \sin i_*$ (km s^{-1})	43.0 ± 0.1 (Spectral)
	$46.2^{+7.7}_{-2.5}$ (RM reloaded)
Differential rotation, α	0.09 ± 0.03 (RM reloaded)
Limb-darkening coeff., u_1	0.333
Limb-darkening coeff., u_2	0.332
<i>..... Updated system parameters </i>	
RV amplitude, K_* (m s^{-1})	165.9 ± 23.7
Mid-transit time, T_0 (BJD)	$2458909.66419 \pm 0.00046$
Transit duration, T_{14} (day)	0.1654 ± 0.0013
Orbital period, P (day)	2.8240932 ± 0.0000046
Radius ratio, R_p/R_*	0.0869 ± 0.0015
Impact parameter, b	0.309 ± 0.044
Orbital inclination, i_p (deg)	86.89 ± 0.49
Semi-major axis, a (au)	0.0474 ± 0.0013
a/R_*	$5.704^{+0.086}_{-0.096}$
Spin-orbit angle, λ (deg)	250.34 ± 0.14
<i>..... Updated planet parameters </i>	
Planetary radius, R_p (R_{Jup})	1.515 ± 0.044
Planetary mass, M_p (M_{Jup})	1.675 ± 0.241
Planetary density, ρ_p (ρ_{Jup})	$0.481^{+0.085}_{-0.079}$
Surface gravity, g_p (m s^{-2})	18.1 ± 2.9
Equilibrium temperature, T_{eq} (K)	2250 ± 62
Semi-amplitude velocity, K_p (km s^{-1})	182 ± 5

¹ Dorval et al. (2020);

² Ahlers et al. (2020).

5.2 Observations and data reduction

5.2.1 Radial velocity measurements with CORALIE and updated planet mass

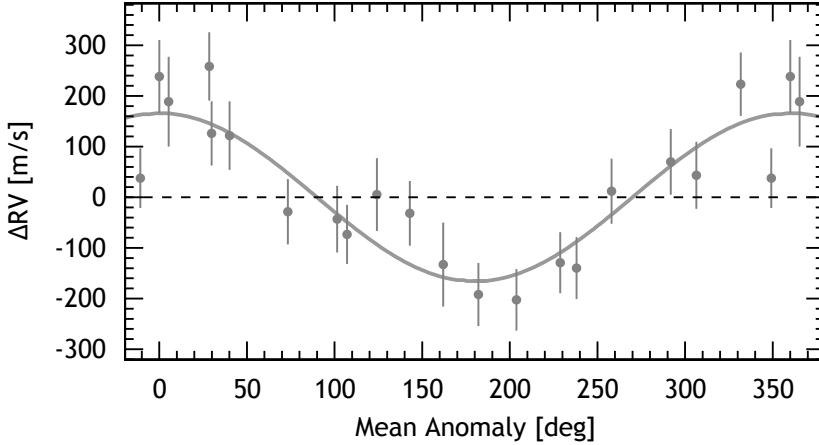


Figure 5.1: CORALIE radial velocity measurements of MASCARA-4, phase folded on the planetary orbital period and corrected for stellar activity. The best-fit Keplerian model to the data is shown as a solid grey line. The semi-amplitude of the stellar reflex motion is $165.9 \pm 23.7 \text{ m s}^{-1}$, corresponding to a planet mass of $1.675 \pm 0.241 M_{\text{Jup}}$.

To refine the mass of MASCARA-4 b, 20 high-resolution spectra were obtained with the CORALIE spectrograph (Baranne et al., 1996, Queloz et al., 2000) at the Swiss 1.2 m Euler telescope at La Silla Observatories, Chile. The observations took place between January 4, 2020 and February 10, 2021. The SNR per pixel at 550 nm varied between 55 and 90, according to sky condition and exposure time (20-30 min depending on target visibility and scheduling requirements).

Radial velocity (RV) measurements were extracted by cross-correlating the spectra with a binary A0 mask. The shape of the cross-correlation functions (CCFs) were dominated by rotational broadening ($\text{FWHM} \approx 55 \text{ km s}^{-1}$) and a linear slope across the continuum due to imperfect flux correction across the CCF window. Similar to the approach demonstrated for WASP-189 (Anderson et al., 2018), we fitted a rotational profile with a linear slope to the CCFs (for more information, see Sect. 2.3.3 in Nielsen, 2021). The inverse bisector-span (BIS, Queloz et al., 2001) was computed on the continuum-corrected CCFs.

The RV fitting were carried out with the Data and Analysis Center for Exoplanets web platform (DACE)¹. The Keplerian model described in Delisle et al. (2016) was fit to the RV data points using a Markov chain Monte Carlo (MCMC) algorithm (Diaz et al., 2014, 2016), while applying Gaussian priors on the stellar mass and planetary orbit (P , T_0 and i_p) from Table 5.1. When allowing for an eccentric orbit, we found an eccentricity consistent with zero and adopted a circular model to avoid overestimating the eccentricity

¹<https://dace.unige.ch/>

(Hara et al., 2019). A traditional RV fit yielded a moderate anti-correlation between the RV-residuals and BIS (weighted Pearson coefficient $R_w = -0.68$). We, therefore, applied a linear detrending of the RVs with BIS in the model. The final RV analysis derives a semi-amplitude of the stellar reflex motion of $165.9 \pm 23.7 \text{ m s}^{-1}$, corresponding to a planet mass of $1.675 \pm 0.241 M_{\text{Jup}}$. We tested the fitting without the detrending step and found no sensible change in the resultant semi-amplitude. The phase folded data, detrended with BIS, is shown in Fig. 5.1 along with the Keplerian model. The planet mass deviates by 2σ from the previous measurement of $3.1 \pm 0.9 M_{\text{Jup}}$ (and RV semi-amplitude $310 \pm 90 \text{ m s}^{-1}$) in Dorval et al. (2020), which relied on one particular data point with large uncertainty. Hence we adopt the revised values.

5.2.2 Photometry with EulerCam

We observed two transits of MASCARA-4 b on February 12 and 29, 2020 using EulerCam, the CCD imager installed at the 1.2 m Euler telescope located at La Silla. The observations were scheduled to be simultaneous with the two nights of observations with ESPRESSO (see Section 5.2.3), delivering updated transit parameters for the analysis of transmission spectroscopic data. For more details on the instrument and associated data reduction procedures the reader is referred to Lendl et al. (2012). As the star is brighter ($V=8.19$) than exoplanet hosts usually observed with EulerCam ($V \sim 10 - 14$, Lendl et al., 2019, 2012, 2013), using a broad-band filter would lead to saturation of the detector. We therefore used a narrower band to avoid saturation issues, namely the *Geneva V1* filter (Rufener & Nicolet, 1988), which peaks at 539 nm and has a transmission above 50% from 509 nm to 562 nm (accounting for detector quantum efficiency). The telescope was also defocused slightly to improve PSF sampling and observation efficiency. An exposure time of 20 s was used throughout both sequences. The light curves shown in Fig. 5.2 were obtained using relative aperture photometry with two bright reference stars and apertures of 26 pixel ($5.6''$) radius. The night of February 12, 2020 was affected by recurrent cloud passages, leading to gaps in the observed data.

We used the EulerCam data to compute the physical system parameters and in particular derive a planetary radius in the *Geneva V1* band, which is comparably close in wavelength covered with ESPRESSO. TESS (Ricker et al., 2015) has previously observed MASCARA-4 b, revealing a slightly asymmetric transit shape created by gravity darkening on the host star and a misaligned planetary orbit (Ahlers et al., 2020). Our ground-based observations do not possess sufficient precision to reveal this effect. However, to propagate the information encoded in the TESS data into our fit, we place Gaussian priors on the transit duration (T_{14}) and the impact parameter (b) corresponding to the values presented by Ahlers et al. (2020). We used a Markov Chain Monte Carlo approach as implemented in *CONAN* (Lendl et al., 2020) to derive the system parameters, fitting for R_p/R_* , b , T_{14} , T_0 and P . With the exception of b and T_{14} for which broad uniform priors were assumed. We assumed a quadratic limb-darkening law with parameters derived with LDCU² (Deline et al., 2022). Correlated noise was modelled individually for each light curve using approximate Matérn-3/2 kernels implemented through *celerite* (Foreman-Mackey et al., 2017). For the light curve of February 12, 2020, we included an evident correlation between the residual flux and the stellar FWHM as a linear trend fitted together with the

²<https://github.com/delinea/LDCU>

transit model and Gaussian Process (GP). We allowed for an additional white noise by inclusion of a jitter term for each light curve.

To derive planetary parameters, we used our derived radial velocity amplitude of $165 \pm 23 \text{ m s}^{-1}$ as presented in Section 5.2.1 and pulled values from a corresponding Normal distribution at each MCMC step. Similarly, normal distributions for M_* and R_* were assumed corresponding to the values inferred from our spectral analysis. The raw and phase-folded light curves are shown in Fig. 5.2, and the resulting updated parameters are given in Table 5.1.

5.2.3 High-resolution transmission spectroscopy with ESPRESSO

Table 5.2: Observing log of MASCARA-4b with ESPRESSO

Night	Date	Exposure time (sec)	N_{spectra}	On-target time (hour)	airmass	seeing (")	S/N@580 nm
1	Feb 12, 2020	360	85	7.5	1.34 - 1.99	0.34 - 0.87	~212
2	Feb 29, 2020	300	96	7.9	1.34 - 2.46	0.32 - 0.77	~208

We observed two transits of MASCARA-4b with ESPRESSO on February 12 and 29, 2020 under ESO program 0104.C-0605 (PI: Wyttenbach). ESPRESSO is a fiber-fed, ultra-stabilized echelle high-resolution spectrograph installed at the incoherent combined Coudé facility of the VLT. The observations were taken with the single-UT HR21 mode, providing a spectral resolving power of $\mathcal{R} \sim 138\,000$, covering the optical wavelength range of 380-788 nm. The observations are summarised in Table 5.2. The exposure time during transit was 360s and 300s in night 1 and night 2 respectively. The airmass ranges from 1.34 to 2.46, and the seeing condition varied from $0.3''$ to $0.9''$. The total on-target time is 7.5h (85 exposures) and 7.9h (96 exposures) in the two nights respectively, delivering an average S/N per pixel of 208 and 212 at 580 nm.

We took the sky-subtracted 1D spectra extracted with the Data Reduction Software (DRS) pipeline, and then corrected for telluric absorption features caused by H_2O and O_2 in the Earth's atmosphere following Allart et al. (2017) using the ESO sky tool `molecfi` (version 4.2, Smette et al., 2015). The tool uses a line-by-line radiative transfer model (LBLRTM) to derive telluric atmospheric transmission spectra and accounts for molecular abundances, instrument resolution, continuum level, and wavelength solution that can best fit observations, whereas other telluric or interstellar contamination such as the absorption of Na I was not removed with this correction.

We also used the ESPRESSO DRS to generate stellar cross-correlation functions (CCFs) with an A0 mask as presented in Wyttenbach et al. (2020). The stellar CCFs outside of the transit were average-combined to build a master out-of-transit CCF, representing the unocculted stellar line shape. We measured the projected spin velocity $v \sin i_*$ and systemic velocity V_{sys} of the target by fitting a rotationally broadened model (Gray, 2005) to the line shape. We found the $v \sin i_*$ of $43.0 \pm 0.1 \text{ km s}^{-1}$ and the V_{sys} of $-5.68 \pm 0.09 \text{ km s}^{-1}$. We then obtained the residual CCFs by subtracting the CCF at each phase from the master out-of-transit CCF. The residual CCFs were later used to extract Rossiter-McLaughlin information as detailed in Section 5.3.2.

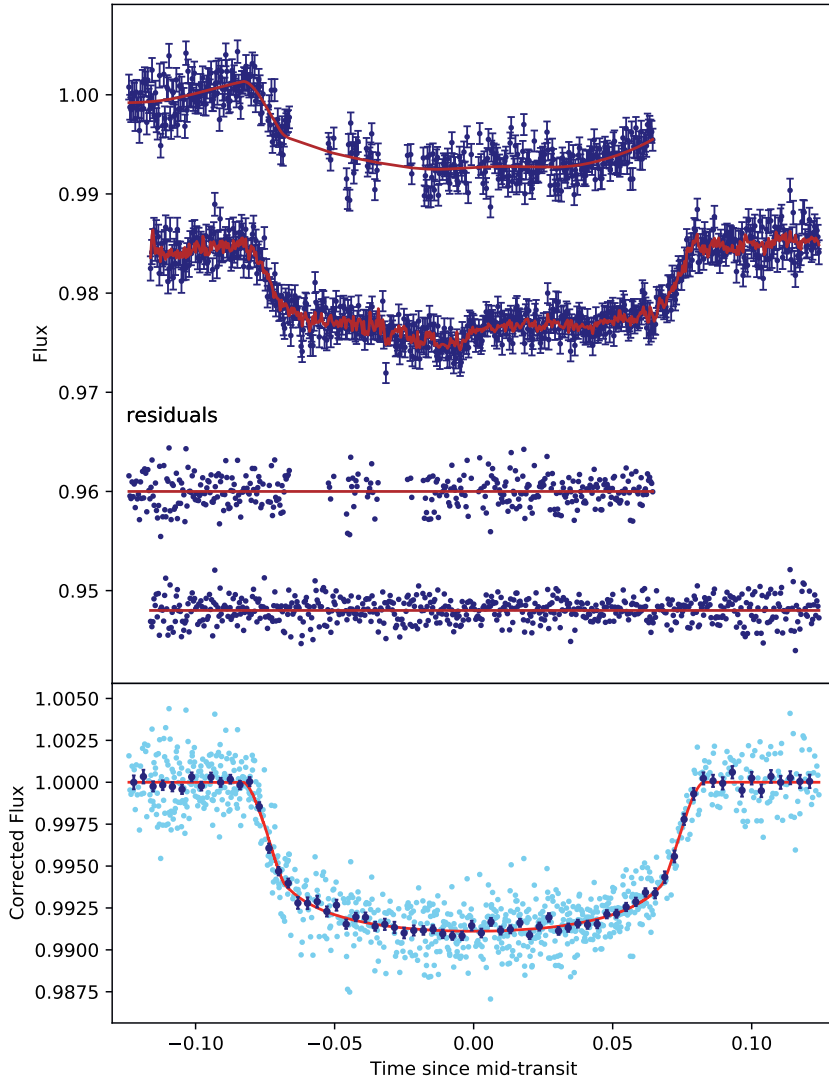


Figure 5.2: EulerCam light curves of MASCARA-4. *Top panel:* raw differential photometry together with the transit and systematic model corresponding to the median posterior values. The top two light curves are the data, while the bottom two light curves show the residuals to these models. *Bottom panel:* Systematics-corrected, phase-folded data together with the transit model. The unbinned data points are shown in light blue, while the dark blue points show the data binned into 2-minute intervals.

5.3 Data analysis

5.3.1 Stellar pulsations

In residual CCFs we note a strong rippled pattern caused by the stellar pulsations as shown in Fig. 5.3. The pulsations generate streak features throughout the course of observations, entangling with the Rossiter-McLaughlin and planetary signal during transit. We empirically mitigated the stellar pulsation pattern in CCFs following Wyttenbach et al. (2020). To achieve this, we suppose the pulsation features in the two-dimensional diagram (Fig. 5.3) stay static in terms of radial velocity, which can be approximated with positive or negative Gaussian profiles. We co-added the out-of-transit residual CCFs before ingress and after egress respectively, where the pulsation pattern appears symmetric before and after transit. We fit a Gaussian profile to the strongest peak in the combined out-of-transit residual CCFs and subtracted the fitted Gaussian component from all the individual out-of-transit CCFs, while the rest in-transit spectra remain untouched. Then the steps above were repeated to iteratively remove one Gaussian component at a time, until the major pulsation features were cleaned (5 iterations in our case, and the results are not sensitive to the number of iterations). The pulsation signal is mitigated while some structure remains visible in Fig. 5.3 bottom panel.

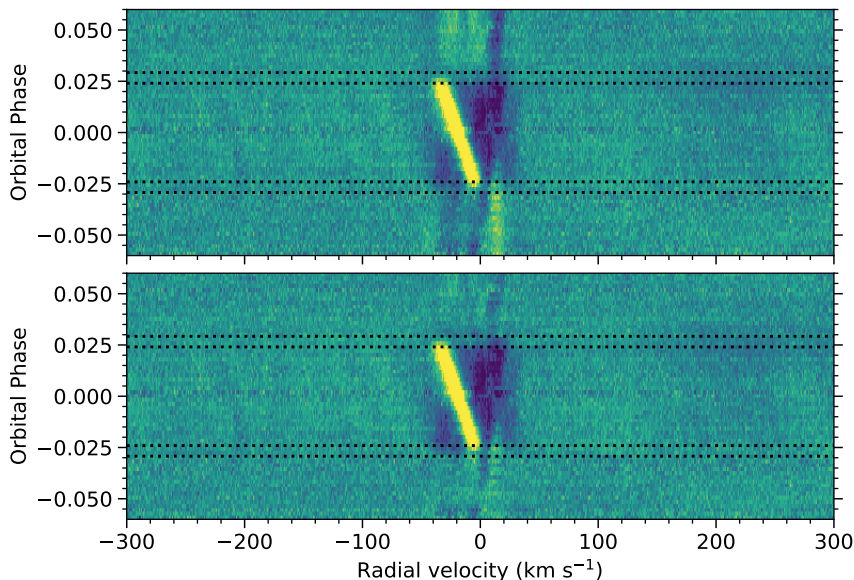


Figure 5.3: Map of the residual CCFs at different orbital phases before (top panel) and after (bottom panel) the correction of stellar pulsation. Data of two transits were binned in orbital phase with a step size of 0.002. The horizontal dotted lines denote the timings of four transit contacts. The slanted yellow streak during transit delineates the deformation of stellar lines as the planet moving across the stellar disk. The ripples seen in the out-of-transit residual CCFs in the top panel are attributed to stellar pulsation.

5.3.2 Rossiter-McLaughlin reloaded

The Rossiter-McLaughlin (RM) effect (also known as the Doppler shadow) is the deformation of the stellar lines as a result of the planet blocking part of the stellar disk during transit. It encodes information of the stellar rotation $v \sin i_*$ and the projected misalignment angle λ between the planet's orbital axis and the star's rotation axis. We used the reloaded RM method (Cegla et al., 2016) to model the doppler shift of the CCF profiles due to the occultation by the planet during transit. To extract RM information from the data, we combined the residual CCFs from both transits by binning in orbital phase with a step size of 0.002 and then fit the residual CCF at each phase with a Gaussian profile to determine the local RV of the occulted stellar surface. The measured local RVs plotted against orbital phases are shown in Fig. 5.4. We model the local RVs by computing the brightness-weighted average rotational velocity of the stellar surface blocked by the planet at each phase. Here we fixed the parameters such as a/R_* , R_p/R_* and i_p to the values listed in Table 5.1, while making the spin-orbit angle λ , the stellar spin velocity v , inclination i_* , and differential rotation rate α free parameters. Fitting the model to the measured local RVs, we derived $\alpha = 0.09 \pm 0.03$, $\lambda = 250.34 \pm 0.14^\circ$, and $v \sin i_* = 46.2^{+7.7}_{-2.5} \text{ km s}^{-1}$. The values are consistent with the previous measurement of $\lambda = 244.9^{+2.7}_{-3.6}$ and $v \sin i_* = 45.66^{+1.1}_{-0.9} \text{ km s}^{-1}$ by Dorval et al. (2020), with the slight difference in the spin-orbital angle likely resulting from the systematic differences in P and T_0 . Since we updated P and T_0 from the simultaneous photometry as the spectroscopic observations, the updated epoch is more reliable for our analysis of the local RVs. We caution that the uncertainties quoted here are underestimations because they did not account for systematics in the transit epoch and system parameters.

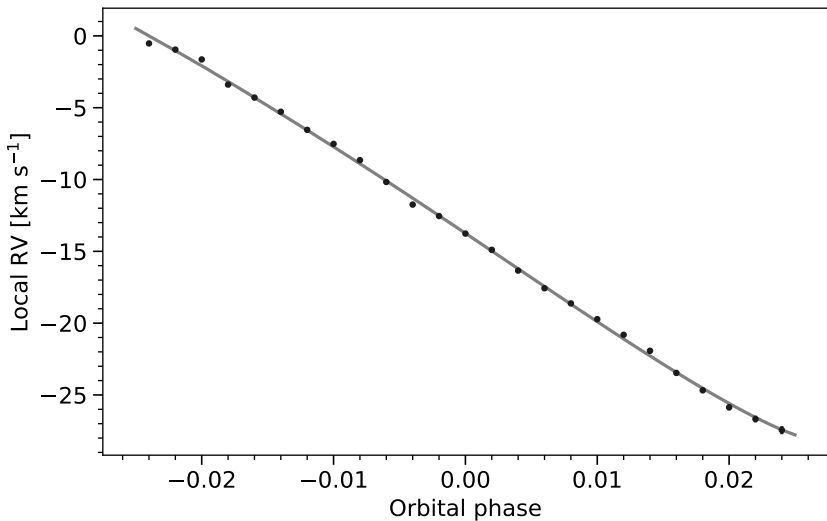


Figure 5.4: Local radial velocities (RVs) of the occulted stellar surface regions as measured from the yellow shadow in Fig. 5.3. The gray line is the best-fit RM reloaded model to the local RV data points.

5.3.3 Modeling RM and CLV effects

To disentangle the stellar signal from the planetary signal, we modeled the transit effects on stellar lines, including the Rossiter-McLaughlin (RM) and center-to-limb variation (CLV) effects, following (Casasayas-Barris et al., 2019, Yan et al., 2017). We first computed synthetic stellar spectrum at different limb-darkening angles (μ) using Spectroscopy Made Easy tool (Valenti & Piskunov, 1996) with VALD line lists (Ryabchikova et al., 2015). The stellar disk was divided into cells of size $0.01 R_* \times 0.01 R_*$, each assigned with a spectrum obtained by the interpolation to its corresponding μ and applying a radial velocity shift according to its local rotational velocity. We then integrated the whole stellar disk while excluding the region blocked by the planet during transit. We divided the integrated spectrum at each phase through the out-of-transit stellar spectrum, resulting in the model of RM+CLV effects such as shown in Fig 5.5 (panel b). The system and stellar parameters used in the modeling are presented in Table 5.1, including the best-fit parameters $\alpha = 0.09$, $\lambda = 250.3^\circ$, and $v \sin i_* = 48.6 \text{ km s}^{-1}$ obtained via RM reloaded method in Section 5.3.2.

5.3.4 Transmission spectrum

Using the telluric corrected 1D spectra, we extracted the transmission spectrum following the similar procedure in previous studies (such as Casasayas-Barris et al., 2019, Wyttenbach et al., 2015). It is summarised as follows. The spectra were median-normalised and shifted to the stellar rest frame. The out-of-transit spectra were co-added to build the master stellar spectrum, which was then removed from each individual spectrum via division. In the residuals, there remained sinusoidal wiggles as also seen in other ESPRESSO data (Borsa et al., 2021, Casasayas-Barris et al., 2021, Kesseli et al., 2022, Tabernero et al., 2021). We applied a Gaussian smoothing filter with a width of 5 \AA to each exposure and removed it to correct for the low-frequency noise. Moreover, outliers exceeding 4σ threshold in a sliding 25 \AA window were corrected through linear interpolation over nearby pixels. Finally, we combined the data of both transits by binning in orbital phase with a step size of 0.002 .

The in-transit residuals at this stage contain the variation due to RM+CLV effects and the absorption of the planet. Following Yan & Henning (2018), we fit the data with a model composed of both the stellar effects (as detailed in Section 5.3.3) and the planetary absorption signal (modeled as a Gaussian profile) assuming the expected planetary orbital motion amplitude (K_p) as listed in Table 5.1. The free parameters include the Gaussian amplitude (h), Gaussian width (FWHM), wind speed (v_{wind}), and a scaling factor of the stellar effects (f) to account for the fact that the effective absorption radius can be larger than the nominal planet radius used in the RM+CLV model. The fitting process was performed with PyMultiNest (Buchner et al., 2014), a Python interface for the Bayesian inference technique MultiNest (Feroz et al., 2009). Once obtaining the best-fit values, we removed the stellar RM+CLV effects from the residuals, which were then average-combined in the planet rest frame to form the 1D transmission spectrum such as presented in Fig 5.5 panel e.

5.3.5 Cross-correlation analysis

In addition to inspecting individual lines, we carried out cross-correlation analyses (Brogi et al., 2012, Snellen et al., 2010) to co-add hundreds of absorption lines in the full range

of the optical transmission spectrum to search for atoms (Hoeijmakers et al., 2018, 2019, Kesseli et al., 2022). We computed transmission models of different atoms and ions (Fe I, Fe II, Mg I, etc.) for cross-correlation analysis using the radiative transfer tool `petitRADTRANS` (Mollière et al., 2019). Here we assumed an isothermal temperature profile of 2500 K, a continuum level of 1 mbar, and a gray cloud deck at 1 mbar. The volume mixing ratios (VMR) were set to the solar abundance. We utilized the formula for cross-correlation as presented in (Hoeijmakers et al., 2020a, 2018, 2019),

$$c(v, t) = \frac{\sum_i x_i(t) T_i(v)}{\sum_i T_i(v)}, \quad (5.1)$$

where $x_i(t)$ is the observation at time t . $T_i(v)$ is the transmission model of the species shifted to a radial velocity v , such that the CCF effectively is a weighted average of multiple absorption lines, representing the average strength of the absorption. Following this convention allows us to compare the line strengths across different ultra-hot Jupiters presented in previous cross-correlation studies. However, we caution that such CCF amplitudes depend on the specific models used. This will be further discussed in the comparison to other planets in Section 5.5.1.

The transmission templates were cross-correlated with the telluric corrected spectra in the wavelength range of 380-685 nm (beyond which the spectra are heavily contaminated by telluric lines, therefore excluded in the analysis). This led to the stellar CCFs dominated by signals from the stellar spectra. We then obtained the residual CCFs by removing the average out-of-transit CCF and mitigated the stellar pulsation pattern following Section 5.3.1. Similar as the transmission spectrum, the residual CCFs contains both the stellar RM+CLV effects and the planetary signal. We carried out the same cross-correlation analysis on the synthetic stellar spectra computed in Section 5.3.3 to simulate the RM+CLV contribution to the residual CCFs, which was multiplied by a scaling factor f and then removed from the data to obtain the final CCFs originating from the planetary absorption. The values of free parameters including f , the Gaussian amplitude of the absorption signal h , the Gaussian FWHM and the central velocity offset v_{wind} were determined similarly as presented in Section 5.3.4.

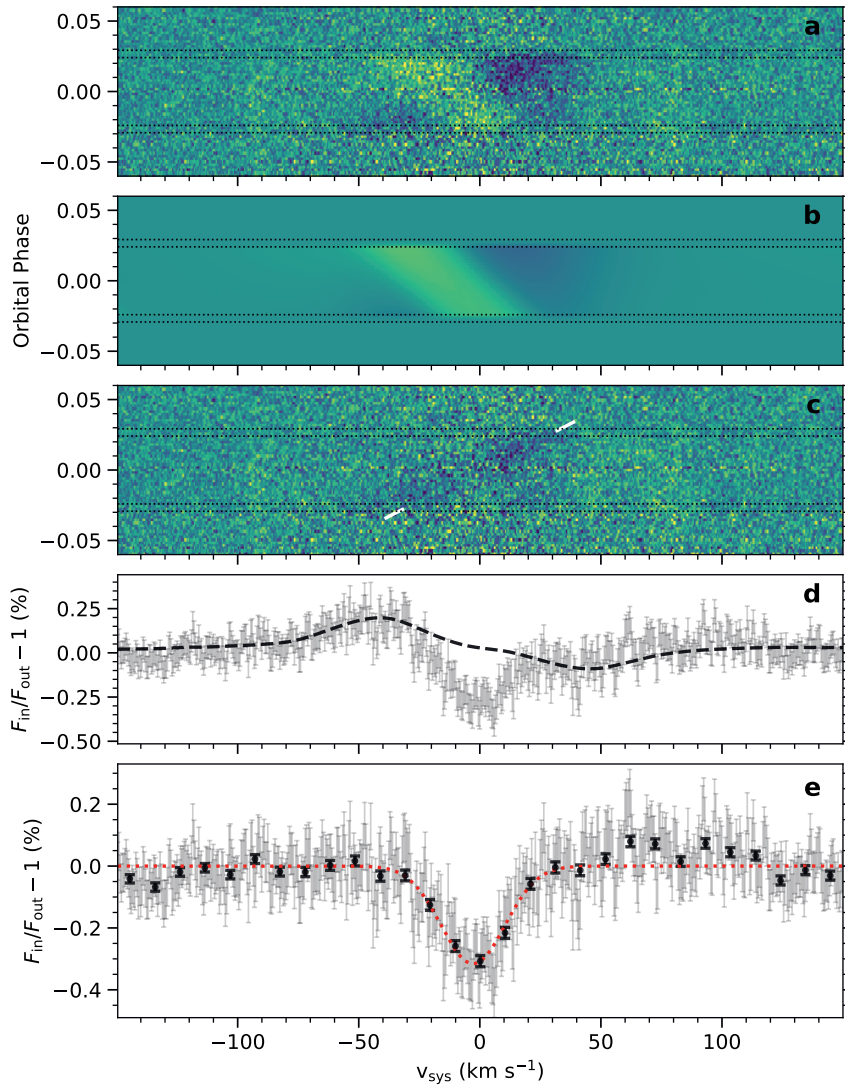


Figure 5.5: H α line transmission spectrum analysis of MASCARA-4b . *Panel a*: residuals after removing the master out-of-transit spectrum and binning in orbital phase by 0.002, containing the stellar RM+CLV effects and the planetary absorption. *Panel b*: best-fit RM+CLV model to the data in panel a. *Panel c*: difference between the data (in panel a) and the RM+CLV model (in panel b) to isolate the planetary absorption signal, as traced by the slanted white line. *Panel d*: transmission spectrum in grey obtained by average-combining the in-transit residuals in panel a (without the correction of RM+CLV effects) in the planet rest frame. The black dashed line is the RM+CLV model in panel b combined in the planet rest frame. *Panel e*: transmission spectrum in grey obtained by average-combining the cleaned residuals in panel c in the planet rest frame. The black points show the transmission spectrum binned every 15 data points. The red dotted line shows the best-fit Gaussian profile to the planetary absorption feature of H α .

5.4 Results

5.4.1 Detection of individual lines of H I, Na I, Ca II, Mg I, Fe I, Fe II

We report the detection of individual absorption lines of H α , H β , Na I D1&D2, Ca II H&K, Mg I, Fe I, and Fe II in MASCARA-4 b . The transmission spectra around these absorption lines are shown in Fig. 5.6, and the measured properties are summarised in Table 5.3.

The centre of the absorption features generally agree with zero, while H α , H β , and Na I doublet appear blueshifted by up to ~ -4 km s $^{-1}$, which is usually interpreted as the evidence of day-to-night side wind (Brogi et al., 2016, Casasayas-Barris et al., 2019, Hoeijmakers et al., 2018, Seidel et al., 2021, Snellen et al., 2010). The various velocity offsets of different species may indicate that the lines probe distinct atmospheric layers dominated by different dynamic processes.

The wind velocity offset for the Na I doublet differs from each other by $\sim 2\sigma$. We suppose this may be systematics as a result of multiple sodium absorptions by the interstellar medium located around 13 to 24 km s $^{-1}$ away from the line center. We mitigated the effect by excluding this velocity range at the barycentric rest-frame when calculating the transmission spectrum, but some artefacts might still persist to contribute to the line offset.

We also note in Fig. 5.9 panel c the 'gap' in the absorption signal when the planetary trail intersects the Doppler shadow, meaning that the planetary transmission lines overlap with the stellar lines from the region blocked by the planet. At this moment, the effective size of the planet appears larger because of the absorption, therefore enhancing the RM effect. This is not accounted for in our RM+CLV modelling, so we commonly see such under-correction that leads to the gap near the overlapping orbital phases. We quantified the effect of the under-correction on the planetary absorption depths by excluding the overlapping orbital phases (e.g. from -0.015 to 0.015) when fitting the planetary signal and co-adding the transmission spectra. We found that the absorption amplitude increases by $\sim 20\%$ - 25% for lines such as H α , sodium, and ionised iron, typically around 2σ of our measurements. The nominal uncertainties shown in Table 5.3 did not account for such systematic noise, therefore likely to be underestimations.

5.4.2 Detection of species in cross-correlation

In addition to elements with individual lines detected in the transmission spectrum, we performed cross-correlation analyses for a range of atoms, ions, and molecules, guided by their observability at high spectral resolution as presented in Kesseli et al. (2022). Here we present the detection of Mg I, Ca I, Cr I, Fe I, and Fe II in Fig. 5.7 and Table 5.4. We found no evidence of other species such as Ti I, Ti II, V I, V II, Mn I, Co I, Ni I, TiO, VO.

The lack of detection of Ti I, Ti II, and TiO are commonly seen in UHJs, although not well understood. Temperatures in the atmosphere seem to play a key role in determining the chemical composition. For example, KELT-9 b shows strong Ti II and no Ti I. Therefore the lack of Ti I is likely attributed to the dominant ionization at the extreme temperature of 4000 K (Hoeijmakers et al., 2018). The detection of Ti I, Ti II, and TiO was found in WASP-189b (Prinoth et al., 2022) with a temperature of ~ 2700 K. For other UHJs with slightly lower temperatures (including WASP-76 b, WASP-121 b, HAT-P-70 b MASCARA-2 b, and MASCARA-4 b), there is no conclusive detection of Ti in any form. This has been proposed to be due to Ti being trapped in condensates on the night side of those cooler

Table 5.3: Summary of individual line detection in the transmission spectrum of MASCARA-4b .

Line	λ_0 (Å)	h (%)	N_{sc}	S/N	f	FWHM (km s ⁻¹)	v_{wind} (km s ⁻¹)
H α	6564.61	-0.317 ± 0.021	48.4 ± 3.3	14.8	1.89	31.4 ± 2.4	-3.0 ± 1.0
H β	4862.72	-0.143 ± 0.030	21.9 ± 4.5	4.8	1.49	27.2 ± 8.1	-4.5 ± 2.3
Ca II H	3969.59	-0.705 ± 0.082	107.6 ± 12.6	8.6	1.48	23.0 ± 3.0	0.2 ± 1.3
Ca II K	3934.77	-0.844 ± 0.082	128.9 ± 12.5	10.3	1.31	29.6 ± 3.1	0.4 ± 1.5
Na I D1	5897.55	-0.168 ± 0.014	25.6 ± 2.2	11.9	1.32	28.6 ± 2.8	-1.8 ± 1.1
Na I D2	5891.58	-0.214 ± 0.017	32.7 ± 2.6	12.4	1.37	19.9 ± 2.1	-3.6 ± 0.7
Mg I	5174.12	-0.151 ± 0.017	23.0 ± 2.6	8.7	1.04	22.6 ± 3.5	1.5 ± 1.3
Mg I	5185.05	-0.125 ± 0.019	19.1 ± 2.9	6.5	1.08	25.2 ± 5.8	2.3 ± 1.6
Fe I	4046.96	-0.162 ± 0.025	24.8 ± 3.8	6.6	1.04	27.8 ± 4.4	-5.0 ± 2.1
Fe I	4384.78	-0.135 ± 0.016	20.6 ± 2.5	8.3	1.16	29.2 ± 4.1	-0.0 ± 1.6
Fe II	4925.30	-0.226 ± 0.022	34.5 ± 3.3	10.3	1.13	13.1 ± 1.7	-0.1 ± 0.6
Fe II	5019.83	-0.211 ± 0.020	32.2 ± 3.0	10.8	1.11	19.1 ± 2.5	-0.7 ± 0.8

λ_0 is the central wavelength of the line in vacuum. h , FWHM, and v_{wind} are the amplitude, width, and center of the best-fit Gaussian profile to the planetary absorption. S/N is simply calculated as the value of h divided by its uncertainty. N_{sc} represents the number of atmospheric scale heights that the peak absorption corresponds to. f is the scaling factor applied to the stellar RM+CLV model.

Table 5.4: Summary of cross-correlation detection.

Species	S/N	K_p (km s ⁻¹)	h (%)	f	FWHM (km s ⁻¹)	v_{wind} (km s ⁻¹)
Mg I	6.3	153 ⁺⁶⁰ ₋₆₂	0.0221 ± 0.0009	0.54	23.8 ± 0.8	-0.5 ± 1.6
Ca I	6.3	207 ⁺⁵³ ₋₆₀	0.0039 ± 0.0001	0.69	22.7 ± 1.2	-3.2 ± 1.5
Cr I	6.7	204 ⁺¹⁴ ₋₄₅	0.0114 ± 0.0006	0.42	16.3 ± 0.6	-3.9 ± 1.0
Fe I	25.3	204 ⁺¹³ ₋₂₁	0.0150 ± 0.0001	0.35	22.5 ± 0.2	-2.4 ± 0.4
Fe II	11.8	179 ⁺¹⁴ ₋₁₂	0.0444 ± 0.0011	0.62	16.5 ± 0.4	-1.2 ± 0.6

S/N is the signal-to-noise ratio at the maximum in the K_p - V_{sys} map as shown in Fig. 5.7 bottom row. The noise level is measured in the map as the standard deviation in the velocity range of (-150, -75) and (75, 150) km s⁻¹, away from the peak signal. The uncertainties of parameters are computed following the method as described in Kesseli et al. (2022). h , f , FWHM, and v_{wind} are defined the same as in Table 5.3

planets (Kesseli et al., 2022, Parmentier et al., 2013, Spiegel et al., 2009).

5.4.3 Neutral and Ionized iron in MASCARA-4b and other UHJs

Here we focus on properties of Fe I and Fe II absorption in MASCARA-4b and draw comparisons with previous detection in other ultra-hot Jupiters.

The absorption strength of Fe II exceeds Fe I, and is more than an order of magnitude higher than what is predicted under the assumption of a hydrostatic atmospheric model. This has been commonly seen in other UHJs such as KELT-9b (Hoeijmakers et al., 2019), MASCARA-2b (Hoeijmakers et al., 2020a), HAT-P-70b (Bello-Arufe et al., 2022) and WASP-189b (Prinoth et al., 2022). The contribution from the hydrostatic region of atmospheres is often too small to account for the measured absorption level of Fe II. Several deviations from the model assumption may help explain the strong absorption by Fe II, for

instance, photochemistry in the upper atmosphere, non local thermodynamic equilibrium (non-LTE) effects, hydrodynamic outflows (Hoeijmakers et al., 2019, Huang et al., 2017, Prinoth et al., 2022). These all suggest that Fe II traces the upper atmospheres, higher than Fe I does. In particular, hydrodynamic outflows can raise the species to the extended upper atmosphere, followed by progressive ionisation of Fe I in the exosphere, giving rise to strong Fe II absorption features. Moreover, the strong lines of Fe II and Mg II observed in the near-ultraviolet (NUV) in WASP-121b also provide evidence of the exospheric origins of the ionic species (Sing et al., 2019).

As shown in Table 5.4, the FWHM of Fe I signal in MASCARA-4 b is larger than that of Fe II. This has also been observed in MASCARA-2b (Hoeijmakers et al., 2020a), while HAT-P-70b shows the opposite trend that Fe II is broader than Fe I (Bello-Arufe et al., 2022). This discrepancy of line width adds to the indication that neutral and ionised iron may probe different region in the atmosphere. Fe I traces deep down layers, while Fe II originates from the upper atmosphere, where the distinct dynamic regimes contribute to the different line widths and radial velocities (Bello-Arufe et al., 2022, Brogi et al., 2016, Hoeijmakers et al., 2019, Louden & Wheatley, 2015, Seidel et al., 2019, Showman et al., 2013). For instance, super-rotational jets may be present in the lower atmospheres of MASCARA-4 b and MASCARA-2b, resulting in broadened Fe I signatures. Whereas, the atmosphere of HAT-P-70b may undergo strong outflow in the upper atmosphere, broadening Fe II signal instead.

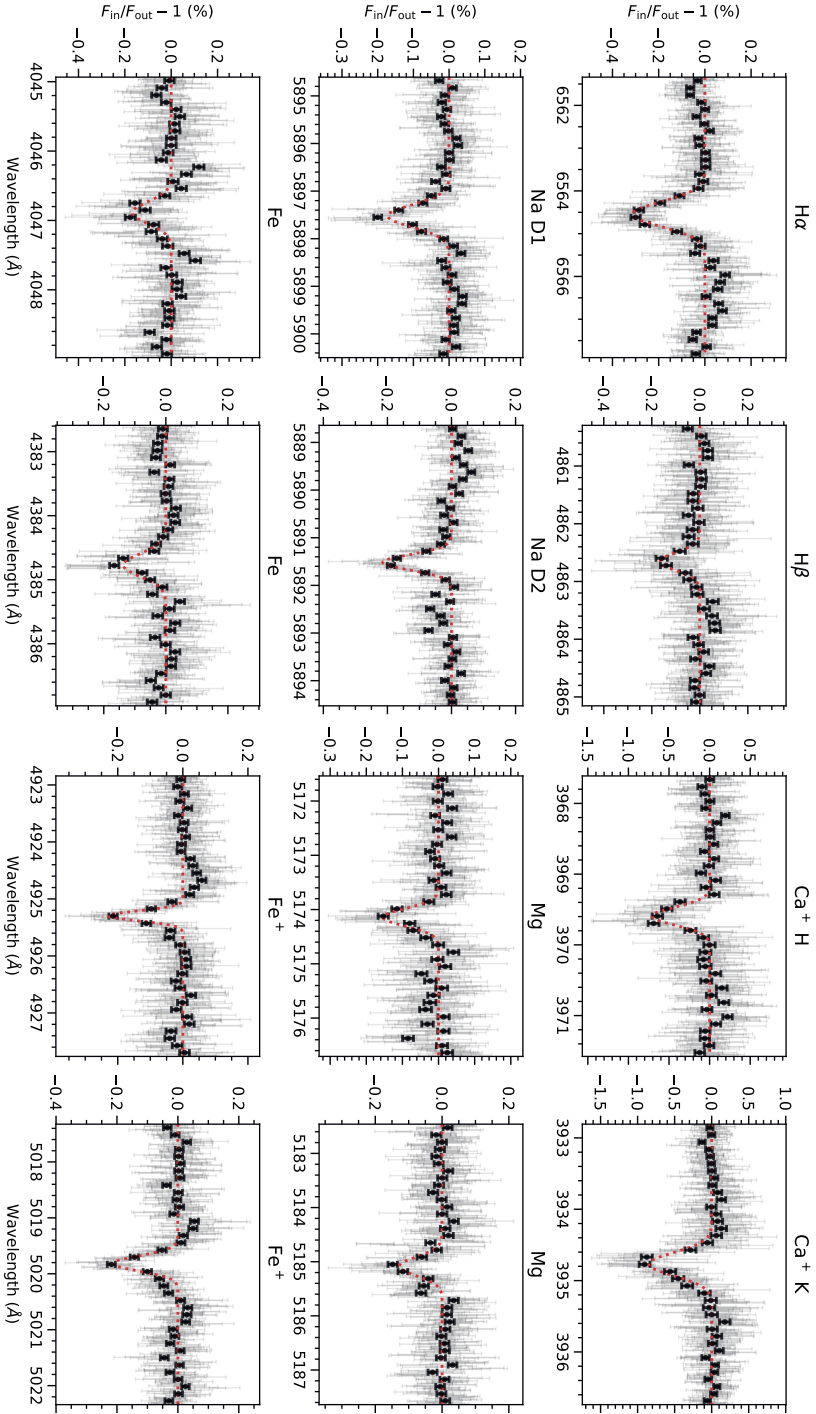


Figure 5.6: Transmission spectrum around H α , H β , Na I D1&D2, Ca II H&K, Mg I, Fe I, and Fe II lines, averaged over both nights of observation. The black points show the transmission spectrum binned every 15 grey data points. The red dotted line shows the best-fit Gaussian profile to the planetary absorption feature.

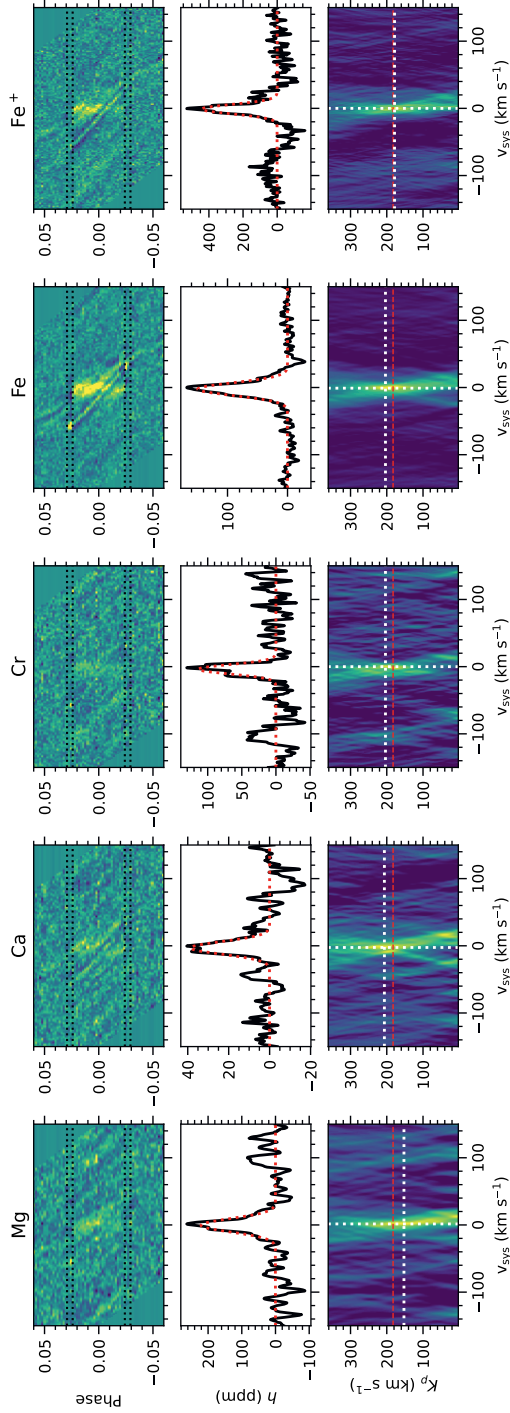


Figure 5.7: Cross-correlation signatures of Mg I, Ca I, Cr I, Fe I, and Fe II, averaged over both nights of observation. *Top row*: two-dimensional residual cross-correlation functions at the planet rest frame corresponding to the expected orbital velocity K_p . The black dotted lines denote the timings of four transit contacts. The vertical signature in yellow around zero velocity illustrates the planetary transmission signal. The narrow slanted shape is caused by imperfect correction of the stellar RM effect. *Middle row*: one-dimensional CCF by co-adding all in-transit residual CCFs shown in the top panel. The red dotted line shows the best-fit Gaussian profile to the planetary signal, the parameters of which are summarised in Table 5.4. *Bottom row*: a stack of co-added CCFs assuming a range of planetary velocity K_p (in y axis). The white dotted lines indicate the maximum in the K_p - v_{sys} map, and the red dashed line marks the expected K_p .

5.5 Discussion

5.5.1 Disentangling the hydrostatic atmosphere and extended exosphere of UHJs

As the detection of atoms with high-resolution transmission spectroscopy accumulates quickly, a small sample of ultra-hot Jupiters starts to build up, providing us with the opportunity to study potential trends of atomic signatures in the UHJ population. Among various species, H I, Na I, Mg I, Ca II, Fe I, and Fe II, have been commonly detected in a handful of UHJs, including KELT-9b (Borsa et al., 2019, Cauley et al., 2019, Hoeijmakers et al., 2019, Turner et al., 2020, Wyttenbach et al., 2020, Yan & Henning, 2018, Yan et al., 2019), MASCARA-2b (Casasayas-Barris et al., 2020, Hoeijmakers et al., 2020a, Nugroho et al., 2020, Stangret et al., 2020), WASP-121b (Borsa et al., 2021, Cabot et al., 2020, Gibson et al., 2020, Hoeijmakers et al., 2020b, Merritt et al., 2021), WASP-76b (Casasayas-Barris et al., 2021, Kesseli et al., 2022, Seidel et al., 2021, Tabernero et al., 2021), WASP-189b (Prinoth et al., 2022), HAT-P-70b (Bello-Arufe et al., 2022). We compile properties of the detections (including the transmission amplitude h and the FWHM of each species) in Table 5.5.

Fig. 5.8 shows the sample of UHJs with the absorption amplitude (h) of each species plotted against the typical transmission strength of absorbers extending one scale height ($2H_0R_p/R_*^2$). Under the assumption of hydrostatic atmospheres, we expect the line strength of one species to be proportional to the typical transmission amplitude $2H_0R_p/R_*^2$, if the absorption forms at a similar pressure level. In this case, the slope of the linear correlation represents the vertical extent of the atom in UHJ atmospheres in units of scale height H_0 . According to Fig. 5.8, neutral metal species such as Mg I, Fe I, (and possibly Na I) follow the trend well, with the Pearson correlation coefficients r close to 1. The number of scale heights (see the slopes in Fig. 5.8) probed by Na I, Mg I, and Fe I decreases with the atomic mass of the element. Another underlying assumption for the linear correlation is that the abundances of the neutral species do not vary significantly in all the UHJs. The good correlations shown in Fig. 5.8 seem to hint at the validity of this hypothesis, which could be verified by future retrieval analysis to constrain the abundances in these UHJs.

On the other hand, H α and Fe II are two apparent exceptions of the correlation. In particular, although the scale height of WASP-76b is large, only upper limits have been estimated for H α and Fe II (Casasayas-Barris et al., 2021, Kesseli et al., 2022). Instead, this agrees with the argument that the absorption of H α probes extended upper atmospheres where the hydrostatic and LTE assumptions no longer apply. Hence the Fe II signatures, with such a similar behaviour as H α , likely also originate from UHJ exospheres.

In this light, we find a positive correlation of absorption signals between Fe II and H α as shown in Fig. 5.9, consolidating that they probe the similar atmospheric region and process. The planet WASP-76b, with only an upper limit detection of the H α absorption, also show no evidence of Fe II, well in line with the correlation. WASP-121b is a baffling case where the detection of Fe II in the optical is debated (the tentative detection was claimed in Ben-Yami et al. (2020), Borsa et al. (2021), Merritt et al. (2021), but contradicted in Gibson et al. (2020), Hoeijmakers et al. (2020b)), while the strong detection in the NUV (Sing et al., 2019) does suggest its presence in the extended exosphere up to $2R_p$. Based on the strong H α detection in WASP-121b (Borsa et al., 2021, Cabot et al., 2020), we expect

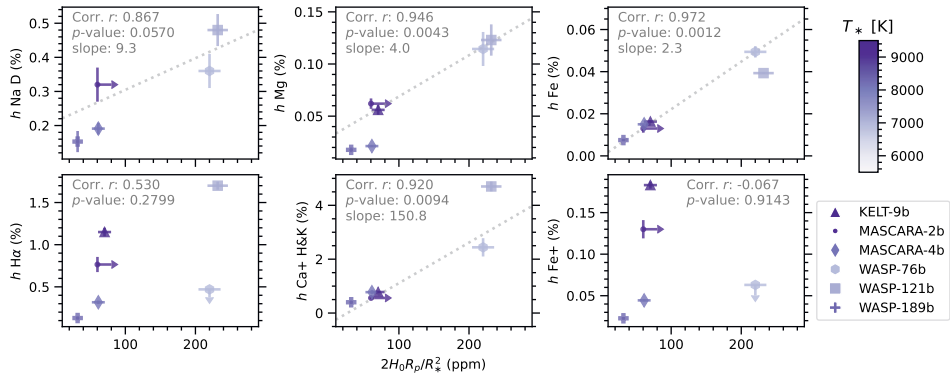


Figure 5.8: Correlation of observed line strengths (h) of different species with expected transmission strengths of absorbers extending one atmospheric scale height ($2H_0 R_p / R_*^2$) for different UHJs. The color saturation of data points represents the temperature of the host star. The data used in this plot are compiled in Table 5.5. Planets with high upper limits on mass (e.g. HAT-P-70b) are omitted in the plot. The Pearson correlation coefficients r and the p -values for testing non-correlation are calculated for each species. For metals such as Mg I and Fe I, r close to 1 and p -value close to 0 indicate strong linear correlation of absorption amplitudes with scale heights. The linear fit to the data points is delineated with dotted gray lines, the slope of which represents the number of scale heights that a certain species probes.

significant Fe II absorption if it follows the trend. Further observations are needed to unravel this. We also note that in order to ensure the trend is not obstructed by the model-dependency of the CCF signal, we compared individual Fe II lines in transmission spectra of KELT-9b (Cauley et al., 2019, Hoeijmakers et al., 2019), MASCARA-2b (Casasayas-Barris et al., 2020), and MASCARA-4 b (this work), and confirm that the correlation with $H\alpha$ still holds.

Therefore, our comparison of atomic transmission features among the UHJ population hints at two distinct regimes of origin, the hydrostatic lower atmosphere and the extended exosphere. The linear correlation between the absorption strengths of metals (such as Na I, Mg I, and Fe I), and the expected transmission amplitudes under the hydrostatic assumption validates their origin from the hydrostatic lower atmosphere. On the other hand, hydrogen and ions such as Fe II deviate from the scale height correlation, possibly because of the prevailing contribution from hydrodynamic outflows in the upper atmosphere. The positive relation of absorption strength between Fe II and $H\alpha$ is further indicative of their exospheric origins (as discussed in Section 5.5.2). The overall picture for Ca II is less clear, probably involving contribution of both regimes. The absorption strengths of Ca II are commonly large enough to be attributed to the extended upper atmospheres, sometimes even beyond the Roche lobe (Bello-Arufe et al., 2022, Borsa et al., 2021). Yet we find no clear correlation between Ca II and $H\alpha$, while the linear trend with scale heights still hold to some extent (see Fig. 5.8). Our speculation is that both lower and upper atmospheric regimes contribute to the absorption, considering Ca I atoms are prone to be readily ionized in the lower atmosphere in contrast to Fe I, the ionization of which may only be significant in the upper atmosphere. A larger sample size is required to draw more solid conclusions.

We caution that studying an ensemble of UHJs is challenging because of two aspects. First, it is difficult to account for the uncertainty of measurements either from different instruments or from different data reduction. For instance, systematic differences have been found in $H\alpha$ in KELT-9b (Cauley et al., 2019, Turner et al., 2020, Wyttenbach et al., 2020, Yan & Henning, 2018) and MASCARA-2b (Casasayas-Barris et al., 2019). However, the systematics are not expected to be large enough to break the general trend that we show here. Second, the model-dependency of cross-correlation signals presents challenges for the comparison of the UHJ population. Previous studies of individual UHJs use cross-correlation templates that are modeled differently. A standard set of models such as presented in Kitzmann et al. (2021) will be beneficial if it can be commonly used in such analyses. Yet the choice of temperature in the model affects the relative weights assigned to weak versus strong lines, which changes the amplitude of CCFs by up to a factor of two.

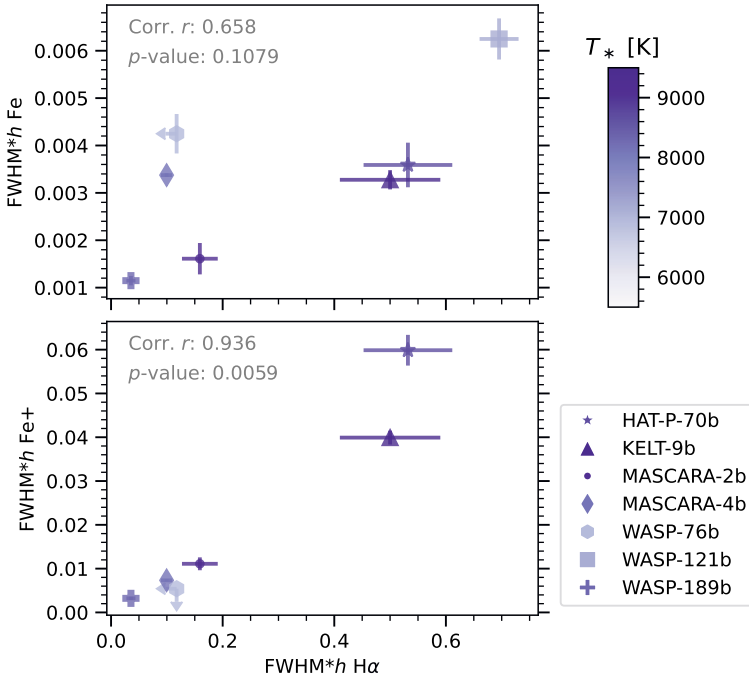


Figure 5.9: Absorption level of Fe I or Fe II against $H\alpha$ in UHJs. The absorption level, taking into account both the amplitude and width of the atomic absorption profile (as a proxy for the equivalent width), is proportional to the total number of the absorbing species in the optically thin limit. We note the strong correlation of $H\alpha$ with Fe II (bottom panel), but less significant with Fe I (top panel).

5.5.2 Hydrodynamic exospheres as probed via $H\alpha$ and ions

The positive correlation of absorption signals between Fe II and $H\alpha$ as shown in Fig. 5.9 indicates that both species trace the similar atmospheric region in UHJs. H I and He I

absorption lines have been previously modeled as a probe for the escaping exosphere (Allan & Vidotto, 2019, Dos Santos et al., 2022, García Muñoz & Schneider, 2019, Huang et al., 2017, Lampón et al., 2021, Oklopčić & Hirata, 2018, Wyttenbach et al., 2020, Yan et al., 2021), which is expected to be the consequence of hydrodynamic outflows driven by stellar X-ray, extreme Ultraviolet (EUV) or NUV radiation. The driving mechanism may depend on the stellar type, as early A type stars are not expected to emit strongly at EUV (Fosati et al., 2018), while having high levels of NUV flux (García Muñoz & Schneider, 2019). The modeling of outflows also extends to heavy atoms such as C, O, Si by Koskinen et al. (2013), suggesting that heavy elements dragged to the upper atmospheres stay well mixed as a result of collisions with rapidly escaping hydrogen. Gebek & Oza (2020) modeled Na and K in evaporative exospheres to interpret high-resolution transmission observations. Furthermore, the strong Mg I, Mg II, and Fe II lines in the NUV are discussed as tracers of upper atmospheres and hydrodynamic escapes (Bourrier et al., 2014, Dwivedi et al., 2019, Sing et al., 2019), while the optical lines have not been explored. Based on the presented correlation of absorption signals between Fe II and H α , we suggest that Fe II lines in the optical also probe exospheres of UHJs. Therefore, further modeling of Fe II in exosphere can help constrain the structure of upper atmosphere, outflows, and the mass loss process.

Without the intention to model any particular atmosphere in detail, we aim to get insights into the trend in the UHJ population by some simplified estimations as follows. We examine the role of hydrodynamic outflows and photoionisation of atoms in the absorption signals of H I and Fe II in UHJs. For a rough estimation, we assume the extended exosphere as a homogeneous optically thin cloud subject to stellar high energy radiation. In the optically thin limit, the absorption level is proportional to the total mass of the absorbing material regardless of the shape of the cloud (Gebek & Oza, 2020, Hoeijmakers et al., 2020b). Hence, the absorption signal depends on the mass loss rate \dot{M} that determines the inflow of absorbing material to the exosphere and the ionisation degree f_X of the element. More details of the estimation can be found in Appendix 5.A. We find that the photoionisation plays a marginal role in the discrepancy of absorption strengths because the degree of ionization is expected to vary by less than a factor of a few among different UHJs. Instead, the amount of absorption is dominated by the planetary mass loss \dot{M} driven by the stellar EUV or NUV flux, which usually varies by orders of magnitudes from system to system. Therefore, we argue that the dominant outflow drives the positive correlation between the H α and Fe II absorption (see Fig. 5.9), and they likely trace the exospheres of UHJs. The absorption level reflects the properties of individual planets such as the mass loss rate and the irradiation environment.

Although the sample size of UHJs with detailed spectral characterisation is still small, we suggest that the correlation between Fe II and H α absorption signal is expected from the analytical estimation. It therefore calls for more future observations on UHJs to populate this plot. Detailed modeling of individual planets will be valuable for constraining the hydrodynamic outflows and mass loss rate as traced by atomic absorption lines in the optical.

5.6 Conclusion

With the purpose of detailed characterisation of the ultra-hot Jupiter MASCARA-4 b, we carried out transit photometry and radial velocity measurements using EulerCam and

CORALIE at the 1.2 m Euler telescope, delivering a refined planet mass of $1.675 \pm 0.241 M_{\text{Jup}}$, together with other updated system and planet parameters. We analysed the optical transmission spectrum of MASCARA-4 b observed with the high-resolution spectrograph ESPRESSO at the VLT and report the detection of various species in the atmosphere, including H I, Na I, Mg I, Ca I, Ca II, Cr I, Fe I, and Fe II. This adds MASCARA-4 b to the ensemble of UHJs showing a profusion of atomic absorption features. Putting the measurements into perspective, we explored the trends of atomic absorption features within the UHJ population, indicating two distinct atmospheric regimes as probed through different absorption signatures. The absorption by metals such as Mg I and Fe I appears to trace the hydrostatic region of atmospheres as the line strengths correlate well with the scale heights of different planets. The H α and Fe II absorption strengths, which deviate from the scale height correlation, yet show a positive relation with each other among the UHJ population. Through analytical estimations, we suggest that the correlation is consistent with the exospheric origin of Fe II and H α absorption in UHJs, driven by the dominant outflows subject to stellar high-energy radiation. This shows the potential of using both species as probes for the hydrodynamic escape and mass loss of UHJs. Studying the diverse atomic transmission signatures allows us to disentangle the hydrostatic and the exospheric regime of the extremely irradiated planets.

5.A Analytical estimation of atomic absorption in exospheres

We consider the gas composed of atomic hydrogen in the upper atmosphere (exosphere) escaping the planet with a velocity of u and a constant mass loss rate \dot{M} . The conservation of mass provides

$$\dot{M} = 4\pi R_c^2 u \rho, \quad (5.2)$$

where R_c is the size of the exobase, ρ is the density of hydrogen, and $u = x_u v_{\text{esc}}$ is a fraction of the planet's escape velocity $v_{\text{esc}} = \sqrt{2GM_p/R_p}$.

The energy-limited mass loss rate following Erkaev et al. (2007) is given by

$$\dot{M} = \frac{\pi R_c^2 F_{\text{EUV}} \epsilon}{\Phi_0 K}, \quad (5.3)$$

where R_p is the planet radius, F_{EUV} is the stellar EUV flux at the location of the planet, ϵ is the heating efficiency, Φ_0 is the gravitational potential at the planetary radius ($\Phi_0 = GM_p/R_p$), and $K(\frac{R_{\text{RI}}}{R_p})$ is the coefficient accounting for the potential difference between the Roche lobe boundary (R_{RI}) and the planetary surface (R_p) as a result of stellar tidal forces.

Combining Equation 5.2 and 5.3, we get the number density of H atom in the exosphere as a result of outflows

$$\rho = \frac{\epsilon F_{\text{EUV}}}{2x_u K v_{\text{esc}}^3} \approx \rho_0 \left(\frac{\epsilon F_{\text{EUV}}}{F_0} \right) \left(\frac{v_0}{v_{\text{esc}}} \right)^3, \quad (5.4)$$

where $F_0 = 450 \text{ erg cm}^{-2} \text{ s}^{-1}$, $v_{\text{esc}} = 60 \text{ km s}^{-1}$, and $\rho_0 = 10^{-15} \text{ g cm}^{-3}$, as informed by previous simulations such as Allan & Vidotto (2019), Murray-Clay et al. (2009).

Equation 5.4 suggests that under the assumption of the energy-limited mass loss, the exospheric density ρ scales with the planet's escape velocity (or gravitational potential) and the EUV flux received.

In addition to the outflow, the photoionisation of species also plays a role in determining the level of transmission signal. For a rough estimation of the photoionisation, we simply assume the extended exosphere as a homogeneous optically thin cloud subject to stellar EUV radiation. The characteristic temperature of the exosphere is determined by the balance of heating (Q) and cooling (C) following Murray-Clay et al. (2009).

$$Q = \epsilon F_{\text{EUV}} \sigma_{v_0} n_n, \quad (5.5)$$

where σ_{v_0} is the cross section for the photoionisation of hydrogen and n_n is the number density of neutral hydrogen. For the cooling term, we assume it is driven by radiative losses resulting from collisional excitation of Ly α line

$$C = 7.5 \times 10^{-19} n_n n_+ \exp[-1.183 \times 10^5/T], \quad (5.6)$$

where n_+ is the number density of protons, equivalent to the number density of electrons.

Considering the photochemistry of H I, we solve for the ionisation balance (the rate of photoionisation and radiative recombination) to estimate the degree of ionization f_{H} .

$$\frac{F_{\text{EUV}} \sigma_{v_0} n_n}{e_{\text{in}}} = n_+ n_e \alpha_{\text{rec}}, \quad (5.7)$$

where $\sigma_{v_0} = 1.89 \times 10^{-18} \text{cm}^2$ is the cross section for photoionisation of hydrogen (Spitzer, 1978); the recombination coefficient $\alpha_{\text{rec}} = 2.7 \times 10^{-13} (T/10^4)^{-0.9}$ taken from Storey & Hummer (1995); $n_+ = n_e = n f_{\text{H}}$ and $n_n = n (1 - f_{\text{H}})$, where $n = \rho/m_0$, m_0 is the mass of H atom; e_{in} is the input photon energy, assumed to be 20 eV, and the heating efficiency is $\epsilon = 1 - 13.6\text{eV}/e_{\text{in}} = 0.32$.

Combining Equation 5.4, 5.5, 5.6, and 5.7, we solve for the ionization degree of hydrogen and the temperature as follows

$$\begin{aligned} \frac{1}{f_{\text{H}}} &= 1 + 0.015 / (T^{0.9} \exp[-1.183 \times 10^5/T]), \\ \frac{1}{f_{\text{H}}} &= \frac{0.4\rho_0}{m_0 F_0} \left(\frac{v_0}{v_{\text{esc}}} \right)^3 \exp[-1.183 \times 10^5/T]. \end{aligned} \quad (5.8)$$

Similarly, for other species such as Fe I, the ionisation balance of Fe combined with Equation 5.7 gives

$$\frac{1}{f_{\text{Fe}}} = 1 + \frac{1 - f_{\text{H}}}{f_{\text{H}}} \frac{\sigma_{\text{H}} \alpha_{\text{rec,Fe}}}{\sigma_{\text{Fe}} \alpha_{\text{rec,H}}}, \quad (5.9)$$

where $\sigma_{\text{Fe}} = 3.66 \times 10^{-18} \text{cm}^2$ (Verner et al., 1996), the recombination coefficient $\alpha_{\text{rec,Fe}} = 3.7 \times 10^{-12} (T/300)^{-0.65}$ (Woodall et al., 2007).

Hence, the exospheric temperature and degree of ionisation depend on the planet's potential in terms of v_{esc} in our simplified model, as shown in Fig. 5.11.

In the optically thin limit, the equivalent width of absorption is proportional to the total mass of the absorbing material (Gebek & Oza, 2020, Hoeijmakers et al., 2020b). For neutral hydrogen and ionised iron, they can be written as follows

$$\begin{aligned}\mathcal{T}_{\text{H}} &\sim \rho(1 - f_{\text{H}}) \sim \rho_0 \left(\frac{\epsilon F_{\text{EUV}}}{F_0} \right) \left(\frac{v_0}{v_{\text{esc}}} \right)^3 (1 - f_{\text{H}}), \\ \mathcal{T}_{\text{Fe}^+} &\sim \rho_{\text{Fe}} f_{\text{Fe}} \sim \rho_0 \left(\frac{\epsilon F_{\text{EUV}}}{F_0} \right) \left(\frac{v_0}{v_{\text{esc}}} \right)^3 A_{\text{Fe}} f_{\text{Fe}},\end{aligned}\tag{5.10}$$

where a constant mixing of the metal species is assumed, A_{Fe} is the mass fraction of iron. We note that the photoionisation term (f_{H} and f_{Fe}) can result in variations of the signal strength from different planets by a factor of 4 at most (see Fig. 5.11). Whereas, equation 5.10 contains the linear term of F_{EUV} that usually varies by orders of magnitudes from system to system. Therefore, the absorption signal from the exosphere is dominated by the planetary outflow \dot{M} induced by the EUV flux, which drives the positive correlation between $\text{H}\alpha$ and Fe II as we note in Section 5.5.1. Hence such correlation is indeed expected, which reflects properties such as the mass-loss rate and EUV irradiation of different UHJs.

For simplicity we did not take into account the fraction of atoms at the right state (e.g. the principal quantum number $n=2$ for $\text{H}\alpha$ absorption). This requires non-local thermal equilibrium (NLTE) calculation of the radiation field and gets even more complicated for the case of Fe II where we combined multiple lines in the observation. The ionisation of Fe II is also ignored here. We do not attempt to make detailed interpretation of observed lines in any particular system. Instead, our aim is to draw the relation between $\text{H}\alpha$ and Fe II across the UHJ population. These assumptions hopefully do not deter the overall trend, yet we need to rely on detailed simulations for a definite answer.

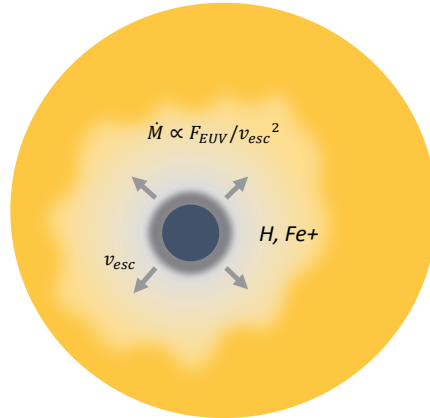


Figure 5.10: Schematic of a transiting ultra-hot Jupiter with a hydrostatic lower atmosphere and a optically-thin escaping exosphere.

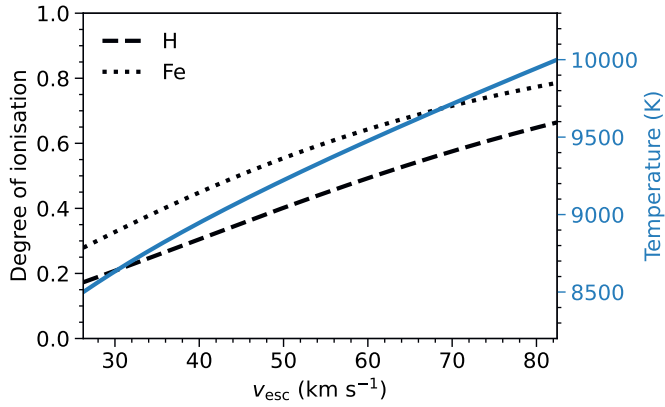


Figure 5.11: Estimated temperature and degree of ionization of H and Fe for different planets with a range of v_{esc} . The ionisation fractions are not expected to vary drastically across different UHJs.

5.B Summary of UHJs with detailed characterisation with high-resolution transmission spectroscopy

Table 5.5: Properties of atomic absorption features detected in transmission spectra of ultra-hot Jupiters.

	HAT-P-70b	KELT-9b	MASCARA-2b	MASCARA-4b	WASP-76b	WASP-121b	WASP-189b
R_p/R_*	0.099	0.082	0.113	0.087	0.109	0.125	0.061
T_{eq} (K)	2562 ± 52	3921 ± 182	2260 ± 50	2250 ± 62	2228 ± 120	2358 ± 52	2641 ± 31
T_* (K)	8450 ± 690	9600 ± 400	8980 ± 130	7800 ± 200	6329 ± 65	6586 ± 59	8000 ± 100
R_p (R_{Jup})	1.87 ± 0.15	1.926 ± 0.047	1.83 ± 0.07	1.515 ± 0.044	1.863 ± 0.083	1.865 ± 0.044	1.619 ± 0.021
M_p (M_{Jup})	< 6.78	2.88 ± 0.35	< 3.5	1.675 ± 0.241	0.894 ± 0.014	1.183 ± 0.064	1.99 ± 0.16
H_0 (km)	> 184	704 ± 95	> 302	430 ± 66	1206 ± 102	967 ± 65	485 ± 40
h H α (%)	1.560 ± 0.150	1.150 ± 0.050	0.765 ± 0.090	-0.317 ± 0.021	< 0.470	1.700 ± 0.048	0.13 ± 0.02
FWHM H α (km s $^{-1}$)	34.1 ± 3.9	51.2 ± 2.6	20.8 ± 3.4	31.4 ± 2.4	-	40.9 ± 1.7	27.4 ± 4.6
h Fe I (%)	0.037 ± 0.003	0.016 ± 0.001	0.013 ± 0.002	0.0150 ± 0.0001	0.049 ± 0.003	0.039 ± 0.002	0.0075 ± 0.0004
FWHM Fe I (km s $^{-1}$)	9.7 ± 1.0	20.1 ± 1.0	12.39 ± 1.69	22.5 ± 0.2	8.6 ± 0.7	15.9 ± 1.1	15.3 ± 1.0
h Fe II (%)	0.437 ± 0.017	0.183 ± 0.004	0.130 ± 0.011	0.0444 ± 0.0011	< 0.063	-	0.023 ± 0.002
FWHM Fe II (km s $^{-1}$)	13.7 ± 0.6	21.8 ± 0.7	8.54 ± 0.87	16.5 ± 0.4	-	-	14.1 ± 1.2
h Na I D (%)	0.655 ± 0.150	$> 0.095 \pm 0.007$	0.320 ± 0.050	0.191 ± 0.017	0.360 ± 0.050	0.480 ± 0.047	0.153 ± 0.031
h Mg I (%)	0.131 ± 0.018	0.056 ± 0.005	0.062 ± 0.005	0.0221 ± 0.0009	0.114 ± 0.016	0.123 ± 0.015	0.018 ± 0.002
h Ca II (%)	3.750 ± 0.370	0.780 ± 0.040	0.560 ± 0.050	0.775 ± 0.082	2.440 ± 0.340	4.700 ± 0.180	0.40 ± 0.05
References	(1),(2)	(3)-(10)	(11)-(15)	(16)-(18)	(19)-(24)	(25)-(28)	(29)-(31)

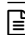
For the calculation of the lower atmosphere scale height H_0 , we assume a mean molecular weight μ of 2.3. The amplitude of Na I absorption (h Na I D) takes the average value of the Na I doublet at 5891 and 5897 Å. The h Ca II takes the average value of the Ca II H & K lines at 3969 and 3934 Å. Properties of Mg I, Fe I, and Fe II are taken from cross-correlation outcomes.

(1) Zhou et al. (2019), (2) Bello-Arufe et al. (2022), (3) Gaudi et al. (2017), (4) Yan & Henning (2018), (5) Cauley et al. (2019), (6) Borsa et al. (2019), (7) Hoeijmakers et al. (2019), (8) Yan et al. (2019), (9) Turner et al. (2020), (10) Wyttenbach et al. (2020), (11) Talens et al. (2018), (12) Casasayas-Barris et al. (2020), (13) Hoeijmakers et al. (2020a), (14) Nugroho et al. (2020), (15) Stangret et al. (2020), (16) Dorval et al. (2020), (17) Ahlers et al. (2020), (18) this work, (19) West et al. (2016), (20) Ehrenreich et al. (2020), (21) Taberner et al. (2021), (22) Seidel et al. (2021), (23) Casasayas-Barris et al. (2021), (24) Kesseli et al. (2022), (25) Delrez et al. (2016), (26) Cabot et al. (2020), (27) Hoeijmakers et al. (2020b), (28) Borsa et al. (2021), (29) Anderson et al. (2018), (30) Prinoth et al. (2022), (31) Stangret et al. (2022).

6

DESTINYs: Diverse outcomes of binary-disk interactions

Circumstellar disks play an essential role in the outcomes of planet formation. Disks do not evolve in isolation, as about half of solar-type stars were born in binary or multiple systems. The presence of stellar companions modifies the morphology and evolution of disks, potentially resulting in a different planet population. Resolving disks in binary systems provides the opportunity to examine the influence of stellar companions on the outcomes of planet formation. We aim to investigate and compare disks in stellar multiple systems with near-infrared scattered-light imaging as part of the Disk Evolution Study Through Imaging of Nearby Young Stars (DESTINYs) large program. We used polarimetric differential imaging with SPHERE/IRDIS at the VLT to search for scattered light from the circumstellar disks in three multiple systems, CHX 22, S CrA, and HP Cha. We performed astrometric and orbit analyses for the stellar companions using archival HST, VLT/NACO, and SPHERE data to better understand the interplay between disks and companions. Combined with the age and orbital constraints, the observed disk structures in scattered light provide insights into the evolutionary history and the impact of the stellar companions. The small grains in CHX 22 form a tail-like structure surrounding the close binary, which likely results from a close encounter and capture of a clouddlet. S CrA shows intricate structures (tentative ringed and spiral features) in the circumprimary disk as a possible consequence of perturbations by companions. The circumsecondary disk is truncated and connected to the primary disk via a streamer, suggesting tidal interactions. In HP Cha, the primary disk is less disturbed and features a tenuous streamer, through which the material flows towards the companions. The comparison of the three systems spans a wide range of binary separation (50 – 500 au) and illustrates the decreasing influence on disk structures with the distance of companions. This agrees with the statistical analysis of exoplanet population in binaries, that planet formation is likely obstructed around close binary systems, while it is not suppressed in wide binaries.

 **Zhang, Y.**, Ginski, C., Huang, J., Zurlo, A., Beust, H., et al. (2023) Disk Evolution Study Through Imaging of Nearby Young Stars (DESTINYs): Diverse outcomes of binary-disk interactions. *A&A*, 672, A145.

6.1 Introduction

Circumstellar disks as the birthplaces of planets play an important role in the outcomes of planet formation. Dust in the disks undergoing growth into pebbles and planetesimals constitute the building blocks of planetary embryos. Therefore the properties of dust and their evolution significantly influence the planet formation processes (Drazkowska et al., 2022). In turn, gas giants formed in disks affect the distribution of solids and disk structures. Recent high angular resolution observations of circumstellar disks across a wide wavelength range reveal near ubiquitous substructures (rings, spirals, and cavities) which may be carved by newborn planets (Andrews et al., 2018, Bae et al., 2018, Benisty et al., 2022, Lodato et al., 2019). Therefore understanding the interplay between disks and massive objects is essential for unraveling planet formation.

Studies of circumstellar disks have been mostly focused on isolated stars. However, it is well established that about half of solar-type stars were born in multiple systems (Duquennoy & Mayor, 1991, Raghavan et al., 2010), hence the potential effects of binarity on disk evolution and planet formation are not negligible. In particular, the gravitational perturbation and tidal truncation due to the close central binaries or outer companions will immensely impact the morphology of the disks, such as opening large inner cavities, truncating disk sizes, inducing spiral features, or warping and misaligning inner and outer disk regions (Artymowicz & Lubow, 1994, Benisty et al., 2017, Marino et al., 2015, Papaloizou & Pringle, 1977, Ragusa et al., 2020, Rosotti & Clarke, 2018). The presence of companions may also dictate the evolution of gas and dust in disks (Ribas et al., 2018, Rosotti & Clarke, 2018, Zagaria et al., 2021a,b). Dedicated surveys of star-forming regions suggest that protoplanetary disks in multiple systems are more compact and less massive than disks around isolated stars (Akeson et al., 2019, Cox et al., 2017, Manara et al., 2019, Rota et al., 2022, Zurlo et al., 2021, 2020).

Despite the dominance of destructive processes around multiple stars, several disks in such systems have been previously imaged in scattered light, such as GG Tau (Keppler et al., 2020), GW Ori (Kraus et al., 2020), and UX Tau (Ménard et al., 2020, Zapata et al., 2020), for which detailed hydrodynamical simulations have been dedicated in order to provide insights into the influence of stellar companions on disk structures. Observations and simulations of disks in binaries provide opportunities to examine the plausibility of planet formation in various conditions, which can be further linked to the demographics of exoplanets in multiple stellar systems.

Among the five-thousand exoplanets discovered to date, more than two hundred were discovered in multiple systems (Martin, 2018, Schwarz et al., 2016), suggesting that planet formation in such systems indeed occurs. Most of these planets are found surrounding individual components of the binaries (called S-type architecture) as opposed to circumbinary planets (called P-type). Multiplicity surveys of planet-hosting stars have been carried out using direct imaging (e.g., Bohn et al., 2020, Eggenberger et al., 2007, Ginski et al., 2021b, 2016, 2012, Mugrauer & Ginski, 2015, Mugrauer & Michel, 2020, Ngo et al., 2015). The statistical analyses of the impact of binaries on planet frequencies remain inconclusive as a result of the incompleteness of both planet detection and stellar companion detection. Some studies suggested a significant deficit of stellar companions for the planet-hosting sample in contrast to the field population (e.g., Kraus et al., 2016, Roell et al., 2012, Wang et al., 2014a,b), while others found no clear evidence of distinguishable planet fre-

quency between binaries and single stars except for close stellar companions < 100 au (e.g., Asensio-Torres et al., 2018, Bonavita & Desidera, 2007, 2020, Horch et al., 2014). Synthesizing previous surveys of planet hosts, Moe & Kratter (2021) found planet suppression to be a gradual function of binary separation within ~ 200 au and no influence from wide companions beyond 200 au. It is also suggested that the impact of stellar companions becomes more important for higher-mass planets since massive close-in giant planets (hot Jupiters) are more common in multiple systems (Fontanive et al., 2019, Ngo et al., 2016, Ziegler et al., 2020), implying that either giant planet formation is more efficient in wide binaries, or dynamical perturbations from stellar companions more likely result in orbital migration of giant planets (Fontanive et al., 2019, Su et al., 2021). In terms of the distribution of planet properties, Desidera & Barbieri (2007) and Ngo et al. (2017) indicated that planet parameters such as mass, period, and eccentricity are indistinguishable between single and multiple systems, while Moutou et al. (2017) suggested that the multiplicity of eccentric-planet hosts is higher than circular-planet hosts, as expected from numerical simulations (Kaib et al., 2013). Therefore the trend remains to be explored.

Directly capturing the interactions between disks and stellar companions opens a window into the starting conditions of the planet formation process in these complex systems. Here we present the detection of circumstellar dust around three T Tauri multiple systems for the first time, using polarimetric differential imaging with SPHERE/IRDIS on ESO's Very Large Telescope (VLT) (Beuzit et al., 2019) as part of the Disk Evolution Study Through Imaging of Nearby Young Stars (DESTINYs) programme (Ginski et al., 2021a, 2020). In the DESTINYs samples, we did not specifically select targets based on their stellar multiplicity. The three multiple systems are covered in the survey because they meet the criteria that the stars are optically bright members of nearby young star-forming regions and show near and mid-infrared excesses in their SED. The snapshots of these systems provide an excellent comparison of the diverse morphology of disks in different evolutionary stages and binary configurations. Combined with analyses of age, mass, and orbital motion of the stellar systems, the structures of the disks provide further indications of the impact of stellar companions on the evolution of circumstellar disks and prospects for planet formation in such systems.

This paper is organized as follows. In Section 6.2, we introduce the properties of the three targeted multiple systems, namely, CHX 22, S CrA, and HP Cha, with a particular focus on age and mass. The observations and data reduction are described in Section 6.3. We present the analyses of polarimetric and astrometric data of each system in Section 6.4. These in conjunction with the knowledge of system properties are considered in Section 6.5 to infer the disk structure and evolution history. Comparing the three systems, we finally discuss the implications for planet formation in binary systems. The summary is presented in Section 6.6.

Table 6.1: Properties of the targeted young binary (or triple) systems.

Object	RA (h m s)	Dec (d m s)	Parallax (mas)	Age (Myr)	Separation (au)	SpT	Mass (M_{\odot})	Ref.
CHX 22	11 12 42.69	-77 22 23.1	5.2302 ± 0.1675	~ 5	~ 50	G8 & K7	1.8 & 0.8	1, 4
S CrA	19 01 08.60	-36 57 19.0	6.2291 ± 0.0683	~ 1	~ 200	K6 & K6	1 & 1	2
HP Cha	11 08 14.94	-77 33 52.2	5.3381 ± 0.0352	~ 10	~ 500	G5 & M1 & M3.5	1.4 & 0.8 & 0.3	3, 4

¹ Daemgen et al. (2013);² Gahm et al. (2018);³ Schmidt et al. (2013);⁴ Manara et al. (2017);

Parallax: Gaia Collaboration et al. (2022).

6.2 Individual system properties

In order to determine the evolutionary stage of the targets, we summarized previous studies of the properties of each system, in particular, the age and stellar mass, as also listed in Table 6.1.

CHX 22

CHX 22 is a weakly (or non) accreting T Tauri star with a close binary companion separated by $\sim 0.24''$ (~ 50 au) (Daemgen et al., 2013). CHX 22 is located in the Chamaeleon I (Cha I) cloud, which is among the nearest young star-forming regions at a distance of 192 ± 6 pc (Dzib et al., 2018). The age distribution of Cha I was previously determined to peak around 3–4 Myr (Luhman, 2007) based on an old distance estimate of 160 ± 15 pc (Whittet et al., 1997). The updated GAIA DR3 distance would result in a luminosity increase of $\Delta \log L \sim 0.15$, therefore implying a younger age. Assuming a distance to Cha I of 160 pc, Daemgen et al. (2013) estimated the ages to be 16_{-10}^{+30} and $9_{-6.5}^{+16}$ Myr for the A and B components respectively, and the masses of 1.3 and $0.8 M_{\odot}$ using Siess et al. (2000) isochrones. Manara et al. (2017) derived a mass of $1.62 M_{\odot}$ for the A component using the Baraffe et al. (2015) isochrones. Taking into account the distance change, we scaled the mass and age using the luminosity and effective temperature reported in the literature and Siess et al. (2000) isochrones. We adopted the masses of 1.8 and $0.8 M_{\odot}$ for the binary and the age of ~ 5 Myr.

S CrA

S CrA is an archetypal system of the classical T Tauri stars with rich emission lines as a result of the accretion from circumstellar disks and emission from stellar or disk winds. The stars show significant spectroscopic variability because of the variable extinction from the circumstellar dust (Gahm et al., 2008). The binary separation is $\sim 1.3''$ (~ 200 au). The stellar parameters have been extensively studied with resolved high-resolution spectra of both stars (Gahm et al., 2018, Sullivan et al., 2019). The study by Gahm et al. (2018) suggested that despite the different levels of veiling, both stars had quite similar properties with an effective temperature of 4250 K, and a mass of $1 M_{\odot}$. Sullivan et al. (2019) estimated age of ~ 1 Myr using the Baraffe et al. (2015) isochrones, determined different spectral types for the two stars (K7 & M1), and obtained lower temperatures (4000 & 3700 K) and masses (0.7 & $0.45 M_{\odot}$). We adopt the estimation by Gahm et al. (2018) since the total mass of $\sim 2M_{\odot}$ is more consistent with our orbit analysis as presented in Section 6.4.2.

Table 6.2: Observing log of three young binary (or triple) systems with SPHERE/IRDIS.

Object	Date	Filter	DIT (s)	NDIT	N_{cycle}	on-target time (min)	seeing (")	τ_0 (ms)
CHX 22	2020-02-18	BB_H	2	24	14	44.8	0.43 – 0.96	11.5
CHX 22	2020-02-28	BB_H	8	8	13	55.5	0.6 – 1.17	5.2
S CrA	2021-09-08	BB_H	8	2	42	44.8	0.46 – 0.77	5.8
HP Cha	2020-01-13	BB_H	64	1	14	59.7	0.33 – 0.54	8.5

DIT: integration time per exposure. NDIT: number of exposures per half-wave plate position. N_{cycle} : number of full polarimetric cycles. τ_0 : atmospheric coherence time.

HP Cha

HP Cha A, also named Glass I, is a G-type WTTS in the Cha I star-forming region, with a wide companion at $2.4''$ (~ 500 au) (Chelli et al., 1988). The companion itself was later resolved into a close binary B and C (Daemgen et al., 2013, Schmidt et al., 2013). The B and C components show significant variation in separation (from 70 to 180 mas), indicating a highly inclined and/or eccentric orbit. Schmidt et al. (2013) derived a mass of 1.26, 0.76, and $0.28 M_{\odot}$ for the three stars and an age of ~ 2 Myr. Manara et al. (2017) derived a mass of $1.26 M_{\odot}$ for the A component and $1.00 M_{\odot}$ for the BC component. Similar to CHX 22, we used the stellar temperature and luminosity reported in Manara et al. (2017) and scaled the mass and age according to the updated distance to Cha I cloud. We adopted a mass of 1.4, 0.8, and $0.3 M_{\odot}$ respectively, and the age of ~ 10 Myr. However, we caution that the age derived from evolutionary models is rather uncertain (Pecaut et al., 2012).

Table 6.3: Archival HST, VLT/NACO, VLT/SPHERE, and ALMA observations included in this work.

Object	Epoch	Instrument	Program ID	Filter/Transition
S CrA	1999-02-21	HST/WFPC2	GO-7418	F814W
S CrA	2002-10-29	VLT/NACO	70.D-0444(A)	H
S CrA	2010-08-08	VLT/NACO	085.C-0373(A)	K_S
S CrA	2012-06-09	VLT/NACO	089.C-0196(A)	L
S CrA	2015-06-25	VLT/SPHERE	095.C-0787(A)	K_S
CHX 22	2016-01-25	ALMA	2015.1.00333.S	CO $J = 3 - 2$
HP Cha	2015-05-21	ALMA	2013.1.01075.S	CO $J = 3 - 2$

6.3 Observations and data reduction

6.3.1 SPHERE/IRDIS observations

We present new observations on three young binary (or triple) star systems, CHX 22, S CrA, and HP Cha, with SPHERE/IRDIS in dual-beam polarimetric imaging mode in the H -band (de Boer et al., 2020, Dohlen et al., 2008, Langlois et al., 2014, van Holstein et al., 2020). The observing setup was similar for the three targets. The main observing sequence was performed in pupil-tracking mode, and the primary star behind a coronagraph with an inner working angle of 92.5 mas (Carbillet et al., 2011, van Holstein et al., 2017). The science frames were followed by center calibration frames, flux calibration frames, and sky frames, taken without the coronagraph.

We observed CHX 22 on 18 Feb 2020 with an integration time of 2s per exposure for a total of 24 exposures per half-wave-plate position. We obtained 14 full polarimetric cycles amounting to a total integration time of 44.8 min. The observations, however, were not deep enough to clearly reveal the circumstellar features. Therefore another epoch was taken on 28 Feb 2020, with an integration time of 8×8 s per half-wave-plate position, resulting in 13 polarimetric cycles during the total 55.5 min on-target time. The integration time of the flux reference frame was set to 4 s to prevent saturation. Similarly, HP Cha and S CrA were observed on 13 Jan 2020 and 8 Sep 2021, with an integration time of 64 s and 8×2 s, amounting to 14 and 42 full polarimetric cycles, and a total exposure time of 59.7 min and 44.8 min, respectively. The observations were performed under excellent weather conditions as summarized in Table 6.2.

We reduced the data using the IRDIS Data Reduction for Accurate Polarimetry pipeline (IRDAP, van Holstein et al., 2020) with the default setup. In principle, the data reduction for multiple stellar systems works similarly as for single systems. Whereas, one potential complication originates from the astrophysical stellar polarization. IRDAP removes the residual stellar polarization by directly measuring it in an annulus around the central star in the Stokes Q and U images. Yet this is not straightforward for multiple systems as the two (or multiple) components of the system may have different astrophysical polarization (for instance, due to different dust surroundings). This was indeed the case for HP Cha, where we found that the degree of linear polarization measured around the primary star ($\sim 0.27 \pm 0.1\%$) significantly differed from that around the companions ($\sim 1.6 \pm 0.2\%$). Therefore, the HP Cha data required two separate removals of stellar polarization centering on either the primary or the companions. The calibration centered on the primary revealed the circumprimary disk, while the calibration centered on the companion better preserved details of the circumsecondary disk. After subtracting the polarized stellar halos around both components individually, we combined the two versions of stokes images weighted with a linear gradient as a function of the distance to its center of calibration. This allowed us to reveal the scattered light from the circumstellar material around both components simultaneously.

6.3.2 Archival HST, VLT/NACO, and SPHERE data

In order to extract the astrometric information and to constrain the potential orbital motion of the binaries, we exploited archival observations for a large span of epochs taken with VLT/NACO (Lenzen et al., 2003, Rousset et al., 2003), VLT/SPHERE, and Hubble Space Telescope (HST). S CrA was observed with the Wide Field and Planetary Camera (WFPC2) on the HST on 21 Feb 1999 (Stapelfeldt, 1997). In addition, we inspected the archival images of S CrA taken with VLT/NACO on 29 Oct 2002, 8 Aug 2010, and 9 Jun 2012 in the H , K_S , and L band respectively, and reduced them following the standard procedure (including sky subtraction, aligning of individual exposures, and stacking) using the ESO eclipse software package and the jitter routine (Devillard, 1999). S CrA has been previously observed with VLT/SPHERE on multiple epochs. We selected the one taken on 25 Jun 2015 in the K -band for the astrometric analysis to fill in the temporal gap between the NACO observations in 2012 and our new SPHERE observations in 2021. The archival observations are summarized in Table 6.3.

For CHX 22 and HP Cha, we extracted the astrometric information from the pub-

lished literature. Both systems were observed with the 4-meter telescope at the Cerro Tololo Inter-American Observatory (CTIO) on 4 May 1994 (Ghez et al., 1997). CHX 22 was observed with VLT/NACO on 26 Mar 2006, 13 May 2007, 19 Feb 2008, and 20 Feb 2009 (Lafrenière et al., 2008, Vogt et al., 2012). HP Cha was observed with VLT/NACO on 20 Feb 2003, 25 Mar 2006, 20 Feb 2008, and 20 Feb 2009 (Correia et al., 2006, Lafrenière et al., 2008, Schmidt et al., 2013). The astrometric measurements are compiled in Table 6.4.

6.3.3 Archival ALMA data

We inspected archival ALMA observations of the three systems to obtain a better overview of the disk morphology. A brief summary of the observations is presented in Table 6.3.

CHX 22 was observed on 25 January 2016 and 30 March 2016 as part of program 2015.1.00333.S (P.I.: I. Pascucci). A non-detection of the millimeter continuum from this program was presented in Long et al. (2018). We retrieved the raw data from the ALMA archive and reprocessed it with the ALMA pipeline using the CASA software package (THE CASA TEAM et al., 2022). We imaged the CO $J = 3 - 2$ line at a velocity resolution of 0.25 km s^{-1} with the `tclean` implementation of the multi-scale CLEAN algorithm (Cornwell, 2008) and a robust value of 1.0. To handle the irregular emission pattern, we used CASA’s auto-multithresh algorithm (Kepley et al., 2020) to generate the CLEAN mask. After applying a primary beam correction to the resulting image cube, we generated a moment 0 map by summing up emission between LSRK velocities of 2.5 and 6.5 km s^{-1} , and a moment 1 map by calculating the intensity-weighted velocities.

HP Cha was observed on 21 May 2015 as part of the program 2013.1.01075.S (PI: Daemgen). The $880 \mu\text{m}$ continuum and $^{12}\text{CO } J = 3 - 2$ line were observed in Band 7. The correlator was set up with four spectral windows (SPWs). The SPW covering the CO $J = 3 - 2$ line was centered at 345.797 GHz and had a bandwidth of 468.750 MHz and channel widths of 122.07 kHz. The other three SPWs were centered at 334.016, 335.974, and 347.708 GHz, and each one had a bandwidth of 2 GHz and channel widths of 15.625 MHz. The cumulative on-source integration time was 1 minute. We directly retrieved the data product from the archive and performed no further reprocessing, as the goal is not to present detailed analyses of the ALMA observations, but to show qualitative comparisons to scattered light images.

6.4 Results

6.4.1 Polarimetric analysis

We detected polarized scattered light from the circumstellar disks around individual stars in the three systems. The total and polarized intensity images are presented in Fig. 6.1.

CHX 22

The circumstellar material forms a tail-like structure extending from the north to the southeast of the close binary. It is marginally resolved that the dust tail splits into two streams at the southern end as the scattered signal decays and merges into the noise. The dust tail extends out by $\sim 650 \text{ au}$, which is larger than the scale of binary separation by an order of magnitude. CHX 22 has also been observed in the mm wavelength with ALMA showing non-detection in the continuum (Long et al., 2018, Pascucci et al., 2016), while the extended

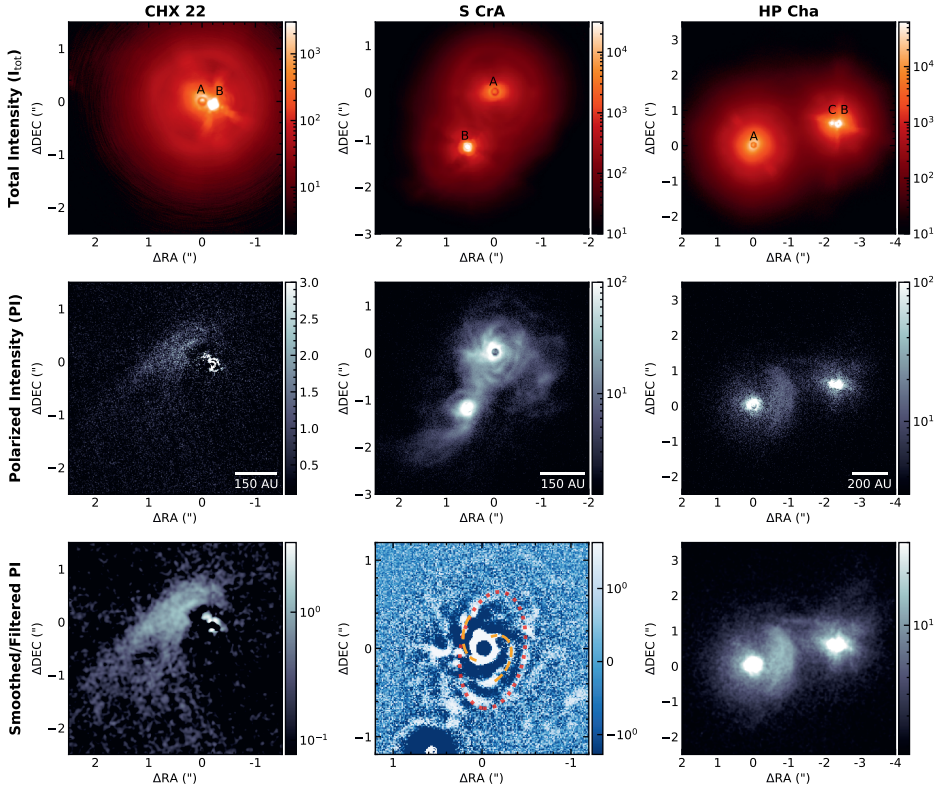


Figure 6.1: SPHERE/IRDIS images of the three multiple systems, centered on the primary stars. Each column shows one system, namely CHX 22, S CrA, and HP Cha. Top row: total intensity images. Middle row: polarized intensity images. Bottom row: processed PI images for better visualization of features. The PI image of CHX 22 is smoothed through convolution with a Gaussian kernel with a width of 2 pixels, revealing the dust tail clearly. The PI image of S CrA is high-pass filtered by subtracting the Gaussian smoothed image from the original image, to highlight the potential ring (red dotted ellipse) and spiral features (orange dashed curves). The PI image of HP Cha is also Gaussian smoothed. In the colorbars we show the scaling of the figures in arbitrary units to indicate the significance of the various detected structures. For a flux calibrated version of the polarimetric observations we refer to Appendix 6.E.

emission from CO gas was detected. The overlay of the SPHERE image and the ALMA CO emission is shown in Fig. 6.2.

S CrA

The disturbed disks with a profusion of fractured structures are present in S CrA. In the primary disk, we tentatively identified an elliptical ring (PA ~ -9.3 deg) as well as two spirals interior to that ring, as delineated in the high-pass filtered image as shown in the bottom-central panel of Fig. 6.1. The ring was determined by fitting an ellipse to the polarized intensity (PI) image of the circumpriary disk. The center of the star is offset from the center of the ellipse along the minor axis, indicating that the ringed structure has a certain

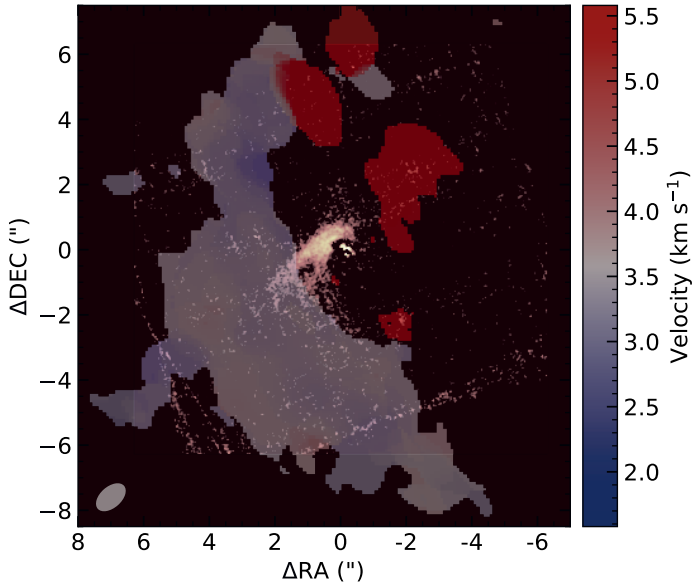


Figure 6.2: Overlay of SPHERE scattered-light image (background) and the ALMA moment 1 map of CO gas emission of CHX 22 (colormap centered on the systemic velocity of $\sim 3.6 \text{ km s}^{-1}$). The gray ellipse denotes the beam ($1.07'' \times 0.65''$) of ALMA observations.

vertical height and is inclined with respect to the line of sight by $i \sim 57$ deg. Utilizing the projected offset (u) of the ellipse-center from the star-center, we traced the height (h) of the elliptical ring via the relation $u = h \sin i$ (de Boer et al., 2016). It suggests that the disk height is ~ 23 au at the radius of ~ 107 au, meaning an aspect ratio $h/r \sim 0.21$, which is at the high end of T Tauri disks and similar to disks around IM Lup and MY Lup (Avenhaus et al., 2018). The spectral energy distribution (SED) of the system also indicates a flared disk (Sicilia-Aguilar et al., 2013).

The disk around the south-east stellar companion is connected with the material in the circumprimary disk, and features a streamer towards the south-east direction. The streamer is also marginally visible in the total intensity images of the system. We compared the HST/WFPC2 image taken in 1998 against the SPHERE/IRDIS observation in 2021, and found no obvious change in the shape over the decades, as shown in Fig. 6.7. However, we do notice the slight movement of the position angle of the companion through the offset between the peak signal and the overlaid contour.

HP Cha

The circumstellar disk around the primary is clearly detected with a flared shape as indicated by the bright rim at the west side (see the annotation in Fig. 6.3). As the Stokes Q and U patterns of the rim correspond to an illumination source located at the position of companions B and C, therefore the bright rim delineates the edge and height of the cir-

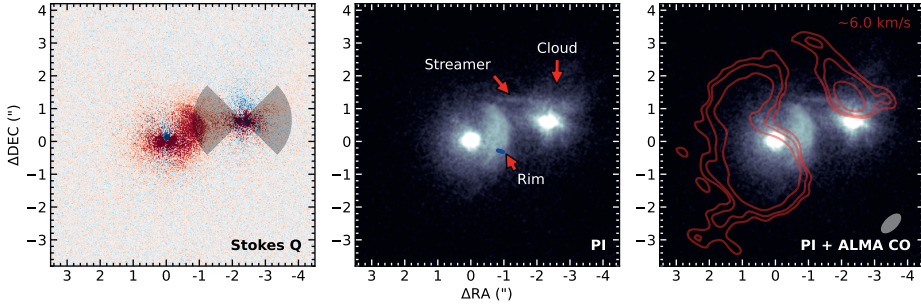


Figure 6.3: Left panel: Stokes Q image of HP Cha. The angle of linear polarization in the Stokes Q pattern of the rim corresponds to an illumination source located at the position of companions BC (as delineated by the butterfly shadow centered at companions). Central panel: smoothed PI image where we identified the rim in the circumprimary disk, the streamer connecting the circumprimary and circumsecondary disk, and the nebulous envelope surrounding the BC components. The blue bar delineates the disk height at the most extended point of the outer rim. Right panel: overlay of ALMA CO gas emission (red contour) at the radial velocity of $\sim 6.0 \text{ km s}^{-1}$. The contours delineate the flux level of $[3, 5, 10, 50]\sigma$, where σ is the standard deviation as measured in the image background. The gray ellipse denotes the beam ($0.77'' \times 0.40''$) of ALMA observations.

cumprimary disk which is illuminated by the companions from the exterior. Due to the external illumination of the primary disk by the binary companion, we can draw conclusions on the orbital geometry of the system. Since we noted a clear loss of scattered light signal in the intermediate region of the circumprimary disk (i.e. between the inner disk region and the externally illuminated rim), we conclude that the companions BC must be located slightly behind the primary star along our line of sight, such that the intermediate region of the primary disk surface is not illuminated by the companion, therefore not as bright as the outer rim. Taking advantage of this unique back-illuminated feature, we traced roughly by eye the disk height to be $h = 42 \pm 10$ au at the most extended point of the outer rim (as annotated in Fig. 6.3), which has been corrected for the disk inclination ($i \sim 37$ deg) derived from the mm-wavelength continuum observation (Francis & van der Marel, 2020). We caution that the height estimate has a large uncertainty subject to the exact position of the rim edge that one identified. We then estimated the size of the disk as seen in scattered light along the major axis to be $r \sim 260$ au by measuring the scale before the intensity drops below 3σ over the background. The flaring of the disk is therefore $h/r \sim 0.16$. The disk around HP Cha is comparable to other T Tauri disks as presented in Avenhaus et al. (2018).

The disk around the BC components is less regularly shaped, forming a nebulous structure surrounding the close binary. We marginally identify the major axis of the nebulous envelope to be east-west oriented, which coincides with the orbital plane of the close binary. The nebulous envelope around the companions is connected to the disk around the primary through a tenuous streamer as annotated in Fig. 6.3.

6.4.2 Astrometry and orbit analysis

We carried out astrometric measurements on the available observations and utilized them to constrain the orbits of the stellar companions. As our SPHERE/IRDIS main observing sequences were conducted with the primary star masked by a coronagraph (see Section 6.3.1), thus we used the flux reference frames without the coronagraph for more precise extraction of the astrometry. For the archival NACO data taken without a coronagraph (see Section 6.3.2), the stacked image in each epoch was used for the astrometric analysis.

We fit both the primary and secondary stars simultaneously using a model composed of two Gaussian profiles as implemented in the `astropy` model fitting package. The separation and position angle were then calculated from the positions of the Gaussian centers, with the astrometric calibration (including the pixel scale and the true north correction) for each instrument and epoch taken into account. The applied astrometric calibration can be found in Table 6.5. Our results together with previous astrometric measurements found in the literature are presented in Table 6.4.

With the astrometric measurements spanning across two decades, we utilized the `orbitize!` package (Blunt et al., 2020) to constrain the orbital configuration of the binary systems. We used the OFTI sampling method (Blunt et al., 2017) with 10^5 runs. The parallax and the prior system mass involved in the orbit fitting were adopted from Table 6.1. The orbital motion together with OFTI solutions, and the resulting posterior distributions of semi-major axis, inclination, and eccentricity for each individual system are shown in Fig. 6.4 and 6.5.

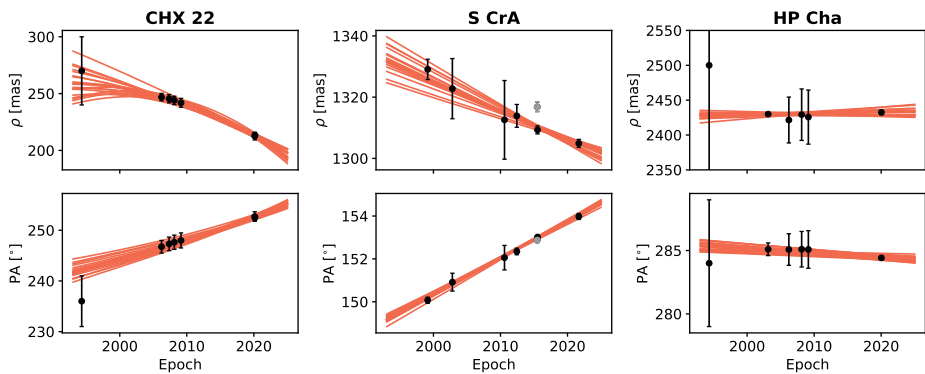


Figure 6.4: Separation (first row) and position angle (second row) of the companions relative to the primaries in CHX 22, S CrA, and HP Cha versus time. The astrometric data were summarized in Table 6.4. The red lines represent twenty randomly selected OFTI orbital solutions. The gray astrometric data points in S CrA were excluded from the orbital fitting as explained in Table 6.4

CHX 22

As shown in Fig. 6.5, the resulting posterior distributions suggest two groups of solutions for the eccentricity, one clustering around 0.4, and the other higher than 0.8. However the `orbitize!` tool is not well suited for eccentricities close to 1, and we suspect the

accumulation of solutions towards the upper edge of the prior to be artificial. In order to better explore this issue, we fit the astrometry with another MCMC-based code developed by Beust et al. (2016), that makes use of universal Keplerian variables instead of classical ones (Danby, 1987), and thus can naturally handle highly eccentric as well as unbound orbits with $e \geq 1$ in a continuous manner. The posterior distributions are shown in Fig. 6.12. Now without the prior limitation $e < 1$, the peak close to $e \sim 1$ has disappeared, while the one at $e \sim 0.4$ persists. The consistent peaks around $e \sim 0.4$ with both codes suggests that the bound solutions with intermediate eccentricities are favored. Moreover, it is not surprising to find some solutions with unbound orbits due to the paucity of astrometric data and the small coverage of the orbit. However the fact that we note a sharp drop at $e = 1$ in the posterior distribution of the eccentricity is a strong indication in favor of a bound orbit.

S CrA

The orbital separation and position angle of S CrA show clear and steady motion over the baseline of two decades (see Fig. 6.4). The orbital solutions favor a small inclination $i = 25 \pm 12$ deg and a moderate eccentricity $e = 0.4_{-0.1}^{+0.2}$ as shown in Fig. 6.5. The constraint on the system mass suggests a total mass of $\sim 2M_{\odot}$, which agrees with the estimation by Gahm et al. (2018).

HP Cha

The astrometric measurements of the BC component with respect to the primary barely show any orbital motion beyond the uncertainties because of the large separation (see Fig. 6.4). Therefore, the orbital configuration around the primary is not well-constrained. However, the relative motion between B and C is apparent, suggesting a highly eccentric ($e \sim 0.9$) and a nearly edge-on ($i \sim 100^{\circ}$) orbit for the binary BC (see Fig. 6.6).

Table 6.4: Astrometry of the targeted multiple-star systems as extracted from our SPHERE/IRDIS observations as well as archival data taken with SPHERE, NACO, and HST.

Object	Epoch (MJD)	Sep (mas)	PA (deg)	Ref.
CHX 22	49470	270 ± 30	236 ± 5	2
	53820.36777	246.9 ± 3.3	246.743 ± 1.245	2
	54233.98285	245.5 ± 3.6	247.312 ± 1.338	2
	54515.19528	244.0 ± 3.7	247.635 ± 1.401	2
	54882.37337	241.9 ± 3.9	247.991 ± 1.483	2
	58898.24507	212.6 ± 3.4	252.706 ± 0.944	1
	58908.16592	213.4 ± 2.0	252.506 ± 0.559	1
S CrA	51230.96126	1329.1 ± 3.3	150.071 ± 0.142	1
	52576.05926	1322.8 ± 9.8	150.915 ± 0.417	1
	55416.21256	1312.6 ± 12.8	152.057 ± 0.571	1
	56087.38416	1313.9 ± 3.7	152.347 ± 0.155	1
	57198.31135	1316.8 ± 1.5	152.877 ± 0.112	1 [†]
	57215.40732	1309.3 ± 1.3	153.021 ± 0.059	4
	59466.04295	1304.9 ± 1.3	153.979 ± 0.140	1
HP Cha A(BC)	49476	2500 ± 500	284 ± 5	3
	52690.20849	2430 ± 2	285.1 ± 0.5	3
	53819.41198	2421.5 ± 32.9	285.077 ± 1.244	3
	54516.39621	2429.2 ± 36.9	285.103 ± 1.401	3
	54882.40637	2425.7 ± 38.8	285.084 ± 1.482	3
	58861.32325	2432.5 ± 3.3	284.417 ± 0.156	1
HP Cha B(C)	53819.41198	70.2 ± 10.9	94.834 ± 2.801	3
	54882.40637	98.4 ± 1.6	87.322 ± 1.497	3
	58861.32325	179.2 ± 4.4	83.841 ± 1.374	1

[†] This epoch was excluded from the orbit fitting as it showed significant deviation from the well-constrained orbital motion (see Fig. 6.4). This is likely attributed to the inaccurate calibration of the pixel scale for SPHERE observations at the K_S -band.

¹ this work,

² Vogt et al. (2012),

³ Schmidt et al. (2013),

³ Sullivan et al. (2019).

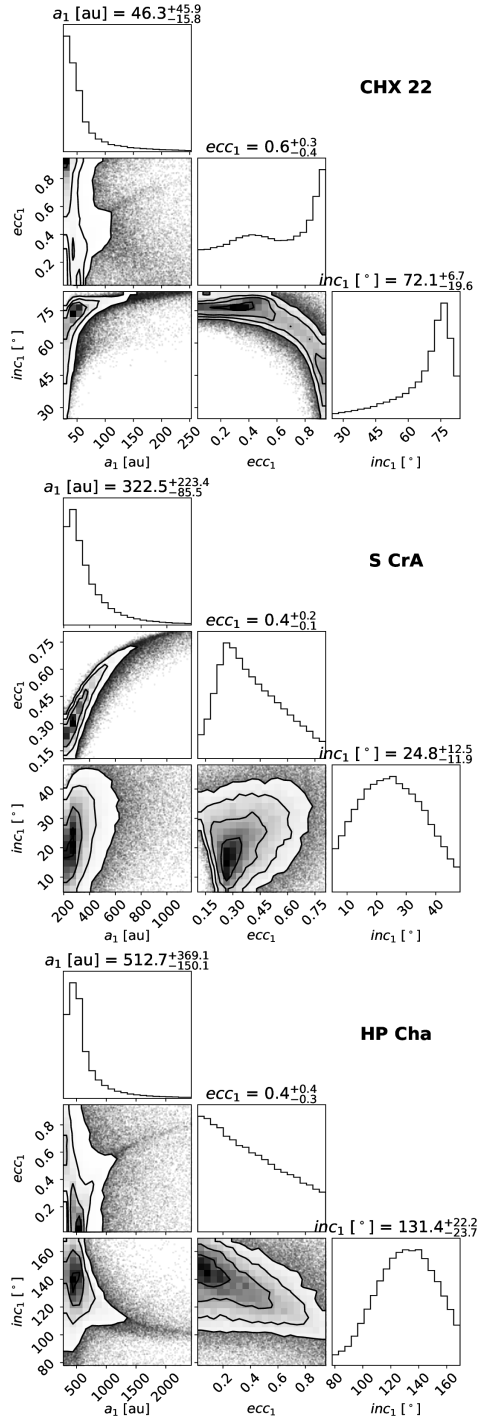


Figure 6.5: Posterior distributions of semi-major axis a_1 , inclination inc_1 , and eccentricity ecc_1 for the orbits of companions in CHX 22, S CrA, and HP Cha.

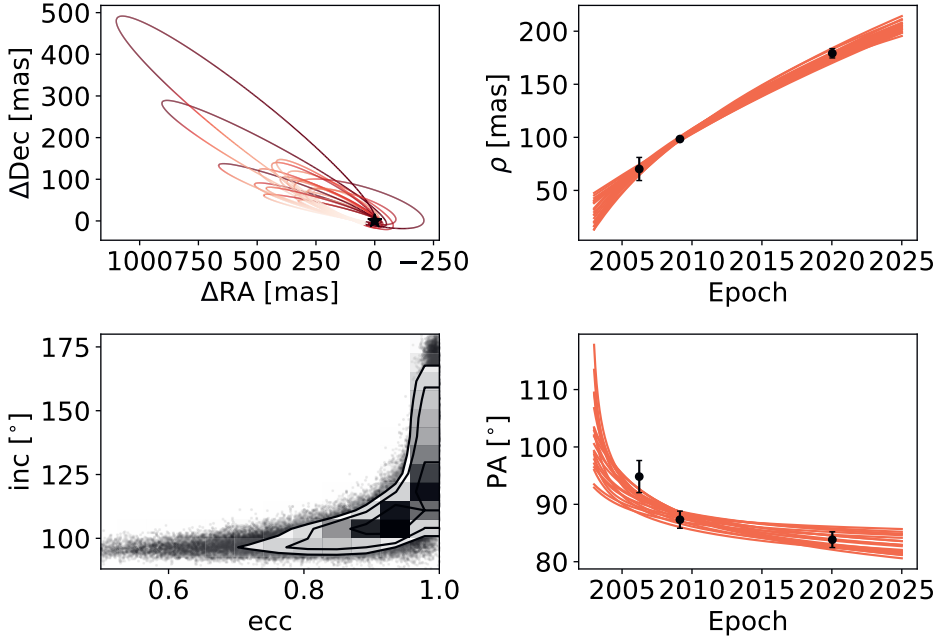


Figure 6.6: Orbital constraints of the binary HP Cha BC. Top left, top right, and bottom right panel: the orbital motion in RA-Dec space, the change of separation, and position angle with time. The red lines represent twenty randomly selected OFTI solutions. Bottom left panel: the posterior distribution of inclination versus eccentricity.

Table 6.5: Calibration applied in our astrometric analysis.

Epoch	Instrument	Filter	Pixel scale (mas pixel ⁻¹)	True north correction (deg)	Ref.
2002-10-29	VLT/NACO	<i>H</i>	27.01 ± 0.05	0.08 ± 0.18	1
2010-08-08	VLT/NACO	<i>K_S</i>	13.231 ± 0.020	0.67 ± 0.13	2
2012-06-09	VLT/NACO	<i>L</i>	27.193 ± 0.059	0.568 ± 0.115	3
2015-06-25	VLT/SPHERE	<i>K_S</i>	12.267 ± 0.009	-1.75 ± 0.10	4

¹ Chauvin et al. (2010),

² Ginski et al. (2014),

³ Maire et al. (2016),

³ Launhardt et al. (2020).

6.5 Discussion

6.5.1 Individual systems

CHX 22

The scale of the observed dust tail is drastically different from the scale of the inner binary system. It therefore raises the question of whether the dust is the tidal tail thrown out from the original circumstellar disk due to the interaction with the stellar companion, or if it is exterior material flowing into the binary system. Given the tail-like structure, system age, and orbital configuration, we discuss the following possible scenarios, 1) stellar flyby, 2) periodic perturbation, and 3) cloud capture.

The first scenario refers to the case that the companion is in an unbound or extremely eccentric orbit. The circumstellar disk around the primary was tidally stripped during the parabolic or hyperbolic flyby event. For instance, simulations of prograde stellar flybys could result in tail-shaped structures for the ejected circumprimary material (Clarke & Pringle, 1993, Vorobyov et al., 2020), resembling the observations of CHX 22. Similar dust tails have been observed in young systems such as Z CMa (Dong et al., 2022, Liu et al., 2016), and are proposed to be induced by stellar flybys. Assuming a typical open-orbit solution like shown in Fig. 6.12, we estimated that the temporal window of such a close encounter ($<0.24''$) is only around 50 years, in contrast to the age of the system (~ 5 Myr). The probability of capturing such a moment in time is rather small. Moreover, as we also noted in Section 6.4.2 that the binary orbit probably has an intermediate eccentricity, therefore we argue that the stellar flyby scenario is unlikely. This leads to the second scenario that the close companion with an eccentric orbital motion may periodically strip away the disk material as it passes through the pericenter (~ 50 au, see Fig. 6.12). Again, given the age estimation of CHX 22, it is less plausible that the relics of the continuously periodic interaction remain observable after such a long time. However, we acknowledge that the age derived from isochrones has large systematic uncertainties, hence we cannot rule out a younger age for the system. Nevertheless, this does not change the outcome that the primordial disk has likely gone, as suggested by the non-detection of the dust continuum emission (Long et al., 2018, Pascucci et al., 2016). A stringent dust mass upper limit of $\sim 0.2M_{\oplus}$ was put, suggesting a deficit of large grains in the system. This adds to the implication that the circumprimary disk has already dispersed due to photoevaporation and/or been significantly truncated by the close companion (Long et al., 2018). It is intriguing that small grains still persist across an extensive scale.

Both the above scenarios suppose that the dust tail is the outcome of the disk-binary interaction. Alternatively, we suggest that the circumstellar dust tail may be the infalling material from an encounter with nearby molecular clouds. The shape of the circumstellar material bending towards the stars remarkably matches the arc-shaped envelopes as simulated in Dullemond et al. (2019). Such arc shapes have been observed in other systems including AB Aur (Grady et al., 1999), HD 100546 (Ardila et al., 2007), SU Aur (Akiyama et al., 2019, Ginski et al., 2021a), FU Ori (Liu et al., 2016, Takami et al., 2018), and DR Tau (Mesa et al., 2022). According to the column density map of the Chamaeleon molecular cloud complex as observed with the Herschel space telescope (Alves de Oliveira et al., 2014), CHX 22 resides in a moderately dust-rich region, therefore possibly undergoing such encounter with clouds. In ALMA CO emission of CHX 22 as shown in Fig. 6.2, we

found large-scale gas emission associated to CHX 22. The gas emission shares similar velocities as the systemic velocity of CHX 22 ($\sim 3.6 \text{ km s}^{-1}$). It forms a streamer-like structure from roughly North to South-West, confirming the presence of remnant cloud material in the direct vicinity of CHX 22.

S CrA

The disk structure of S CrA is full of intriguing details. In Section 6.4.1, we identified potential ring and spiral features in the circumprimary disk. Here we attempt to assess the plausibility and discuss the implications provided that the features are real. As discussed in Section 6.4.1, the geometric center of the ring feature is offset from the stellar position along its minor axis, with the east side (left-hand side) of the ring closer to the stellar position. This not only implies a certain vertical height of the disk at the separation of the ring but also that the east side of the ring is the near side of the disk, namely, the side of the disk that is tilted toward the observer. It makes sense intuitively that the east side (i.e. the near side) of the ring indeed shows higher brightness than the far side because of the stronger forward scattering. In order to quantify the brightness contrast due to the scattering phase functions, we measured the intensity within a small aperture (5 pixels) at both the near side and the far side of the ring, and compare the contrast ratio to that of several other disks with similar inclinations, such as HD 34282 (de Boer et al., 2021), LkCa15 (Thalmann et al., 2016, 2014), IM Lup (Avenhaus et al., 2018), and PDS 70 (Hashimoto et al., 2012, Keppler et al., 2018). The contrast ratio in S CrA is ~ 1.3 , lower than that of ~ 7 in HD 34282 and IM Lup, while similar to that of 1.6 in LkCa15 and 2.8 in PDS 70. Given the large scatter in different disks, it is inconclusive based on this argument whether the ellipse-like structure that we identified in S CrA corresponds to a ring in the disk or not. However, while the brightness contrast between forward and back scattering is on the low end of disk observations, we note that indeed the side that should be forward scattering in this tentative ring (the east side) is the brighter side, as expected from dust scattering phase functions. Combined with the offset along the minor axis, as expected from the viewing geometry of a ring in a flared disk surface, this gives a reasonable indication that we trace a ring in the disk around the primary component.

In addition, the two spiral structures also seem inclined, because the southern spiral appears foreshortened as launched from the nearside compared to the northern spiral. This appears similar to the simulated images of spiral features seen at such viewing angles as presented in Dong et al. (2016). We performed deprojection of the PI image assuming a disk inclination of 57 deg (as inferred from the elliptical ring in Section 6.4.1) and a flaring index of 1.2 (a typical value as found in Avenhaus et al. (2018)) using the python package `diskmap` (Stolker et al., 2016). The deprojected image is presented in Fig. 6.8, where we estimated the pitch angle of the two spiral arms to be ~ 30 deg. We caution that the pitch angle could change subject to the assumed disk parameters such as the actual inclination of the features. However, the uncertainty due to this inclination effect is marginal since the launching areas of the spirals are close to the major axis of the disk. Hydrodynamical simulations suggest that the pitch angle of spiral arms and the azimuthal separation between two arms positively correlate with the mass of the companion (Fung & Dong, 2015, Zhu et al., 2015). The pitch angle of ~ 30 deg and the nearly 180-degree separation between both arms are therefore consistent with the scenario that the spirals

are launched by the perturbation from the stellar companion (Fung & Dong, 2015), as in the case of HD 100453 (Benisty et al., 2017).

If the inclined ring is real, it cannot be explained by the perturbation from the outer stellar companion. Instead, other mechanisms such as a second perturber are needed to induce the ringed structure (Bae et al., 2022). With our SPHERE observations reduced with the angular differential imaging (ADI) technique, we can rule out the presence of companions more massive than $8\text{--}10 M_{\text{Jup}}$ in between the A and B components, and $\sim 3\text{--}5 M_{\text{Jup}}$ beyond 300 au (see Sec 6.B). Whereas, this can be complicated by the fact that the companion may still be embedded in the disk at the young age of ~ 1 Myr, which will significantly relax the mass limit. Therefore, further high-contrast imaging studies to search for planets in the system are interesting.

Through our orbit analysis of the S CrA binary (see Section 6.4.2), we found the orbital plane is likely close to face-on with an inclination of 25 ± 12 deg. This value is consistent with the inner disk inclination for both stellar components, 28 ± 3 deg and 22 ± 6 deg respectively (GRAVITY Collaboration et al., 2017). This is, however, in tension with the inclination (~ 53 deg) of the tentative ring and spiral features as seen in our SPHERE observations. Interestingly, the spectroscopic analyses by Gahm et al. (2018) found the inclinations of the stars to be ~ 60 deg, similar to that of the outer disk observed in the scattered light but misaligned with the inner disk observed in the NIR-interferometry. The dust continuum emission from outer disks around both stars was observed with ALMA but unresolved (Cazzoletti et al., 2019), therefore providing no information on the disk inclination. The ALMA ^{12}CO and ^{13}CO emission is dominated by the signal from the extensive envelope, showing intricate kinematic patterns with streamers and outflows. Deeper observations via optically thin tracers such as C^{18}O are required to probe the embedded disks. A detailed analysis of the gas emission can be found in the work by Gupta et al. (submitted). In addition, searching for shock tracers such as SO and SO_2 (Booth et al., 2018, Garufi et al., 2022, Tafalla et al., 2010) may be interesting as the streamer across the stellar companion appears to connect onto east side of the primary disk. Alternatively, future long-baseline ALMA observations resolving the outer disk in S CrA and determining the disk inclination will help unravel the whole picture.

If the spin-orbit misalignment is real, which is not uncommon in wide binary systems (Hale, 1994, Justesen & Albrecht, 2020), the circumstellar disks were initially aligned with the stellar rotation axis as the material collapsed around each star, and later got aligned with the orbital plane as a result of the gravitational torque by the companion (Lubow & Ogilvie, 2000). The misalignment of individual circumstellar disks with the binary orbital plane seems not so surprising (e.g., Brinch et al., 2016, Fernández-López et al., 2017, Jensen & Akeson, 2014, Manara et al., 2019, Rota et al., 2022, Williams et al., 2014). Theoretical studies by Foucart & Lai (2014) suggest that the large disk-orbit misalignment could be maintained over the entire disk lifetime. Therefore, circumstellar disks in wide binaries are not necessarily coplanar with the binary orbit despite the tendency towards alignment (Jensen, 2020).

The appearance of the disk in S CrA is reminiscent of GW Ori with misaligned rings as disturbed by gravitational interactions in the multiple star system (Kraus et al., 2020). In GW Ori, the ringed structures are attributed to the tearing caused by the misaligned orbital plane with the disk. Likewise, the stellar companion in S CrA may also play an im-

portant role in warping the circumprimary disk. Dedicated hydrodynamic simulations of the system will be essential for understanding the delicate substructures and the influence of the binary-disk interaction.

HP Cha

The circumprimary disk around HP Cha appears to be a transition disk with a single ring in the mm dust continuum (Francis & van der Marel, 2020, Long et al., 2018), while no dust continuum emission was detected around the BC components. We inspected the archival CO emission data observed with ALMA and found gaseous material around both the primary and the secondary components, as also revealed in our scattered light image. In Fig. 6.3, we overlaid the average image of four frequency channels from 345.7894 GHz to 345.7887 GHz, corresponding to the radial velocity of 5.72–6.32 km s⁻¹. The maps of more channels can be found in Fig. 6.13. The gas emission also delineates a streamer connecting the primary and companions, while it extends further north and appears more curved than the streamer observed in scatter light. The slight offset may be because only the bottom side of the streamer structure is illuminated by the companions which are located behind the primary star along our line of sight. Since the systemic velocity of HP Cha is ~ 3.8 km s⁻¹, therefore the gas emission shown in Fig. 6.3 is red-shifted with respect to the systemic velocity, meaning the material in the streamer flowing from the circumprimary disk to the secondary binary (combined with our previous constraint from the scattered light that the binary is spatially located behind the primary). The feeding flow from the primary disk may be responsible for the disturbed, nebulous envelope around the BC components. In addition, the extremely eccentric orbit of the close binary likely contributed to stirring up the material. On the other hand, the circumprimary disk maintains a regular shape, indicating that the interaction is not as violent as in the case of S CrA.

6.5.2 Binary-disk interactions and planet formation

Following the sequence from CHX 22 to S CrA and HP Cha, we note that as the binary separation increases, the binary-disk interaction is less violent and destructive. The primitive disk in the close binary CHX 22 ($a < 50$ au) has likely been truncated significantly and has dissipated via internal photoevaporation as there is no evidence for millimeter continuum and little NIR excess (see the discussion in Long et al., 2018).

S CrA may be undergoing a similar truncating process that the circumprimary disk is losing material through the streamer connected via the companion. However, as the binary separation in S CrA ($a \sim 300$ au) is much larger than that in CHX 22, substantial material may still remain for a longer timescale. The companion truncates the circumprimary disk in a few orbital timescales (~ 5000 yr) as a result of Lindblad resonances (Artymowicz & Lubow, 1994). We roughly estimated the expected disk size based on the analytical models by Artymowicz & Lubow (1994) and Manara et al. (2019). Adopting the system parameters including equal stellar masses, $a \sim 320$ au, and $e \sim 0.4$, as derived from our orbital analysis in Section 6.4.2, the outer edge of the primary disk would be truncated at around $0.16a - 0.21a$ (50 – 70 au) depending on the disk viscosity. As the current disk size is well above 100 au, the truncation is likely ongoing, and the material streams towards the circumsecondary disk, which can either end up around the companion or get stripped away through the south-east tail.

The mass transfer from the circumprimary disk to the companion is also observed in HP Cha, with a more tenuous streamer than the one in S CrA. The turbulent scene in S CrA is plausibly attributed to the moderate orbital eccentricity ~ 0.4 . The larger separation of the HP Cha BC components to the primary ($a \sim 500$ au) may also contribute, such that the secular timescale as a result of disk truncation is different from that of S CrA. The analytic prediction of the tidally truncated disk size for HP Cha is pending due to the unconstrained orbital configuration. A conservative estimation implies a truncated circumprimary disk size of $0.35a \sim 175$ au, which is smaller than the extent of the disk as observed in scattered light (~ 260 au). The tidal truncation likely takes effects on shaping the primary disk as we note the sharp drop-off of flux at the edge of the rim (Fig. 6.3). Nevertheless, the circumprimary disk evolution in HP Cha is probably not significantly altered by the stellar companions in contrast to S CrA.

This decreasing influence on circumprimary disk evolution at larger binary separations agrees well with the statistics from millimeter-wavelength studies. Surveys of protoplanetary disks in star-forming regions with ALMA have found that dust disks in multiple systems with separations less than 200 au tend to be more compact and less massive than the counterparts around single stars, while the influence is marginal in wide binary systems (Akeson et al., 2019, Cox et al., 2017, Manara et al., 2019). The sizes of gas disks in multiple systems are consistent with predictions from tidal truncation by companions (Rota et al., 2022). Studies by Rosotti & Clarke (2018), Zagaria et al. (2021a,b) suggested that disks perturbed by close companions undergo faster gas and dust evolution than those around single stars. Therefore the disk lifetime may not be long enough to form planets in close binaries.

As a consequence of the various extents of binary-disk interactions, the planet formation in stellar multiple systems likely has diverse outcomes. The formation and survival of planets in close binaries are expectedly rare, subject to the tidal truncation of disks and the later excitation of high eccentricities. Although there are systems like CHX 22 with late-stage infall that may potentially form secondary circumbinary disks, they are probably far from massive enough for efficient planet formation. The stellar multiplicity rate of planet-hosting stars is suggested to be lower than field stars for close companion separations (< 50 au), providing evidence of suppressed planet formation in systems with close-in companions (Kraus et al., 2016, Wang et al., 2014a,b). The statistics are consistent with the expectation from disk observations.

For binary systems with wide separations, the opportunity for planet formation is not significantly undermined. Statistical analyses tend to find no evidence for distinguishable planet occurrence or distribution of planet properties between single and binary systems (Bonavita & Desidera, 2007, Horch et al., 2014, Ngo et al., 2017). This agrees well with our observations of non-disturbed circumprimary disks, for instance, HP Cha, where the planet formation is expected to be not different from that around single stars. On the other hand, there is growing evidence that giant planet formation may be boosted in wide binaries (Fontanive et al., 2019, Ngo et al., 2016). Studies on planetesimal dynamics in highly inclined ($i > 30$ deg) binary systems suggest that despite the truncation of disks, the planetesimals could pile up within the stability radius to allow for planet formation (Batygin et al., 2011, Xie et al., 2011). Moreover, the presence of stellar companions or planets may induce substructures that assist to concentrate dust particles, resulting in efficient

streaming instability and formation of planetary embryos (Baehr et al., 2022, Johansen & Youdin, 2007). We argue that the formation of a planetary object in such a disturbed disk is indeed likely given the ring-like feature we identified in S CrA which may be caused by an unseen embedded object. The stellar companion could also play an important role in the dynamical evolution of planetary embryos after the dispersion of the gas disk. The further growth of embryos to terrestrial planets could be enhanced in binary systems with intermediate separation (Zhang et al., 2018). Consequently, planet formation may even be enhanced in favorable circumstances. Future observations of newborn planets in binary systems such as S CrA and HP Cha will provide insights into the processes.

6.6 Conclusion

We presented the detection of circumstellar dust in three multiple systems, CHX 22, S CrA, and HP Cha, using polarimetric differential imaging with SPHERE/IRDIS. Combining the disk morphology with constraints on the age and binary orbits, we unraveled the evolution history and the impact of the stellar companions on the disks.

- The dust in CHX 22 forms an extended tail-like structure surrounding the close binary. Considering the likely bound orbit of the companion and the age of the system, we suggest that the dust tail may be secondary material resulting from a late-stage cloud capture event, instead of being relics from the stellar flyby or tidal truncation. The primordial disk in the binary has probably dispersed or been significantly truncated via the interaction with the close companion.
- The violent interaction between disk and binary is well captured in S CrA showing intricate disk structures as a consequence of perturbations by the companion with a moderately eccentric orbit. We presented evidence for a ring and spiral features in the disk. While the spirals are consistent with perturbations from the known stellar companion, the ring-like feature would require other mechanisms such as a second (lower mass) perturber in the system. The circumssecondary disk is truncating the primary disk, and material is transferred via a streamer connecting both disks.
- In contrast, HP Cha with a larger binary separation shows a less fierce interaction. We detected a regularly shaped disk around the primary with a tenuous streamer feeding material towards the nebulous disk around the companions.

The comparison of the three systems (spanning a wide range of binary separation from 50 to 500 au) illustrates the decreasing influence on disk structure and evolution with the distance of companions. It implies that planet formation in disks is likely obstructed around close binary systems, while barely undermined in wide binaries, which agrees with the statistical analyses of disk census and exoplanet population in binaries.

6.A Morphology of disks in S CrA

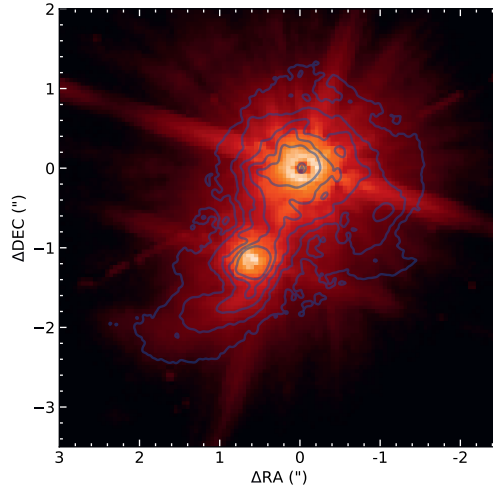


Figure 6.7: HST observations of S CrA. The blue contour delineates the flux level of $[5, 10, 20, 40, 80]\sigma$ in the SPHERE PI image, where σ is the standard deviation as measured in the image background.

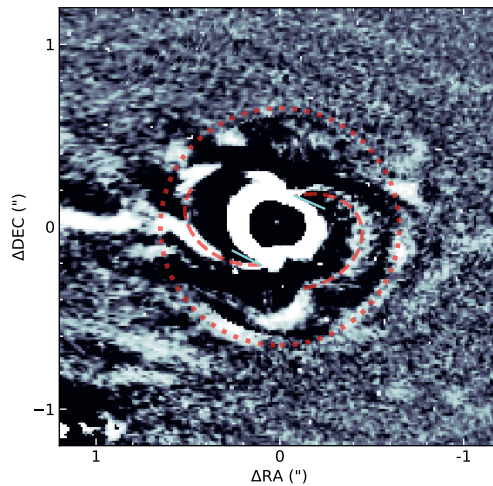


Figure 6.8: Deprojected PI image of S CrA assuming a disk inclination of 57 deg. The ring and spirals are delineated in red dashed lines. The pitch angle of spirals is estimated to be ~ 30 deg.

6.B SPHERE ADI imaging of the system S CrA

We performed a data reduction for the ADI images of the system around S CrA. To process the data we used a custom routine to perform background subtraction, flat-fielding, centering of the images, and the VIP code (Gomez Gonzalez et al., 2017) to perform the principal component analysis (PCA) to get the final images and contrast. The 5σ contrast was calculated with the VIP code as the $\sigma \times \text{noise}$ of the ADI image divided for the throughput. The calculation takes into account the small sample statistics correction presented in Mawet et al. (2014).

In the final processed image the stellar binary companion is clearly visible in the FoV, very saturated in the images. Also, three very likely background companion candidates (cc) are visible in the FoV (see Fig. 6.9). We report in Table 6.6 their coordinates. To calculate the astrometry we applied the same routines presented in Zurlo et al. (2021, 2020). Further high-contrast imaging follow-up of the system will confirm the nature of the stars identified.

To calculate the mass limits for putative sub-stellar companions in the system, we used the contrast curves calculated for the PCA image, shown in Fig. 6.10 and used the COND evolutionary models for substellar companions as presented in Baraffe et al. (2003, 2015). The age for the system used in the analysis is 1 Myr.

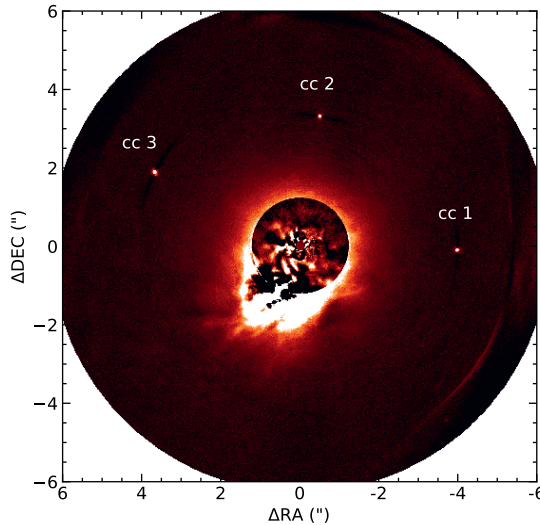


Figure 6.9: PCA image of S CrA with two principal components subtracted.

Table 6.6: Astrometric positions for the 3 (putative background) companion candidates identified in the ADI images.

Object	ΔRA (mas)	ΔDec (mas)
cc 1	-4010 ± 5	-172 ± 5
cc 2	-544 ± 5	3232 ± 5
cc 3	3632 ± 5	1829 ± 5

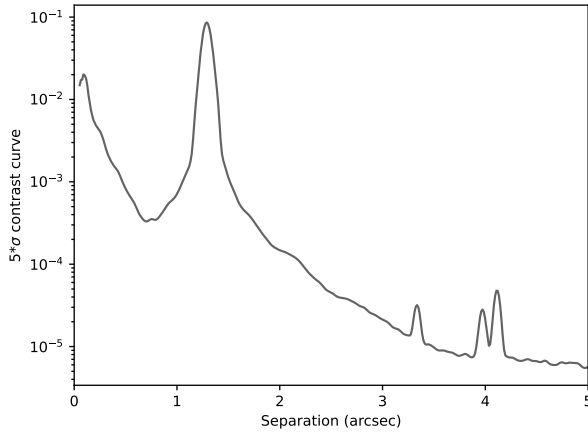


Figure 6.10: Contrast curve at 5σ -level for the ADI image of the system S CrA.

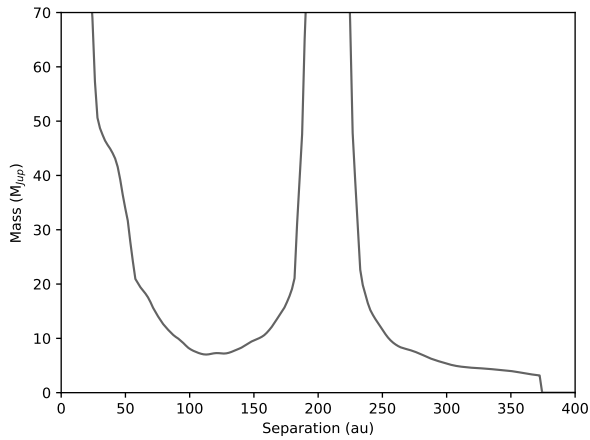


Figure 6.11: Mass limits for companions around the star S CrA, calculated from the contrast curve in Fig. 6.10.

6.C Orbit fitting for CHX 22 with the possibility of unbound orbits

We present in Fig. 6.12 the orbital fitting results for CHX 22 using the universal Keplerian variable code by Beust et al. (2016). This code allows for assessing unbound orbits in contrast to the analysis shown in 6.4.2.

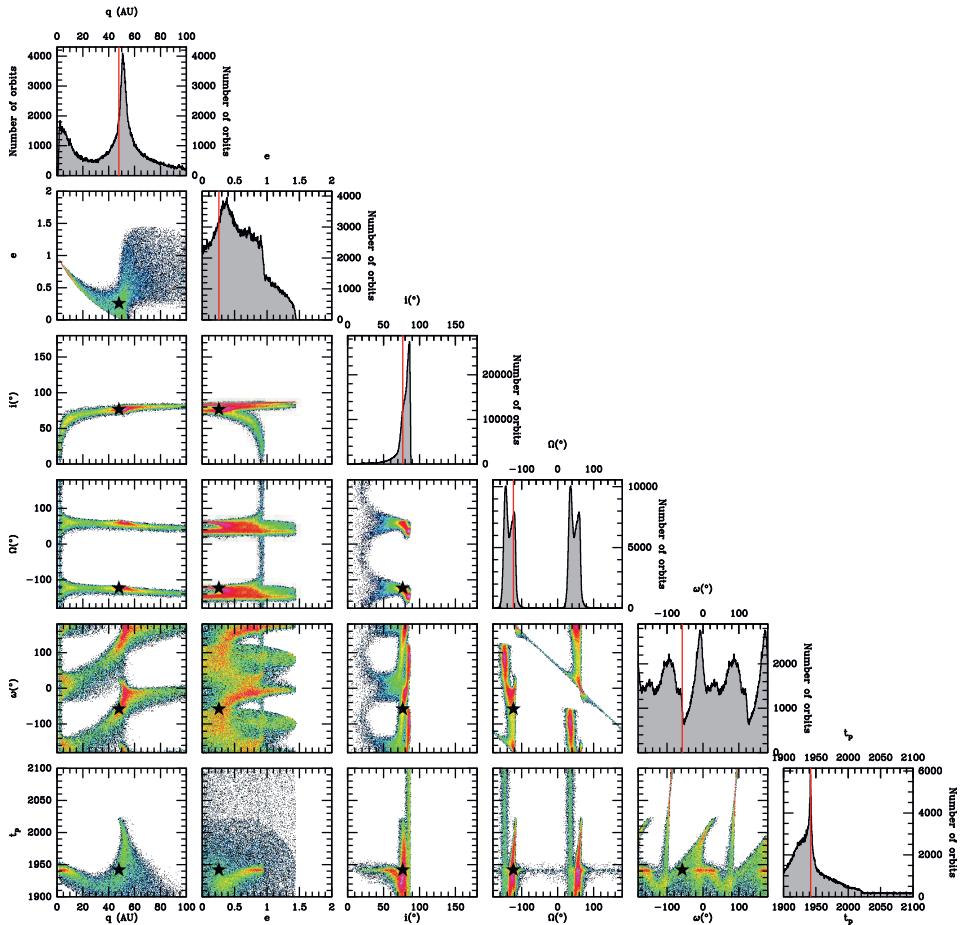


Figure 6.12: Posterior distributions of orbital elements of the close companion in CHX 22 using the universal Keplerian variable code by Beust et al. (2016), with the possibility of unbound orbits ($e > 1$). In all plots, the red bars (for histograms) and the black stars (in correlation maps) stand for the best- χ^2 solution of the posterior distribution. For compatibility with unbound solutions, the first variable fitted is the periastron q instead of the semi-major axis a . The 180° periodicity of distributions of the longitude of ascending node (Ω) and the argument of periastron (ω) is a degeneracy inherent to the astrometric fit with no radial velocity data.

6.D SPHERE and ALMA data overlay

We present in Fig. 6.13 the overlay of the scattered-light image and channel maps of ALMA CO emission for HP Cha. The streamer feature seen in scattered light can also be recognized in the gas emission in redshifted channels.

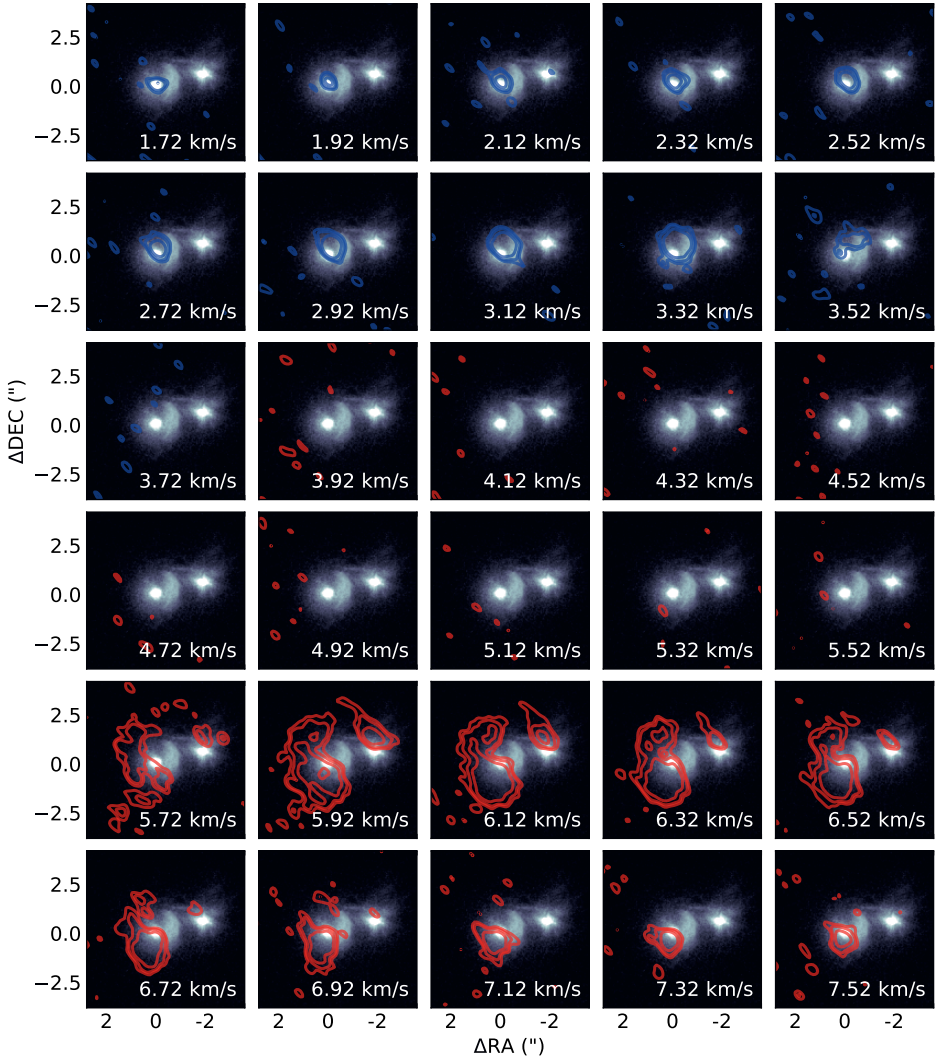


Figure 6.13: SPHERE PI image of HP Cha with the ALMA CO $J = 3 - 2$ channel maps as contours. The contours delineate the flux level of $[3, 5, 10, 50]\sigma$, where σ is the standard deviation as measured in the image background. The contours of channels redshifted relative to the systemic velocity ($\sim 3.8 \text{ km s}^{-1}$) are shown in red, and blueshifted channels are shown in blue.

6.E Coronagraphic images of CHX 22, S CrA, and HP Cha

We present the Stokes Q , U , Q_ϕ , and U_ϕ polarized flux images obtained from SPHERE/IRDIS observations of the three multiple systems in Fig. 6.14, 6.15, and 6.16.

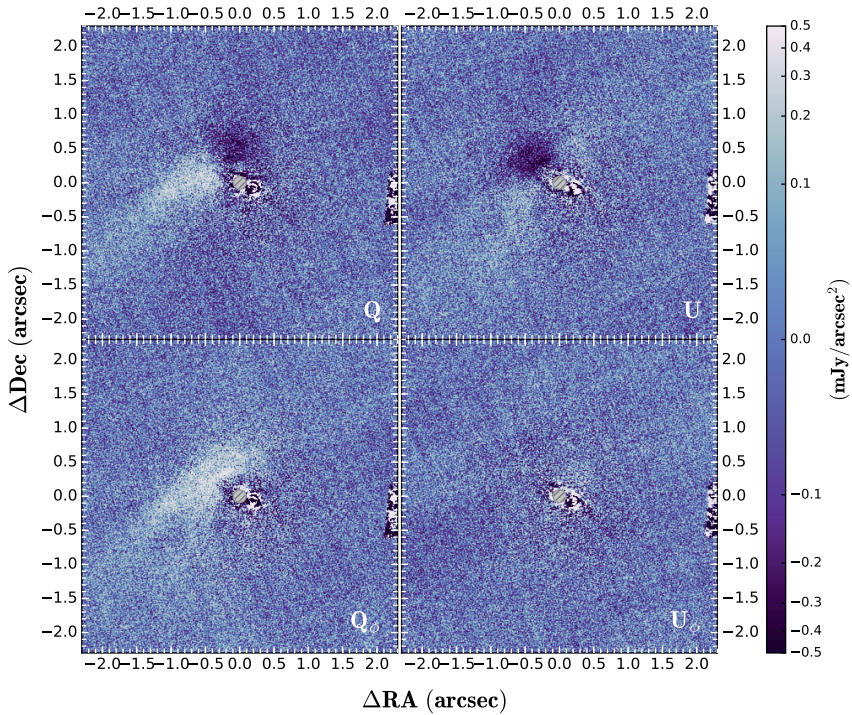


Figure 6.14: Stokes Q , U , Q_ϕ , and U_ϕ polarized flux images of CHX 22 derived from SPHERE/IRDIS observations. The size of the coronagraphic mask is indicated with the grey, hashed circle.

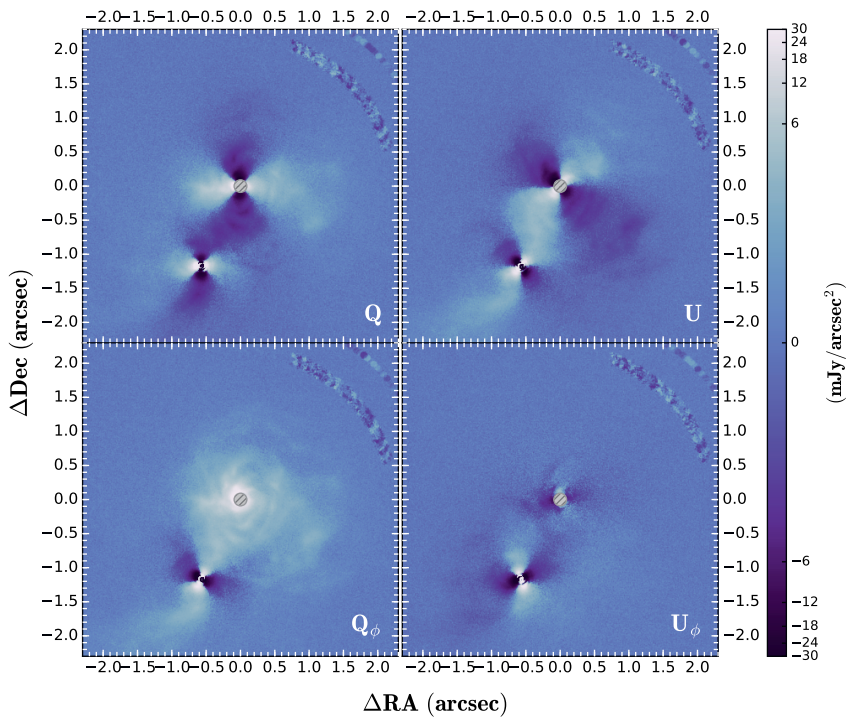


Figure 6.15: Similar as Fig. 6.14, but for S CrA.

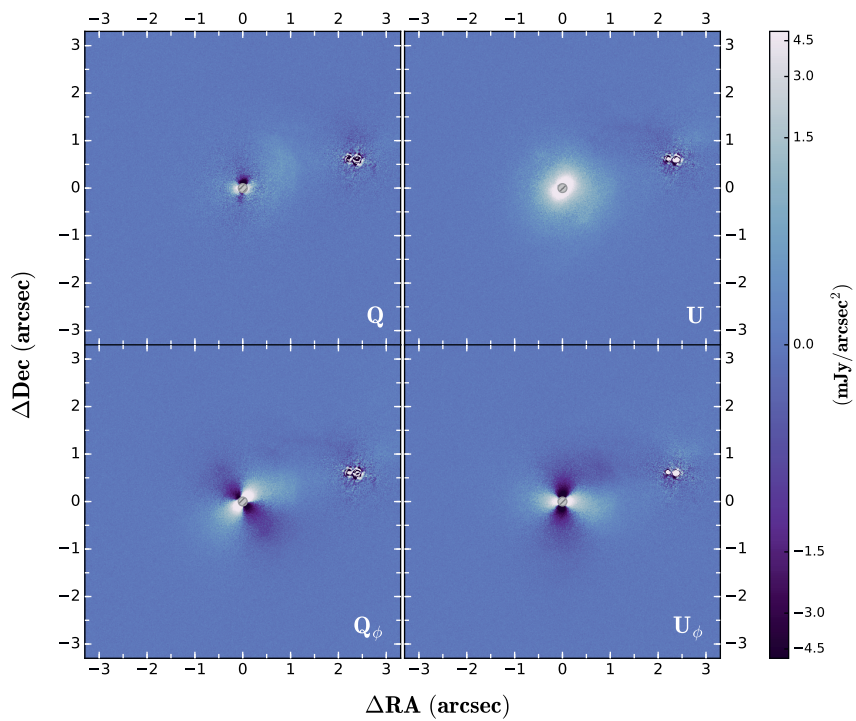


Figure 6.16: Similar as Fig. 6.14, but for HP Cha.

Bibliography

- Acharyya, K., Fuchs, G. W., Fraser, H. J., van Dishoeck, E. F., & Linnartz, H. 2007, *A&A*, 466, 1005
- Ackerman, A. S. & Marley, M. S. 2001, *ApJ*, 556, 872
- Ahlers, J. P., Kruse, E., Colón, K. D., et al. 2020, *ApJ*, 888, 63
- Akeson, R. L., Jensen, E. L. N., Carpenter, J., et al. 2019, *ApJ*, 872, 158
- Akiyama, E., Vorobyov, E. I., Liu, H. B., et al. 2019, *AJ*, 157, 165
- Allan, A. & Vidotto, A. A. 2019, *MNRAS*, 490, 3760
- Allart, R., Bourrier, V., Lovis, C., et al. 2019, *A&A*, 623, A58
- Allart, R., Bourrier, V., Lovis, C., et al. 2018, *Science*, 362, 1384
- Allart, R., Lovis, C., Pino, L., et al. 2017, *A&A*, 606, A144
- Aller, K. M., Liu, M. C., Magnier, E. A., et al. 2016, *ApJ*, 821, 120
- Alonso-Floriano, F. J., Snellen, I. A. G., Czesla, S., et al. 2019, *A&A*, 629, A110
- Altwegg, K., Balsiger, H., Bar-Nun, A., et al. 2015, *Science*, 347, 1261952
- Alves de Oliveira, C., Schneider, N., Merín, B., et al. 2014, *A&A*, 568, A98
- Anderson, D. R., Temple, L. Y., Nielsen, L. D., et al. 2018, *arXiv e-prints*, arXiv:1809.04897
- Andretta, V., Giampapa, M. S., Covino, E., Reiners, A., & Beeck, B. 2017, *ApJ*, 839, 97
- Andrews, S. M., Huang, J., Pérez, L. M., et al. 2018, *ApJ*, 869, L41
- Anglada-Escudé, G., Amado, P. J., Barnes, J., et al. 2016, *Nature*, 536, 437
- Arcangeli, J., Désert, J.-M., Line, M. R., et al. 2018, *ApJ*, 855, L30
- Ardila, D. R., Golimowski, D. A., Krist, J. E., et al. 2007, *ApJ*, 665, 512
- Artymowicz, P. & Lubow, S. H. 1994, *ApJ*, 421, 651
- Asensio-Torres, R., Janson, M., Bonavita, M., et al. 2018, *A&A*, 619, A43
- Avenhaus, H., Quanz, S. P., Garufi, A., et al. 2018, *ApJ*, 863, 44

- Bae, J., Isella, A., Zhu, Z., et al. 2022, arXiv e-prints, arXiv:2210.13314
- Bae, J., Pinilla, P., & Birnstiel, T. 2018, *ApJ*, 864, L26
- Baehr, H., Zhu, Z., & Yang, C.-C. 2022, *ApJ*, 933, 100
- Bally, J. & Langer, W. D. 1982, *ApJ*, 255, 143
- Baraffe, I., Chabrier, G., Barman, T. S., Allard, F., & Hauschildt, P. H. 2003, *A&A*, 402, 701
- Baraffe, I., Homeier, D., Allard, F., & Chabrier, G. 2015, *A&A*, 577, A42
- Baranne, A., Queloz, D., Mayor, M., et al. 1996, *A&AS*, 119, 373
- Barman, T. S., Macintosh, B., Konopacky, Q. M., & Marois, C. 2011, *ApJ*, 733, 65
- Batygin, K., Morbidelli, A., & Tsiganis, K. 2011, *A&A*, 533, A7
- Bello-Arufe, A., Cabot, S. H. C., Mendonça, J. M., Buchhave, L. A., & Rathcke, A. D. 2022, *AJ*, 163, 96
- Ben-Yami, M., Madhusudhan, N., Cabot, S. H. C., et al. 2020, *ApJ*, 897, L5
- Benisty, M., Dominik, C., Follette, K., et al. 2022, arXiv e-prints, arXiv:2203.09991
- Benisty, M., Stolker, T., Pohl, A., et al. 2017, *A&A*, 597, A42
- Benneke, B. & Seager, S. 2013, *ApJ*, 778, 153
- Beust, H., Bonnefoy, M., Maire, A. L., et al. 2016, *A&A*, 587, A89
- Beuzit, J. L., Vigan, A., Mouillet, D., et al. 2019, *A&A*, 631, A155
- Birkby, J. L., de Kok, R. J., Brogi, M., et al. 2013, *MNRAS*, 436, L35
- Birkby, J. L., de Kok, R. J., Brogi, M., Schwarz, H., & Snellen, I. A. G. 2017, *AJ*, 153, 138
- Blake, C. H., Charbonneau, D., & White, R. J. 2010, *ApJ*, 723, 684
- Blunt, S., Nielsen, E. L., De Rosa, R. J., et al. 2017, *AJ*, 153, 229
- Blunt, S., Wang, J. J., Angelo, I., et al. 2020, *AJ*, 159, 89
- Bohn, A. J., Ginski, C., Kenworthy, M. A., et al. 2021, *A&A*, 648, A73
- Bohn, A. J., Southworth, J., Ginski, C., et al. 2020, *A&A*, 635, A73
- Bonavita, M. & Desidera, S. 2007, *A&A*, 468, 721
- Bonavita, M. & Desidera, S. 2020, *Galaxies*, 8, 16
- Bonnet, H., Abuter, R., Baker, A., et al. 2004, *The Messenger*, 117, 17
- Boogert, A. C. A., Blake, G. A., & Tielens, A. G. G. M. 2002, *ApJ*, 577, 271

- Boogert, A. C. A., Tielens, A. G. G. M., Ceccarelli, C., et al. 2000, *A&A*, 360, 683
- Booth, A. S., Walsh, C., Kama, M., et al. 2018, *A&A*, 611, A16
- Borsa, F., Allart, R., Casasayas-Barris, N., et al. 2021, *A&A*, 645, A24
- Borsa, F., Rainer, M., Bonomo, A. S., et al. 2019, *A&A*, 631, A34
- Borsa, F., Scandariato, G., Rainer, M., et al. 2015, *A&A*, 578, A64
- Borucki, W. J., Koch, D., Basri, G., et al. 2010, *Science*, 327, 977
- Boss, A. P. 1997, *Science*, 276, 1836
- Botelho, R. B., Milone, A. d. C., Meléndez, J., et al. 2020, *MNRAS*, 499, 2196
- Bourrier, V., Lecavelier des Etangs, A., Ehrenreich, D., et al. 2018, *A&A*, 620, A147
- Bourrier, V., Lecavelier des Etangs, A., & Vidal-Madjar, A. 2014, *A&A*, 565, A105
- Bowler, B. P., Blunt, S. C., & Nielsen, E. L. 2020, *AJ*, 159, 63
- Bowler, B. P., Liu, M. C., Shkolnik, E. L., & Dupuy, T. J. 2013, *ApJ*, 774, 55
- Brinch, C., Jørgensen, J. K., Hogerheijde, M. R., Nelson, R. P., & Gressel, O. 2016, *ApJ*, 830, L16
- Brogi, M., de Kok, R. J., Albrecht, S., et al. 2016, *ApJ*, 817, 106
- Brogi, M., de Kok, R. J., Birkby, J. L., Schwarz, H., & Snellen, I. A. G. 2014, *A&A*, 565, A124
- Brogi, M. & Line, M. R. 2019, *AJ*, 157, 114
- Brogi, M., Snellen, I. A. G., de Kok, R. J., et al. 2012, *Nature*, 486, 502
- Bryan, M. L., Benneke, B., Knutson, H. A., Batygin, K., & Bowler, B. P. 2018, *Nature Astronomy*, 2, 138
- Buchner, J., Georgakakis, A., Nandra, K., et al. 2014, *A&A*, 564, A125
- Burningham, B., Faherty, J. K., Gonzales, E. C., et al. 2021, *MNRAS*, 506, 1944
- Burningham, B., Marley, M. S., Line, M. R., et al. 2017, *MNRAS*, 470, 1177
- Butler, R. P., Marcy, G. W., Williams, E., Hauser, H., & Shirts, P. 1997, *ApJ*, 474, L115
- Caballero, J. A., Guàrdia, J., López del Fresno, M., et al. 2016, in *Society of Photo-Optical Instrumentation Engineers (SPIE) Conference Series*, Vol. 9910, Proc. SPIE, 99100E
- Cabot, S. H. C., Bello-Arufe, A., Mendonça, J. M., et al. 2021, *AJ*, 162, 218
- Cabot, S. H. C., Madhusudhan, N., Welbanks, L., Piette, A., & Gandhi, S. 2020, *MNRAS*, 494, 363

- Carbillet, M., Bendjoya, P., Abe, L., et al. 2011, *Experimental Astronomy*, 30, 39
- Casasayas-Barris, N., Orell-Miquel, J., Stangret, M., et al. 2021, *A&A*, 654, A163
- Casasayas-Barris, N., Pallé, E., Yan, F., et al. 2019, *A&A*, 628, A9
- Casasayas-Barris, N., Pallé, E., Yan, F., et al. 2020, *A&A*, 640, C6
- Cauley, P. W., Kuckein, C., Redfield, S., et al. 2018, *AJ*, 156, 189
- Cauley, P. W., Shkolnik, E. L., Ilyin, I., et al. 2019, *AJ*, 157, 69
- Cazzoletti, P., Manara, C. F., Liu, H. B., et al. 2019, *A&A*, 626, A11
- Cegla, H. M., Lovis, C., Bourrier, V., et al. 2016, *A&A*, 588, A127
- Chabrier, G. 2003, *PASP*, 115, 763
- Charbonneau, D., Brown, T. M., Latham, D. W., & Mayor, M. 2000, *ApJ*, 529, L45
- Charbonneau, D., Brown, T. M., Noyes, R. W., & Gilliland, R. L. 2002, *ApJ*, 568, 377
- Chauvin, G., Lagrange, A. M., Bonavita, M., et al. 2010, *A&A*, 509, A52
- Chauvin, G., Lagrange, A. M., Dumas, C., et al. 2004, *A&A*, 425, L29
- Chauvin, G., Lagrange, A. M., Zuckerman, B., et al. 2005, *A&A*, 438, L29
- Chelli, A., Zinnecker, H., Carrasco, L., Cruz-Gonzalez, I., & Perrier, C. 1988, *A&A*, 207, 46
- Clarke, C. J. & Pringle, J. E. 1993, *MNRAS*, 261, 190
- Clayton, D. D. & Nittler, L. R. 2004, *ARA&A*, 42, 39
- Cornwell, T. J. 2008, *IEEE Journal of Selected Topics in Signal Processing*, 2, 793
- Correia, S., Zinnecker, H., Ratzka, T., & Sterzik, M. F. 2006, *A&A*, 459, 909
- Cox, E. G., Harris, R. J., Looney, L. W., et al. 2017, *ApJ*, 851, 83
- Cridland, A. J., Bosman, A. D., & van Dishoeck, E. F. 2020, *A&A*, 635, A68
- Crossfield, I. J. M., Barman, T., Hansen, B., & Frewen, S. 2019a, *Research Notes of the American Astronomical Society*, 3, 24
- Crossfield, I. J. M., Lothringer, J. D., Flores, B., et al. 2019b, *ApJ*, 871, L3
- Cruz, K. L., Kirkpatrick, J. D., & Burgasser, A. J. 2009, *AJ*, 137, 3345
- Cutri, R. M., Skrutskie, M. F., van Dyk, S., et al. 2003, *VizieR Online Data Catalog*, II/246
- Daemgen, S., Petr-Gotzens, M. G., Correia, S., et al. 2013, *A&A*, 554, A43
- Danby, J. M. A. 1987, *Celestial Mechanics*, 40, 303

-
- de Boer, J., Ginski, C., Chauvin, G., et al. 2021, *A&A*, 649, A25
- de Boer, J., Langlois, M., van Holstein, R. G., et al. 2020, *A&A*, 633, A63
- de Boer, J., Salter, G., Benisty, M., et al. 2016, *A&A*, 595, A114
- de Kok, R. J., Brogi, M., Snellen, I. A. G., et al. 2013, *A&A*, 554, A82
- Deline, A., Hooton, M. J., Lendl, M., et al. 2022, *A&A*, 659, A74
- Delisle, J. B., Ségransan, D., Buchschacher, N., & Alesina, F. 2016, *A&A*, 590, A134
- Delrez, L., Santerne, A., Almenara, J. M., et al. 2016, *MNRAS*, 458, 4025
- Deming, D., Wilkins, A., McCullough, P., et al. 2013, *ApJ*, 774, 95
- Desidera, S. & Barbieri, M. 2007, *A&A*, 462, 345
- Devillard, N. 1999, in *Astronomical Society of the Pacific Conference Series*, Vol. 172, *Astronomical Data Analysis Software and Systems VIII*, ed. D. M. Mehringer, R. L. Plante, & D. A. Roberts, 333
- Díaz, R. F., Almenara, J. M., Santerne, A., et al. 2014, *MNRAS*, 441, 983
- Díaz, R. F., Ségransan, D., Udry, S., et al. 2016, *A&A*, 585, A134
- Dohlen, K., Langlois, M., Saisse, M., et al. 2008, in *Society of Photo-Optical Instrumentation Engineers (SPIE) Conference Series*, Vol. 7014, *Ground-based and Airborne Instrumentation for Astronomy II*, ed. I. S. McLean & M. M. Casali, 70143L
- Dong, R., Fung, J., & Chiang, E. 2016, *ApJ*, 826, 75
- Dong, R., Liu, H. B., Cuello, N., et al. 2022, *Nature Astronomy*, 6, 331
- Dorval, P., Talens, G. J. J., Otten, G. P. P. L., et al. 2020, *A&A*, 635, A60
- Dos Santos, L. A., Vidotto, A. A., Vissapragada, S., et al. 2022, *A&A*, 659, A62
- Drake, M. J. 2005, *Meteoritics and Planetary Science*, 40, 519
- Drzkowska, J., Bitsch, B., Lambrechts, M., et al. 2022, *arXiv e-prints*, arXiv:2203.09759
- Dullemond, C. P., Küffmeier, M., Goicovic, F., et al. 2019, *A&A*, 628, A20
- Duquennoy, A. & Mayor, M. 1991, *A&A*, 248, 485
- Dwivedi, N. K., Khodachenko, M. L., Shaikhislamov, I. F., et al. 2019, *MNRAS*, 487, 4208
- Dzib, S. A., Loinard, L., Ortiz-León, G. N., Rodríguez, L. F., & Galli, P. A. B. 2018, *ApJ*, 867, 151
- EGgenberger, A., Udry, S., Chauvin, G., et al. 2007, *A&A*, 474, 273
- Ehrenreich, D., Bourrier, V., Wheatley, P. J., et al. 2015, *Nature*, 522, 459

- Ehrenreich, D., Lovis, C., Allart, R., et al. 2020, *Nature*, 580, 597
- Eisenhauer, F., Abuter, R., Bickert, K., et al. 2003, in *Society of Photo-Optical Instrumentation Engineers (SPIE) Conference Series*, Vol. 4841, *Instrument Design and Performance for Optical/Infrared Ground-based Telescopes*, ed. M. Iye & A. F. M. Moorwood, 1548–1561
- Erkaev, N. V., Kulikov, Y. N., Lammer, H., et al. 2007, *A&A*, 472, 329
- Evans, T. M., Sing, D. K., Wakeford, H. R., et al. 2016, *ApJ*, 822, L4
- Faherty, J. K., Rice, E. L., Cruz, K. L., Mamajek, E. E., & Núñez, A. 2013, *AJ*, 145, 2
- Faherty, J. K., Riedel, A. R., Cruz, K. L., et al. 2016, *ApJS*, 225, 10
- Faria, J. P., Suárez Mascareño, A., Figueira, P., et al. 2022, *A&A*, 658, A115
- Federman, S. R., Lambert, D. L., Sheffer, Y., et al. 2003, *ApJ*, 591, 986
- Fernández-López, M., Zapata, L. A., & Gabbasov, R. 2017, *ApJ*, 845, 10
- Feroz, F., Hobson, M. P., & Bridges, M. 2009, *MNRAS*, 398, 1601
- Feuchtgruber, H., Lellouch, E., Orton, G., et al. 2013, *A&A*, 551, A126
- Follert, R., Dorn, R. J., Oliva, E., et al. 2014, in *Society of Photo-Optical Instrumentation Engineers (SPIE) Conference Series*, Vol. 9147, *Proc. SPIE*, 914719
- Fontanive, C., Rice, K., Bonavita, M., et al. 2019, *MNRAS*, 485, 4967
- Foreman-Mackey, D., Agol, E., Ambikasaran, S., & Angus, R. 2017, *AJ*, 154, 220
- Fossati, L., Koskinen, T., Lothringer, J. D., et al. 2018, *ApJ*, 868, L30
- Foucart, F. & Lai, D. 2014, *MNRAS*, 445, 1731
- Francis, L. & van der Marel, N. 2020, *ApJ*, 892, 111
- Fung, J. & Dong, R. 2015, *ApJ*, 815, L21
- Gahm, G. F., Petrov, P. P., Tambovsteva, L. V., et al. 2018, *A&A*, 614, A117
- Gahm, G. F., Walter, F. M., Stempels, H. C., Petrov, P. P., & Herczeg, G. J. 2008, *A&A*, 482, L35
- Gaia Collaboration, Brown, A. G. A., Vallenari, A., et al. 2018, *A&A*, 616, A1
- Gaia Collaboration, Vallenari, A., Brown, A. G. A., et al. 2022, *arXiv e-prints*, arXiv:2208.00211
- Gaidos, E., Hirano, T., Mann, A. W., et al. 2020, *MNRAS*, 495, 650
- Gandhi, S., Madhusudhan, N., Hawker, G., & Piette, A. 2019, *AJ*, 158, 228

-
- Gao, P., Thorngren, D. P., Lee, G. K. H., et al. 2020, *Nature Astronomy*, 4, 951
- García Muñoz, A. & Schneider, P. C. 2019, *ApJ*, 884, L43
- Garufi, A., Podio, L., Codella, C., et al. 2022, *A&A*, 658, A104
- Gaudi, B. S., Stassun, K. G., Collins, K. A., et al. 2017, *Nature*, 546, 514
- Gebek, A. & Oza, A. V. 2020, *MNRAS*, 497, 5271
- Ghez, A. M., White, R. J., & Simon, M. 1997, *ApJ*, 490, 353
- Giacobbe, P., Brogi, M., Gandhi, S., et al. 2021, *Nature*, 592, 205
- Gibson, N. P., Merritt, S., Nugroho, S. K., et al. 2020, *MNRAS*, 493, 2215
- Gillon, M., Triaud, A. H. M. J., Demory, B.-O., et al. 2017, *Nature*, 542, 456
- Ginski, C., Facchini, S., Huang, J., et al. 2021a, *ApJ*, 908, L25
- Ginski, C., Ménard, F., Rab, C., et al. 2020, *A&A*, 642, A119
- Ginski, C., Mugrauer, M., Adam, C., Vogt, N., & van Holstein, R. G. 2021b, *A&A*, 649, A156
- Ginski, C., Mugrauer, M., Seeliger, M., et al. 2016, *MNRAS*, 457, 2173
- Ginski, C., Mugrauer, M., Seeliger, M., & Eisenbeiss, T. 2012, *MNRAS*, 421, 2498
- Ginski, C., Schmidt, T. O. B., Mugrauer, M., et al. 2014, *MNRAS*, 444, 2280
- Gomez Gonzalez, C. A., Wertz, O., Absil, O., et al. 2017, *AJ*, 154, 7
- Goto, M., Usuda, T., Takato, N., et al. 2003, *ApJ*, 598, 1038
- Grady, C. A., Woodgate, B., Bruhweiler, F. C., et al. 1999, *ApJ*, 523, L151
- GRAVITY Collaboration, Garcia Lopez, R., Perraut, K., et al. 2017, *A&A*, 608, A78
- GRAVITY Collaboration, Nowak, M., Lacour, S., et al. 2020, *A&A*, 633, A110
- Gray, D. F. 2005, *The Observation and Analysis of Stellar Photospheres*
- Guillot, T. & Hueso, R. 2006, *MNRAS*, 367, L47
- Guilluy, G., Andretta, V., Borsa, F., et al. 2020, arXiv e-prints, arXiv:2005.05676
- Haffert, S. Y., Bohn, A. J., de Boer, J., et al. 2019, *Nature Astronomy*, 3, 749
- Hale, A. 1994, *AJ*, 107, 306
- Hara, N. C., Boué, G., Laskar, J., Delisle, J. B., & Unger, N. 2019, *MNRAS*, 489, 738
- Hashimoto, J., Dong, R., Kudo, T., et al. 2012, *ApJ*, 758, L19
- Hirano, T., Krishnamurthy, V., Gaidos, E., et al. 2020, arXiv e-prints, arXiv:2006.13243

- Hoeijmakers, H. J., Cabot, S. H. C., Zhao, L., et al. 2020a, *A&A*, 641, A120
- Hoeijmakers, H. J., Ehrenreich, D., Heng, K., et al. 2018, *Nature*, 560, 453
- Hoeijmakers, H. J., Ehrenreich, D., Kitzmann, D., et al. 2019, *A&A*, 627, A165
- Hoeijmakers, H. J., Seidel, J. V., Pino, L., et al. 2020b, *A&A*, 641, A123
- Horch, E. P., Howell, S. B., Everett, M. E., & Ciardi, D. R. 2014, *ApJ*, 795, 60
- Horne, K. 1986, *PASP*, 98, 609
- Huang, C., Arras, P., Christie, D., & Li, Z.-Y. 2017, *ApJ*, 851, 150
- Huensch, M., Schmitt, J. H. M. M., & Voges, W. 1998, *A&AS*, 132, 155
- Huitson, C. M., Sing, D. K., Vidal-Madjar, A., et al. 2012, *MNRAS*, 422, 2477
- Husser, T. O., Wende-von Berg, S., Dreizler, S., et al. 2013, *A&A*, 553, A6
- Janson, M., Gratton, R., Rodet, L., et al. 2021, *Nature*, 600, 231
- Jensen, E. 2020, in *Five Years After HL Tau: A New Era in Planet Formation (HLTAU2020)*, 40
- Jensen, E. L. N. & Akeson, R. 2014, *Nature*, 511, 567
- Johansen, A. & Youdin, A. 2007, *ApJ*, 662, 627
- Jones, A., Noll, S., Kausch, W., Szyszka, C., & Kimeswenger, S. 2013, *A&A*, 560, A91
- Jørgensen, J. K., Müller, H. S. P., Calcutt, H., et al. 2018, *A&A*, 620, A170
- Jørgensen, J. K., van der Wiel, M. H. D., Coutens, A., et al. 2016, *A&A*, 595, A117
- Justesen, A. B. & Albrecht, S. 2019, *A&A*, 625, A59
- Justesen, A. B. & Albrecht, S. 2020, *A&A*, 642, A212
- Kaib, N. A., Raymond, S. N., & Duncan, M. 2013, *Nature*, 493, 381
- Kaltenegger, L. 2017, *ARA&A*, 55, 433
- Kammerer, J., Lacour, S., Stolker, T., et al. 2021, *A&A*, 652, A57
- Kepley, A. A., Tsutsumi, T., Brogan, C. L., et al. 2020, *PASP*, 132, 024505
- Keppler, M., Benisty, M., Müller, A., et al. 2018, *A&A*, 617, A44
- Keppler, M., Penzlin, A., Benisty, M., et al. 2020, *A&A*, 639, A62
- Kesseli, A. Y. & Snellen, I. A. G. 2021, *ApJ*, 908, L17
- Kesseli, A. Y., Snellen, I. A. G., Casasayas-Barris, N., Mollière, P., & Sánchez-López, A. 2022, *AJ*, 163, 107

-
- Kirk, J., Alam, M. K., López-Morales, M., & Zeng, L. 2020, *AJ*, 159, 115
- Kitzmann, D., Heng, K., Rimmer, P. B., et al. 2018, *ApJ*, 863, 183
- Kitzmann, D., Hoeijmakers, J. H., Grimm, S. L., et al. 2021, arXiv e-prints, arXiv:2112.11380
- Knutson, H. A., Charbonneau, D., Allen, L. E., Burrows, A., & Megeath, S. T. 2008, *ApJ*, 673, 526
- Knutson, H. A., Charbonneau, D., Allen, L. E., et al. 2007, *Nature*, 447, 183
- Konopacky, Q. M., Barman, T. S., Macintosh, B. A., & Marois, C. 2013, *Science*, 339, 1398
- Koskinen, T. T., Harris, M. J., Yelle, R. V., & Lavvas, P. 2013, *Icarus*, 226, 1678
- Kratter, K. & Lodato, G. 2016, *ARA&A*, 54, 271
- Kraus, A. L., Ireland, M. J., Cieza, L. A., et al. 2014, *ApJ*, 781, 20
- Kraus, A. L., Ireland, M. J., Huber, D., Mann, A. W., & Dupuy, T. J. 2016, *AJ*, 152, 8
- Kraus, S., Kreplin, A., Young, A. K., et al. 2020, *Science*, 369, 1233
- Kreidberg, L., Bean, J. L., Désert, J.-M., et al. 2014a, *Nature*, 505, 69
- Kreidberg, L., Bean, J. L., Désert, J.-M., et al. 2014b, *ApJ*, 793, L27
- Kreidberg, L. & Oklopčić, A. 2018, *Research Notes of the American Astronomical Society*, 2, 44
- Krijt, S., Bosman, A. D., Zhang, K., et al. 2020, *ApJ*, 899, 134
- Kroupa, P. 2001, *MNRAS*, 322, 231
- Kulow, J. R., France, K., Linsky, J., & Loyd, R. O. P. 2014, *ApJ*, 786, 132
- Lafrenière, D., Jayawardhana, R., Brandeker, A., Ahmic, M., & van Kerkwijk, M. H. 2008, *ApJ*, 683, 844
- Lagrange, A. M., Gratadour, D., Chauvin, G., et al. 2009, *A&A*, 493, L21
- Lambert, D. L., Sheffer, Y., Gilliland, R. L., & Federman, S. R. 1994, *ApJ*, 420, 756
- Lambrechts, M. & Johansen, A. 2012, *A&A*, 544, A32
- Lampón, M., López-Puertas, M., Czesla, S., et al. 2021, *A&A*, 648, L7
- Lampón, M., López-Puertas, M., Lara, L. M., et al. 2020, *A&A*, 636, A13
- Landman, R., Sánchez-López, A., Mollière, P., et al. 2021, *A&A*, 656, A119
- Langer, W. D., Graedel, T. E., Frerking, M. A., & Armentrout, P. B. 1984, *ApJ*, 277, 581
- Langer, W. D. & Penzias, A. A. 1993, *ApJ*, 408, 539

- Langlois, M., Dohlen, K., Vigan, A., et al. 2014, in Society of Photo-Optical Instrumentation Engineers (SPIE) Conference Series, Vol. 9147, Ground-based and Airborne Instrumentation for Astronomy V, ed. S. K. Ramsay, I. S. McLean, & H. Takami, 91471R
- Launhardt, R., Henning, T., Quirrenbach, A., et al. 2020, *A&A*, 635, A162
- Lendl, M., Anderson, D. R., Bonfanti, A., et al. 2019, *MNRAS*, 482, 301
- Lendl, M., Anderson, D. R., Collier-Cameron, A., et al. 2012, *A&A*, 544, A72
- Lendl, M., Bouchy, F., Gill, S., et al. 2020, *MNRAS*, 492, 1761
- Lendl, M., Gillon, M., Queloz, D., et al. 2013, *A&A*, 552, A2
- Lenzen, R., Hartung, M., Brandner, W., et al. 2003, in Society of Photo-Optical Instrumentation Engineers (SPIE) Conference Series, Vol. 4841, Instrument Design and Performance for Optical/Infrared Ground-based Telescopes, ed. M. Iye & A. F. M. Moorwood, 944–952
- Lin, D. N. C., Bodenheimer, P., & Richardson, D. C. 1996, *Nature*, 380, 606
- Lin, D. N. C. & Papaloizou, J. 1986, *ApJ*, 309, 846
- Line, M. R., Brogi, M., Bean, J. L., et al. 2021, *Nature*, 598, 580
- Line, M. R., Wolf, A. S., Zhang, X., et al. 2013, *ApJ*, 775, 137
- Liu, H. B., Takami, M., Kudo, T., et al. 2016, *Science Advances*, 2, e1500875
- Liu, M. C., Dupuy, T. J., & Allers, K. N. 2013, *Astronomische Nachrichten*, 334, 85
- Lockwood, A. C., Johnson, J. A., Bender, C. F., et al. 2014, *ApJ*, 783, L29
- Lodato, G., Dipierro, G., Ragusa, E., et al. 2019, *MNRAS*, 486, 453
- Long, F., Herczeg, G. J., Pascucci, I., et al. 2018, *ApJ*, 863, 61
- Lothringer, J. D., Barman, T., & Koskinen, T. 2018, *ApJ*, 866, 27
- Louden, T. & Wheatley, P. J. 2015, *ApJ*, 814, L24
- Lubow, S. H. & Ogilvie, G. I. 2000, *ApJ*, 538, 326
- Luhman, K. L. 2007, *ApJS*, 173, 104
- Lyons, J. R., Gharib-Nezhad, E., & Ayres, T. R. 2018, *Nature Communications*, 9, 908
- Macintosh, B., Graham, J. R., Barman, T., et al. 2015, *Science*, 350, 64
- Macintosh, B., Graham, J. R., Ingraham, P., et al. 2014, *Proceedings of the National Academy of Science*, 111, 12661
- Madhusudhan, N. 2018, in *Handbook of Exoplanets*, ed. H. J. Deeg & J. A. Belmonte, 104
- Madhusudhan, N. 2019, *ARA&A*, 57, 617

- Madhusudhan, N., Amin, M. A., & Kennedy, G. M. 2014, *ApJ*, 794, L12
- Madhusudhan, N., Harrington, J., Stevenson, K. B., et al. 2011, *Nature*, 469, 64
- Maire, A.-L., Langlois, M., Dohlen, K., et al. 2016, in *Society of Photo-Optical Instrumentation Engineers (SPIE) Conference Series*, Vol. 9908, *Ground-based and Airborne Instrumentation for Astronomy VI*, ed. C. J. Evans, L. Simard, & H. Takami, 990834
- Manara, C. F., Tazzari, M., Long, F., et al. 2019, *A&A*, 628, A95
- Manara, C. F., Testi, L., Herczeg, G. J., et al. 2017, *A&A*, 604, A127
- Mansfield, M., Bean, J. L., Oklopčić, A., et al. 2018, *ApJ*, 868, L34
- Marconi, A., Di Marcantonio, P., D’Odorico, V., et al. 2016, in *Society of Photo-Optical Instrumentation Engineers (SPIE) Conference Series*, Vol. 9908, *Proc. SPIE*, 990823
- Marino, S., Perez, S., & Casassus, S. 2015, *ApJ*, 798, L44
- Marois, C., Lafrenière, D., Doyon, R., Macintosh, B., & Nadeau, D. 2006, *ApJ*, 641, 556
- Marois, C., Zuckerman, B., Konopacky, Q. M., Macintosh, B., & Barman, T. 2010, *Nature*, 468, 1080
- Martin, D. V. 2018, in *Handbook of Exoplanets*, ed. H. J. Deeg & J. A. Belmonte, 156
- Mawet, D., Milli, J., Wahhaj, Z., et al. 2014, *ApJ*, 792, 97
- Mawet, D., Pueyo, L., Lawson, P., et al. 2012, in *Society of Photo-Optical Instrumentation Engineers (SPIE) Conference Series*, Vol. 8442, *Space Telescopes and Instrumentation 2012: Optical, Infrared, and Millimeter Wave*, ed. M. C. Clampin, G. G. Fazio, H. A. MacEwen, & J. Oschmann, Jacobus M., 844204
- Mawet, D., Wizinowich, P., Dekany, R., et al. 2016, in *Society of Photo-Optical Instrumentation Engineers (SPIE) Conference Series*, Vol. 9909, *Adaptive Optics Systems V*, ed. E. Marchetti, L. M. Close, & J.-P. Véran, 99090D
- Mayor, M. & Queloz, D. 1995, *Nature*, 378, 355
- McDonald, I., Zijlstra, A. A., & Boyer, M. L. 2012, *MNRAS*, 427, 343
- McLaughlin, D. B. 1924, *ApJ*, 60, 22
- McLean, I. S., Becklin, E. E., Bendiksen, O., et al. 1998, in *Society of Photo-Optical Instrumentation Engineers (SPIE) Conference Series*, Vol. 3354, *Infrared Astronomical Instrumentation*, ed. A. M. Fowler, 566–578
- Meadows, V. S., Reinhard, C. T., Arney, G. N., et al. 2018, *Astrobiology*, 18, 630
- Ménard, F., Cuello, N., Ginski, C., et al. 2020, *A&A*, 639, L1
- Merritt, S. R., Gibson, N. P., Nugroho, S. K., et al. 2021, *MNRAS*, 506, 3853

- Mesa, D., Ginski, C., Gratton, R., et al. 2022, *A&A*, 658, A63
- Milam, S. N., Savage, C., Brewster, M. A., Ziurys, L. M., & Wyckoff, S. 2005, *ApJ*, 634, 1126
- Miles, B. E., Biller, B. A., Patapis, P., et al. 2022, arXiv e-prints, arXiv:2209.00620
- Miotello, A., Bruderer, S., & van Dishoeck, E. F. 2014, *A&A*, 572, A96
- Moe, M. & Kratter, K. M. 2021, *MNRAS*, 507, 3593
- Mollière, P. & Snellen, I. A. G. 2019, *A&A*, 622, A139
- Mollière, P., Stolker, T., Lacour, S., et al. 2020, *A&A*, 640, A131
- Mollière, P., van Boekel, R., Bouwman, J., et al. 2017, *A&A*, 600, A10
- Mollière, P., Wardenier, J. P., van Boekel, R., et al. 2019, *A&A*, 627, A67
- Morbidelli, A., Levison, H. F., Tsiganis, K., & Gomes, R. 2005, *Nature*, 435, 462
- Mordasini, C., van Boekel, R., Mollière, P., Henning, T., & Benneke, B. 2016, *ApJ*, 832, 41
- Morley, C. V., Fortney, J. J., Marley, M. S., et al. 2012, *ApJ*, 756, 172
- Morley, C. V., Skemer, A. J., Miles, B. E., et al. 2019, *ApJ*, 882, L29
- Moutou, C., Vigan, A., Mesa, D., et al. 2017, *A&A*, 602, A87
- Mugrauer, M. & Ginski, C. 2015, *MNRAS*, 450, 3127
- Mugrauer, M. & Michel, K.-U. 2020, *Astronomische Nachrichten*, 341, 996
- Murray-Clay, R. A., Chiang, E. I., & Murray, N. 2009, *ApJ*, 693, 23
- Muzerolle, J., Hartmann, L., & Calvet, N. 1998, *AJ*, 116, 2965
- Neuhäuser, R., Guenther, E. W., Wuchterl, G., et al. 2005, *A&A*, 435, L13
- Ngo, H., Knutson, H. A., Bryan, M. L., et al. 2017, *AJ*, 153, 242
- Ngo, H., Knutson, H. A., Hinkley, S., et al. 2016, *ApJ*, 827, 8
- Ngo, H., Knutson, H. A., Hinkley, S., et al. 2015, *ApJ*, 800, 138
- Nielsen, E. L., De Rosa, R. J., Macintosh, B., et al. 2019, *AJ*, 158, 13
- Nielsen, L. D. 2021, PhD thesis, iD: unige:155470
- Ninan, J. P., Stefansson, G., Mahadevan, S., et al. 2020, *ApJ*, 894, 97
- Noll, S., Kausch, W., Barden, M., et al. 2012, *A&A*, 543, A92
- Nortmann, L., Pallé, E., Salz, M., et al. 2018, *Science*, 362, 1388
- Nugroho, S. K., Gibson, N. P., de Mooij, E. J. W., et al. 2020, *MNRAS*, 496, 504

- Nugroho, S. K., Kawahara, H., Gibson, N. P., et al. 2021, *ApJ*, 910, L9
- Öberg, K. I., Murray-Clay, R., & Bergin, E. A. 2011, *ApJ*, 743, L16
- Oklopčić, A. 2019, *ApJ*, 881, 133
- Oklopčić, A. & Hirata, C. M. 2018, *ApJ*, 855, L11
- Owen, J. E. 2019, *Annual Review of Earth and Planetary Sciences*, 47, 67
- Palle, E., Nortmann, L., Casasayas-Barris, N., et al. 2020, *A&A*, 638, A61
- Papaloizou, J. & Pringle, J. E. 1977, *MNRAS*, 181, 441
- Parmentier, V., Line, M. R., Bean, J. L., et al. 2018, *A&A*, 617, A110
- Parmentier, V., Showman, A. P., & Lian, Y. 2013, *A&A*, 558, A91
- Pascucci, I., Testi, L., Herczeg, G. J., et al. 2016, *ApJ*, 831, 125
- Pecaut, M. J. & Mamajek, E. E. 2016, *MNRAS*, 461, 794
- Pecaut, M. J., Mamajek, E. E., & Bubar, E. J. 2012, *ApJ*, 746, 154
- Pepe, F., Cristiani, S., Rebolo, R., et al. 2021, *A&A*, 645, A96
- Podsiadlowski, P., Pringle, J. E., & Rees, M. J. 1991, *Nature*, 352, 783
- Pollacco, D. L., Skillen, I., Collier Cameron, A., et al. 2006, *PASP*, 118, 1407
- Pollack, J. B., Hubickyj, O., Bodenheimer, P., et al. 1996, *Icarus*, 124, 62
- Pontoppidan, K. M., Dullemond, C. P., van Dishoeck, E. F., et al. 2005, *ApJ*, 622, 463
- Prantzos, N., Aubert, O., & Audouze, J. 1996, *A&A*, 309, 760
- Prinoth, B., Hoeijmakers, H. J., Kitzmann, D., et al. 2022, *Nature Astronomy*, 6, 449
- Qi, C., Öberg, K. I., Wilner, D. J., et al. 2013, *Science*, 341, 630
- Queloz, D., Henry, G. W., Sivan, J. P., et al. 2001, *A&A*, 379, 279
- Queloz, D., Mayor, M., Weber, L., et al. 2000, *A&A*, 354, 99
- Quirrenbach, A., Amado, P. J., Caballero, J. A., et al. 2016, in *Society of Photo-Optical Instrumentation Engineers (SPIE) Conference Series*, Vol. 9908, Proc. SPIE, 990812
- Rafikov, R. R. 2011, *ApJ*, 727, 86
- Raghavan, D., McAlister, H. A., Henry, T. J., et al. 2010, *ApJS*, 190, 1
- Ragusa, E., Alexander, R., Calcino, J., Hirsh, K., & Price, D. J. 2020, *MNRAS*, 499, 3362
- Redfield, S., Endl, M., Cochran, W. D., & Koesterke, L. 2008, *ApJ*, 673, L87

- Reid, I. N., Cruz, K. L., Kirkpatrick, J. D., et al. 2008, *AJ*, 136, 1290
- Ribas, Á., Macías, E., Espallat, C. C., & Duchêne, G. 2018, *ApJ*, 865, 77
- Ricker, G. R., Winn, J. N., Vanderspek, R., et al. 2015, *Journal of Astronomical Telescopes, Instruments, and Systems*, 1, 014003
- Roell, T., Neuhäuser, R., Seifahrt, A., & Mugrauer, M. 2012, *A&A*, 542, A92
- Rosotti, G. P. & Clarke, C. J. 2018, *MNRAS*, 473, 5630
- Rossiter, R. A. 1924, *ApJ*, 60, 15
- Rota, A. A., Manara, C. F., Miotello, A., et al. 2022, *A&A*, 662, A121
- Rousset, G., Lacombe, F., Puget, P., et al. 2003, in *Society of Photo-Optical Instrumentation Engineers (SPIE) Conference Series*, Vol. 4839, *Adaptive Optical System Technologies II*, ed. P. L. Wizinowich & D. Bonaccini, 140–149
- Rufener, F. & Nicolet, B. 1988, *A&A*, 206, 357
- Rustamkulov, Z., Sing, D. K., Mukherjee, S., et al. 2022, arXiv e-prints, arXiv:2211.10487
- Ryabchikova, T., Piskunov, N., Kurucz, R. L., et al. 2015, *Phys. Scr*, 90, 054005
- Salz, M., Czesla, S., Schneider, P. C., et al. 2018, *A&A*, 620, A97
- Salz, M., Czesla, S., Schneider, P. C., & Schmitt, J. H. M. M. 2016, *A&A*, 586, A75
- Sanz-Forcada, J., Micela, G., Ribas, I., et al. 2011, *A&A*, 532, A6
- Schmidt, T. O. B., Vogt, N., Neuhäuser, R., Bedalov, A., & Roell, T. 2013, *A&A*, 557, A80
- Schwarz, R., Funk, B., Zechner, R., & Bazsó, Á. 2016, *MNRAS*, 460, 3598
- Seager, S. 2010, *Exoplanet Atmospheres: Physical Processes*
- Seager, S. & Sasselov, D. D. 2000, *ApJ*, 537, 916
- Seidel, J. V., Ehrenreich, D., Allart, R., et al. 2021, *A&A*, 653, A73
- Seidel, J. V., Ehrenreich, D., Wytttenbach, A., et al. 2019, *A&A*, 623, A166
- Serindag, D. B. & Snellen, I. A. G. 2019, *ApJ*, 871, L7
- Shokry, A., Rivinius, T., Mehner, A., et al. 2018, *A&A*, 609, A108
- Showman, A. P., Fortney, J. J., Lewis, N. K., & Shabram, M. 2013, *ApJ*, 762, 24
- Sicilia-Aguilar, A., Henning, T., Linz, H., et al. 2013, *A&A*, 551, A34
- Siess, L., Dufour, E., & Forestini, M. 2000, *A&A*, 358, 593
- Sing, D. K., Fortney, J. J., Nikolov, N., et al. 2016, *Nature*, 529, 59

- Sing, D. K., Lavvas, P., Ballester, G. E., et al. 2019, *AJ*, 158, 91
- Smette, A., Sana, H., Noll, S., et al. 2015, *A&A*, 576, A77
- Smith, R. L., Pontoppidan, K. M., Young, E. D., & Morris, M. R. 2015, *ApJ*, 813, 120
- Snedden, C., Pilachowski, C. A., & Vandenberg, D. A. 1986, *ApJ*, 311, 826
- Snellen, I., de Kok, R., Birkby, J. L., et al. 2015, *A&A*, 576, A59
- Snellen, I. A. G., Brandl, B. R., de Kok, R. J., et al. 2014, *Nature*, 509, 63
- Snellen, I. A. G., de Kok, R. J., de Mooij, E. J. W., & Albrecht, S. 2010, *Nature*, 465, 1049
- Spake, J. J., Sing, D. K., Evans, T. M., et al. 2018, *Nature*, 557, 68
- Sparks, W. B. & Ford, H. C. 2002, *ApJ*, 578, 543
- Spiegel, D. S., Silverio, K., & Burrows, A. 2009, *ApJ*, 699, 1487
- Spitzer, L. 1978, *Physical processes in the interstellar medium*
- Stangret, M., Casasayas-Barris, N., Pallé, E., et al. 2022, *A&A*, 662, A101
- Stangret, M., Casasayas-Barris, N., Pallé, E., et al. 2020, *A&A*, 638, A26
- Stapelfeldt, K. 1997, T Tauri Star Snapshot Survey: A Census of Protoplanetary Disks, HST Proposal ID 7387. Cycle 7
- Stolker, T., Dominik, C., Min, M., et al. 2016, *A&A*, 596, A70
- Stolker, T., Quanz, S. P., Todorov, K. O., et al. 2020, *A&A*, 635, A182
- Storey, P. J. & Hummer, D. G. 1995, *MNRAS*, 272, 41
- Su, X.-N., Xie, J.-W., Zhou, J.-L., & Thebault, P. 2021, *AJ*, 162, 272
- Sullivan, K., Prato, L., Edwards, S., Avilez, I., & Schaefer, G. H. 2019, *ApJ*, 884, 28
- Tabernerero, H. M., Zapatero Osorio, M. R., Allart, R., et al. 2021, *A&A*, 646, A158
- Tafalla, M., Santiago-García, J., Hacar, A., & Bachiller, R. 2010, *A&A*, 522, A91
- Takami, M., Fu, G., Liu, H. B., et al. 2018, *ApJ*, 864, 20
- Takeda, G., Ford, E. B., Sills, A., et al. 2007, *ApJS*, 168, 297
- Talens, G. J. J., Justesen, A. B., Albrecht, S., et al. 2018, *A&A*, 612, A57
- Thalmann, C., Janson, M., Garufi, A., et al. 2016, *ApJ*, 828, L17
- Thalmann, C., Mulders, G. D., Hodapp, K., et al. 2014, *A&A*, 566, A51
- THE CASA TEAM, Bean, B., Bhatnagar, S., et al. 2022, arXiv e-prints, arXiv:2210.02276

- Trapman, L., Bosman, A. D., Rosotti, G., Hogerheijde, M. R., & van Dishoeck, E. F. 2021, *A&A*, 649, A95
- Tremblin, P., Amundsen, D. S., Chabrier, G., et al. 2016, *ApJ*, 817, L19
- Tremblin, P., Amundsen, D. S., Mourier, P., et al. 2015, *ApJ*, 804, L17
- Tremblin, P., Chabrier, G., Baraffe, I., et al. 2017, *ApJ*, 850, 46
- Tremblin, P., Padioleau, T., Phillips, M. W., et al. 2019, *ApJ*, 876, 144
- Tsuji, T. 2016, *PASJ*, 68, 84
- Turner, J. D., de Mooij, E. J. W., Jayawardhana, R., et al. 2020, *ApJ*, 888, L13
- Turrini, D., Schisano, E., Fonte, S., et al. 2021, *ApJ*, 909, 40
- Valenti, J. A. & Piskunov, N. 1996, *A&AS*, 118, 595
- van der Marel, N., Bosman, A. D., Krijt, S., Mulders, G. D., & Bergner, J. B. 2021, *A&A*, 653, L9
- van Dishoeck, E. F. & Black, J. H. 1988, *ApJ*, 334, 771
- van Holstein, R. G., Girard, J. H., de Boer, J., et al. 2020, *A&A*, 633, A64
- van Holstein, R. G., Snik, F., Girard, J. H., et al. 2017, in *Society of Photo-Optical Instrumentation Engineers (SPIE) Conference Series*, Vol. 10400, *Society of Photo-Optical Instrumentation Engineers (SPIE) Conference Series*, ed. S. Shaklan, 1040015
- van Holstein, R. G., Stolker, T., Jensen-Clem, R., et al. 2021, *A&A*, 647, A21
- Veras, D., Crepp, J. R., & Ford, E. B. 2009, *ApJ*, 696, 1600
- Verner, D. A., Ferland, G. J., Korista, K. T., & Yakovlev, D. G. 1996, *ApJ*, 465, 487
- Vidal-Madjar, A., Désert, J. M., Lecavelier des Etangs, A., et al. 2004, *ApJ*, 604, L69
- Vidal-Madjar, A., Lecavelier des Etangs, A., Désert, J. M., et al. 2003, *Nature*, 422, 143
- Vigan, A., Fontanive, C., Meyer, M., et al. 2021, *A&A*, 651, A72
- Vigan, A., Otten, G. P. P. L., Muslimov, E., et al. 2018, in *Society of Photo-Optical Instrumentation Engineers (SPIE) Conference Series*, Vol. 10702, *Ground-based and Airborne Instrumentation for Astronomy VII*, ed. C. J. Evans, L. Simard, & H. Takami, 1070236
- Visser, R., van Dishoeck, E. F., & Black, J. H. 2009, *A&A*, 503, 323
- Vogt, N., Schmidt, T. O. B., Neuhäuser, R., et al. 2012, *A&A*, 546, A63
- Vorobyov, E. I., Skliarevskii, A. M., Elbakyan, V. G., et al. 2020, *A&A*, 635, A196
- Wakeford, H. R., Visscher, C., Lewis, N. K., et al. 2017, *MNRAS*, 464, 4247

-
- Waldmann, I. P., Rocchetto, M., Tinetti, G., et al. 2015, *ApJ*, 813, 13
- Wang, J., Fischer, D. A., Xie, J.-W., & Ciardi, D. R. 2014a, *ApJ*, 791, 111
- Wang, J., Kolecki, J. R., Ruffio, J.-B., et al. 2022, *AJ*, 163, 189
- Wang, J., Xie, J.-W., Barclay, T., & Fischer, D. A. 2014b, *ApJ*, 783, 4
- Wang, J. J., Ruffio, J.-B., Morris, E., et al. 2021a, *AJ*, 162, 148
- Wang, J. J., Vigan, A., Lacour, S., et al. 2021b, *AJ*, 161, 148
- West, R. G., Hellier, C., Almenara, J. M., et al. 2016, *A&A*, 585, A126
- Whittet, D. C. B., Prusti, T., Franco, G. A. P., et al. 1997, *A&A*, 327, 1194
- Williams, J. P., Mann, R. K., Di Francesco, J., et al. 2014, *ApJ*, 796, 120
- Wilson, T. L. 1999, *Reports on Progress in Physics*, 62, 143
- Wolszczan, A. & Frail, D. A. 1992, *Nature*, 355, 145
- Woodall, J., Agúndez, M., Markwick-Kemper, A. J., & Millar, T. J. 2007, *A&A*, 466, 1197
- Woods, P. M. 2009, arXiv e-prints, arXiv:0901.4513
- Wright, J. T., Marcy, G. W., Butler, R. P., & Vogt, S. S. 2004, *ApJS*, 152, 261
- Wytttenbach, A., Ehrenreich, D., Lovis, C., Udry, S., & Pepe, F. 2015, *A&A*, 577, A62
- Wytttenbach, A., Lovis, C., Ehrenreich, D., et al. 2017, *A&A*, 602, A36
- Wytttenbach, A., Mollière, P., Ehrenreich, D., et al. 2020, *A&A*, 638, A87
- Xie, J.-W., Payne, M. J., Thébault, P., Zhou, J.-L., & Ge, J. 2011, *ApJ*, 735, 10
- Xuan, J. W., Wang, J., Ruffio, J.-B., et al. 2022, *ApJ*, 937, 54
- Yan, D., Guo, J., Huang, C., & Xing, L. 2021, *ApJ*, 907, L47
- Yan, F. & Henning, T. 2018, *Nature Astronomy*, 2, 714
- Yan, F., Pallé, E., Fosbury, R. A. E., Petr-Gotzens, M. G., & Henning, T. 2017, *A&A*, 603, A73
- Yan, Y. T., Zhang, J. S., Henkel, C., et al. 2019, *ApJ*, 877, 154
- Zagaria, F., Rosotti, G. P., & Lodato, G. 2021a, *MNRAS*, 504, 2235
- Zagaria, F., Rosotti, G. P., & Lodato, G. 2021b, *MNRAS*, 507, 2531
- Zapata, L. A., Rodríguez, L. F., Fernández-López, M., et al. 2020, *ApJ*, 896, 132
- Zeng, L., Jacobsen, S. B., Sasselov, D. D., et al. 2019, *Proceedings of the National Academy of Science*, 116, 9723

- Zhang, Y., Li, Q., Xie, J.-W., et al. 2018, *ApJ*, 861, 116
- Zhang, Y., Snellen, I. A. G., Bohn, A. J., et al. 2021a, *Nature*, 595, 370
- Zhang, Y., Snellen, I. A. G., & Mollière, P. 2021b, *A&A*, 656, A76
- Zhou, G., Huang, C. X., Bakos, G. Á., et al. 2019, *AJ*, 158, 141
- Zhu, Z., Dong, R., Stone, J. M., & Rafikov, R. R. 2015, *ApJ*, 813, 88
- Ziegler, C., Tokovinin, A., Briceño, C., et al. 2020, *AJ*, 159, 19
- Zurlo, A., Cieza, L. A., Ansdell, M., et al. 2021, *MNRAS*, 501, 2305
- Zurlo, A., Cieza, L. A., Pérez, S., et al. 2020, *MNRAS*, 496, 5089

Summary

How did we come into existence? Are we alone? The origin of life and our place in the universe have been enduring quests of human beings. It was only three decades ago when astronomers began studying exoplanets, planets outside our solar system. In 1995, the first exoplanet around a main sequence star, 51 Pegasi b, was discovered, leading to the development of exoplanetary science. Since then, the field has proceeded rapidly with more than 5000 diverse exoplanets discovered to date. These discoveries include a population of close-in planets to their host stars, known as hot Jupiters, a class of young massive giant planets, called super Jupiters, and planets with intermediate sizes between the Earth and the Neptune, named super-Earths and mini-Neptunes. The presence of these strange worlds that have no counterparts in the solar system poses challenges to our perception of planet formation and evolution but also opens exciting new windows of understanding.

With the number of detected exoplanets growing rapidly, we are entering an era of characterizing their properties in detail. Observations of exoplanet atmospheres open an essential avenue for a further level of characterization beyond the dimension of planet masses and sizes. The study of exoplanet atmospheres aims at unveiling their chemical compositions, which play a vital role in retracing the formation history of planets, assessing the habitability and searching for extraterrestrial life. This can be achieved by spectroscopic observations, that is, dispersing lights into different wavelengths (or colors). As different species absorb lights at different wavelengths and result in unique signatures in the spectra, hence the chemical constituents can be identified through spectroscopy.

The spectral characterization of exoplanet atmospheres benefits from high resolving power, which resolves the atomic or molecular features into individual spectral lines that facilitate the disentanglement of different species and even isotopologues. In addition, the position and shape of spectral lines bears a wealth of information on dynamical processes in atmospheres. As such, the spectral analyses allow us to chart thermal structures, winds, clouds/hazes, and atmospheric escapes of exoplanets. The application of high resolution spectroscopy in studying atmospheres of gas giant exoplanets is explored in chapter 2-5 of this dissertation.

In the quest for giant planet formation, while three major scenarios have been proposed, including core accretion, gravitational instability, and cloud fragmentation, fundamental questions remain unanswered. Linking atmospheric composition to planet formation has been one of the most challenging frontiers of planetary science. The atmospheric elemental abundance ratios, such as the carbon-to-oxygen (C/O) and nitrogen-to-carbon (N/C) ratios, are believed to provide important clues. As temperature decreases in protoplanetary disks with the distance from the central star, molecules freeze out onto dust grains and are removed from the gas phase to the solid phase, changing the elemental abundance ratios in the gas and solid reservoirs. Planets formed at different locations with respect to molecular icelines and/or incorporated different amounts of solids are expected to show distinct chemical abundance ratios in their atmospheres, providing implications

for formation pathways, birth locations, and the relative contributions of gas versus solid accretion. Similarly, isotope abundance ratios, such as D/H and $^{12}\text{C}/^{13}\text{C}$, are suggested to be powerful tracers for the formation and evolution history of planets. With state-of-the-art facilities and techniques, it becomes feasible to combine multiple observational probes to disentangle the subtleties of planet formation processes. This is investigated in chapter 2 and 3 in particular.

Chapter 2: First detection of minor isotopologue ^{13}CO in an exoplanet

Isotopologues in planetary atmospheres are believed to be able to reveal how planets were formed. This idea is inspired by measurements of isotopic ratios (such as deuterium-to-hydrogen ratios) in our own solar system, which vary significantly across different planets. These variations are likely linked to the isotope ratios in protoplanetary disks, which are affected by temperature and irradiation-dependent processes known as fractionation. By detecting and analyzing isotopes in exoplanet atmospheres, we can constrain where the planet formed, how much gas and solids contributed to its formation, and how much atmospheric loss it has experienced (as heavy isotopes are less prone to escape from atmospheres). This chapter presents the first detection of the minor isotopologue of carbon monoxide ^{13}CO in the atmosphere of a super Jupiter named YSES-1 b using the near-infrared integral-field spectrograph SINFONI at the VLT, marking the first time that isotopic measurements have been extended to exoplanets. Through modeling of planetary atmospheres and Bayesian retrieval analyses, we determined the carbon isotope ratio in the planetary atmosphere to be $^{12}\text{CO}/^{13}\text{CO}\sim 31$, which means a factor of two enhancement of ^{13}C compared to the local interstellar medium ($^{12}\text{C}/^{13}\text{C}\sim 68$). This finding suggests that the planet was plausibly formed outside the CO iceline and mainly acquired carbon from accretion of ^{13}C -enriched ices. It opens up an exciting new avenue of connecting atmospheric characteristics to planet formation.

Chapter 3: First detection of minor isotopologue ^{13}CO in a brown dwarf

After detecting ^{13}CO in the exoplanet YSES 1b, we extended our method to an exoplanet analog called 2M0355, which is a young, isolated brown dwarf with comparable mass and effective temperature to the super Jupiter companion. Interestingly, this study revealed no ^{13}CO enrichment in the brown dwarf based on archival observations taken with the high-resolution spectrograph NIRSPEC at the Keck observatory. The carbon isotope ratio in the brown dwarf ($^{12}\text{CO}/^{13}\text{CO}\sim 100$) is in stark contrast to that in the exoplanet, hinting at different formation processes. To further investigate this benchmark object, we conducted follow-up observations of this brown dwarf using the upgraded state-of-the-art spectrograph CRIFES at the VLT, and were able to confirm the constraint on the carbon isotope ratio. Additionally, we suggest that the oxygen isotope ratio ($^{16}\text{O}/^{18}\text{O}$) can now be studied in bright super Jupiters and brown dwarfs using high-resolution spectroscopy. The comparison of atmospheric compositions in giant exoplanets and brown dwarfs plays an important role in unraveling their distinction in terms of formation pathways.

Chapter 4: Search for He I airglow emission from hot Jupiter

Gaseous planets that orbit very closely to their host stars can undergo significant atmospheric erosion due to the intense high-energy radiation from their stars. This process

is especially relevant for planets that are smaller than Neptune, driving the evolution of their atmospheres. One powerful way to study atmospheric escape in these planets is to look for the absorption of helium atoms in their atmospheres, which has been successfully detected in a dozen of exoplanet atmospheres during transiting. However, the helium absorption is inconclusive in determining the atmospheric mass loss on its own because it is difficult to separate the effects of atmospheric escape from the exospheric temperature using helium absorption alone. To overcome this challenge, we aimed at searching for helium airglow emission to be combined with the absorption to better constrain the upper atmospheres. We carried out this search in the non-transiting hot Jupiter τ Bootis b using the near-infrared spectrograph CARMENES at the Calar Alto Observatory. Although it resulted in a non-detection, our study provides important information about the detection limits of helium airglow emission in exoplanets, and we believe that next-generation telescopes will be able to measure this emission. Detecting helium airglow emission will be crucial in studying the atmospheric structure, mass loss rates, and bulk-atmospheric evolution of gaseous planets that are located very close to their host stars.

Chapter 5: Disentangle hydrostatic and exospheric regimes of ultra-hot Jupiters

The strong high-energy stellar irradiation on close-in hot Jupiters results in two distinct regimes in their atmospheres, the hydrostatic lower atmosphere and the hydrodynamic exosphere. Understanding the dynamics of these regions requires the measurement of different atoms or molecules. In this chapter, we characterized the atmosphere of the ultra-hot Jupiter MASCARA-4b, which has an equilibrium temperature above 2000 K, using transmission spectroscopic observations taken with the optical high-resolution spectrograph ESPRESSO at the VLT. Our measurements detected a variety of absorbing species, including H I, Na I, Fe I, and Fe II in the planetary atmosphere. To put the results into context, we compared our findings to those of seven other ultra-hot Jupiters and investigated the trend of these atomic absorption strengths. We found that neutral metal species trace the hydrostatic regime, while hydrogen and ionized metals probe the hydrodynamic exosphere and atmospheric escape. This comparison allowed us to take the first step towards analyzing high-resolution spectroscopic results at a population level, making it possible to distinguish between different dynamic regimes of highly-irradiated atmospheres.

Chapter 6: Diverse outcomes of binary-disk interactions

To gain insights into planet formation, it is necessary to understand circumstellar disks, the birthplace of planets. As approximately half of solar-type stars are born in multiple stellar systems, the presence of stellar companions can modify the morphology and evolution of disks, potentially influencing the outcomes of planet formation. In this chapter, we used polarimetric differential imaging with SPHERE/IRDIS at the VLT to resolve circumstellar disks in three multiple systems: CHX 22, S CrA, and HP Cha, as part of the Disk Evolution Study Through Imaging of Nearby Young Stars (DESTINY) large program. The observed disk morphology, in combination with astrometric and orbit analyses for the stellar companions, allows for a better understanding of the interplay between disks and companions. The comparison of the three systems spans a wide range of binary separations (50 – 500 au) and illustrates the decreasing influence of companions on disk structures with increasing separation. This finding is consistent with the statistical analysis of exoplanet populations

in binaries, which suggests that planet formation is likely hindered around close binary systems, while it is not suppressed in wide binaries.

Outlook: unravel the origin of planets

Moving forward, a key step to better understand the origin of exoplanets is to extend the characterization of exoplanet atmospheres to a larger sample. With the ability to reliably retrieve formation tracers, such as elemental and isotopic compositions, from near-infrared high-resolution spectra, we will be able to address the questions through population-level analyses of young giant planets and brown dwarfs and compare different classes of sub-stellar objects. This will enable us to explore the trends in atmospheric constituents with stellar and planetary properties, such as mass and orbital separation, and assess the plausibility of various formation scenarios. The census of chemical composition will contribute to bridging the gap between atmospheric observations and planet formation and evolution, and addressing the fundamental question of what sets the boundary between planets and brown dwarfs.

Looking towards the future, the upcoming thirty-meter class telescopes, such as the Extremely Large Telescope (ELT) with first light expected in five years, and the next-generation flagship space telescope, will routinely deliver characterizations of smaller exoplanets with the potential of investigating atmospheric biosignatures and habitability. The ELT will be particularly promising for probing rare isotopes, such as deuterium, in exoplanets, which is one of the most informative tracers of planet formation and atmospheric evolution. Hopefully, we will begin answering the ultimate questions of how unique our solar system is and how we got here.

Nederlandse Samenvatting

Hoe zijn we ontstaan? Zijn we alleen? De oorsprong van het leven en onze plek in het universum zijn al lang een zoektocht van de mensheid. Pas drie decennia geleden begonnen astronomen met het bestuderen van exoplaneten, planeten buiten ons zonnestelsel. In 1995 werd de eerste exoplaneet rond een hoofdreeksster, 51 Pegasi b, ontdekt, wat leidde tot de ontwikkeling van de exoplanetenwetenschap. Sindsdien is het veld snel voortgeschreden met meer dan 5000 diverse exoplaneten die tot op heden zijn ontdekt. Deze ontdekkingen omvatten een populatie van dichtbijgelegen planeten bij hun gastheersterren, bekend als 'hete Jupiters', een klasse van jonge, massieve reuzenplaneten, genaamd 'super-Jupiters', en planeten met tussenliggende maten tussen de Aarde en de Neptunus, genaamd 'super-Aardes' en 'mini-Neptunussen'. De aanwezigheid van deze vreemde werelden zonder tegenhangers in het zonnestelsel stelt uitdagingen aan ons begrip van planeetvorming en -evolutie, maar opent ook spannende nieuwe vensters van begrip.

Met het snel groeiende aantal gedetecteerde exoplaneten betreden we een tijdperk van gedetailleerde karakterisering van hun eigenschappen. Observaties van exoplaneet atmosferen openen een essentiële weg naar verdere karakterisering buiten de dimensie van planeetmassa's en -groottes. De studie van exoplaneet atmosferen heeft als doel hun chemische samenstelling te onthullen, die een cruciale rol speelt bij het achterhalen van de vormingsgeschiedenis van planeten, het beoordelen van de bewoonbaarheid en het zoeken naar buitenaards leven. Dit kan worden bereikt door spectroscopische waarnemingen, waarbij licht wordt verspreid in verschillende golflengten (of kleuren). Aangezien verschillende soorten licht absorberen bij verschillende golflengten en unieke handtekeningen in de spectra veroorzaken, kunnen de chemische bestanddelen worden geïdentificeerd via spectroscopie.

De spectrale karakterisering van exoplaneet atmosferen profiteert van een hoge resolutie, die atomaire of moleculaire kenmerken oplost in individuele spectraallijnen, wat de ontwarring van verschillende soorten en zelfs isotopologen vergemakkelijkt. Bovendien bieden de positie en vorm van spectraallijnen een schat aan informatie over dynamische processen in de atmosfeer. Als zodanig stellen spectrale analyses ons in staat om thermische structuren, winden, wolken/nevels en atmosferische ontsnappingen van exoplaneten in kaart te brengen. Hoofdstuk 2 tot 5 van deze dissertatie onderzoeken de toepassing van hoge-resolutie-spectroscopie bij het bestuderen van de atmosferen van gasreuzen-exoplaneten.

In de zoektocht naar de vorming van gasreuzen blijven er fundamentele vragen onbeantwoord, ondanks de drie belangrijkste voorgestelde scenario's, namelijk kerngroei, gravitationele instabiliteit en wolkfragmentatie. Het verbinden van atmosferische samenstelling met planeetvorming is een van de meest uitdagende fronten van de planetenwetenschap. De verhoudingen van elementaire overvloed in de atmosfeer, zoals de koolstof-tot-zuurstof (C/O) en stikstof-tot-koolstof (N/C) ratio's, zouden belangrijke aanwijzingen moeten bieden. Naarmate de temperatuur afneemt in protoplanetaire schijven met de af-

stand tot de centrale ster, bevrozen moleculen op stofdeeltjes en worden ze verwijderd van de gasfase naar de vaste fase, wat de elementaire overvloedverhoudingen in de gas- en vaste reservoirs verandert. Planeten die op verschillende locaties worden gevormd met betrekking tot moleculaire ijslijnen en/of verschillende hoeveelheden vaste stoffen opnemen, zullen naar verwachting verschillende chemische overvloedverhoudingen in hun atmosferen vertonen, wat implicaties heeft voor vormingswegen, geboorteplaatsen en de relatieve bijdragen van gas versus vaste-stofaccrétie. Evenzo worden isotoopverhoudingen, zoals D/H en $^{12}\text{C}/^{13}\text{C}$, voorgesteld als krachtige tracers voor de vormings- en evolutiegeschiedenis van planeten. Met state-of-the-art faciliteiten en technieken wordt het haalbaar om meerdere observationele probes te combineren om de subtiliteiten van planeetvormingsprocessen te ontrafelen. Dit wordt met name onderzocht in hoofdstuk 2 en 3.

Hoofdstuk 2: Eerste detectie van het lichte isotopoloog ^{13}CO in een exoplaneet

Isotopen in planetaire atmosferen kunnen onthullen hoe planeten zijn gevormd. Dit idee is geïnspireerd door metingen van isotopenverhoudingen, zoals de deuterium-tot-waterstofverhouding, in ons eigen zonnestelsel. Deze verhoudingen verschillen aanzienlijk tussen verschillende planeten en zijn waarschijnlijk verbonden met de isotoopverhoudingen in protoplanetaire schijven. Deze verhoudingen worden beïnvloed door temperatuur- en stralingsafhankelijke processen die fractionatie worden genoemd. Door isotopen in exoplaneet atmosferen te detecteren en te analyseren, kunnen we bepalen waar de planeet is gevormd, hoeveel gas en vaste stoffen hebben bijgedragen aan de vorming ervan, en hoeveel atmosferisch verlies het heeft ondergaan (aangezien zware isotopen minder vatbaar zijn om te ontsnappen uit atmosferen).

Dit hoofdstuk presenteert de eerste detectie van het lichte isotopoloog van koolmonoxide ^{13}CO in de atmosfeer van een super-Jupiter genaamd YSES-1b, met behulp van de nabij-infrarood integraalveldspectrograaf SINFONI op de VLT. Dit markeert de eerste keer dat isotopenmetingen zijn uitgebreid naar exoplaneten. Door modellering van planetaire atmosferen en Bayesiaanse ophalingsanalyses hebben we de koolstofs isotoopverhouding in de planetaire atmosfeer bepaald op $^{12}\text{CO}/^{13}\text{CO} \sim 31$, wat betekent dat er een factor van twee versterking van ^{13}C is vergeleken met het lokale interstellair medium ($^{12}\text{C}/^{13}\text{C} \sim 68$). Dit resultaat suggereert dat de planeet waarschijnlijk buiten de CO-ijslijn is gevormd en hoofdzakelijk koolstof heeft verworven door accretie van ^{13}C -verrijkte ijsdeeltjes. Dit opent een spannende nieuwe weg om atmosferische kenmerken te verbinden met de vorming van planeten.

Hoofdstuk 3: Eerste detectie van het lichte isotopoloog ^{13}CO in een bruine dwerg

Na de detectie van ^{13}CO in de exoplaneet YSES-1b hebben we onze methode uitgebreid naar een exoplaneet-analoog genaamd 2M0355, een jonge, geïsoleerde bruine dwerg met vergelijkbare massa en effectieve temperatuur als de super-Jupiter-begleider. Interessant genoeg toonde deze studie geen verrijking van ^{13}CO in de bruine dwerg op basis van archiefwaarnemingen die waren genomen met de hoogwaardige spectrograaf NIRSPEC op de Keck-sterrenwacht. De koolstofs isotoopverhouding in de bruine dwerg ($^{12}\text{CO}/^{13}\text{CO} \sim 100$) staat in schril contrast met die in de exoplaneet en duidt op verschillende vormingsprocessen. Om dit benchmarkobject verder te onderzoeken, hebben we vervolgwaaarnemingen

van deze bruine dwerg uitgevoerd met behulp van de vernieuwde state-of-the-art spectrograaf CRIRES aan de VLT en waren we in staat de beperking op de koolstofsotoopverhouding te bevestigen. Bovendien stellen we voor dat de zuurstofsotoopverhouding ($^{16}\text{O}/^{18}\text{O}$) nu kan worden bestudeerd in heldere super-Jupiters en bruine dwergen met behulp van hoogwaardige spectroscopie. Het vergelijken van de atmosferische samenstellingen van reuzen-exoplaneten en bruine dwergen speelt een belangrijke rol bij het ontrafelen van hun onderscheidende vormingspaden.

Hoofdstuk 4: Zoeken naar He I airglow emissie van een hete Jupiter

Gasreuzen die zich zeer dicht bij hun moedersterren bevinden, kunnen aanzienlijke atmosferische erosie ondergaan als gevolg van de intense hoogenergetische straling van hun sterren. Dit proces is vooral relevant voor planeten die kleiner zijn dan Neptunus en drijft de evolutie van hun atmosferen aan. Een krachtige manier om atmosferische ontsnapping in deze planeten te bestuderen, is door te kijken naar de absorptie van heliumatomen in hun atmosferen, wat met succes is gedetecteerd in een dozijn exoplaneet-atmosferen tijdens overgangen. De heliumabsorptie is echter niet doorslaggevend om het atmosferische massaverlies op zichzelf te bepalen, omdat het moeilijk is om de effecten van atmosferische ontsnapping van de exosferische temperatuur te scheiden met alleen heliumabsorptie. Om dit probleem op te lossen, hebben we ons gericht op het zoeken naar helium-airglow-emissie om deze te combineren met de absorptie om de bovenste atmosferen beter te beperken. We hebben deze zoektocht uitgevoerd bij de niet-transiterende hete Jupiter τ Bootis b met behulp van de nabij-infrarood-spectrograaf CARMENES op het Calar Alto Observatorium. Hoewel dit leidde tot een niet-detectie, biedt onze studie belangrijke informatie over de detectielimieten van helium-airglow-emissie in exoplaneten, en we geloven dat telescopen van de volgende generatie in staat zullen zijn om deze emissie te meten. Het detecteren van helium-airglow-emissie zal cruciaal zijn bij het bestuderen van de atmosferische structuur, massaverliespercentages en bulk-atmosferische evolutie van gasreuzen die zeer dicht bij hun moedersterren staan.

Hoofdstuk 5: Ontwarren van hydrostatische en exosferische regimes van ultra-hete Jupiters

De krachtige hoogenergetische straling van nabije hete Jupiters resulteert in twee verschillende atmosferische regimes: de hydrostatische onderste atmosfeer en de hydrodynamische exosfeer. Om de dynamiek van deze regio's te begrijpen, zijn metingen van verschillende atomen of moleculen nodig. In dit hoofdstuk karakteriseren we de atmosfeer van de ultra-hete Jupiter MASCARA-4b, met een evenwichtstemperatuur van meer dan 2000 K, door gebruik te maken van transmissiespectroscopische waarnemingen met de hoogoplossende optische spectrograaf ESPRESSO op de VLT. Onze metingen detecteren verschillende absorberende soorten, waaronder H I, Na I, Fe I en Fe II in de planetaire atmosfeer. Om onze resultaten in context te plaatsen, vergelijken we onze bevindingen met die van zeven andere ultra-hete Jupiters en onderzoeken we de trend van deze atomaire absorptiesterktes. We ontdekken dat neutrale metaalsoorten het hydrostatische regime traceren, terwijl waterstof en geïoniseerde metalen de hydrodynamische exosfeer en atmosferische ontsnapping onderzoeken. Deze vergelijking stelt ons in staat om de eerste stap te zetten naar de analyse van hoogoplossende spectroscopische resultaten op

populatie-niveau, waardoor het mogelijk wordt om verschillende dynamische regimes van hoog-geïrriteerde atmosferen te onderscheiden.

Hoofdstuk 6: Diverse uitkomsten van interacties tussen dubbelsterren en schijven

Om inzicht te krijgen in de vorming van planeten is het begrijpen van circumstellaire schijven, de geboorteplaats van planeten, nodig. Aangezien ongeveer de helft van de sterren van het zonnetype in meervoudige stersystemen worden geboren, kan de aanwezigheid van stellaire metgezellen de morfologie en evolutie van de schijven wijzigen en mogelijk de uitkomsten van planeetvorming beïnvloeden. In dit hoofdstuk hebben we gepolariseerde differentiële beeldvorming gebruikt met SPHERE/IRDIS op de VLT om circumstellaire schijven in drie meervoudige systemen op te lossen: CHX 22, S CrA, en HP Cha, als onderdeel van het grote programma Disk Evolution Study Through Imaging of Nearby Young Stars (DESTINYS). De waargenomen schijfmorfologie, in combinatie met astrometrische en baananalyses voor de stellaire metgezellen, maakt het mogelijk om een beter begrip te krijgen van de wisselwerking tussen schijven en metgezellen. De vergelijking van de drie systemen beslaat een breed scala aan binaire scheidingen (50 – 500 au) en illustreert de afnemende invloed van metgezellen op schijfstructuren bij toenemende scheiding. Deze bevinding is consistent met de statistische analyse van exoplaneetpopulaties in binaire systemen, die suggereert dat planeetvorming waarschijnlijk wordt belemmerd in nauwe binaire systemen, terwijl het niet wordt onderdrukt in wijdverspreide binaire systemen.

Uitzicht: de oorsprong van planeten ontrafelen

Om de oorsprong van exoplaneten beter te begrijpen en de karakterisering van exoplaneet atmosferen uit te breiden tot een grotere steekproef, is vooruitkijken een belangrijke stap. Door het gebruik van formatietracers zoals elementaire en isotopische samenstellingen uit nabij-infrarood hoge-resolutie spectra, kunnen we populatie-niveau-analyses van jonge gasreuzen en bruine dwergen uitvoeren en verschillende klassen van sub-stellaire objecten vergelijken om zo vragen te beantwoorden. Dit stelt ons in staat om trends in atmosferische bestanddelen te verkennen met stellaire en planetaire eigenschappen, zoals massa en orbitale scheiding, en de plausibiliteit van verschillende formatiescenario's te beoordelen. Het bepalen van de chemische samenstelling kan bijdragen aan het overbruggen van de kloof tussen atmosferische waarnemingen en planeetvorming en -evolutie. Op deze manier kunnen we de fundamentele vraag beantwoorden wat de grens tussen planeten en bruine dwergen bepaalt.

Kijkend naar de toekomst zullen de komende dertig-meter klasse telescopen, zoals de Extremely Large Telescope (ELT), met het verwachte eerste licht binnen vijf jaar, en de volgende generatie vlaggenschip ruimtetelescopen, routinematig karakterisering kunnen leveren van kleinere exoplaneten. Hierdoor is het mogelijk om hun atmosferische biosignaturen en bewoonbaarheid te onderzoeken. De ELT zal bijzonder veelbelovend zijn voor het onderzoeken van zeldzame isotopen, zoals deuterium, in exoplaneten. Dit is namelijk een van de meest informatieve tracers voor planeetvorming en atmosferische evolutie. Met deze ontwikkelingen hopen we de ultieme vragen te kunnen beantwoorden over de uniciteit van ons zonnestelsel en hoe we hier zijn gekomen.

List of Publications

1. **Zhang, Y.**, Snellen, I. A. G., Mollière, P., Alonso-Floriano, F. J., Webb, R. K., Brogi, M., & Wytenbach, A. (2020) Search for He I airglow emission from the hot Jupiter τ Boo b. **A&A**, 641, A161.
2. **Zhang, Y.**, Snellen, I. A. G., Bohn, A. J., Mollière, P., Ginski, C., Hoeijmakers, H. J., Kenworthy, M. A., Mamajek, E. E., Meshkat, T., Reggiani, M., & Snik, F. (2021) The ^{13}CO -rich atmosphere of a young accreting super-Jupiter. **Nature**, 595, 370.
3. **Zhang, Y.**, Snellen, I. A. G., & Mollière, P. (2021) The $^{12}\text{CO}/^{13}\text{CO}$ isotopologue ratio of a young, isolated brown dwarf. Possibly distinct formation pathways of super-Jupiters and brown dwarfs. **A&A**, 656, A76.
4. **Zhang, Y.**, Snellen, I. A. G., Wytenbach, A., Nielsen, L. D., Lendl, M., Casasayas-Barris, N., Chaverot, G., Kesseli, A. Y., Lovis, C., Pepe, F. A., Psaridi, A., Seidel, J. V., Udry, S., & Ulmer-Moll, S. (2022) Transmission spectroscopy of the ultra-hot Jupiter MASCARA-4b. Disentangling the hydrostatic and exospheric regimes of ultra-hot Jupiters. **A&A**, 666, A47.
5. **Zhang, Y.**, Snellen, I. A. G., Brogi, M., & Birkby, J. L. (2022) VLT/CRIRES science verification observations: A hint of C^{18}O in the young brown dwarf 2M0355. **Res. Notes AAS**, 6, 194.
6. **Zhang, Y.**, Ginski, C., Huang, J., Zurlo, A., Beust H., Bae, J., Benisty, M., Garufi, A., Hogerheijde, M.R., van Holstein, R.G., Kenworthy, M., Langlois, M., Manara, C.F., Pinilla, P., Rab, C., Ribas, A., Rosotti, G.P., & Williams, J. (2023) Disk Evolution Study Through Imaging of Nearby Young Stars (DESTINYs): Diverse outcomes of binary-disk interactions. **A&A**, 672, A145.

Curriculum Vitæ

I was born in Datong, a city located in the northern province of Shanxi, China, on May 10, 1995. Growing up, I developed a fascination with the mysteries of the universe, fueled by books and cartoons that explored the cosmos. This early interest culminates in my decision to major in astronomy in college. From 2013 to 2017, I studied astronomy at Nanjing University, located in eastern China. During my undergraduate studies, I became particularly interested in exoplanets and began exploring different aspects of this fast-moving field. Under the guidance of Prof. Jiwei Xie, I completed my Bachelor's research project, simulating terrestrial planet formation in highly inclined binary systems. In 2016, I had the opportunity to conduct a summer internship at the European Southern Observatory (ESO), where I worked on digging into Kepler lightcurves to search for unusual transiting events.

The short experience at ESO inspired me to pursue a PhD degree overseas. In 2017, I came to Leiden University for the Master's program in astronomy and data science. During my time there, I conducted research projects related to exoplanets and protoplanetary disks. Under the supervision of Prof. Ignas Snellen, I used novel techniques to search for molecular signatures in the atmospheres of directly imaged exoplanets. Additionally, my work on the dust evolution in protoplanetary disks, supervised by Prof. Michiel Hogerheijde, provided me with new perspectives on the birth environment of planets.

After obtaining my Master's degree (*cum laude*, 2019), I was thrilled to be offered a PhD position in the group of Ignas Snellen at Leiden University to continue my exploration of exoplanet atmospheres. My PhD studies were not without challenges, as the pandemic limited the possibility of travel and communication. Nonetheless, this allowed me to focus on the research per se, leading to the first detection of minor isotopologues in exoplanet atmospheres. This discovery marks a highlight of my PhD and is presented in this dissertation.

Now, as I move forward in my career, I am honored to be awarded the 51 Pegasi b postdoctoral fellowship to start a new journey in the United States. As of October 2023, I will be a post-doctoral researcher at California Institute of Technology and continue to delve deeper into the characterization of exoplanet atmospheres and their connections to planet formation. I am eager to see what the future holds as we continue to push the boundaries of discovery.

Acknowledgments

Although pursuing a PhD is a personal journey, I have never been alone during the process and could not have made it this far without the help of many people.

First, I sincerely thank all the support staff (secretarais, IT helpdesk) at the Sterrewacht and University for sorting out miscellaneous problems and keep everything running smoothly.

I would like to express my deepest gratitude to my supervisor, Ignas, for the guidance and support for my career. Thank you for providing me with freedom in choosing any research project I wanted to work on (as one can easily tell from the broad range of topics in this dissertation). I appreciate your dedication to my academic and personal growth. Your insights during discussions have helped me develop the intuition for data as an observer, and your attitude towards science is an inspiring model. I am honored to have worked with you.

I am also thankful to other staff members at the Observatory, including Aline, Anthony, Ewine, Matt, Michiel, Nienke, and Yamila, with whom I had interactions, for your generous support and care for PhD students.

I would like to extend my appreciation to previous and current PhDs and postdocs in the Leiden exoplanet community, including Alex, Alex, Alex, Amy, Andrew, Aurora, Aurélien, Christian, Christiaan, Darío, Dilovan, Javi, Jens, Joe, Mantas, Núria, Patrick, Paul, Paul, Rico, Sam, Sebastiaan, Sid, and Tomas, who have provided a friendly and stimulating environment in the group. I obtained plenty of inspiration, advice, and help from the discussions with you all.

I am grateful to my collaborators, Paul, Laura, and Christian, for their guidance and great science. I hope to continue our collaboration in the future.

I would also like to thank the Master students, Rosa and Merel, who chose to work on research projects with me. Your enthusiasm and dedication have been impressive, and I have gained valuable experiences through mentoring you.

I am grateful to Shunsheng, Yuan, Zhenlin, and other fellow PhD students for sharing the journey and encouraging each other along the way.

I further thank my close friends in Leiden, Na, Yao, and Yu, with whom I enjoyed numerous dinners and movie nights. These warm memories are invaluable to me.

Last but not least, I express my gratitude to my parents and friends in China for their unwavering support throughout my academic journey. Whenever I feel lost, they always uplift me with their encouragement and love, sustaining me through the ups and downs.

I am grateful for the six years in Leiden, long enough that it almost becomes my second hometown. Thanks to all the people I have met and the experiences I have had, my perspective has been reshaped and my horizons have expanded immensely. No regrets.

